Tempo and Mode of Earth's Great Oxidation Event

Dissertation

der Mathematisch-Naturwissenschaftlichen Fakultät

der Eberhard Karls Universität Tübingen

zur Erlangung des Grades eines

Doktors der Naturwissenschaften

(Dr. rer. nat.)

vorgelegt von

Julius Christopher Havsteen

aus Kopenhagen, Dänemark

Tübingen

2024

Gedruckt mit Genehmigung der Mathematisch-Naturwissenschaftlichen Fakultät der Eberhard Karls Universität Tübingen.

Tag der mündlichen Qualifikation:	26.04.2024
Dekan:	Prof. Dr. Thilo Stehle
1. Berichterstatter/-in:	Prof. Dr. Ronny Schönberg
2. Berichterstatter/-in:	Prof. Dr. Martin Van Kranendonk

[redacted]

"Gazing deeper into your inner, cellular and molecular structure and that of the life around you, it is soon obvious that you are related to the other animals, and indeed that all living things form one kin. You see that you are fundamentally the same as them in all respects but one: they seem to be completely fulfilled by simply being, whereas you are driven to ask more and more questions..."

TIM LENTON & ANDREW WATSON
– REVOLUTIONS THAT MADE THE EARTH

Declaration

This dissertation is the result of my own work. Exceptions, which include collaborative efforts, are specifically indicated in Chapter 1 under section 1.3. Notably, Chapters 4 and 5 represent one published and one accepted manuscript submitted to the Journals *Precambrian Research* and the *South African Journal of Geology*, respectively. This work has not been previously submitted, in part or whole, to any university or institution for any degree, diploma, or other qualification. This work has been professionally formatted, not proofread, by JustDocumentz™ in accordance with the policies of Eberhard Karl University of Tübingen as communicated in writing to me by the University's doctoral office at the Faculty of Science.

Acknowledgments

[redacted]

Abstract

This PhD thesis investigates the temporal dynamics and mechanisms of the Great Oxidation Event (GOE), focusing on geological formations from the Transvaal Supergroup in South Africa. It integrates sedimentological observations with geochemical proxies to critical geological questions related to the tempo and mode of the GOE, as well as the links between atmospheric and marine oxygenation. The work is divided into three main work packages.

The first work package combines sedimentological field observations with advanced geochemical provenance proxies (provenance discrimination diagrams, zircon distribution patterns and Sr–Nd isotope systematics) to understand the depositional history of the 2353±18 Ma to 2316±7 Ma Duitschland and Rooihoogte formations in the Transvaal Area of the Transvaal Supergroup. The study concludes that the Duitschland and Rooihoogte formations are deposited contemporaneously, yet they represent distinct sedimentological expressions, each reflecting sedimentological characteristics influenced by their respective distance to the paleoshore line. This is critically important because both formations record some of the most pronounced shifts from mass-independent fractionation of sulfur isotopes (MIF-S) to mass-dependent fractionation of sulfur isotopes (MDF-S) in the geological record, a key indicator for atmospheric O_2. Consequently, the disappearance of MIF-S in these two formations should be interpreted as indicative of a single-step atmospheric change rather than as part of a prolonged and dynamic oxygenation trajectory with oscillations over the MIF-S threshold.

With all evidence from the first work package indicating a contemporaneous deposition of the Duitschland and Rooihoogte formations, the second work package shifts focus to the temporal marine oxygen evolution of the atmosphere-ocean system during their deposition. Interestingly, while the Duitschland and Rooihoogte formations have been studied extensively concerning atmospheric oxygenation through multiple sulfur isotope systematics, comparatively little work has been done on the contemporary marine oxygenation state. Accordingly, this work package presents chemostratigraphic transects from four widely spaced drill cores within the Transvaal Basin that intersect the Duitschland and Rooihoogte formations, extending into the lower segments of the overlying Timeball Hill formation. Combined analysis of multiple geochemical redox-sensitive proxies (total S and total organic C, redox-sensitive trace element systematics, $\delta^{13}C$, $\delta^{34}S$ and $\delta^{98}Mo$) indicates a dynamic evolution of the marine oxygenation state. The data suggest an initial transition from a stratified

oceanic state to oxic-suboxic conditions preceding the demise of MIF-S, followed by a subsequent transition to anoxic-suboxic settings. These findings imply a geobiological-driven feedback mechanism, where early atmospheric oxygenation during the GOE is causally linked to a contemporaneous decline of the marine redox state, at least within the Transvaal Basin.

The third work package focuses on the ~2.4 Ga Hotazel Formation - a banded iron formation (BIF) that is remarkable in the global geological record for its unique cyclicity of BIF layers intertwined with Mn-rich layers (up to >50 wt.%) relative to the about 1 wt.% MnO typically found in BIFs. Currently, no consensus exists for the genesis of the Hotazel Formation, but the two most commonly proposed models in the literature are an '*Upwelling Model'* and a '*Hydrothermal Plume Model'*. The *Upwelling model* envisions that deep waters enriched in Fe^{2+} and Mn^{2+} are transported onto the continental shelf and deposited according to their redox potential, with Fe precipitating more distal than Mn. However, the model fails to address the sedimentological observation that Mn-layers deposited on larger water depths relative to Fe-layers. The *Hydrothermal Plume Model* suggests a low-temperature hydrothermal vent system that supplies Fe^{2+} and Mn^{2+} to a restricted back-arc basin with a fully oxygenated water column. Yet, the model does not explain the absence of geochemical indications of such hydrothermal activity. This work package proposes a third model, the *'Bioproductivity Model'*, in which fluctuations in the intensity of marine primary productivity drive the expansion and contraction of oxygen minimum zones (OMZs) on the shelf. This process ultimately leads to a series of dissolution-precipitation of Fe-Mn cycles within the OMZ, termed OMZ-redirection. When dissolved O_2 begins to increase in the lower reaches of the OMZ, Fe and Mn start to reprecipitate based on their redox potential, with Fe precipitating before Mn. This creates an inversed precipitation sequence compared to typical Fe-Mn redox dynamics and explains the sedimentological pattern of Mn being deposited at deeper water depths than Fe. Furthermore, the model effectively explains the geochemical signatures of exceptionally light $\delta^{56}Fe$ and remarkably heavy $\delta^{98}Mo$ values. Iron isotopes are driven to increasingly negative values by the repeated iterations of precipitation-dissolution cycles during OMZ-redirection. Simultaneously, any isotopically light Mo, initially co-precipitated with Fe-Mn-(hydr)oxides in the uppermost water column, becomes immobilized in the anoxic sediment of the OMZ, preventing it from reaching reprecipitated Mn-layers beneath the OMZ. As a result, Mn-layers from the Hotazel Formation exhibit low Mo concentrations and heavy $\delta^{98}Mo$ compositions.

Zusammenfassung

In dieser Doktorarbeit werden die zeitliche Dynamik und die Mechanismen der Großen Sauerstoffkatastrophe (engl. Great Oxidation Event; GOE) untersucht, wobei der Schwerpunkt auf geologischen Formationen aus der Transvaal Supergruppe in Südafrika liegt. Hierbei werden sedimentologische Beobachtungen mit geochemischen Proxies zu kritischen geologischen Fragen im Zusammenhang mit dem Tempo und der Art des GOE sowie den Verbindungen zwischen atmosphärischer und mariner Sauerstoffanreicherung integriert. Diese Arbeit ist in folgende drei Arbeitspakete unterteilt:

Das erste Arbeitspaket kombiniert sedimentologische Feldbeobachtungen mit modernen geochemischen Proxies für die sedimentologische Provenanz (Provenanzunterscheidungs-diagramme, Zirkon Verteilungsmuster und Sr-Nd-Isotopensystematik), um die Ablagerungsgeschichte der 2353±18 Ma bis 2316±7 Ma Duitschland- und Rooihoogte-Formationen im Transvaal Becken der Transvaal Supergruppe zu verstehen. Die Studie kommt hierbei zu dem Schluss, dass die Duitschland- und die Rooihoogte-Formation gleichzeitig abgelagert wurden, jedoch sedimentologische Unterschiede aufweisen, die durch ihre Entfernung zur Paläoküstenlinie erklärbar sind. Diese Erkenntnis ist von entscheidender Bedeutung, da beide Formationen einige der ausgeprägtesten Verschiebungen von der massenunabhängigen Fraktionierung von Schwefelisotopen (MIF-S) zur massenabhängigen Fraktionierung von Schwefelisotopen (MDF-S) in den geologischen Aufzeichnungen aufweisen, ein Schlüsselindikator für die Präsenz von atmosphärischen O_2. Folglich sollte das Verschwinden von MIF-S in diesen beiden Formationen als Hinweis auf einen einstufigen atmosphärischen Wandel interpretiert werden und nicht als Teil einer langfristigen, dynamischen Variation im Sauerstoffgehalt mit häufigem Überschreiten der MIF-S-Schwelle.

Da alle Belege aus dem ersten Arbeitspaket auf eine zeitgleiche Ablagerung der Duitschland- und Rooihoogte-Formationen hindeuten, verlagert sich der Schwerpunkt des zweiten Arbeitspakets auf die marine Sauerstoffentwicklung des Atmosphäre-Ozean-Systems während ihrer Ablagerung. Interessanterweise wurden die Duitschland- und Rooihoogte-Formationen hinsichtlich der atmosphärischen Sauerstoffanreicherung bereits durch eine Vielzahl von Schwefel-Isotopen-Systemen umfassend untersucht, während der zeitgenössische Zustand der marinen Sauerstoffanreicherung vergleichsweise wenig erforscht wurde. Dementsprechend werden in diesem zweiten Arbeitspaket chemostratigraphische Transekte von vier weit

auseinander liegenden Bohrkernen im Transvaal-Becken vorgestellt, welche die Duitschland- und Rooihoogte-Formationen durchteufen und sich bis in die unteren Segmente der darüber liegenden Timeball Hill-Formation erstrecken. Eine kombinierte Analyse mehrerer geochemischer redoxsensitiver Proxies, einschließlich Gesamtgehalte von S und organischem C, Spurenelement-Systematiken, als auch $\delta^{13}C$, $\delta^{34}S$ und $\delta^{98}Mo$ Isotopien, deutet auf eine dynamische Entwicklung des marinen Sauerstoffgehalts hin. Die Daten deuten auf einen anfänglichen Übergang von einer sauerstoffstratifizierten Wassersäule zu oxisch-suboxischen Bedingungen hin, der dem Verschwinden des MIF-S Signals vorausging. Dies ist gefolgt von einem anschließenden Übergang zu anoxisch-suboxischen Bedingungen. Diese Ergebnisse deuten auf einen geobiologisch bedingten Rückkopplungsmechanismus hin, bei dem die frühe atmosphärische Sauerstoffanreicherung, während des GOE, kausal mit einer gleichzeitigen Verringerung des marinen Sauerstoffgehaltes verbunden ist, zumindest im Transvaal-Becken.

Das dritte Arbeitspaket konzentriert sich auf die Hotazel-Formation (~2,4 Ga) - eine gebänderte Eisenformation (engl. Banded iron formation; BIF), die in der globalen geologischen Aufzeichnung durch ihre einzigartige Zyklizität der hervorsticht. Sie enthält außergewöhnlich Mn-reiche Schichten (bis zu >50 Gew.-%) im Vergleich zu den etwa 1 Gew.-% MnO, die typischerweise in BIFs gefunden werden. Derzeit besteht keinen Konsens über die Entstehung der Hotazel-Formation. Die in der Literatur am häufigsten vorgeschlagenen Modelle sind ein "Upwelling-Modell" und ein "Hydrothermal Plume-Modell". Ersteres geht davon aus, dass mit Fe^{2+} und Mn^{2+} angereicherte Tiefenwässer auf den Kontinentalschelf transportiert und entsprechend ihrem Redoxpotenzial abgelagert werden, wobei Fe weiter entfernt von der Küste ausfällt als Mn. Dieses Modell geht jedoch nicht auf die sedimentologische Beobachtung ein, dass die Mn-reichen Schichten im Vergleich zu den Fe-reichen Schichten in größeren Wassertiefen abgelagert wurden. Das Hydrothermal-Plume-Modell hingegen, geht von einem niedrigtemperierten Hydrothermal-System aus, welches Fe^{2+} und Mn^{2+} in ein vom offenen Ozean abgeschnittenes Backarc-Becken mit einer vollständig oxigenierten Wassersäule liefert. Dieses Modell erklärt jedoch nicht das Fehlen von geochemischen Hinweisen auf eine solche hydrothermale Aktivität. In diesem Arbeitspaket wird ein drittes Modell vorgeschlagen, das "Bioproduktivitätsmodell", bei dem Schwankungen in der Intensität der marinen Primärproduktivität die Ausdehnung und Schrumpfen von Sauerstoffminimumzonen (engl. Oxygen minimum zones; OMZ) auf dem Schelf beeinflussen. Dieser Prozess führt letztlich zu einer Reihe von Auflösungs- und Ausfällungs-Zyklen von Fe und Mn innerhalb der OMZ, ein Phänomen, das als OMZ-Umverteilung (engl. OMZ-redirection) bezeichnet wird. Wenn der

gelöste O_2-Gehalt in den unteren Bereichen der OMZ ansteigt, beginnen Fe und Mn auf der Grundlage ihres Redoxpotenzials auszufallen, wobei Fe vor Mn ausfällt. Dies führt zu einer umgekehrten Ausfällungssequenz im Vergleich zur typischen Fe-Mn-Redoxdynamik und erklärt das sedimentologische Muster der Ablagerung von Mn in tieferen Wassertiefen gegenüber Fe. Darüber hinaus erklärt das Modell effektiv die geochemischen Signaturen von außergewöhnlich leichten δ^{56}Fe- und bemerkenswert schweren δ^{98}Mo-Werten. Die Eisenisotope werden durch die wiederholten Iterationen der Niederschlags-Auflösungs-Zyklen während der OMZ-Umverteilung in Richtung zunehmend negativere Werte getrieben. Gleichzeitig wird jegliches isotopisch leichtes Mo, das ursprünglich zusammen mit Fe-Mn-(Hydr)-Oxiden in der obersten Wassersäule ausgefällt wurde, im anoxischen Sediment der OMZ fixiert, so dass es die wiederausgefällten Mn-Schichten unterhalb der OMZ nicht erreichen kann. Infolgedessen weisen die Mn-Schichten aus der Hotazel-Formation niedrige Mo-Konzentrationen und hohe δ^{98}Mo-Zusammensetzungen auf.

This abstract is translated into German from its English version by Markus Gogouvitis

Contents

List of Figures

List of Tables

Acronyms

BD:	Below detection limit
BIF:	Banded iron formation
D/R:	Duitschland and Rooihoogte formations
DIR:	Dissimilatory iron reduction
DMR:	Dissimilatory manganese reduction
ETA:	Eastern Transvaal Area
Ga:	Billion years ago
GOE:	Great Oxidation Event
GWA:	Griqualand West Area
GWB:	Griqualand West Basin
HREE:	Heavy rare earth elements
ICPMS:	Inductively coupled plasma mass spectrometry
IRMS:	Isotope ratio mass spectrometer
JM:	Johnson Matthey
LJE:	Lomagundi–Jatuli Event
LREE:	Light rare earth elements
MC-ICP-MS:	Multicollector Inductively Coupled Plasma Mass Spectrometry
MDF-S:	Mass-dependent fractionation of sulfur isotopes
MIF-S:	Mass-independent fractionation of sulfur isotopes
My:	Million years
NIST:	National Institute for Standards and Technology
OMZ:	Oxygen minimum zone
P-OMZ:	Perennial oxygen minimum zone
PAL:	Present atmospheric level

PAAS:	Post Archean average shale
REE:	Rare earth elements
RSTE:	Redox-sensitive trace element
SRM:	Standard reference material
TB:	Transvaal Basin
TOC:	Total organic carbon
TS:	Total sulfur
VPDB:	Vienna Pee Dee Belemnite
WTA:	Western Transvaal Area
XRF:	X-ray fluorescence

Chapter 1

Introduction

1.1 Problem Statement

For roughly the first ca. 2.5 Ga of Earth's history, the planet's atmosphere was largely devoid of free molecular oxygen (Holland, 1994; Holland, 2002). The subsequent oxygenation of the planet's atmosphere towards the present 21 vol.% occurred in two main O_2 pulses: One around the Archean-Paleoproterozoic boundary and another at the end of the Neoproterozoic Era (e.g., Bekker et al., 2004; Holland, 2002, 2006; Och & Shields-Zhou, 2012). The first of these oxygenation pulses is referred to as the Great Oxidation Event and occurred from approximately ca. 2.45 to 2.32 Ga (Bekker et al., 2004; Hannah et al., 2004). During this period, free molecular oxygen accumulated for the first time to levels exceeding ~10^{-6} of present atmospheric levels (PAL) (Farquhar, Bao, et al., 2000; Pavlov & Kasting, 2002; Zahnle et al., 2006). The GOE can be intimately linked with the evolution of oxygenic photosynthesis (Blankenship & Hartman, 1998), introducing a potent new oxidizing power to the atmosphere-ocean system that, over time, drastically rearranged the source-sink balance of the planetary surface reservoirs (e.g., Brocks et al., 1999; Catling et al., 2001; Holland, 2002). In the aftermath of the GOE between ca. 2.3 and 2.1 Ga, atmospheric oxygen levels are hypothesized to have experienced an 'oxygen overshoot', known as the Lomagundi–Jatuli Event (LJE). During the LJE, an estimated 12 to 22 times the current atmospheric O_2 inventory was liberated through carbon burial, resulting in the largest positive $\delta^{13}C$ isotope excursion in carbonate rocks ever recorded (e.g., Bekker & Holland, 2012; Karhu & Holland, 1996). However, this interpretation is not unequivocally accepted, with some studies suggesting that the $\delta^{13}C$ excursion is not a global phenomenon but rather facies-dependent and, as such, does not reflect global perturbations in the redox state of the Earth system (e.g., Prave et al., 2022). Irrespective of the current discourse, it is indisputable that atmospheric O_2 levels surged during the GOE, which left substantial shreds of evidence in the geological record (Fig. 1.1), such as the appearance of Fe-hydroxides in terrestrial sediment deposits (Beukes et al., 2002), redox-sensitive trace element enrichment in marine shales (Anbar et al., 2007; Wille et al., 2007) and the disappearance of detrital pyrite, siderite and uraninite (Rasmussen & Buick, 1999). Yet, the

most striking proxy for the earliest accumulation of free molecular oxygen in the atmosphere derives from sulfur isotope systematics since mass-independent fractionation of sulfur isotopes (MIF-S) disappears once atmospheric O_2 concentrations reach levels higher than 10^{-6} of PAL (Catling & Zahnle, 2020; Farquhar, Bao, et al., 2000; Pavlov & Kasting, 2002) (Fig 1.1). The underlying fundamental mechanism is rooted in the premise that increasing ozone levels effectively blocks a significant portion of the ultraviolet radiation originating from the sun. This ensures that the photochemically induced disproportionation of S, responsible for MIF-S isotopic signatures, stopped once atmospheric oxygen levels reached this threshold (Bains-Sahota & Thiemens, 1989; Farquhar, Savarino, et al., 2000; Zmolek et al., 1999). From a theoretical perspective, the transition from MIF-S to MDF-S stands out as an excellent chemostratigraphic marker horizon for atmospheric O_2 concentrations. Despite the elegance of this idea, the $\Delta^{3x}S$ record has proven surprisingly complicated to interpret and has complicated rather than simplified our understanding of GOE. The seemingly global asynchronous collapse of $\Delta^{3x}S$ to near zero values (Izon et al., 2022; Philippot et al., 2018; Uveges et al., 2023) underscores the need for further investigation of global plus local chronostratigraphic correlations that archives the disappearance of MIF-S, crustal recycling of MIF-S signals, refined atmospheric modelling and an improved understanding of planetary tipping points through geobiological feedback loops.

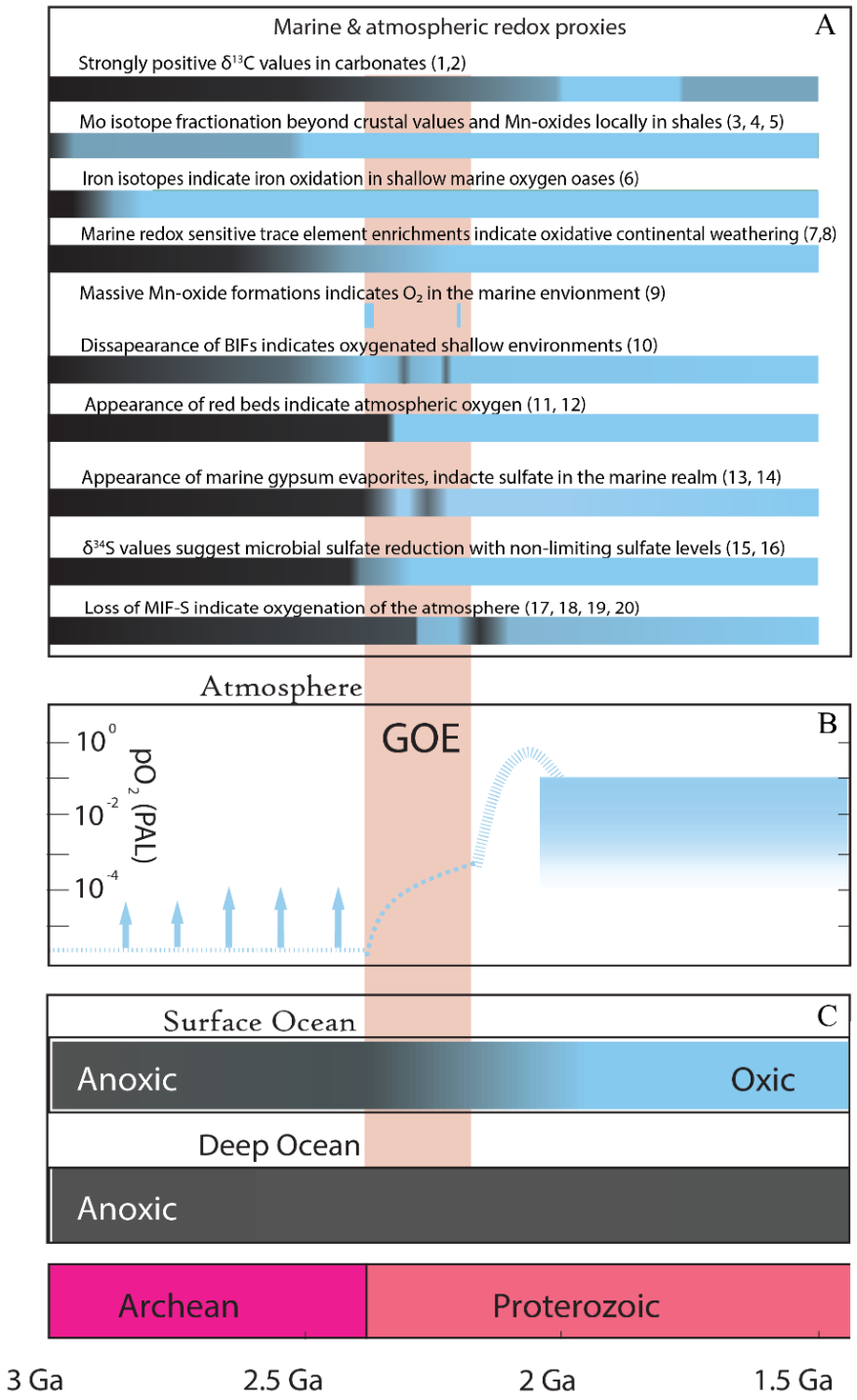

Figure 1.1. *Redox evolutions of Earth's atmosphere-ocean system around the Great Oxidation Event.* Panel **A** shows the emergence and disappearance of various redox proxies. Blue colors indicates the presence of free molecular oxygen based on the specific parameter, while dark grey colors suggest its absence, according the specific proxy. References for the different redox proxies are given in Supplementary Table S1. Panel B and C illustrates the atmospheric and marine oxygen evolution between 3 and 1.5 Ga and are modified from Alcott et al. (2019).

While signs of substantial atmospheric oxygenation are absent in the geological record before the GOE, multiple paleoenvironmental redox studies indicate intermediate shallow marine oxygenation unfolding some 100 to 300 million years earlier (Anbar et al., 2007; Brocks et al., 1999; Eroglu et al., 2017; Kurzweil et al., 2015; Ossa et al., 2018; Roué et al., 2021; Wille et al., 2007) and potentially even around or earlier than 2.8 Ga (Eickmann et al., 2018; Falcón et al., 2010; Planavsky et al., 2014; Rosing & Frei, 2004). The prevalent view is that oxygenic phototrophs thrived in so-called 'oxygen oases' within the shallow marine realm of the Neoarchean. This localized oxygen production induced oxygenation in shallow waters that momentarily sparked redox cycling on the continents for short episodes that are commonly referred to as 'whiffs of oxygen' (Anbar et al., 2007; Lyons et al., 2014; Voegelin et al., 2010; Warchola et al., 2018; Wille et al., 2007)

The apparent decoupling of marine and atmospheric oxygenation remains poorly understood. However, it does relate to factors such as the origin of photosynthesis, global tectonics, the source-sink balance of Earth's surface reservoirs as well as the mixing and gas equilibration speed between such reservoirs (Buick, 2008; Farquhar et al., 2011; Holland, 2002; Kump & Barley, 2007; Olson et al., 2013). To this point, no single model for the redox evolution of the planet has sufficiently balanced the global redox budget leading up to and during the GOE (Kasting, 2013). Despite the development of several models, the question of whether the different drivers and the temporal evolution of atmospheric oxygenation followed an oscillating or sudden trajectory remains unresolved (e.g., Bekker et al., 2004; Gumsley et al., 2017; Izon et al., 2022; Luo et al., 2016; Poulton et al., 2021; Warke et al., 2020).

To improve our current understanding of the complex interplay of geobiological mechanisms leading up to, during and following the GOE, it is crucially important to gather more sedimentological and geochemical evidence and to interpret paleoenvironmental redox conditions grounded in field observations. Environmental redox conditions vary temporally, spatially and postdepositionally, and thus, any redox proxy is meaningless if not interpreted within a sound sedimentological framework.

1.2 Purpose of Study

The purpose of this study relies on two key objectives:

1. To understand whether the GOE followed a sudden or oscillating pathway.
2. To improve current knowledge regarding the coevolution of the atmosphere-ocean system during the onset of the GOE.

The exact stratigraphic correlation of strata recording the transition from MIF-S to MDF-S is not unequivocally accepted, both between different cratons and even within individual sedimentary basins (e.g., Gumsley et al., 2017; Philippot et al., 2018; Rasmussen et al., 2013; Schröder et al., 2016). For instance, in the Transvaal Supergroup (South Africa), the Duitschland and Rooihoogte formations both record some of the most pronounced shifts from MIF-S to MDF-S in the global geological record (e.g., Guo et al., 2009; Luo et al., 2016; Poulton et al., 2021). Still, it is unclear whether the Duitschland and Rooihoogte formations represent two distinct formations deposited in two separate basins (e.g., Gumsley et al., 2017; Moore et al., 2012) or were deposited contemporaneously but at varying distances from paleo-shoreline (e.g., Coetzee, 2001; Schröder et al., 2016). This distinction is critically important when viewed in the light of the GOE — a correlative deposition would indicate a sudden atmospheric pulse of O_2 accumulation, whereas a decoupled depositional history would indicate an oscillating oxygen trajectory of Earth's atmosphere.

In addition, while earlier studies of multiple sulfur isotope systematics of the Duitschland and Rooihoogte formations have been instrumental to our understanding of atmospheric oxygenation (Guo et al., 2009; Izon et al., 2022; Luo et al., 2016; Poulton et al., 2021), comparatively little work has been done on the contemporary marine realm during their deposition. Marine and atmospheric redox evolution is closely linked through geobiological feedback mechanisms and rapid gas exchange between the upper ocean and the atmosphere (Liss & Johnson, 2014; Olson et al., 2013). The ca. ~2353 ± 18 Ma to 2.316 ± 7 Ma Duitschland and Rooihoogte formations (Hannah et al., 2004; Zeh et al., 2020) and the ca. ~2413 ± 15 Ma Hotazel Formation (Schier et al., 2020) thus provide an excellent case study to investigate the causality between marine and atmospheric oxygenation within the Transvaal Supergroup. By comparing several marine redox proxies (e.g., $\delta^{98}Mo$, $\delta^{56}Fe$, $\delta^{13}C$ and $\delta^{34}S$) to the disappearance of MIF-S in the geological record, we aim to improve our understanding of the tempo and mode of the atmosphere-ocean system redox evolution during the onset of the GOE.

The *CIMERA-Agouron GOE scientific drill cores* intersect both the Duitschland and Rooihoogte formations as well as the lowermost parts of the overlying Timeball Hill Formation. The access to these drill cores thus provides an excellent opportunity to both investigate the stratigraphic relations between the Duitschland and Rooihoogte formations and, simultaneously, study the marine response to the earliest signs of O_2 accumulation in the atmosphere. Similarly, samples from the MP72 drill core intersecting the Hotazel Formation (a banded iron formation), deposited just prior to the Duitschland and Rooihoogte formations but in another preserved structural basin of the Transvaal Supergroup, also help to investigate the temporal evolution of the marine redox landscape at the onset of the GOE.

1.3 Thesis Overview and Contributions of Authors

This thesis is compiled in the *'monograph including manuscripts'* format, in which individual chapters are written in a format targeted towards scientific publication. Such a thesis structure requires that each chapter can be read individually without the broader framework of the thesis. Hence, redundancy occurs between different chapters, especially regarding sections concerning 'introduction' and 'analytical methods'. Also, please be aware that different chapters in this thesis either adhere to British or American English writing standards, as dictated by the specific guidelines of the scientific journal in which the work is published. Following university policies, each chapter title and the relative contribution of other researchers to different chapters are listed below.

Chapter 1: Published paper

Title: Evidence for contemporaneous deposition of the Duitschland and Rooihoogte formations (Transvaal Supergroup): Implications for the Tempo and Mode of Earth's Great Oxidation

Authors: **Julius C. Havsteen**, Ilka C. Kleinhanns, Stefan Schröder, Benjamin Eickmann, Gareth Izon; Markus D. Gogouvitis, Rebeun Ngobeli, Nicolas J. Beukes, Ronny Schoenberg

Author Position: 1

Scientific ideas: 75 %

Data generation: 80 %

Analysis and interpretation: 75 %

Writing: 85 %

Chapter 2: Accepted paper

Title: Atmospheric oxygenation at the onset of Earth's Great Oxidation forced marine anoxia

Authors: **Julius C. Havsteen**, Benjamin Eickmann, Gareth Izon, Ilka C. Kleinhanns, Carolina Rosca1, Nicolas J. Beukes, Ronny Schoenberg

Author Position: 1

Scientific ideas: 95 %

Data generation: 85 %

Analysis and interpretation: 100 %

Writing: 95 %

Chapter 3: Unpublished manuscript

Title: The Hotazel Formation: Unraveling the Interplay between Bioproductivity, Oxygen Minimum Zones and Archean Marine Redox Evolution

Authors (Preliminary): **Julius C. Havsteen**, Albertus Smith, Dillan Fitton, Gina Stooß, Benjamin Eickmann, Ilka C. Kleinhanns, Ronny Schoenberg

Author Position: 1

Scientific ideas: 95 %

Data generation: 33 %

Analysis and interpretation: 95 %

Writing: 98 %

1.4 References

Anbar, A. D., Duan, Y., Lyons, T. W., Arnold, G. L., Kendall, B., Creaser, R. A., Kaufman, A. J., Gordon, G. W., Scott, C., & Garvin, J. (2007). A whiff of oxygen before the great oxidation event? *Science*, *317*(5846), 1903-1906.

Bains-Sahota, S. K., & Thiemens, M. H. (1989). A mass-independent sulfur isotope effect in the nonthermal formation of S2F10. *The Journal of Chemical Physics*, *90*(11), 6099-6109.

Bekker, A., & Holland, H. (2012). Oxygen overshoot and recovery during the early Paleoproterozoic. *Earth and Planetary Science Letters*, *317*, 295-304.

Bekker, A., Holland, H., Wang, P.-L., Rumble Iii, D., Stein, H., Hannah, J., Coetzee, L., & Beukes, N. (2004). Dating the rise of atmospheric oxygen. *Nature*, *427*(6970), 117.

Bekker, A., Karhu, J., & Kaufman, A. (2006). Carbon isotope record for the onset of the Lomagundi carbon isotope excursion in the Great Lakes area, North America. *Precambrian Research*, *148*(1-2), 145-180.

Bekker, A., & Kaufman, A. J. (2007). Oxidative forcing of global climate change: a biogeochemical record across the oldest Paleoproterozoic ice age in North America. *Earth and Planetary Science Letters*, *258*(3-4), 486-499.

Bekker, A., Kaufman, A. J., Karhu, J. A., Beukes, N. J., Swart, Q. D., Coetzee, L. L., & Eriksson, K. A. (2001). Chemostratigraphy of the Paleoproterozoic Duitschland Formation, South Africa: implications for coupled climate change and carbon cycling. *American Journal of Science*, *301*(3), 261-285.

Beukes, N. J., Dorland, H., Gutzmer, J., Nedachi, M., & Ohmoto, H. (2002). Tropical laterites, life on land, and the history of atmospheric oxygen in the Paleoproterozoic. *Geology*, *30*(6), 491-494.

Beukes, N. J., Swindell, E. P., & Wabo, H. (2016). Manganese deposits of Africa. *Episodes Journal of International Geoscience*, *39*(2), 285-317.

Blankenship, R. E., & Hartman, H. (1998). The origin and evolution of oxygenic photosynthesis. *Trends in biochemical sciences*, *23*(3), 94-97.

Brocks, J. J., Logan, G. A., Buick, R., & Summons, R. E. (1999). Archean molecular fossils and the early rise of eukaryotes. *Science*, *285*(5430), 1033-1036.

Buick, R. (2008). When did oxygenic photosynthesis evolve? *Philosophical Transactions of the Royal Society B: Biological Sciences*, *363*(1504), 2731-2743.

Cameron, E. (1982). Sulphate and sulphate reduction in early Precambrian oceans. *Nature*, *296*(5853), 145-148.

Canfield, D. E. (2005). The early history of atmospheric oxygen: homage to Robert M. Garrels. *Annu. Rev. Earth Planet. Sci.*, *33*, 1-36.

Catling, D. C., & Zahnle, K. J. (2020). The archean atmosphere. *Science advances*, *6*(9), eaax1420.

Catling, D. C., Zahnle, K. J., & McKay, C. P. (2001). Biogenic methane, hydrogen escape, and the irreversible oxidation of early Earth. *Science*, *293*(5531), 839-843.

Coetzee, L. L. (2001). *Genetic stratigraphy of the Paleoproterozoic Pretoria Group in the western Transvaal* University of Johannesburg, M.Sc. thesis (unpublished), 210 p.].

Eickmann, B., Hofmann, A., Wille, M., Bui, T. H., Wing, B. A., & Schoenberg, R. (2018). Isotopic evidence for oxygenated Mesoarchaean shallow oceans. *Nature Geoscience*, *11*(2), 133-138.

Eroglu, S., van Zuilen, M. A., Taubald, H., Drost, K., Wille, M., Swanner, E. D., Beukes, N. J., & Schoenberg, R. (2017). Depth-dependent δ13C trends in platform and slope settings of the Campbellrand-Malmani carbonate platform and possible implications for Early Earth oxygenation. *Precambrian Research*, *302*, 122-139.

Falcón, L. I., Magallón, S., & Castillo, A. (2010). Dating the cyanobacterial ancestor of the chloroplast. *The ISME journal*, *4*(6), 777-783.

Farquhar, J., Bao, H., & Thiemens, M. (2000). Atmospheric influence of Earth's earliest sulfur cycle. *Science*, *289*(5480), 756-758.

Farquhar, J., Savarino, J., Jackson, T. L., & Thiemens, M. H. (2000). Evidence of atmospheric sulphur in the martian regolith from sulphur isotopes in meteorites. *Nature*, *404*(6773), 50-52.

Farquhar, J., Zerkle, A. L., & Bekker, A. (2011). Geological constraints on the origin of oxygenic photosynthesis. *Photosynthesis research*, *107*(1), 11-36.

Gumsley, A. P., Chamberlain, K. R., Bleeker, W., Soderlund, U., de Kock, M. O., Larsson, E. R., & Bekker, A. (2017). Timing and tempo of the Great Oxidation Event. *Proc Natl Acad Sci U S A*, *114*(8), 1811-1816. https://doi.org/10.1073/pnas.1608824114

Guo, Q., Strauss, H., Kaufman, A. J., Schröder, S., Gutzmer, J., Wing, B., Baker, M. A., Bekker, A., Jin, Q., & Kim, S.-T. (2009). Reconstructing Earth's surface oxidation across the Archean-Proterozoic transition. *Geology*, *37*(5), 399-402.

Hannah, J. L., Bekker, A., Stein, H. J., Markey, R. J., & Holland, H. D. (2004). Primitive Os and 2316 Ma age for marine shale: implications for Paleoproterozoic glacial events and the rise of atmospheric oxygen. *Earth and Planetary Science Letters*, *225*(1-2), 43-52.

Holland, H. (1994). Early Proterozoic atmospheric change. *Early life on Earth*.

Holland, H. D. (2002). Volcanic gases, black smokers, and the Great Oxidation Event. *Geochimica et Cosmochimica Acta*, *66*(21), 3811-3826.

Holland, H. D. (2006). The oxygenation of the atmosphere and oceans. *Philosophical Transactions of the Royal Society B: Biological Sciences*, *361*(1470), 903-915.

Izon, G., Luo, G., Uveges, B. T., Beukes, N., Kitajima, K., Ono, S., Valley, J. W., Ma, X., & Summons, R. E. (2022). Bulk and grain-scale minor sulfur isotope data reveal complexities in the dynamics of Earth's oxygenation. *Proceedings of the National Academy of Sciences*, *119*(13), e2025606119.

Karhu, J. A., & Holland, H. D. (1996). Carbon isotopes and the rise of atmospheric oxygen. *Geology*, *24*(10), 867-870.

Kasting, J. F. (2013). What caused the rise of atmospheric O2? *Chemical Geology*, *362*, 13-25.

Kump, L. R., & Barley, M. E. (2007). Increased subaerial volcanism and the rise of atmospheric oxygen 2.5 billion years ago. *Nature*, *448*(7157), 1033.

Kurzweil, F., Wille, M., Gantert, N., Beukes, N. J., & Schoenberg, R. (2016). Manganese oxide shuttling in pre-GOE oceans–evidence from molybdenum and iron isotopes. *Earth and Planetary Science Letters*, *452*, 69-78.

Kurzweil, F., Wille, M., Schoenberg, R., Taubald, H., & Van Kranendonk, M. J. (2015). Continuously increasing δ98Mo values in Neoarchean black shales and iron formations from the Hamersley Basin. *Geochimica et Cosmochimica Acta*, *164*, 523-542.

Liss, P. S., & Johnson, M. T. (2014). *Ocean-atmosphere interactions of gases and particles*. Springer Nature.

Luo, G., Ono, S., Beukes, N. J., Wang, D. T., Xie, S., & Summons, R. E. (2016). Rapid oxygenation of Earth's atmosphere 2.33 billion years ago. *Science advances*, *2*(5), e1600134.

Lyons, T. W., Reinhard, C. T., & Planavsky, N. J. (2014). The rise of oxygen in Earth's early ocean and atmosphere. *Nature*, *506*(7488), 307.

Moore, J. M., Polteau, S., Armstrong, R., Corfu, F., & Tsikos, H. (2012). The age and correlation of the Postmasburg Group, southern Africa: Constraints from detrital zircon grains. *Journal of African Earth Sciences*, *64*, 9-19.

Och, L., & Shields-Zhou, G. A. (2012). The Neoproterozoic oxygenation event: Environmental perturbations and biogeochemical cycling. *Earth-Science Reviews*, *110*, 26–57. https://doi.org/10.1016/j.earscirev.2011.09.004

Olson, S. L., Kump, L. R., & Kasting, J. F. (2013). Quantifying the areal extent and dissolved oxygen concentrations of Archean oxygen oases. *Chemical Geology*, *362*, 35-43.

Ossa, F. O., Hofmann, A., Wille, M., Spangenberg, J. E., Bekker, A., Poulton, S. W., Eickmann, B., & Schoenberg, R. (2018). Aerobic iron and manganese cycling in a redox-stratified Mesoarchean epicontinental sea. *Earth and Planetary Science Letters*, *500*, 28-40.

Ostrander, C. M., Nielsen, S. G., Owens, J. D., Kendall, B., Gordon, G. W., Romaniello, S. J., & Anbar, A. D. (2019). Fully oxygenated water columns over continental shelves before the Great Oxidation Event. *Nature Geoscience*, *12*(3), 186–191.

Pavlov, A., & Kasting, J. (2002). Mass-independent fractionation of sulfur isotopes in Archean sediments: strong evidence for an anoxic Archean atmosphere. *Astrobiology*, *2*(1), 27-41.

Philippot, P., Ávila, J. N., Killingsworth, B. A., Tessalina, S., Baton, F., Caquineau, T., Muller, E., Pecoits, E., Cartigny, P., & Lalonde, S. V. (2018). Globally asynchronous sulphur isotope signals require re-definition of the Great Oxidation Event. *Nature communications*, *9*(1), 2245.

Planavsky, N. J., Asael, D., Hofmann, A., Reinhard, C. T., Lalonde, S. V., Knudsen, A., Wang, X., Ossa Ossa, F., Pecoits, E., & Smith, A. J. (2014). Evidence for oxygenic photosynthesis half a billion years before the Great Oxidation Event. *Nature Geoscience*, *7*(4), 283-286.

Poulton, S. W., Bekker, A., Cumming, V. M., Zerkle, A. L., Canfield, D. E., & Johnston, D. T. (2021). A 200-million-year delay in permanent atmospheric oxygenation. *Nature*, *592*(7853), 232-236. https://doi.org/10.1038/s41586-021-03393-7

Prave, A., Kirsimäe, K., Lepland, A., Fallick, A., Kreitsmann, T., Deines, Y. E., Romashkin, A., Rychanchik, D., Medvedev, P., & Moussavou, M. (2022). The grandest of them all: the Lomagundi–Jatuli Event and Earth's oxygenation. *Journal of the Geological Society*, *179*(1).

Rasmussen, B., Bekker, A., & Fletcher, I. R. (2013). Correlation of Paleoproterozoic glaciations based on U–Pb zircon ages for tuff beds in the Transvaal and Huronian Supergroups. *Earth and Planetary Science Letters*, *382*, 173-180. https://doi.org/10.1016/j.epsl.2013.08.037

Rasmussen, B., & Buick, R. (1999). Redox state of the Archean atmosphere: evidence from detrital heavy minerals in ca. 3250–2750 Ma sandstones from the Pilbara Craton, Australia. *Geology*, *27*(2), 115-118.

Rosing, M. T., & Frei, R. (2004). U-rich Archaean sea-floor sediments from Greenland–indications of> 3700 Ma oxygenic photosynthesis. *Earth and Planetary Science Letters*, *217*(3-4), 237-244.

Roué, L., Kurzweil, F., Wille, M., Wegwerth, A., Dellwig, O., Münker, C., & Schoenberg, R. (2021). Stable W and Mo isotopic evidence for increasing redox-potentials from the Paleoarchean towards the Paleoproterozoic deep ocean. *Geochimica et Cosmochimica Acta*, *309*, 366-387.

Schier, K., Bau, M., Smith, A. J. B., Beukes, N. J., Coetzee, L. L., & Viehmann, S. (2020). Chemical evolution of seawater in the Transvaal Ocean between 2426 Ma (Ongeluk Large Igneous Province) and 2413 Ma ago (Kalahari Manganese Field). *Gondwana Research*, *88*, 373-388. https://doi.org/10.1016/j.gr.2020.09.001

Schröder, S., Bedorf, D., Beukes, N., & Gutzmer, J. (2011). From BIF to red beds: Sedimentology and sequence stratigraphy of the Paleoproterozoic Koegas Subgroup (South Africa). *Sedimentary Geology*, *236*(1-2), 25-44.

Schröder, S., Beukes, N. J., & Armstrong, R. A. (2016). Detrital zircon constraints on the tectonostratigraphy of the Paleoproterozoic Pretoria Group, South Africa. *Precambrian Research*, *278*, 362-393.

Uveges, B. T., Izon, G., Ono, S., Beukes, N. J., & Summons, R. E. (2023). Reconciling discrepant minor sulfur isotope records of the Great Oxidation Event. *Nature communications*, *14*(1), 279.

Voegelin, A. R., Nägler, T. F., Beukes, N. J., & Lacassie, J. P. (2010). Molybdenum isotopes in late Archean carbonate rocks: implications for early Earth oxygenation. *Precambrian Research*, *182*(1-2), 70-82.

Warchola, T., Lalonde, S. V., Pecoits, E., von Gunten, K., Robbins, L. J., Alessi, D. S., Philippot, P., & Konhauser, K. O. (2018). Petrology and geochemistry of the Boolgeeda Iron Formation, Hamersley Basin, Western Australia. *Precambrian Research*, *316*, 155-173. https://doi.org/10.1016/j.precamres.2018.07.015

Warke, M. R., Di Rocco, T., Zerkle, A. L., Lepland, A., Prave, A. R., Martin, A. P., Ueno, Y., Condon, D. J., & Claire, M. W. (2020). The Great Oxidation Event preceded a Paleoproterozoic "snowball Earth". *Proceedings of the National Academy of Sciences*.

Wille, M., Kramers, J. D., Nägler, T. F., Beukes, N., Schröder, S., Meisel, T., Lacassie, J., & Voegelin, A. (2007). Evidence for a gradual rise of oxygen between 2.6 and 2.5 Ga from Mo isotopes and Re-PGE signatures in shales. *Geochimica et Cosmochimica Acta*, *71*(10), 2417-2435.

Young, G. M., Long, D. G., Fedo, C. M., & Nesbitt, H. W. (2001). Paleoproterozoic Huronian basin: product of a Wilson cycle punctuated by glaciations and a meteorite impact. *Sedimentary Geology*, *141*, 233-254.

Zahnle, K., Claire, M., & Catling, D. (2006). The loss of mass-independent fractionation in sulfur due to a Palaeoproterozoic collapse of atmospheric methane. *Geobiology*, *4*(4), 271-283.

Zeh, A., Wilson, A. H., & Gerdes, A. (2020). Zircon U-Pb-Hf isotope systematics of Transvaal Supergroup – Constraints for the geodynamic evolution of the Kaapvaal Craton and its hinterland between 2.65 and 2.06 Ga. *Precambrian Research*, *345*. https://doi.org/10.1016/j.precamres.2020.105760

Zmolek, P., Xu, X., Jackson, T., Thiemens, M. H., & Trogler, W. C. (1999). Large mass independent sulfur isotope fractionations during the photopolymerization of 12CS2 and 13CS2. *The Journal of Physical Chemistry A*, *103*(15), 2477-2480.

1.5 Supplementary Materials

Table S1.1. Compilation of all references used in Figure 1.1

Redox proxy	Number	References
Positive $\delta^{13}C$ isotope excursions in carbonates	1, 2	Karhu and Holland (1996), Bekker et al. (2001)
Mo isotope fractionation beyond crustal values & Mn-oxides in shales	3, 4, 5	Planavsky et al. (2014), Kurzweil et al. (2016), Ostrander et al. (2019)
$\delta^{56}Fe$ indicate iron oxidation in shallow marine settings	6	Eickmann et al. (2018)
Redox sensitive trace element enrichments in shales	7,8	Anbar et al. (2007); Wille et al. (2007)
Depositional ages of massive Mn-oxide deposits	9	Beukes et al. (2016)
Disappearance of BIFs	10	Bekker and Kaufman (2007)
Appearance of red beds	11, 12	Young et al. (2001), Beukes et al. (2002)
Appearance of marine gypsum evaporates	13, 14	Bekker et al. (2006), Schröder et al. (2011)
Transition to sulfate isotopic values (high oceanic sulfate)	15, 16	Cameron (1982), Canfield (2005)
Loss and reappearance of MIF-S signatures	17, 18, 19, 20	Guo et al. (2009), Luo et al. (2016), Philippot et al. (2018), Poulton et al. (2021)

Chapter 2

Molybdenum Isotopes as Paleoredox Proxy: A Review

This work employs a comprehensive suite of paleoredox proxies, including redox-sensitive trace elements (V, Mo, U), total carbon nitrogen and sulfur quantification, light (C, S), and heavy (Fe, Mo) stable isotopes. Additionally, this study also investigates Nd-Sr radiogenic isotope systematics to shed light on the provenance of key formations recording the GOE in the Transvaal Supergroup. A detailed review of all these systems is beyond the scope of this work. Given that this project revolves around oxygen evolution within the atmosphere-ocean system during the GOE and considering the central role Mo isotope systematics play in this regard, an in-depth review of Mo has been prioritized rather than a superficial attempt to address all the geochemical tools utilized in this study. For in-depth reviews of redox-sensitive trace elements, the reader is directed to (e.g., Algeo & Tribovillard, 2009; Bennett & Canfield, 2020; Crombez et al., 2020; Smrzka et al., 2019) for light stable isotopes to for example Sharp (2017); for Fe to Johnson et al. (2020) and to Faure and Mensing (2005) or Tripathy et al. (2012) for Sr and Nd.

2.1 Historical Perspective and Analytical Framework

The molybdenum isotope paleoredox proxy is among the best-established and most extensively studied heavy stable isotope tracers for assessing changes in environmental redox conditions. It was initially proposed for paleoredox applications more than 30 years ago (Emerson & Huested, 1991; Holland, 1984), and subsequent studies in the 1990s and 2000s pioneered and refined our understanding of Mo geochemical behavior in modern settings, while also identifying its strengths and limitations when employed as a paleoredox proxy (Barling et al., 2001; Erickson & Helz, 2000; Helz et al., 1996; Siebert et al., 2003; Wille et al., 2007).

Molybdenum (Mo, Z = 42) is a transition metal characterized by seven stable isotopes with relative abundances ranging from ~10 to 25 %. The stable isotopes of Mo simultaneously cover a substantial mass range of ~8 % from ^{92}Mo to ^{100}Mo.

Mo isotope data are reported relative to the defined NIST-SRM-3134 (NIST 3134) international reference material (Eq. 1). However, to facilitate inter-study comparisons, a 0.25 ‰ offset is applied to account for the offset between the John Matthey (JM) and the NIST 3134 standards (Nägler et al., 2014), using the conversion between various δ-values similar to the approach employed by Craig (1957) for O isotopes (Eq. 2).

$$\delta^{98/95}Mo_{3134} = \left(\frac{^{98}Mo/^{95}Mo_{sample}}{^{98}Mo/^{95}Mo_{3134}} - 1\right) \times 1000 \quad \text{[Eq. 1]}$$

$$\delta^{98/95}Mo_{3134+0.25} = 1.00025 \times \delta^{98/95}Mo_{3134} + 0.25 \quad \text{[Eq. 2]}$$

2.2 The Modern Oceanic Elemental Mo Budget

Ocean inputs: During oxidative weathering, Mo readily oxidized to its hexavalent state Mo(VI), which is mobile and easily transferred from the crust to the oceans. In the oceans, Mo acts conservatively and accumulates readily as molybdate (MoO_4^{2-}) in oxic waters to the extent that it is the most abundant transition metal in modern marine settings (Collier, 1985; Morris, 1975). The Mo influx to the modern ocean is entirely controlled by the riverine input, constituting ~95% of the overall budget, with only a subordinate contribution (~5%) from hydrothermal sources (Miller et al., 2011; Wheat et al., 2002) and a negligible input from dust and aerosols (Morford & Emerson, 1999; Scott et al., 2008). Although estimations for the residence time of Mo vary by ~50% from about 440 to 800 kyr (Colodner et al., 1995; Miller et al., 2011) in the modern ocean, it is still significantly longer than the ocean mixing time of 1.5 kyr (Sarmiento & Gruber, 2006). Accordingly, the average Mo atom is at least circulated ~300 times before leaving the ocean, resulting in a homogenous elemental and isotopic marine Mo pool of ~10^7 nmol kg^{-1} (Bruland, 1983; Collier, 1985; Morris, 1975) and $\delta^{98}Mo_{NIST+0.25}$ = 2.34±0.10 ‰ (Barling et al., 2001; Siebert et al., 2003), respectively.

Ocean sinks: The primary mechanisms for Mo sequestration are 1) adsorption onto Fe-Mn-(hydr)oxides under oxic conditions and 2) removal via anoxic to euxinic sediments underlying oxic to suboxic water masses. These two pathways account for about 30–50 % and 50–65 % of Mo removal in the modern ocean, respectively (Kendall et al., 2017). In highly euxinic settings (anoxic and sulfidic; H_2S > 11 µM), Mo is almost quantitatively removed from the overlying seawater. However, since only ~0.05–0.10 % of the modern ocean is deemed euxinic, this sink is only responsible for the removal of ~6–15 % of the yearly Mo ocean input and is thus reasonably subordinate relative to the suboxic–anoxic and the oxic sinks (Reinhard et al., 2013; Scott et al., 2008). Figure 2.1(A) presents an estimation of the size of input and output

fluxes for the modern ocean and the approximate isotopic offset from seawater associated with each sink.

2.3 Isotopic Mass Balance

Oxic settings (>2.8 Mg O_2/L; Tyson & Pearson, 1991): An uncommon aspect of the molybdenum isotope system is that seawater represents the heaviest isotopic reservoir on the planet, which links to the fact that all oceanic sinks preferentially remove lighter Mo isotopes (Kendall et al., 2017). The largest isotopic fractionation of Mo isotopes occurs during Mo adsorption onto Mn-oxides, which form under oxygenated conditions. Experimental data indicate a mean fractionation factor (α) of 1.0027 at 25 °C, corresponding to an isotopic offset of $\Delta^{98/95}Mo_{solution\text{-}Mn\text{-}oxide} \approx 2.7\pm0.1$ ‰ ($\Delta \sim (\alpha\text{-}1)*1000$) between synthetic seawater and Mn-oxides (Barling & Anbar, 2004; Wasylenki et al., 2008). This result is in agreement with Mo isotopic composition measured in natural Mn-crust ($\Delta^{98/95}Mo_{solution\text{-}Mn\text{-}oxide} \sim 3$‰) (Barling & Anbar, 2004; Siebert et al., 2003). Counterintuitively, despite molybdenum's versatile redox chemistry, the large isotopic fractionation associated with Mo adsorption onto Mn-oxides is not caused by changes in its redox state but rather in its coordination geometry. Molybdate (MoO_4^{2}) in oxic seawater is tetrahedrally coordinated, whereas Mo adsorbed to particle surfaces are octahedrally coordinated in polymolybdate species (e.g., $Mo_6O_{19}^{2-}$) (Kashiwabara et al., 2011; Siebert et al., 2003; Wasylenki et al., 2011). Mo also adsorbs readily onto various Fe-(hydr)oxides such as magnetite, ferrihydrite, goethite and hematite (Goldberg et al., 2009). Specifically, the isotopic offset for these common Fe-(hydr)oxides are quantified to $\Delta^{98/95}Mo = 0.83\pm0.6$ ‰ for magnetite , $\Delta^{98/95}Mo = 1.11\pm0.15$ ‰ for ferrihydrite, $\Delta^{98/95}Mo = 1.40\pm0.48$ ‰ for goethite and $\Delta^{98/95}Mo = 2.19\pm0.54$ ‰ for hematite (Goldberg et al., 2009). This observed pattern arises from the specific Fe-(hydr)oxides adsorption properties for Mo, where both tetrahedrally and octahedrally bound Mo display a decreasing adsorption affinity according to the aforementioned order.

In this respect, a necessary process to consider is the so-called 'Fe–Mn shuttle', involving the adsorptive transport of Mo with Fe-Mn-(hydr)oxides from surface waters to the sediments. If the porewaters or the bottom waters are anoxic or euxinic, manganese oxides undergo dissolution in the manganiferous zone, releasing any adsorbed Mo into the pore fluids. Hereafter, Mo is thiolized in the sulfidic zone of the pore waters to thiomolybdates and immobilized in Fe-sulfides or sulfurized organic matter (Helz et al., 1996; Poulson et al., 2009; Tribovillard et al., 2004). At the same time, if the sediments exhibit an open-system behavior, iron and manganese will

redissolve and undergo multiple redox-induced dissolution-precipitation cycles alternating between oxygenated upper water masses and the anoxic/euxinic bottom waters/porewaters, effectively enriching Mo in the sediments through each cycle. Especially for the Neoarchean and Paleoproterozoic eras, when oxygen was likely localized in shallow water 'oxygen oasis' (Fischer, 1965; Olson et al., 2013), the 'Fe-Mn-shuttle' was particularly important in shallow marine continental margin settings (Kurzweil et al., 2016).

Highly euxinic settings (0 Mg O_2/L and H2S > 11μM; Helz et al., 1996): Under highly euxinic conditions, Mo undergoes thiolation, during which seawater molybdate (MoO_4^{2-}) is quantitatively removed from seawater and transformed into tetrathiomolybdate (MoS_4^{2-}) in the sediment phase. As a consequence, Mo isotopic composition in sediments deposited under highly euxinic bottom water conditions closely approximates the Mo isotopic composition of the overlying ambient seawater and thus serves as a proxy for the marine oxygenation state at the time of deposition (Erickson & Helz, 2000; Helz et al., 1996; Neubert et al., 2008). However, despite the idea's elegance, it is challenged by the difficulty of accurately distinguishing between weakly and strongly euxinic settings in the geological record. Both sedimentological observations, such as the presence of disseminated pyrite, and geochemical indications, like the level of highly reactive iron, are unreliable (Pasquier et al., 2022), complicating the distinction. For example, in the shallow Black Sea, near the chemocline, Mo isotopic compositions vary by up to 3 ‰, a span comparable to the entire natural range (Kendall et al., 2017). The main reason is that incomplete thiolation under marginally euxinic conditions leads to non-quantitative removal of Mo from seawater, and these intermediate thiomolybdate species are associated with significant fractionation (Nägler et al., 2011), leading to large variations in Mo isotopic compositions in the sediments. Furthermore, other contributing factors, including diagenetic alteration, detrital input, and local variability of the marine redox conditions, also play a role (Poulson et al., 2009; Poulson et al., 2006).

Suboxic to anoxic settings (2.8–0 Mg O_2/L; Tyson & Pearson, 1991): Compared to strongly euxinic conditions, where thiolation is the main pathway, Mo accumulates in the sediments under mildly oxygenated to anoxic bottom water conditions through several pathways, including adsorption onto organic compounds (e.g., humic substances) or adsorption onto Fe-Mn-(hydr)oxides and partial thiolation in sulfidic pore waters (Algeo & Lyons, 2006; Dahl et al., 2010; Noordmann et al., 2015). In these intermediate settings, the exact isotopic signature primarily depends on three factors: the relative amount of Fe and Mn and the amount of dissolved

H_2S in the sediment porewaters. Mn-rich (Fe-poor) sediments with low amounts of dissolved porewater H_2S typically display $\delta^{98/95}Mo_{NIST+0.25}$ between -1.0 and +0.4 ‰, whereas Fe-rich (Mn-poor) sediments usually have $\delta^{98/95}Mo_{NIST+0.25}$ values ranging from -0.5 to 2.0 ‰. Lastly, sediments with high pore water H_2S concentrations, yet below 11µM, display $\delta^{98/95}Mo_{NIST+0.25}$ of around 1.6 ‰, with little dependence on Fe-Mn content. The latter pathway dominates the overall isotopic composition of Mo deposited under mildly oxygenated to anoxic conditions in the modern ocean (Kendall et al., 2017). Figure 2.1(B) and Figure 2.1(C) illustrates the approximate range of isotopic compositions of the various marine Mo reservoirs alongside common geological settings exhibiting distinct redox regimes for the modern ocean.

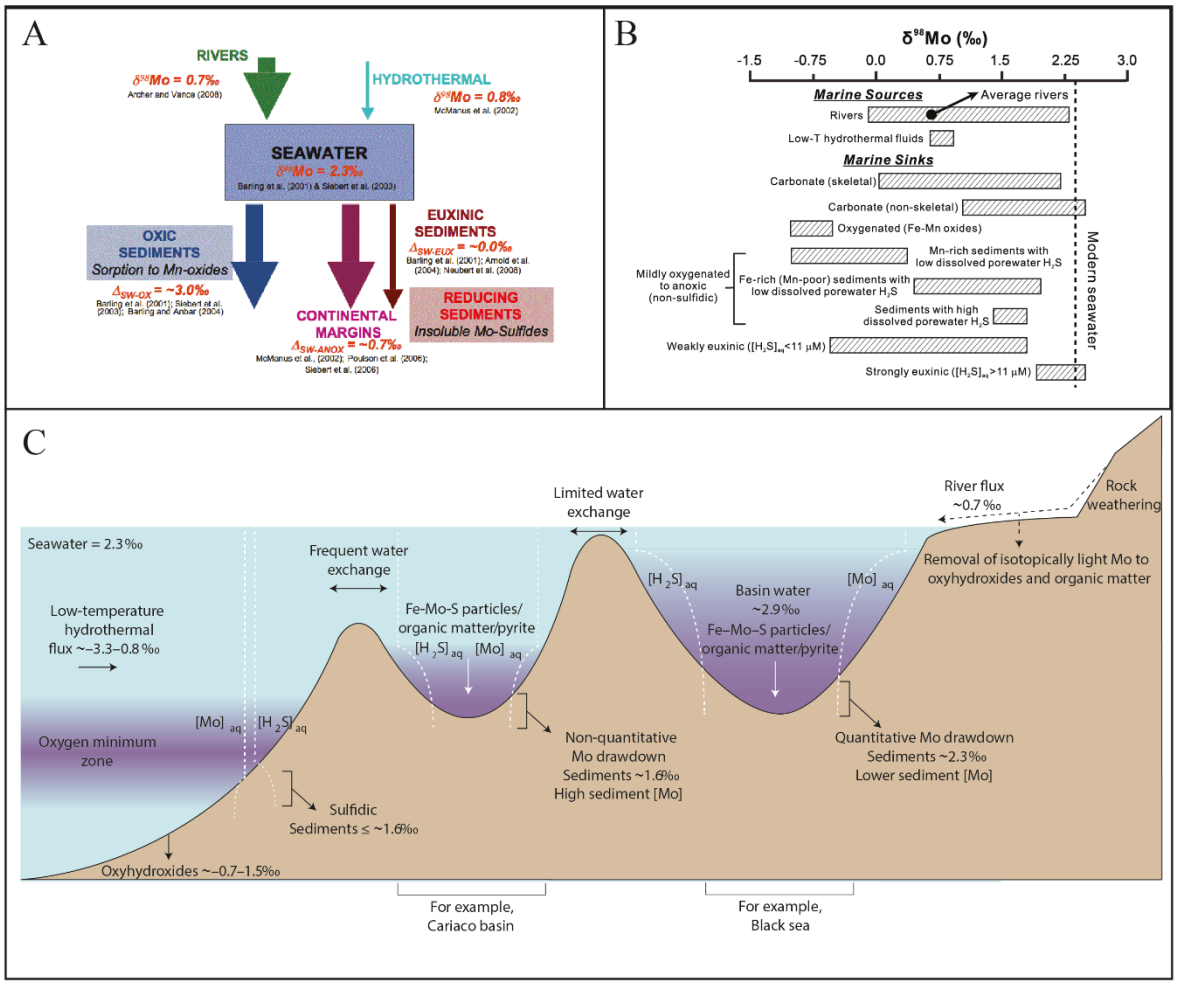

Figure 2.1. **(A):** *Figure illustrating a schematic depiction of the modern marine elemental and isotopic budget*. All relative fractionations are relative to seawater, and the figure is directly adapted from Poulson et al. (2009). **(B):** Approximate variations in molybdenum isotopic compositions of important sources and sinks in the marine environment (figure from Kendall et al. (2017)). **(C):** Schematic illustration of the typical location of various Mo elemental and isotopic sinks from a generalized shelf setting. The figure is from Dickson (2017).

2.4 Paleoenvironmental Reconstruction – Probing Free O_2 in the Neoarchean and Paleoproterozoic Using Mo Isotope Systematics

For paleoenvironmental reconstruction of Neoarchean and Peleoproterozoic environments, Mo isotopes are used to investigate two different yet related mechanisms. Firstly, Mo elemental and isotope systematics can be used to investigate the presence of free molecular oxygen in the environment and, thereby, the onset of oxygenic photosynthesis. Secondly, Mo isotopes can be utilized to understand the global relative distribution of euxinic, suboxic-anoxic and oxic settings in the ocean, which improves our understanding of marine redox dynamics and its relation to biogeochemical processes.

When employing Mo isotopes to infer paleoredox conditions in Earth's deep past, inferences made from the modern ocean cannot be directly transferred to the past. For example, in the modern ocean, only about 0.3 % of oceanic deep waters have O_2 concentration below 5 μM, whereas Neoarchean-Paleoproterozoic deep waters were predominantly anoxic and ferruginous (Knoll et al., 2012). This facilitated much faster removal of Mo from the global ocean, resulting in a much shorter residence time of between 17 to 140 kyr. (Asael, 2015), which starkly contrasts with its current residence time of ~440 to 800 kyr (Colodner et al., 1995; Miller et al., 2011). Despite this significant difference, Mo residence time in Earth's deep past was still considerably longer than, at least, the modern ocean mixing time (1.5 kyr; Sarmiento & Gruber, 2006). A final contrast to acknowledge is that before oxidative weathering, the dissolved riverine Mo load was less significant than today, which, when coupled with the approximately 10 times larger Archean hydrothermal flux (de Wit & Hart, 1993), likely resulted in the Archean marine Mo input that was substantially influenced by hydrothermal sources (Aleisha C. Johnson, 2021).

The combination of these factors establishes that before the GOE, the marine elemental and isotopic Mo budget was controlled to a more considerable extent by anoxic and perhaps suboxic settings, while the euxinic and oxic settings were subordinate Mo removal pathways (Asael et al., 2018). However, the Great Oxidation Event naturally represents the first significant disruption in this equilibrium, making interpretations about the marine redox state at this time particularly insightful. During this interval, the ocean transitioned from the pervasive anoxic and ferruginous conditions characterized by Archean times to a Paleoproterozoic marine realm with common euxinic settings alongside progressively more oxygenated shallow marine environments (Knoll et al., 2012), as for example indicated by the

global increase in Mo concentrations and isotopic compositions at this time (Fig. 2.2). Since the largest Mo isotope fractionation is associated with oxic settings, even slight alterations in the relative distribution of global oxic marine environments can exert a significant impact on the Mo isotopic budget if the conditions persist for extended periods (Dahl et al., 2011; Kendall et al., 2017). However, it should be noted that because the accumulation rate of ferromanganese nodules is typically slow (Morford & Emerson, 1999), over short time spans marine Mo concentrations and isotopic compositions are far more sensitive to the relative changes in the extent of euxinia than to oxygenated conditions (Kendall et al., 2017). Generally stated, organic-rich shales deposited under euxinic bottom water conditions with low Mo concentrations and light isotopic compositions are indicative of periods during which low oxygen environments prevailed in the global ocean. In contrast, organic-rich shales, deposited under euxinic conditions, that exhibit high Mo concentrations and heavier isotopic signatures strongly suggest expanded oxic environments in the global ocean (Dickson, 2017; Kendall et al., 2017). That said, it should be underscored that shales deposited under euxinic conditions may not, in all cases, directly record the isotopic composition of ambient seawater (for reasons elaborated in section 2.3) but may reflect a combination of global and local processes. Consequently, the optimal approach when reconstructing paleoenvironmental redox conditions is coupling Mo isotope data and trace element systematics with additional geochemical redox proxies (e.g., redox-sensitive trace elements, CNS systematics, other light and heavy stable isotope oxygenation proxies) combined with a sound understanding of the geological depositional environment. In conclusion, while organic-rich shales – the main lithotype studied in this work – undoubtedly play an important role in our understanding of the marine oxygenation state through geological time, the inherent challenge of accurately constraining euxinic conditions geochemically and sedimentologically warrants interpretational caution. Therefore, any Mo isotopic value from a black shale should merely be taken as a minimum value for the global seawater composition at that time.

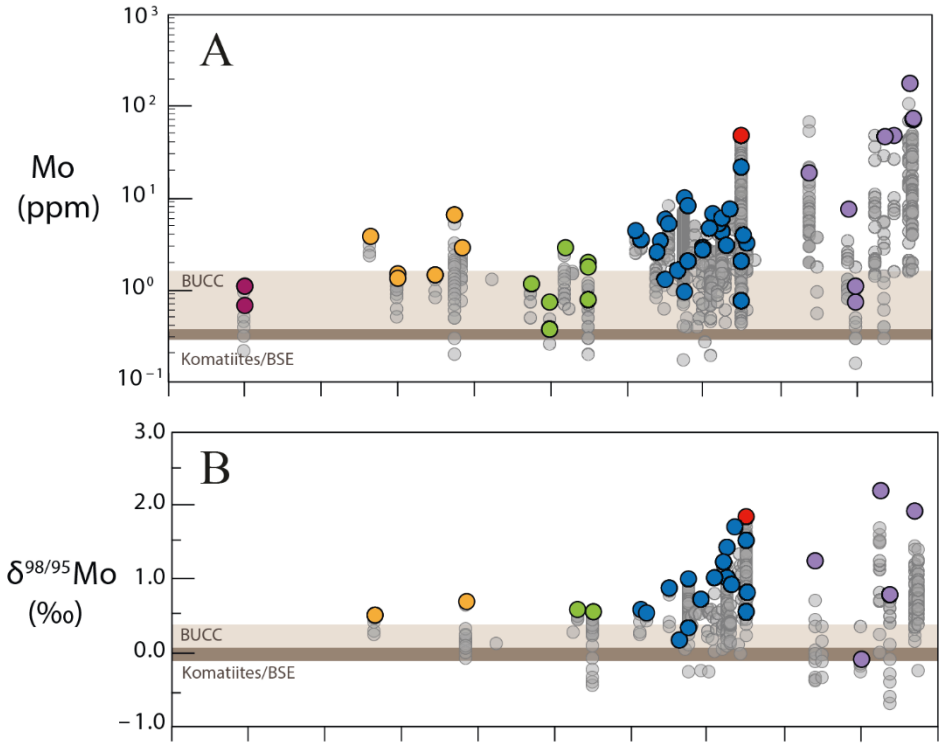

Figure 2.2. *Compilation of Mo elemental **(A)** and isotopic compositions **(B)** from Archean and Paleopreoterozoic black shales* compared to bulk upper continental crust (BUCC) and Komatiiites/bulk silica Earth (BSE). The maximum value of each shale is color coded.

2.5 References

Aleisha C. Johnson, C. M. O., Stephen J. Romaniello, Christopher T. Reinhard, Allison T. Greaney, Timothy W. Lyons, Ariel D. Anbar. (2021). Reconciling evidence of oxidative weathering and atmospheric anoxia on Archean Earth. *Science advances*.

Algeo, T. J., & Lyons, T. W. (2006). Mo–total organic carbon covariation in modern anoxic marine environments: Implications for analysis of paleoredox and paleohydrographic conditions. *Paleoceanography*, *21*(1).

Algeo, T. J., & Tribovillard, N. (2009). Environmental analysis of paleoceanographic systems based on molybdenum–uranium covariation. *Chemical Geology*, *268*(3-4), 211-225.

Asael, D., Rouxel, O., Poulton, S. W., Lyons, T. W., & Bekker, A. (2018). Molybdenum record from black shales indicates oscillating atmospheric oxygen levels in the early Paleoproterozoic. *American Journal of Science*, *318*(3), 275-299.

Asael, D., Rouxel O., Bekker, A., Scott C. (2015). *Dissolved Mo in the Archean oceans – a case study from the 2.63 Ga Jeerinah Formation, Australia* Goldschmidt, Prague.

Barling, J., & Anbar, A. (2004). Molybdenum isotope fractionation during adsorption by manganese oxides. *Earth and Planetary Science Letters*, *217*(3-4), 315-329.

Barling, J., Arnold, G. L., & Anbar, A. (2001). Natural mass-dependent variations in the isotopic composition of molybdenum. *Earth and Planetary Science Letters*, *193*(3-4), 447-457.

Bennett, W. W., & Canfield, D. E. (2020). Redox-sensitive trace metals as paleoredox proxies: A review and analysis of data from modern sediments. *Earth-Science Reviews*, *204*, 103175.

Bruland, K. W. (1983). Trace elements in seawater. *Chemical oceanography*, *8*, 157-200.

Collier, R. W. (1985). Molybdenum in the Northeast Pacific Ocean 1. *Limnology and Oceanography*, *30*(6), 1351-1354.

Colodner, D., Edmond, J., & Boyle, E. (1995). Rhenium in the Black Sea: comparison with molybdenum and uranium. *Earth and Planetary Science Letters*, *131*(1-2), 1-15.

Craig, H. (1957). Isotopic standards for carbon and oxygen and correction factors for mass-spectrometric analysis of carbon dioxide. *Geochimica et Cosmochimica Acta*, *12*(1-2), 133-149.

Crombez, V., Rohais, S., Euzen, T., Riquier, L., Baudin, F., & Hernandez-Bilbao, E. (2020). Trace metal elements as paleoenvironmental proxies: Why should we account for sedimentation rate variations? *Geology*, *48*(8), 839-843. https://doi.org/10.1130/g47150.1

Dahl, T. W., Anbar, A. D., Gordon, G. W., Rosing, M. T., Frei, R., & Canfield, D. E. (2010). The behavior of molybdenum and its isotopes across the chemocline and in the sediments of sulfidic Lake Cadagno, Switzerland. *Geochimica et Cosmochimica Acta*, *74*(1), 144-163.

Dahl, T. W., Canfield, D. E., Rosing, M. T., Frei, R. E., Gordon, G. W., Knoll, A. H., & Anbar, A. D. (2011). Molybdenum evidence for expansive sulfidic water masses in~ 750 Ma oceans. *Earth and Planetary Science Letters*, *311*(3-4), 264-274.

de Wit, M. J., & Hart, R. A. (1993). Earth's earliest continental lithosphere, hydrothermal flux and crustal recycling. *Lithos*, *30*(3-4), 309-335.

Dickson, A. J. (2017). A molybdenum-isotope perspective on Phanerozoic deoxygenation events. *Nature Geoscience*, *10*(10), 721-726.

Emerson, S., & Huested, S. S. (1991). Ocean anoxia and the concentrations of molybdenum and vanadium in seawater. *Marine Chemistry*, *34*, 177-196.

Erickson, B. E., & Helz, G. R. (2000). Molybdenum (VI) speciation in sulfidic waters: stability and lability of thiomolybdates. *Geochimica et Cosmochimica Acta*, *64*(7), 1149-1158.

Faure, G., & Mensing, T. M. (2005). *Principles and applications*. John Wiley & Sons, Inc.

Fischer, A. G. (1965). Fossils, early life, and atmospheric history. In: National Acadamy of Sciences.

Goldberg, T., Archer, C., Vance, D., & Poulton, S. W. (2009). Mo isotope fractionation during adsorption to Fe (oxyhydr) oxides. *Geochimica et Cosmochimica Acta*, *73*(21), 6502-6516.

Helz, G., Miller, C., Charnock, J., Mosselmans, J., Pattrick, R., Garner, C., & Vaughan, D. (1996). Mechanism of molybdenum removal from the sea and its concentration in black shales: EXAFS evidence. *Geochimica et Cosmochimica Acta*, *60*(19), 3631-3642.

Holland, H. D. (1984). *The Chemical Evolution of the Atmosphere and Oceans* (Vol. 2). Princeton University Press. http://www.imoa.info /

Johnson, C., Beard, B., & Weyer, S. (2020). *Iron geochemistry: an isotopic perspective*. Springer.

Kashiwabara, T., Takahashi, Y., Tanimizu, M., & Usui, A. (2011). Molecular-scale mechanisms of distribution and isotopic fractionation of molybdenum between seawater and ferromanganese oxides. *Geochimica et Cosmochimica Acta*, *75*(19), 5762-5784.

Kendall, B., Dahl, T. W., & Anbar, A. D. (2017). The stable isotope geochemistry of molybdenum. *Reviews in Mineralogy and Geochemistry*, *82*(1), 683-732.

Knoll, A. H., Canfield, D. E., & Konhauser, K. O. (2012). *Fundamentals of geobiology*. John Wiley & Sons.

Kurzweil, F., Wille, M., Gantert, N., Beukes, N. J., & Schoenberg, R. (2016). Manganese oxide shuttling in pre-GOE oceans–evidence from molybdenum and iron isotopes. *Earth and Planetary Science Letters*, *452*, 69-78.

Miller, C. A., Peucker-Ehrenbrink, B., Walker, B. D., & Marcantonio, F. (2011). Re-assessing the surface cycling of molybdenum and rhenium. *Geochimica et Cosmochimica Acta*, *75*(22), 7146-7179.

Morford, J. L., & Emerson, S. (1999). Geochemistry of redox sensitive trace metals in sediments. *Geochimica et Cosmochimica Acta*, *63*, 1735–1750.

Morris, A. (1975). Dissolved molybdenum and vanadium in the northeast Atlantic Ocean. Deep Sea Research and Oceanographic Abstracts,

Nägler, T., Neubert, N., Böttcher, M., Dellwig, O., & Schnetger, B. (2011). Molybdenum isotope fractionation in pelagic euxinia: Evidence from the modern Black and Baltic Seas. *Chemical Geology*, *289*(1-2), 1-11.

Nägler, T. F., Anbar, A. D., Archer, C., Goldberg, T., Gordon, G. W., Greber, N. D., Siebert, C., Sohrin, Y., & Vance, D. (2014). Proposal for an international molybdenum isotope measurement standard and data representation. *Geostandards and Geoanalytical Research*, *38*(2), 149-151.

Neubert, N., Nägler, T. F., & Böttcher, M. E. (2008). Sulfidity controls molybdenum isotope fractionation into euxinic sediments: Evidence from the modern Black Sea. *Geology*, *36*(10), 775-778.

Noordmann, J., Weyer, S., Montoya-Pino, C., Dellwig, O., Neubert, N., Eckert, S., Paetzel, M., & Böttcher, M. E. (2015). Uranium and molybdenum isotope systematics in modern euxinic basins: Case studies from the central Baltic Sea and the Kyllaren fjord (Norway). *Chemical Geology*, *396*, 182-195. https://doi.org/10.1016/j.chemgeo.2014.12.012

Olson, S. L., Kump, L. R., & Kasting, J. F. (2013). Quantifying the areal extent and dissolved oxygen concentrations of Archean oxygen oases. *Chemical Geology*, *362*, 35-43.

Pasquier, V., Fike, D., Révillon, S., & Halevy, I. (2022). A global reassessment of the controls on iron speciation in modern sediments and sedimentary rocks: A dominant role for diagenesis. *Geochimica et Cosmochimica Acta*, *335*, 211-230.

Poulson, R. L., McManus, J., Severmann, S., & Berelson, W. M. (2009). Molybdenum behavior during early diagenesis: Insights from Mo isotopes. *Geochemistry, Geophysics, Geosystems*, *10*(6), doi.org/10.1029/2008GC002180.

Poulson, R. L., Siebert, C., McManus, J., & Berelson, W. M. (2006). Authigenic molybdenum isotope signatures in marine sediments. *Geology*, *34*(8), 617-620.

Reinhard, C. T., Planavsky, N. J., Robbins, L. J., Partin, C. A., Gill, B. C., Lalonde, S. V., Bekker, A., Konhauser, K. O., & Lyons, T. W. (2013). Proterozoic ocean redox and biogeochemical stasis. *Proceedings of the National Academy of Sciences*, *110*(14), 5357-5362.

Sarmiento, J. L., & Gruber, N. (2006). *Ocean biogeochemical dynamics*. Princeton University Press.

Scott, C., Lyons, T., Bekker, A., Shen, Y.-a., Poulton, S., Chu, X.-l., & Anbar, A. (2008). Tracing the stepwise oxygenation of the Proterozoic ocean. *Nature*, *452*(7186), 456.

Sharp, Z. (2017). Principles of stable isotope geochemistry.

Siebert, C., Nägler, T. F., von Blanckenburg, F., & Kramers, J. D. (2003). Molybdenum isotope records as a potential new proxy for paleoceanography. *Earth and Planetary Science Letters*, *211*(1-2), 159-171.

Smrzka, D., Zwicker, J., Bach, W., Feng, D., Himmler, T., Chen, D., & Peckmann, J. (2019). The behavior of trace elements in seawater, sedimentary pore water, and their incorporation into carbonate minerals: A review. *Facies*, *65*(4), 1-47.

Tribovillard, N., Riboulleau, A., Lyons, T., & Baudin, F. (2004). Enhanced trapping of molybdenum by sulfurized marine organic matter of marine origin in Mesozoic limestones and shales. *Chemical Geology*, *213*(4), 385-401.

Tripathy, G. R., Singh, S. K., & Krishnaswami, S. (2012). Sr and Nd Isotopes as Tracers of Chemical and Physical Erosion. In *Handbook of Environmental Isotope Geochemistry* (pp. 521-552). https://doi.org/10.1007/978-3-642-10637-8_26

Tyson, R. V., & Pearson, T. H. (1991). Modern and ancient continental shelf anoxia: an overview. *Geological Society, London, Special Publications*, *58*(1), 1-24.

Wasylenki, L. E., Rolfe, B. A., Weeks, C. L., Spiro, T. G., & Anbar, A. D. (2008). Experimental investigation of the effects of temperature and ionic strength on Mo isotope fractionation during adsorption to manganese oxides. *Geochimica et Cosmochimica Acta*, *72*(24), 5997-6005.

Wasylenki, L. E., Weeks, C. L., Bargar, J. R., Spiro, T. G., Hein, J. R., & Anbar, A. D. (2011). The molecular mechanism of Mo isotope fractionation during adsorption to birnessite. *Geochimica et Cosmochimica Acta*, *75*(17), 5019-5031. https://doi.org/10.1016/j.gca.2011.06.020

Wheat, C. G., Mottl, M. J., & Rudnicki, M. (2002). Trace element and REE composition of a low-temperature ridge-flank hydrothermal spring. *Geochimica et Cosmochimica Acta*, *66*(21), 3693-3705.

Wille, M., Kramers, J. D., Nägler, T. F., Beukes, N., Schröder, S., Meisel, T., Lacassie, J., & Voegelin, A. (2007). Evidence for a gradual rise of oxygen between 2.6 and 2.5 Ga from Mo isotopes and Re-PGE signatures in shales. *Geochimica et Cosmochimica Acta*, *71*(10), 2417-2435.

Chapter 3

Evidence for Contemporaneous Deposition of the Duitschland and Rooihoogte Formations (Transvaal Supergroup): Implications for Tempo and Mode of Earth's Great Oxidation

~ This Chapter is dedicated to Prof. Nic Beukes[†] ~

3.1 Abstract

The stratigraphic correlation of the ca. 2353±18 Ma to 2316±7 Ma Duitschland and Rooihoogte formations, Transvaal Supergroup, South Africa, becomes critically important when viewed in the light of the Great Oxidation Event (GOE), since both formations record the transition from mass-independent (MIF-S) to mass-dependent fractionation of sulfur isotopes (MDF-S) indicative of the transition to an oxygenated atmosphere. At present, discrepancies exist as to whether the Duitschland and Rooihoogte formations are two distinct formations formed in an older and younger depositional basin, respectively, or alternatively were deposited contemporaneously in the same basin at different positions to shorelines of the basin. A decoupled depositional history would indicate an oscillating oxygenation trajectory of the planet, whereas a contemporaneous deposition of the two formations would point towards a sudden increase of atmospheric oxygen. To investigate the controversy of a contemporaneous versus a consecutive depositional relationship, this study presents a sedimentological investigation of 11 stratigraphic profiles intersecting the Duitschland to lower Timeball Hill and Rooihoogte to lower Timeball Hill formations. The 11 profiles are correlated between the Transvaal Supergroup in the Transvaal area of South Africa and the adjoining Kanye area in Botswana and show that the Duitschland and Rooihoogte formations are laterally correlative. The sedimentological observations are reinforced by similar major and trace element data as well as Sr–Nd isotope compositions measured in four scientific drill cores, intersecting both the Duitschland and the Rooihoogte formations. Consequently, the documented disappearance of MIF-S in these two formations should be regarded as a single-step atmospheric change, thereby removing the best supporting evidence for a protracted and dynamic oxygenation trajectory. Furthermore, bulk sediment T_{DM}(Nd) of the Duitschland and Rooihoogte formations

consistently display Archean crustal residence ages in the interval between 2.9 Ga and 3.3 Ga for most samples. Geochemical discrimination functions and zircon distribution patterns suggest a collisional tectonic setting and measured bulk sediment Nd isotope data combined with literature zircon Hf isotope data indicate a potential collision between a Rae-type craton and the Kaapvaal craton around 2.5 Ga.

3.2 Introduction

Accumulation of free oxygen in the atmosphere-ocean system is considered one of the major prerequisites in creating a habitable planet featuring eukaryotic life. Earth has undergone several pulses of progressive oxygenation towards the present-day level of 21 vol.% atmospheric molecular oxygen. The first of these pulses is known as the Great Oxidation Event (GOE), which took place some ~2.45–2.32 billion years ago (Ga) (Bekker et al., 2004; Hannah et al., 2004; Luo et al., 2016), and originated as a consequence of the evolution of oxygenic phototrophs (Blankenship & Hartman, 1998). These organisms provided a new and powerful source of oxygen to the atmosphere and thus, once oxygenic phototrophs evolved, oxygen production to the atmosphere-ocean system increased rapidly leading to a reorganization of the planet's oxygen source-sink balance (Brocks et al., 1999; Catling et al., 2001; Holland, 2002; Kump & Barley, 2007). There is further evidence that these organisms already increased the redox potential in the atmosphere-ocean system at least 100 to 300 million years before the GOE (Anbar et al., 2007; Brocks et al., 1999; Eroglu et al., 2017; Franchi, 2018; Kendall et al., 2010; Kurzweil et al., 2015; Ossa Ossa et al., 2018; Roué et al., 2021; Wille et al., 2007) and potentially even around or prior to 2.8 Ga (Eickmann et al., 2018; Falcón et al., 2010; Planavsky et al., 2014; Rosing & Frei, 2004). Regardless, the appearance of oxygen in the atmosphere-ocean system ultimately led to the oxidation of reduced detrital minerals on land (Roscoe, 1976), the appearance of red beds (Chandler, 1980) and the disappearance of mass-independent fractionation of sulfur isotopes (MIF-S) in the geological record at oxygen levels above 0.001% of the present atmospheric level (PAL) (Farquhar et al., 2000; Guo et al., 2009; Luo et al., 2016). Consequently, the geological transition from MIF-S to MDF-S recorded in the marine sediments deposited ~2.45–2.32 Ga ago is an exceptional marker in Earth's progressive oxygenation from a planet with a weakly reducing to neutral atmosphere into a planet with an oxygen-bearing atmosphere. However, recent studies have shown that interpreting the sulfur isotopic record remain hindered by processes such as crustal recycling of material carrying a

MIF-S signal, potential short term atmospheric oscillations and spatial isotopic variability within the marine S-pool (Izon et al., 2022; Philippot et al., 2018; Uveges et al., 2023).

Opinions on the trajectory of planetary oxygenation thus differ, and proposals vary between those that envisage a rapid and unidirectional oxygenation pathway and those that foresee a protracted and oscillatory route (Gumsley et al., 2017; Izon et al., 2022; Luo et al., 2016; Luo et al., 2021; Poulton et al., 2021; Warke & Schröder, 2018). These contrasting interpretations are partly due to (i) global correlation issues between sedimentary successions recording the disappearance of the MIF-S signal on different cratons (Bekker et al., 2020; Hoffman, 2013; Philippot et al., 2018; Rasmussen et al., 2013; Warke et al., 2020), and (ii) unresolved intra-basinal correlations of stratigraphic units critical for the interpretation of the GOE, such as the Duitschland and Rooihoogte formations in the Transvaal Supergroup. Since both the Duitschland and Rooihoogte formations record the transition from MIF-S to MDF-S (Guo et al., 2009; Luo et al., 2016) in their lower parts, their correlation becomes crucially important in terms of understanding atmospheric oxygen dynamics across the GOE. However, both coeval deposition equaling a single MIF-S to MDF-S transition (Coetzee, 2001; Hoffman, 2013; Luo et al., 2016; Schröder et al., 2016; Warke & Schröder, 2018), as well as subsequent deposition amounting to multiple MIF-S to MDF-S transitions (Bekker et al., 2020; Gumsley et al., 2017; Moore et al., 2012; Poulton et al., 2021; Rasmussen et al., 2013) have been postulated for these formations (Fig. 3.1)

The goal of this study is to establish a sedimentological and geochemical framework regarding the stratigraphic and temporal relationship between the Duitschland and Rooihoogte formations in order to constrain the mode of the initial MIF-S to MDF-S transition prior to the deposition of the Timeball Hill Formation as either a sudden event or as an oscillating process (Fig. 3.1). Consequently, 11 stratigraphic profiles intersecting the Duitschland or Rooihoogte formations, were compared and correlated across the entire Transvaal Supergroup from localities where they are known to be present (Fig. 3.2). Furthermore, major and trace element data, as well as radiogenic Sr-Nd isotope signatures of sediments from four scientific drill cores also intersecting the Duitschland and Rooihoogte formations were compared.

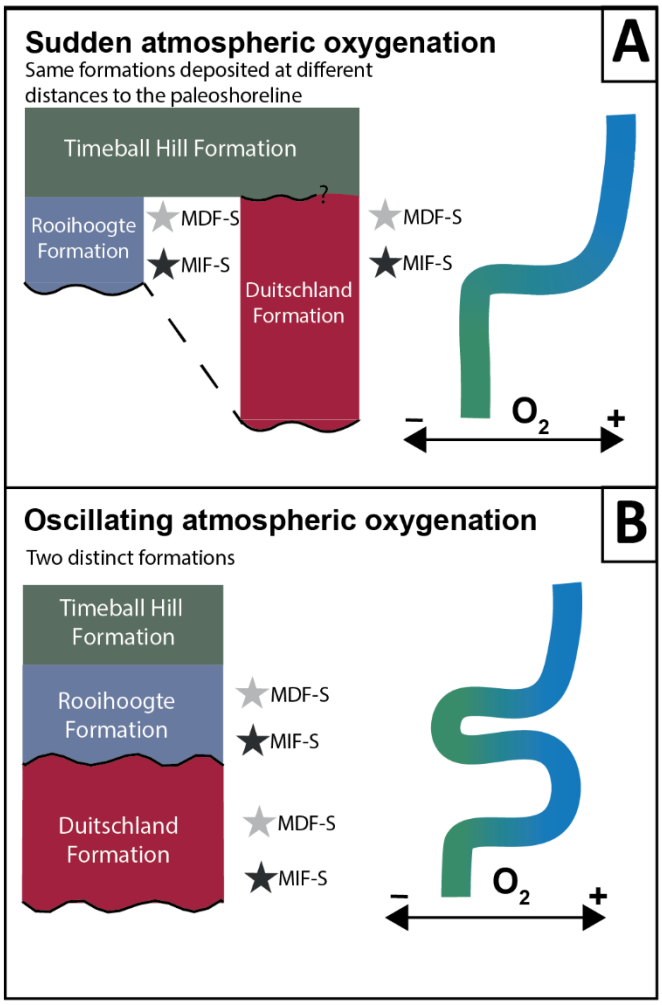

Figure 3.1. *Simple models illustrating the relationship between the Rooihoogte and Duitschland formations and implications on the mode of atmospheric oxygen evolution in the Paleoproterozoic*. **(A)** both formations were deposited contemporaneously with only one change from MIF-S to MDF-S and thus a singular atmospheric increase in oxygen; **(B)** the Duitschland Formation was deposited before the Rooihoogte Formation with two consecutive switches from MIF-S to MDF-S and thus an oscillation in atmospheric oxygen concentrations.

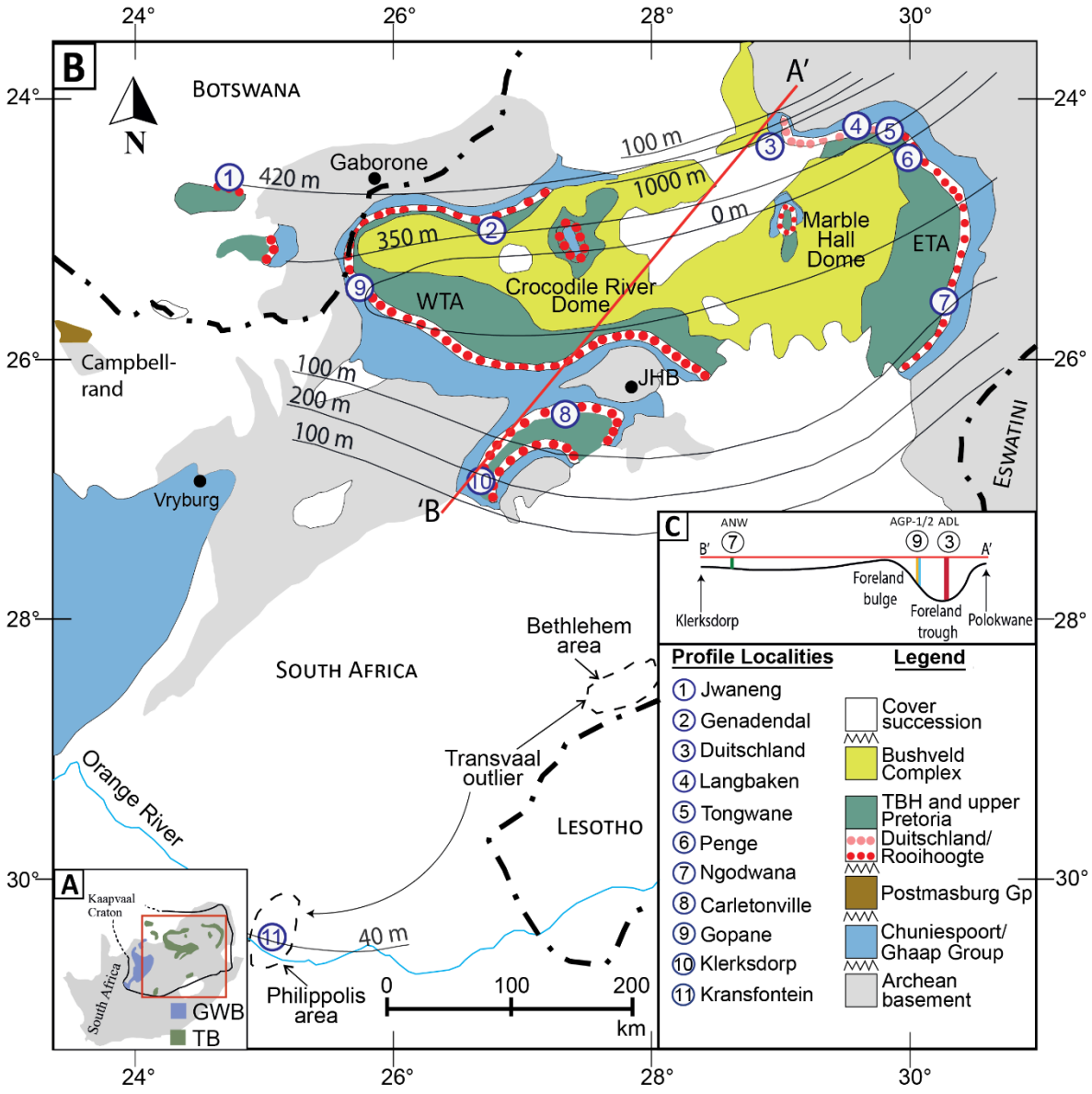

Figure 3.2. **(A)** *Overview of outcrop strata of the Transvaal Supergroup on the Kaapvaal Craton.* **(B)** Zoom in on the Transvaal Basin and adjacent regions with locations of stratigraphic profiles. The isopach map and depositional model are modified from Coetzee (2001) and line A' to B' marks the transects seen in (C). **(C)** Transect of the depositional environment (foreland bulge) from A' to B'.

3.3 Geological Overview

3.3.1 The Transvaal Supergroup

The Transvaal Supergroup is preserved in two outcrop areas referred to as the Griqualand West Basin (GWB) and the Transvaal Basin (TB) (Fig. 3.2A). For the purpose of this study, the TB also includes the outliers in the Jwaneng/Kanye area of Botswana and the Bethlehem and

Phillipolis areas of the Free State Province of South Africa (Fig. 3.2B). However, it is important to note that these 'basins' are likely structurally preserved erosional remnants of an antecedent basin that spanned the entire Kaapvaal Craton (Fig. 3.2A) (Coetzee, 2001), based on the uniformity of stratigraphy in the GWB and TB (Beukes, 1986), and the documentation of Transvaal strata under Phanerozoic cover in Botswana and the Free State of South Africa (McCarthy et al., 2018). For purely reference purposes, the northern part of the TB is further subdivided into a Western Transvaal Area (WTA) and an Eastern Transvaal Area (ETA) separated by the Bushveld Igneous Complex (Fig. 3.2B). The WTA and ETA represent the historic type areas for the lithostratigraphic subdivision in the TB of the Transvaal Supergroup and comprises a lower mainly chemical sedimentary succession, known as the Chuniespoort Group, overlain by the mainly siliciclastic Pretoria Group (Fig. 3.2B). The Chuniespoort Group is composed of a regionally persistent basal siliciclastic unit known as the Black Reef Formation in turn gradationally overlain by carbonates of the Malmani Subgroup, iron formations of the Penge Formation and carbonates and shales of the uppermost Tongwane Formation (Beukes, 1983; Martini, 1979; Schröder et al., 2016). A major erosional unconformity is developed below the Black Reef Formation at the base of the Chuniespoort Group (Fig. 3.2B). The top of the Chuniespoort Group is marked by a major regionally persistent low-angle erosional unconformity that forms the base of the overlying Pretoria Group (Fig 3.2B). The Duitschland and Rooihoogte formations that form the topic of this study have U-Pb maximum depositional ages of 2342±18 Ma and 2353±18 Ma, respectively (Zeh et al., 2020). They directly overlie the unconformity along which a basal chert pebble conglomerate or breccia bed, commonly referred to as the Bevets bed, is developed. The two formations, both composed of interbedded conglomerate, arenite and argillite with subordinate carbonates and cherts, are then overlain by a thick succession of carbonaceous shales representing the lower shale unit of the overlying Timeball Hill Formation (Fig. 3.2B), with a Re-Os isochron age of 2316±7Ma obtained from early diagenetic pyrite grains (Hannah et al., 2004).

3.3.2 Historical Context of the Duitschland and Rooihoogte Formations

The uncertainty as to whether the Duitschland Formation and Rooihoogte Formation should be regarded as one or two formations relies on two points of contention: (1) the nature of the basal conglomerate of the Duitschland Formation and (2) the type of contact between the Duitschland Formation and the overlying Timeball Hill Formation. The basal contact has either been interpreted as gradational (Button, 1973; Catuneanu & Eriksson, 2002) or erosional (Coetzee,

2001; Martini, 1979). Concerning the latter view, there are two schools of thought, namely (i) that the basal conglomerate (locally a chert breccia) is correlative between the Duitschland and Rooihoogte formations (Bekker et al., 2001; Coetzee et al., 2006; Coetzee, 2001; Hoffman, 2013; Luo et al., 2016; Martini, 1979; Schröder et al., 2016; Warke & Schröder, 2018) or (ii) that the Duitschland Formation is its own unconformity-bound unit lying above either the Tongwane or Penge formations of the Chuniespoort Group depending on local erosional patterns and below the Rooihoogte Formation (Bekker et al., 2020; Cheney & Winter, 1995; Eriksson et al., 2001; Gumsley et al., 2017; Moore et al., 2012; Poulton et al., 2021; Rasmussen et al., 2013).

The Duitschland Formation was first defined by Button (1973), who did not recognize the unconformity at the base of the succession and considered it a conformable uppermost unit of the underlying Penge Iron Formation and thus grouped it with the Chuniespoort Group. As a consequence, the Pretoria Group with the basal Bevets conglomerate bed, and thus the Rooihoogte Formation, would be younger than the Duitschland Formation. However, Martini (1979) established a type-reference profile for the Duitschland Formation on Duitschland Farm 95 KS and recognized a succession of shale and carbonates termed the Tongwane Formation, conformably overlying the Penge Formation. Atop lies the Duitschland Formation, which unconformably rests on the Penge or Tongwane formations depending on local erosional patterns and with a chert-pebble conglomerate at its base (Button 1973). That implies that the Duitschland Formation is included in the Pretoria Group and suggests that the basal chert-pebble conglomerate is a lateral equivalent to the Bevets conglomerate at the base of the Rooihoogte Formation. Consequently, the Duitschland Formation could be correlative to the Rooihoogte Formation in other parts of the basin. Likewise, the glacial diamictite immediately overlying the Bevets conglomerate can also be traced laterally across the basin. This correlation would indicate a single uplift period eroding the top of the Chuniespoort Group regionally around the Transvaal Basin and the Kanye Basin (Fig. 3.2B).

The nature of the contact between Duitschland and Timeball Hill formations is equally a source of confusion in the literature. On the Farm Duitschland, the uppermost part of the Duitschland Formation is formed by a carbonate unit that is gradationally overlain by a prominent poorly sorted carbonate and chert breccia, in turn sharply overlain by black carbonaceous shales of the Timeball Hill Formation (Coetzee, 2001; Martini, 1979; Swart, 1999). This breccia may resemble the Bevets bed where the latter overlies a karstic erosional surface on Malmani carbonates at the base of the Rooihoogte Formation, and thus has been responsible for much

of the controversy about the proper stratigraphic setting and correlations of the Duitschland Formation in the Transvaal Basin. Despite the fact that Martini (1979) indicates this breccia to be locally developed where it overlies carbonate units in the upper part of the Duitschland Formation and pinches out laterally, it is considered to be correlative with the regional erosional unconformity at the base of the Rooihoogte Formation and with the Kgwakgwe chert breccia in Botswana (Bekker et al., 2020; Cheney & Winter, 1995; Eriksson et al., 2001; Franchi & Mapeo, 2019; Gumsley et al., 2017; Moore et al., 2012; Poulton et al., 2021; Rasmussen et al., 2013). This interpretation implies that the deposition of the Duitschland Formation preceded that of the Rooihoogte Formation.

The different interpretations of the lower and upper contacts of the Duitschland Formation have led to three different stratigraphic models, namely that the Duitschland Formation (1) represents the final regressive facies of the uppermost Chuniespoort Group (Button, 1973; Button, 1986; Catuneanu & Eriksson, 2002; Eriksson et al., 1993; Moore et al., 2001); (2) represents its own lithostratigraphic entity not belonging to the Chuniespoort or Pretoria Group (Eriksson et al., 2001; Gumsley et al., 2017; Moore et al., 2012) or (3) is correlative to the Rooihoogte Formation at the base of the Pretoria Group (Coetzee, 2001; Guo et al., 2009; Hoffman, 2013; Luo et al., 2016; Martini, 1979; Schröder et al., 2016; Swart, 1999; Warke & Schröder, 2018). These contrasting views are summarized in a decoupled (Fig. 3.3A) vs. coupled (Fig. 3.3B) geologic history between the Duitschland, Rooihoogte and Timeball Hill formations. A decoupled depositional history (Fig. 3.3 Panel A) would require a major unconformity related to deformation between the Chuniespoort Group and the Duitschland Formation, followed by deposition of the Duitschland Formation. A second deformation event then created the unconformity between the Duitschland and Rooihoogte formations and a shift in deposition to the WTA, where the Rooihoogte Formation was deposited, followed by deposition of the Timeball Hill Formation in a conformable manner. Alternatively, contemporaneous deposition (Fig. 3.3; Panel B) would only require deformation and creation of an unconformity at the top of the Chuniespoort Group, followed by contemporaneous deposition of the Duitschland and Rooihoogte successions and the Timeball Hill Formation as a transgressive conformable deep water shale blanket atop both formations. Taken together, a decoupled depositional history would require two significant shifts in provenance, the development of two unconformities, the introduction of a separate sub-basin and two glacial events. In contrast, a coupled depositional history would require one shift in provenance and the development of one basal unconformity.

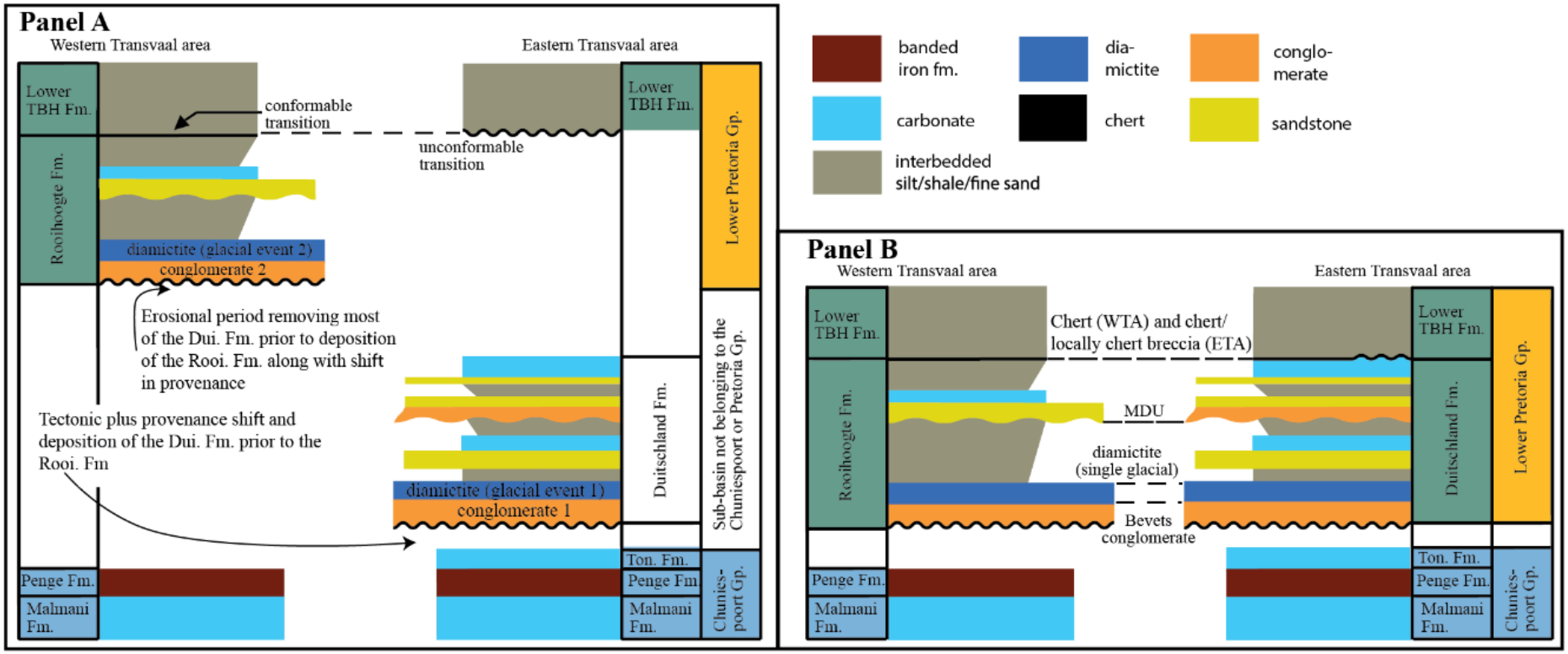

Figure 3.3. *Comparison of the two most commonly proposed stratigraphic correlations between the Duitschland and Rooihoogte formations.* **Panel A** is from Gumsley et al., (2017), while **Panel B** is after Coetzee (2001). The generalized stratigraphy for the Duitschland Formation is from the type locality at Duitschland Farm (northeastern Transvaal Basin (TB); proximal setting) and for the Rooihoogte Formation in the Potchefstroom area (southwestern TB, distal setting). See section 3.3.2 for a detailed discussion of the stratigraphic models and correlations. MDU is the mid-Duitschland unconformity.

3.4 Updated Stratigraphic Correlation of the Lower Pretoria Group

In order to gain a wider stratigraphic view, a regional correlation diagram for strata of the Duitschland, Rooihoogte and basal beds of the Timeball Hill formations was constructed from 11 stratigraphic profiles (outcrops and drill cores) throughout the entire Transvaal Basin (Fig. 3.2 and 3.4, Table 3.1), building on initial correlations by Coetzee (2001). In most of the profiles, the base of the Pretoria Group is marked by a chert breccia where it intersects the Malmani carbonates and correlative Taupone Group in the Kanye area of Botswana, or the Tongwane carbonates. This breccia is here referred to as the Bevets breccia (Fig. 3.4). A flat-pebble chert conglomerate forms the base of the Pretoria Group, where it rests on the BIF of the Penge Formation (Fig. 3.4). This conglomerate can be traced across the Transvaal area between the western profiles at Genadendal and Gopane (profiles 2 and 9) and the eastern profile at Duitschland Farm (profile 3). For the profiles in South Africa and SE Botswana studied here, it is referred to as the Bevets conglomerate. It should be noted that controversy about its position exists in the stratigraphic literature for Botswana (Franchi & Mapeo, 2019; Mapeo et al., 2006). At Duitschland Farm (profile 3), the flat-pebble chert conglomerate is overlain by a glacial diamictite (Coetzee, 2001). This diamictite can be traced eastward to Langbaken (profile 4), southwards to Carletonville (profile 8), Klerksdorp (profile 10) and Kransfonstein (profile 11) and several 100 kilometers westward to Jwaneng (profile 1) in Botswana. The diamictite (here informally referred to as the Bewaarkloof diamictite, Fig.3.4) is conformably overlain by a few meters thick banded iron formation (Jwaneng IF) between profile 1 in Botswana to profile 2 some 200 km further east in South Africa, and profile 8 about 330 km southeast also in South Africa (Fig. 3.2 and 3.4). The next prominent marker horizon is a well-rounded chert pebble conglomerate referred to as the mid-Duitschland sequence boundary (Coetzee, 2001), the Langbaken conglomerate or the mid-Duitschland unconformity (Warke & Schröder, 2018). It is most prominently developed at Langbaken (profile 4) with a thickness of over 20 meters but can be traced westward to Gopane (profile 9) and as far west as Jwaneng in Botswana (profile 1). It is also developed in the southern Transvaal Basin at Carletonville (profile 8) and Klerksdorp (profile 10). Lastly, the capping chert breccia developed at Duitschland Farm (profile 3) and the surrounding area suggests an unconformable contact to the Timeball Hill Formation. This breccia caps a succession of similar chert breccias developed in stromatolitic carbonates.When traced laterally, the unconformity transitions into an apparent conformable contact. For example, at Jwaneng (profile 1), it is difficult to place a clear sharp contact between the uppermost grey shales of the Duitschland Formation and

overlying pyritic black shales of the lowermost Timeball Hill Formation. In the southern profiles (profiles 8, 9, 10 and 11), the contact is located within a section of black shales, and for consistency purposes is placed along a black chert bed in direct contact with highly pyritic shale of the Timeball Hill Formation. The base of the Timeball Hill Formation is further highlighted locally by a tuff layer at Jwaneng (profile 1) and Ngodwana (profile 7), which probably correlates with the Bushy Bend lavas observed at Klerksdorp (profile 10) and Kransfontein (profile 11) (McCarthy et al., 2018).

Table 3.1. Stratigraphic profile references for Fig. 3.2 and 3.4

Profile	Locality type (drill core/outcrop)	Locality	Compiled references
1	JREP-1	Jwaneng	Beukes (unplublished)
2	GD-2	Genadenal	Coetzee, 2001 ; Martini, 1979
3	Outcrop & ADL	Duitschland	Coetzee, 2001 ; Martini, 1979 ; This study
4	Outcrop	Langbaken	Martini, 1979
5	Outcrop	Tongwane	Martini, 1979
6	PA-13	Penge	Beukes, 1978
7	ANW	Ngodwana	This study
8	DP-16; EBA-2/4 & KEA-4*	Carletonville	Brüske, et al 2020 ; Luo, et al. 2016
9	AGP1 & AGP-2	Gopane	This study
10	BH 1740	Klerksdorp	Coetzee, 2001
11	KFN-1	Kransfontein	Mc Carthy et al., 2018

*EBA and KEA drill cores (not included in Fig. 3.2 and 3.4) are from the same area as DP-16 and display the same lithological build-up.

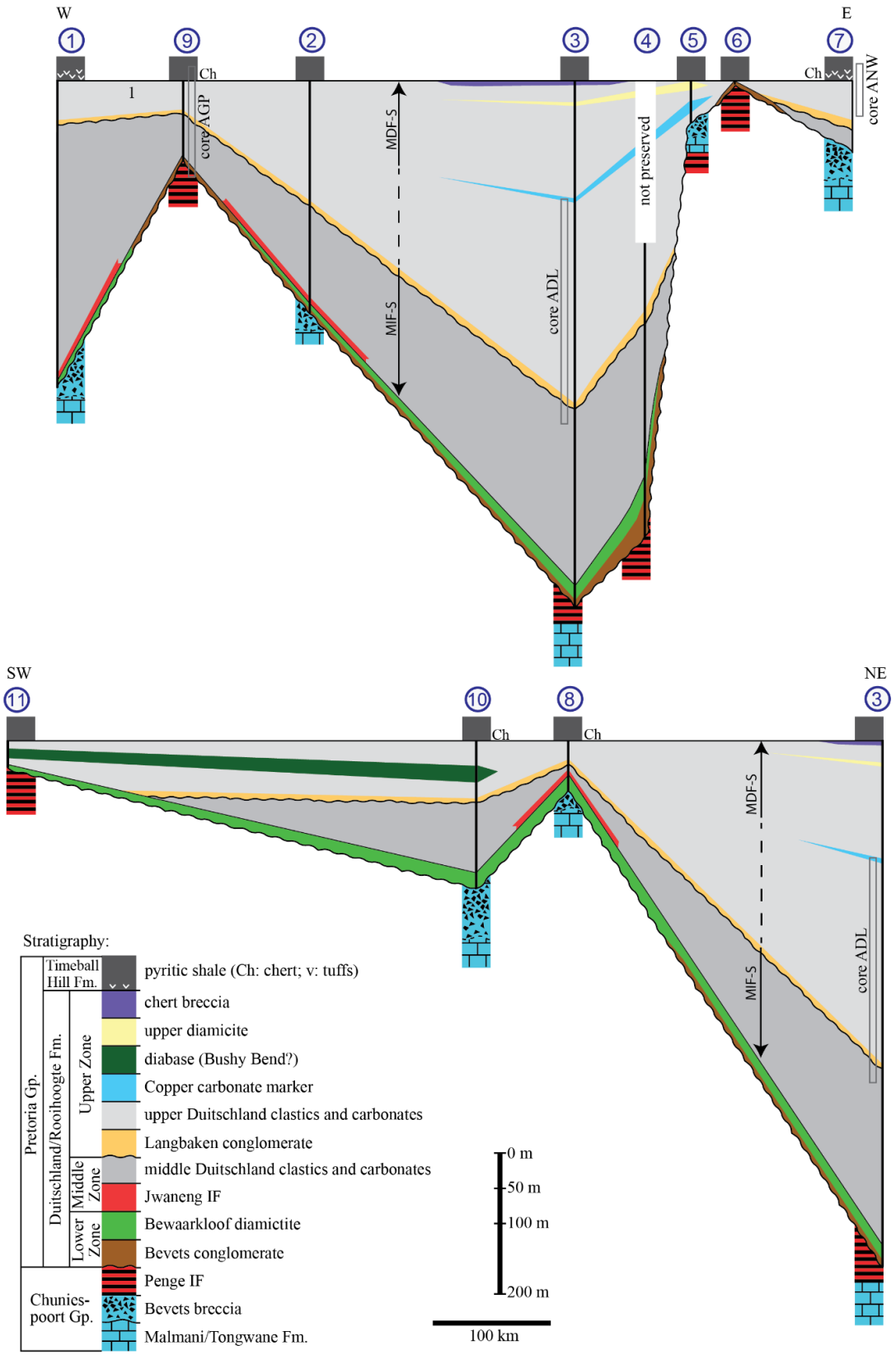

Figure 3.4. *Generalized lithology of 11 stratigraphic profiles throughout the Kaapvaal Craton* (Fig. 3.2). All cores can be stratigraphically correlated based on marker horizons (see section 3.4 for discussion). Profile 3 acts as an anchor profile. Profiles 1 through 7 and 9 are correlated from east to west and profiles 3, 8, 10 and 11 are correlated from northeast to southwest.

Based on the observations described above and illustrated in figure 3.4, it becomes apparent that both the Rooihoogte and Duitschland formations can consistently be correlated throughout the entire Kaapvaal Craton and can be divided into three stratigraphic zones. A lower part (informally referred to as the *Lower Duitschland/Rooihoogte (D/R)* interval) is represented by the Bewaarkloof diamictite and chert pebble conglomerate (Bevets conglomerate), a *Middle D/R* interval is defined between the diamictite and the intraformational-formational Langbaken conglomerate, and is represented by mostly fine-grained siliciclastics. The *Upper D/R* interval is primarily made of interbedded argillites and carbonate beds, which rest below the black shales of the Timeball Hill Formation in most profiles (Fig. 3.4). The stratigraphic diagram thus strongly suggests a correlation between the Duitschland and Rooihoogte formations.

3.5 CIMERA-Agouron GOE Scientific Drill Cores

In 2016 four scientific drill cores intersected the Duitschland-Timeball Hill formations and Rooihoogte-Timeball Hill formations to establish a sound sedimentary and stratigraphic framework of the early Paleoproterozoic formations of the TB and to obtain data to constrain the stratigraphic relationship between the Duitschland and Rooihoogte formations, and thus the GOE record. In the northwestern Gopane area of the TB, two drill cores were selected (AGP-1 and AGP-2; 25°17.359S, 25°44.493E). Drill core AGP-2 (length 85 m) intersects the upper Rooihoogte Formation (*Upper D/R* interval) and the overlying Timeball Hill Formation (*Lower TBH* interval), whereas drill core AGP-1 (length 120 m) only intersects stratigraphy from the Penge Formation to the upper Rooihoogte Formation, corresponding to the intervals *Lower D/R, Middle D/R* and most of the *Upper D/R*. The two other drill cores were drilled at Duitschland Farm (ADL; 24°17.268S, 29°07.491E) and at Ngodwana (ANW; 25°36.239S, 30°37.002E) in the northeastern and southeastern Transvaal Basin (Fig. 3.2B), respectively. The ADL drill core (length 317 m) starts a few meters below the Langbaken conglomerate and ends below the top of the upper Duitschland Formation in the Cu carbonate marker (Martini, 1979), corresponding to most of the *Upper D/R* interval and the very top of the *Middle D/R* interval. This drill core was specifically planned to intersect a poorly exposed part of the succession. The ADL drill core thus corresponds to an interval for which no multiple sulfur isotopic data is available (Guo et al., 2009), representing a knowledge gap in our understanding of the nature of the transition between MIF-S and MDF-S and thus the proposed GOE interval in the Duitschland Formation. The ANW drill core (length 23 m) intersects the upper interval of the Rooihoogte Formation (*Upper D/R* interval) and the lowermost Timeball Hill Formation

(*Lower TBH* interval), stopping several meters above the Langbaken conglomerate. The ANW drill core was supposed to intersect the carbonaceous shale of the Timeball Hill Formation and all three zones of the Rooihoogte Formation, as known from outcrop a few hundred meters from where the hole was spudded. Very surprisingly the basal Bevets chert breccia situated on the Malmani carbonates in the area was intersected much earlier than expected so that both the Langbaken marker bed (MDU) and the *Middle D/R* interval were absent (Fig. 3.4B, Locality 7).In the ANW drill core, the tuff layer within the lower Timeball Hill Formation at 34.00 to 35.44 meters depth. Tuffs are noticeably present just above the Duitschland-Timeball Hill contact at profiles in the far west (1) and east (7) of the transect (Fig. 3.2 and 3.4). Their relationship to the Bushy Bend lavas, which is commonly assigned to the very top of the Rooihoogte Formation (Coetzee, 2001) or lowermost Timeball Hill Formation (Eriksson et al., 1995; Lenhardt et al., 2012), remains currently uncertain. On a basinal scale, it seems chronostratigraphic correlation is not in line with sequence stratigraphic correlations of the sediments. This study uses the tuff layer as the transition marker from the Duitschland and Rooihoogte formations to the Timeball Hill Formation.

During a field campaign in 2018, the cores AGP-1 (n=40 samples), AGP-2 (n=22), ANW (n=17) and ADL (n=34) were carefully sampled at the core facility of the University of Johannesburg, avoiding obvious later alteration zones and secondary veining that is very uncommon in the well-preserved greenschist lower greenschist facies strata. Sampling was focused on geochemical comparison of major and trace element systematics as well as for radiogenic Sr-Nd isotopes of the Duitschland and Rooihoogte formations, but the lower Timeball Hill Formation was sampled as well.

For purposes of stratigraphic sample positions, this study only provides very generalized drill core logs of the four holes (Fig. 3.S1, supplementary information). Original drill hole descriptions can be downloaded from the *CIMERA-Agouron GOE and Biomarker Drilling Project* (https://cimera.co.za/agouron-goe-project/) upon request, while detailed summaries are provided in the supplementary information.

3.6 Analytical Methods

3.6.1 Major Element Analyses

Major element oxide concentrations were determined using X-ray fluorescence analyses (XRF) on a wavelength dispersive Bruker© AXS Pioneer S4 (Rh-tube; 4 kW) at the Isotope

Geochemistry Group of the University of Tuebingen (Germany). Glass beads for XRF analyses were prepared by mixing of 1.5 g of sample powder with 7.5 gram of Merck® Spectromelt A12 and melted at 1200 °C with an Oxiflux system from CBR analytical service. Loss on ignition (LOI) was determined on 1 gram of dried sample powder via overnight ashing in a muffle furnace at 1050 °C. A detailed sample preparation protocol and measuring technique are described in Albut et al. (2018). Major element data for the different drill core samples are presented in Tables 3.2–3.5. Thirty-two standardized samples were measured, and matrix effect corrections were performed using the standard Spectra Software from Bruker©. The standard JB-2 yields values in accordance with GeoReM preferred values (supplementary Tables 3.S1a and 3.S1b).

3.6.2 Trace Element Analyses

Trace element analyses were performed at the Isotope Geochemistry Group of the University of Tuebingen (Germany), following the sample preparation and measuring procedures described in detail by Albut et al. (2018). The powdered samples were ashed at 600 °C for 12 hours to oxidize organic phases. Ashed samples were weighed (ca. 100mg) into Savillex beakers and digested in a mixture of HNO_3 (65%) and HF (48%) for four days on a hotplate at 100°C, with frequent ultrasonic baths. Subsequently, the samples were evaporated, redissolved in 6M HCl and heated for 24 hours at 130 °C. Lastly, the samples were dried and converted to nitric form before being taken up in 2% HNO_3 to yield a nominal dilution factor of 10000. The analyses were performed on a ThermoFisher Scientific© iCap-Qc quadrupole inductively coupled plasma mass spectrometer (Q-ICP-MS) connected to an ESI© SC-2 DX autosampler equipped with an ESI© Fast uptake system (4 mL sample loop). Trace element data for the different drill core samples are presented together with major element composition in Tables 3.2–3.5. Three certified geochemical reference materials (OU-6 (IAG), AGV-2 (USGS) and JB-2 (GSJ)) were measured throughout the study to monitor precision and accuracy of laboratory procedures and measurements. The average concentrations for the respective reference materials are in good conformance with certified values, and the 1 r.s.d. report a full method precision of <5% deviation for key elements (supplementary Tables 3.S2a and b).

3.6.3 Rb-Sr and Sm-Nd Isotope Analyses

All Rb-Sr and Sm-Nd data are presented in Table 3.6. Isotope ratio measurements were performed at the Isotope Geochemistry Group of the University of Tuebingen. Sample powders

were weighted into Teflon beakers and mixed with adequate amounts of tracer solutions enriched in ^{87}Rb-^{84}Sr and ^{149}Sm-^{150}Nd. Digestion was achieved via HF (48%)-HNO_3 (65%) acid attack by placing the closed beakers on a hot plate at 100°C. Digested samples were dried and transformed to chlorides in 6N HCl. The samples were redissolved in 2.5N HCl for chromatographic separation. Rb, Sr and light rare-earth elements were purified by conventional ion exchange chromatography using quartz glass columns filled with BioRad© AG 50W-X8 (200-400 mesh). Strontium separates were cleaned up using Eichrom© Sr spec resin. Subsequent separation of Sm and Nd was achieved using a reverse ion chromatographic procedure using quartz glass columns filled with Eichrom© Ln resin. Sr separates were loaded with Ta-activator on Re single filaments, and isotope ratio measurements were performed in dynamic mode on a modernized and refurbished Finnigan MAT© 262 thermal ionization mass spectrometer (TIMS). Analytical mass fractionation was corrected using an $^{88}Sr/^{86}Sr$ ratio of 8.375209 and exponential law. Measurements of NBS SRM 987 yielded a 0.710256±0.000010 (2SD, n = 7) for the $^{87}Sr/^{86}Sr$-ratio compared to the long-term reproducibility of 0.710247±0.000033 (2SD, n = 804). Rubidium isotopes were determined in static mode using the element-doping technique with Zr and measured on a ThermoFisher Scientific© Neptune Plus multi-collector inductively coupled plasma mass spectrometer (MC-ICPMS). The $^{91}Zr/^{90}Zr$ ratio was adjusted to a value of 0.217933 to yield the certified $^{85}Rb/^{87}Rb$ value for the NBS SRM 984 of 2.593. Total procedural blanks (chemistry and loading) were <159 pg for Sr and <26 pg for Rb and thus negligible. Neodymium was loaded as phosphate on Re double filaments and measured in static mode on a modernized and refurbished FinniganMAT© 262 TIMS. Analytical mass fractionation was corrected with $^{146}Nd/^{144}Nd$ of 0.7219 using exponential law. Repeated measurements of the La Jolla Nd standard gave a $^{143}Nd/^{144}Nd$ ratio of 0.511816±0.000010 (2SD, n = 5) compared to the long-term average of 0.511830±0.000041 (2SD, n = 172). The JNdi-1 Nd standard gave an average $^{143}Nd/^{144}Nd$ ratio of 0.512071±0.000022 (2SD, n = 9) relative to the long-term average of 0.512075±0.000073 (2SD, n=71). Samarium isotopes were measured on a ThermoFisher Scientific© Neptune Plus MC-ICPMS in static mode and analytical mass bias was corrected with $^{147}Sm/^{152}Sm$ of 0.56081. Procedural blanks were <21 pg for Nd and <24 pg for Sm and thus negligible. Repeated measurements NIST3174a yielded an average of 0.516877±0.00001 (2SD, n = 8), which is similar to the long-term laboratory average of 0.51688±0.00005 (2SD, n = 89).

JB-2 from the Geological Survey of Japan and OU-6 from the International Association of Geoanalysts were used as full procedural standards and yielded a $^{143}Nd/^{144}Nd$ ratio of

0.513051±0.000010 (2SE) and 0.512103±0.000010 (2SE), respectively. Samarium and Nd concentrations were measured to 2.06 µg/g and 5.77 µg/g for JB-2 and 5.91 µg/g and 29.8 µg/g for OU-6, respectively. JB-2 and OU-6 $^{87}Sr/^{86}Sr$-ratios were measured to 0.703688±0.000009 (2SE) and 0.729772±0.000009 (2SE) respectively. Concentrations of Rb and Sr were measured to 6.37 and 178.6 for JB-2 and 128.3 and 137.1 for OU-6. Determined values for isotope ratios (only JB-2) and concentrations (JB-2 and OU-6) agree with literature data (Imai et al., 1995; Kane, 2004; Li et al., 2007; Miyazaki & Shuto, 1998). However, to our knowledge, no published $^{143}Nd/^{144}Nd$ and $^{87}Sr/^{86}Sr$ values are currently available for OU-6.

3.7 Analytical Results

The study focuses on analyses obtained on fine-grained siliciclastic components of the different drill cores since these give the best measure for provenance for the Duitschland Formation (ADL) and Rooihoogte Formation (AGP-1, AGP-2, ANW). The following section reports results in the categories shale, silt and fine sand. However, for readability of figures we only plot results as fine-grained siliciclastic components discriminated based on drill core derivation. Samples belonging to either the Duitschland or Rooihoogte formations are based on stratigraphic interpretations in section 3.8.2. For information about the few chemical sediment samples measured, see Tables 3.2–3.5.

3.7.1 Major Elements

The Agouron GOE drill cores have similar major element compositions (Tables 3.2–3.5, Fig. 3.5) and are comparable to the composition of the Post Archean Australian Shale composite (PAAS). Samples from all four drill cores show generally high concentrations of SiO_2 and Al_2O_3 along with moderately high concentrations of $Fe_2O_{3(t)}$, and CaO.

The **shale fraction** for AGP-1 (n=23), AGP-2 (n=4), ADL (n=13) and ANW (n=9) have average concentrations for SiO_2 (64.7, 64.3, 54.6, 62.0 wt%), $Fe_2O_{3(t)}$ (5.8, 5.4, 11.02, 5.7 wt%), Al_2O_3 (15.5, 14.4, 18.0, 17.5 wt%) and CaO (0.4, 0.2, 0.9, 0.1 wt%), respectively. The **silt fraction** of the cores AGP-1 (n=6) and ADL (n=10) display averages for SiO_2 (57.6, 56.6 wt%), $Fe_2O_{3(t)}$ (9.9, 10.9 wt%), Al_2O_3 (17.4, 17.4 wt%) and CaO (0.4, 0.4 wt%), respectively. For AGP-2 (n=1) the silt fraction displays a value of 61.7 wt% SiO_2, 4.6 wt% $Fe_2O_{3(t)}$, 18.4 wt% Al_2O_3 and 0.5 wt% CaO. Note that the ANW drill core does not contain any silt fraction. **Fine-grained sand** samples are only present in the ADL (n=9) core and display average concentrations of 56.1 wt% for SiO_2, 10.1 wt% for Fe_2O_3, 18.3 wt% for Al_2O_3 and 0.3 wt% for

CaO. Major element compositions of the fine-grained siliciclastic components from all drill cores display a relatively well-defined correlation between Al_2O_3 vs. SiO_2, TiO_2, P_2O5 and K_2O respectively, whereas no particular trend is observed between Al_2O_3 and Fe_2O_3, MnO, MgO and CaO (Fig. 3.5).

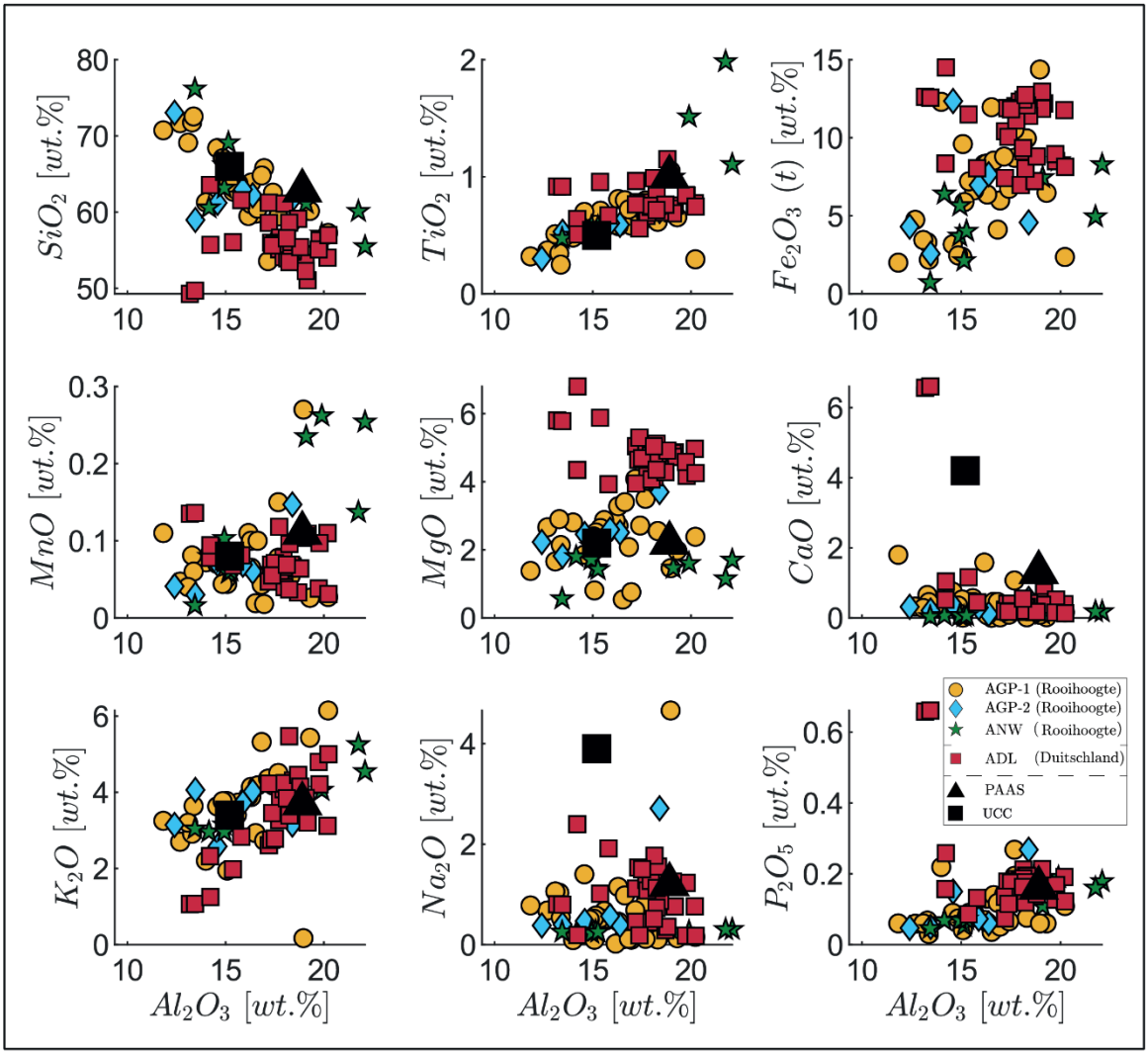

Figure 3.5. *Major element binary correlation plots of fine-grained siliciclastic components (fine sand to shale) of the Duitschland and Rooihoogte formations for the four geochemically analyzed drill cores.* Data from the upper continental crust (UCC) (Taylor & McLennan, 1995) and Post-Archean Australian Shale (PAAS) (Taylor & McLennan, 1985) are plotted as reference.

3.7.2 Rare Earth Elements + Yttrium

The average ∑REE+Y concentrations (Table 3.2–3.5) for the **shale fraction** is 249 µg/g (AGP-1, n=23), 253 µg/g (AGP-2, n=4), 250 µg/g (ADL, n=13) and 267 (ANW, n=9). The ∑REE+Y ranges from 113 to 253 µg/g for AGP-1, with one outlier of 629.19 µg/g (AGP-1 75.59). For the other three drill cores, the ∑REE+Y ranges from 149 to 339 µg/g, 163 to 447 µg/g and 194 to 548 µg/g for AGP-2, ADL and ANW, respectively. For the **silt fraction**, the ∑REE+Y concentrations averages to 257 µg/g (AGP-1, n = 6) and 236 µg/g (ADL, n=10). The single silt sample from AGP-2 displays ∑REE+Y of 196 µg/g. The ∑REE+Y ranges from 149 to 330 µg/g and 169 to 303 µg/g for the AGP-1 and ADL core, respectively. The **fine-grained sand fraction** displays a mean ∑REE+Y of 242 µg/g (ADL, n=9) with a range from 137 to 370 µg/g. The average ∑REE+Y values of the four drill cores are comparable to but exceed values of the average continental crust with ∑REE+Y of 168 µg/g (Taylor and McLennan 1985) and PAAS 210 µg/g (Taylor & McLennan, 1985, 1995). PAAS-normalized REE patterns are relatively flat and unfractionated, albeit slightly varying enrichment factors are indicative for a source comparable to the PAAS (Fig. 3.6). Chondrite normalized REE+Y patterns for the fine-grained siliciclastic components show a clear enrichment in light rare earth elements (LREE) relative to heavy rare earth elements (HREE), with mean chondrite normalized slopes for LREE (La/Sm_{CN}) and HREE (Gd/Yb_{CN}) of 4.29 and 1.36 (AGP-1, n=23), 3.84 and 1.24 (AGP-2, n=5), 4.04 and 1.89 (ADL, n=15) and 3.49 and 1.19 (ANW, n=9) respectively for the **shale fraction**. The **silt fraction** shows average LREE (La/Sm_{CN}) and HREE (Gd/Yb_{CN}) ratios of 4.35 and 1.56 (AGP-1, n = 7), 4.47 and 1.73 (ADL, n=10) and 3.67 and 1.50 for AGP-2 (n=1), respectively. The **fine-grained sand fraction** shows average LREE (La/Sm_{CN}) to HREE (Gd/Yb_{CN}) ratios of 4.43 and 1.60 (ADL, n=9), respectively. The individual cores thus show similar La/Sm_{CN} and Gd/Yb_{CN} ratios, which are comparable to chondrite normalized LREE and HREE slopes of PAAS (La/Sm_{CN} = 4.26; Gd/Yb_{CN} = 1.36).

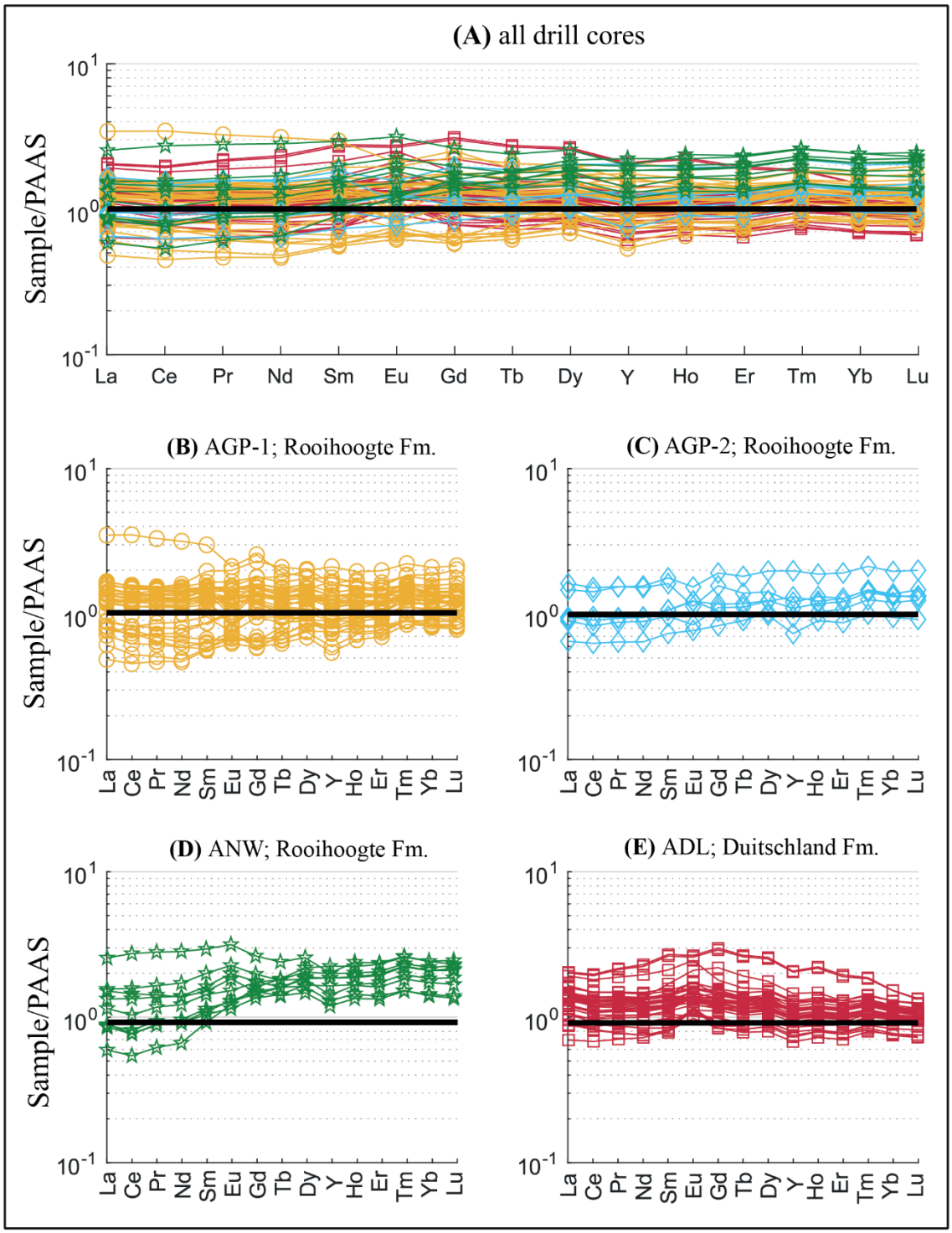

Figure 3.6. *PAAS normalized REE+Y patterns for the fine-grained siliciclastic components (fine sand to shale) of the Duitschland and Rooihoogte formations.* **(A)** compares all four drill cores while **(B)** to **(E)** show the variability within individual drill cores.

3.7.3 Bulk Sediment Rb-Sr and Sm-Nd Isotope Compositions

Rubidium-Sr and Sm-Nd concentrations and their respective isotope ratios are presented in Table 3.6. Strontium isotope ratios display highly radiogenic, present-day isotope compositions caused by elevated $^{87}Rb/^{86}Sr$ ratios ranging from 3.065 to 18.00, inducing high degrees of radiogenic ingrowth of ^{87}Sr in the samples. Rb-Sr isotopic signatures seem to have been reset as the calculated regression age gives 1964±86 Ma albeit a rather higher MSWD of 233 (Fig. 3.7). Consequently, $^{87}Sr/^{86}Sr$ isotope ratios of all samples are back-corrected to 1.96 Ga and compared at that time. Samples from the AGP-1, AGP-2 and ANW drill cores of the Rooihoogte Formation have time-corrected $^{87}Sr/^{86}Sr$ values ranging from 0.73518 to 0.74592 and 0.72032 to 0.73606 and 0.71525 to 0.76338, respectively. Samples from the ADL core (Duitschland Formation) have $^{87}Sr/^{86}Sr$ isotopic compositions at 1.96 Ga ranging from 0.72684 to 0.74571, respectively. Furthermore, there seems to be no particular relation to stratigraphic height, and both studied formations are indistinguishable from each other.

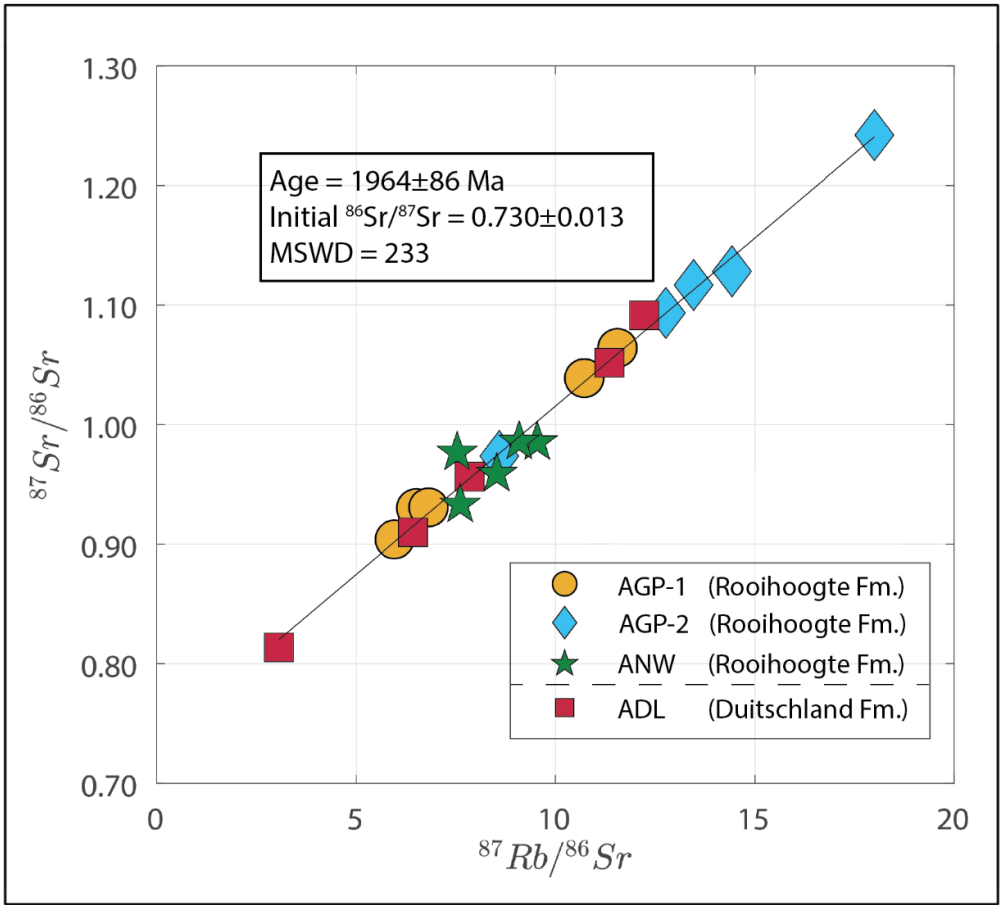

Figure 3.7. *Rb-Sr isochron calculation* (Isoplot version 4.15, Ludwig, 2011). The 1964±86 Ma regression age corresponds roughly to the age of the Bushveld intrusion at 2054.4±1.3 Ma (Scoates and Friedman, 2008). Measurement uncertainties are within symbol size.

Present-day $^{143}Nd/^{144}Nd$ isotope compositions for all four drill cores show only a restricted variation from -22.1 to -31.0 ε Nd_{0Ga} (Table 3.6). Age-corrected Nd isotope compositions show a surprisingly low variation with $\varepsilon Nd_{2.42Ga}$ ranging just over 6 epsilon units accompanied by $^{147}Sm/^{144}Nd$ values typical for the upper continental crust (Table 3.6). There is no discernible difference between obtained $\varepsilon Nd_{2.42Ga}$ values among the different cores, ranging from $\varepsilon Nd_{2.42Ga}$ -2.2 to -5.9 except for samples AGP-1-122.3 and ANW-39.14, which show $\varepsilon Nd_{2.42Ga}$ values of -6.7 and -8.8, respectively. Specifically, the Rooihoogte Formation, represented by the drill cores AGP-1, AGP-2 and ANW, shows $\varepsilon Nd_{2.42Ga}$ values ranging from -2.5 to -5.8, -2.2 to -3.9 and -3.4 to -4.2, respectively, when the samples AGP-1-122.3 ($\varepsilon Nd_{2.42Ga}$ = -6.7) and ANW-39.14 ($\varepsilon Nd_{2.42Ga}$ = -8.8) are excluded. For the Duitschland Formation (ADL) $\varepsilon Nd_{2.42Ga}$ varies between -3.6 and -4.7. Interestingly, all calculated mean crustal residence ages $T_{DM}(Nd)$ yield Archean ages. (Table 3.6). This is independent of the applied calculation modes (linear evolution for depleted mantle following Peucat et al. (1989) or the dynamic evolution for the depleted mantle based on crustal growth curves (Nägler & Kramers, 1998)) and yields similar results. All determined $T_{DM}(Nd)_{linear}$ vary between 2.99 Ga and 3.34 Ga, with two outliers yielding even older ages of 3.55 Ga (AGP-1-122.3) and 4.12 Ga (ANW-39.14). That is significantly older than the major zircon peak interval ~[2400 to 2550 Ma] (Schröder et al., 2016; Zeh et al., 2020).

3.8 Discussion

3.8.1 Sedimentological and Geochemical Arguments for the Duitschland-Rooihoogte Controversy

The strongest argument for stratigraphic equivalence between Duitschland and Rooihoogte formations is the similarity of internal stratigraphy that can be traced around the entire Transvaal Basin (Fig. 3.4). Although units in the Lower and Middle D/R may pinch out laterally due to erosion or non-deposition, the Upper D/R is essentially present in all sections (Eriksson et al., 2001).

Part of the argument for a stratigraphic distinction between the Rooihoogte and Duitschland formations is the development of a chert breccia in the Duitschland area, interpreted as an unconformable contact between the Duitschland and the Timeball Hill formations, in contrast, a sharp conformable contact between the Rooihoogte and Timeball Hill formations. This was used to suggest that the Duitschland Formation represents its own lithostratigraphic unit not belonging to the Chuniespoort or the Pretoria groups (Fig. 3.3, Panel A). However, the sharp-

based chert horizons capping the Rooihoogte Formation in profiles 8, 9 and 10 in the western and southwestern Transvaal Basin and in profile 7 in the east (Fig. 3.4) can be considered lateral equivalents of the chert breccia in the Duitschland area. Importantly, breccia development is localized and limited to shallow-water stromatolitic facies occurring in the Duitschland (profile 3) and Carletonville areas (profiles 8 and 10). The contact can be traced laterally from the Duitschland area (profile 3) westward to a gradational conformable contact without indication of erosion (profiles 1 and 2). It is, therefore, most likely that the development of a seemingly unconformable contact in the Duitschland area (profile 3) relates to the very shallow water conditions in the area, while more continuous sedimentation was recorded elsewhere. In addition, paleocurrents do not vary between the Duitschland and Timeball Hill formations (Coetzee, 2001; Schröder et al., 2016), arguing against a tectonic control on deposition that is implied when treating the Duitschland and Rooihoogte as different formations. Therefore, the contact between the Duitschland and Timeball Hill formations and the Rooihoogte and Timeball Hill formations, respectively, can be considered a higher-order sequence boundary. These observations link the Duitschland Formation stratigraphically to the Rooihoogte Formation.

The lower unconformity separating the Duitschland and Rooihoogte formations from the underlying Chuniespoort Group can be mapped consistently around the preserved outcrop limits of the Pretoria Group, including the Crocodile River and Marble Hall Domes in the Bushveld Complex (Hartzer, 2000). This is typically developed as a flat pebble conglomerate (Bevets conglomerate) overlain by the Bewaarkloof diamictite, but a chert breccia (Bevets breccia) where it intersects carbonates. This is a very irregular surface and most probably represents an ancient karst landscape as observed in other areas (Body, 1982). Collectively, these observations indicate a coupled depositional history of the Duitschland and Rooihoogte formations. The geochemical composition of fine-grained siliciclastics from the Duitschland and Rooihoogte formations also support a coupled depositional history.

Trace element patterns for all drill cores are indistinguishable from each other, as exemplified by REE+Y patterns, which resemble the composition of PAAS (Fig. 3.6). The Major element systematics of the Duitschland and Rooihoogte formations are indistinguishable for TiO_2, MnO, CaO, K_2O, Na_2O and P_2O_5 (Fig. 3.5). However, the sediments from the ADL drill core (Duitschland Formation) are lower in SiO_2, higher in $Fe_2O_{3(t)}$ and clearly more enriched in MgO compared to sediments of the Rooihoogte Formation (AGP-1, AGP-2 and ANW drill

cores). The sedimentological development of the Duitschland and Rooihoogte formations probably incorporate sediments from at least two different provenances, as also suggested by Coetzee (2001), and thus the ADL drill core (Duitschland Formation) might incorporate larger amounts of a more mafic source relative to the slightly more felsic AGP-1, AGP-2 and ANW drill cores (Rooihoogte Formation). Nevertheless, the $\varepsilon Nd_{2.42Ga}$ and $T_{DM}(Nd)$ systematics of sediments fall within a narrow range and cannot be distinguished by core (Table 3.6). It appears that the Rb-Sr isotope system has been reset during the intrusion of the 2054±1.3 Ma Bushveld Igneous Complex (Scoates & Friedman, 2008), Fig. 3.7. The resetting of the Rb-Sr system in all cores of the Duitschland and Rooihoogte formations, which are widely separated, emphasize that initial $^{87}Sr/^{86}Sr$ isotope ratios should not be used for provenance identification or as a proxy for paleo-weathering in the entire Transvaal Basin.

3.8.2 Sequence Stratigraphic and Chemostratigraphic Correlations

Apart from their lithostratigraphy, the Duitschland and Rooihoogte formations also display a remarkably similar internal stratigraphic architecture (Fig. 3.8), which in turn correlates with geochemical proxies for detrital input, sediment maturity, degree of weathering (CIA) and source compositions (Fig. 3.9). Two unconformity-bound sequences make up the Duitschland and Rooihoogte formations, where the lower sequence is represented by the *Lower D/R* and *Middle D/R* interval and the upper sequence by the *Upper D/R* interval, which is overlain by the Timeball Hill Formation (Fig. 3.8).

The unconformity below the Bevets conglomerate forms the base of the lower sequence. Above the conglomerate-diamictite pair, deposits fine upwards rapidly to laminated shales (Gopane-AGP drill core, Duitschland farm and Langbaken) and the Jwaneng BIF (GD-1 and JREP-33 drill cores; Fig. 3.4 and 3.8). This likely represents the post-glacial transgression. The remainder of the Middle D/R interval shows a coarsening-upwards and shallowing-upwards regressive trend, capped by the Langbaken conglomerate bed (MDU) (Fig. 3.8) (Coetzee, 2001; Warke & Schröder, 2018).

The Langbaken conglomerate bed represents incision and erosion at the base of the upper sequence. Overlying the conglomerate, a thin shale and sandstone-dominated interval represents possible transgression. The bulk of the upper sequence consists of meter- and decameter-thick upward coarsening packages from shale through silt to sandstones and oolitic-

stromatolitic carbonates below the contact to the Timeball Hill Formation (Fig. 3.8). This represents overall shallowing of the upper sequence (Coetzee 2001).

The contact between Duitschland and Timeball Hill formations is marked locally (Duitschland farm) by karstification and an abrupt change to deeper-water deposition of pyritic carbonaceous shales. In other locations (Gopane-AGP, BH1740 and DP-16 drill cores), this transgressive trend is represented by stromatolitic carbonates sharply overlain by grey shales that pass upwards to pyritic shales of the Timeball Hill Formation, typically with a thin chert at the contact. The deeper-water pyritic shales are regionally overlain by prograding deltaic deposits of the Timeball Hill Formation (Fig. 3.4 and 3.8) (Coetzee et al., 2006; Coetzee, 2001).

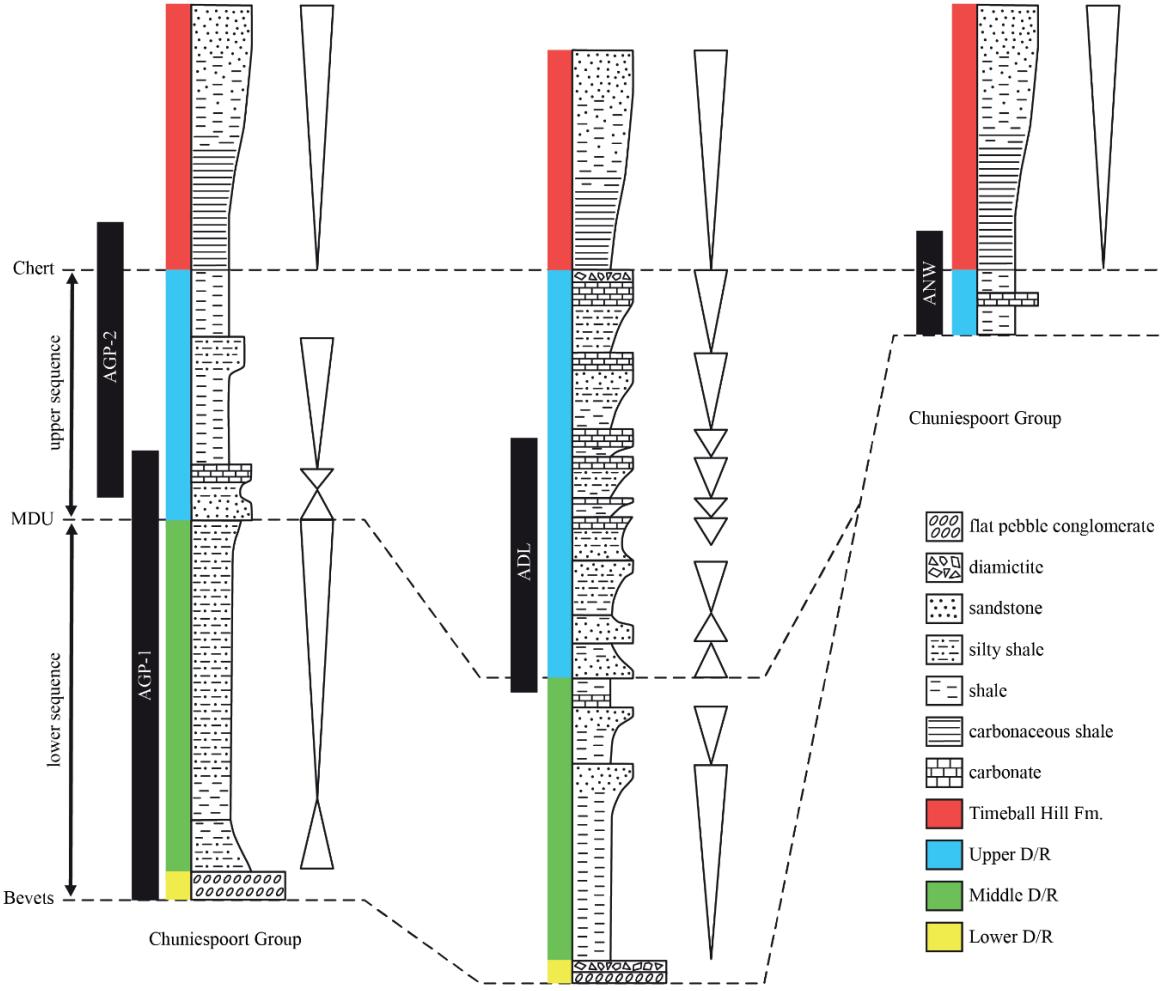

Figure 3.8. *Sequence stratigraphic development and correlation of the Duitschland Formation (ADL drill core) and Rooihoogte Formation (AGP-1, AGP-2 and ANW drill core) between the localities intersecting drill cores sampled for geochemical analyses*. For sedimentological logs and precise correlation of marker horizons between the four geochemically analyzed drill cores, see figure S1 in the supplementary information.

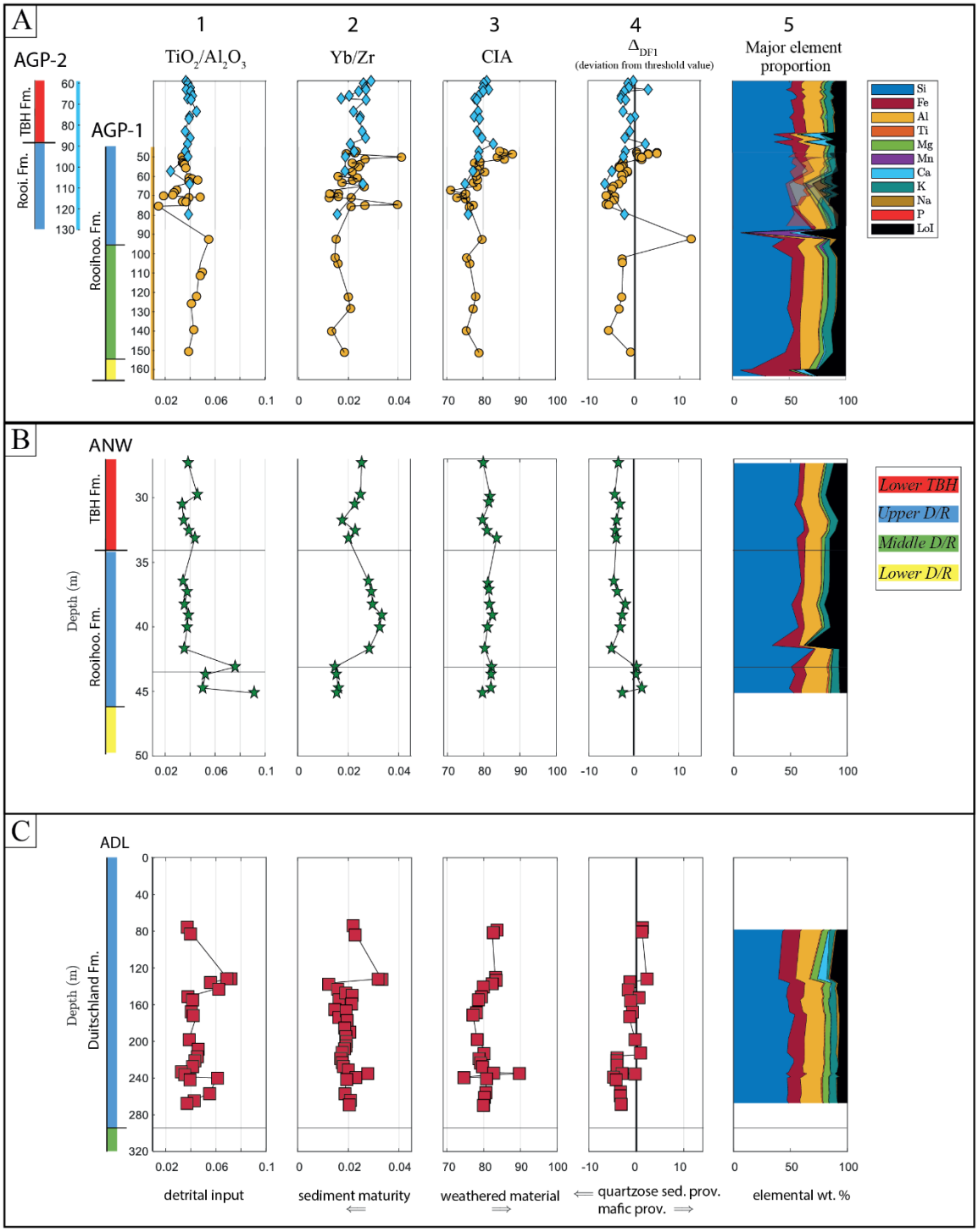

Figure 3.9. *Chemostratigraphic correlation of the drill cores AGP-1, AGP-2 and ANW (Rooihoogte Formation) and ADL (Duitschland Formation).* Columns **1** through **4** encompass fine-grained siliciclastic components (fine sand to shale) and column **5** encompasses all samples. CIA values in column **3** are calculated following the approach described in Gaschnig et al. (2014). Δ_{DF1} in column **4** is a measure of the deviation from the threshold value between a quartzose sedimentary and a mafic provenance in figure 10B for discrimination function 1 (DF1). See section 3.8.2 for further discussion of the individual proxies.

The relationship between the sedimentology (Fig. 3.8) and geochemical proxies for deposition are explored in Fig. 3.9. The "detrital input" represented by TiO_2/Al_2O_3 (Fig. 3.9, column 1) is controlled by the source material and tends to decrease as a function of transport distance due to hydraulic sorting and, thus, preferential deposition closer to the shore of heavy Ti-bearing minerals relative to Al-bearing minerals (Chen et al., 2013; Playter et al., 2018). Following this rationale, TiO_2/Al_2O_3 ratios can be used to track relative sea level changes in the ancient rock record (Chen et al., 2013; Playter et al., 2018). Sediment maturity can, in turn, be estimated by the abundance of heavy minerals, such as zircons, that are concentrated in sediments through sedimentary recycling (McLennan et al., 1993). Thus, decreasing Yb/Zr ratios (Fig. 3.9, column 2) indicate a larger contribution from crustal sources, while higher ratios indicate a larger pelagic clay contribution. Another parameter is the chemical index of alteration (CIA, Fig. 3.9, column 3), which is a measure of the degree of chemical weathering that the rocks have experienced from provenance to deposition. High CIA values reflect intense removal of large ion lithophile elements (e.g., Ca^{2+}, Na^{2+}) relative to their immobile counterparts (e.g., Al^{3+}, Ti^{4+}) (Fedo et al., 1995; Nesbitt & Young, 1982). A fourth parameter calculated is the deviation from threshold value $\Delta_{(DF1)}$ in figure 3.9, column 4. It is a measure of the deviation of the calculated numbers from the discrimination function 1 (DF1, see caption Fig. 3.10B), relative to the threshold line (y=23.771x – 8.321) between a quartzose sedimentary and a mafic provenance in figure 3.10B.

$$\Delta_{DF1} = DF1 - DF2/23.771$$

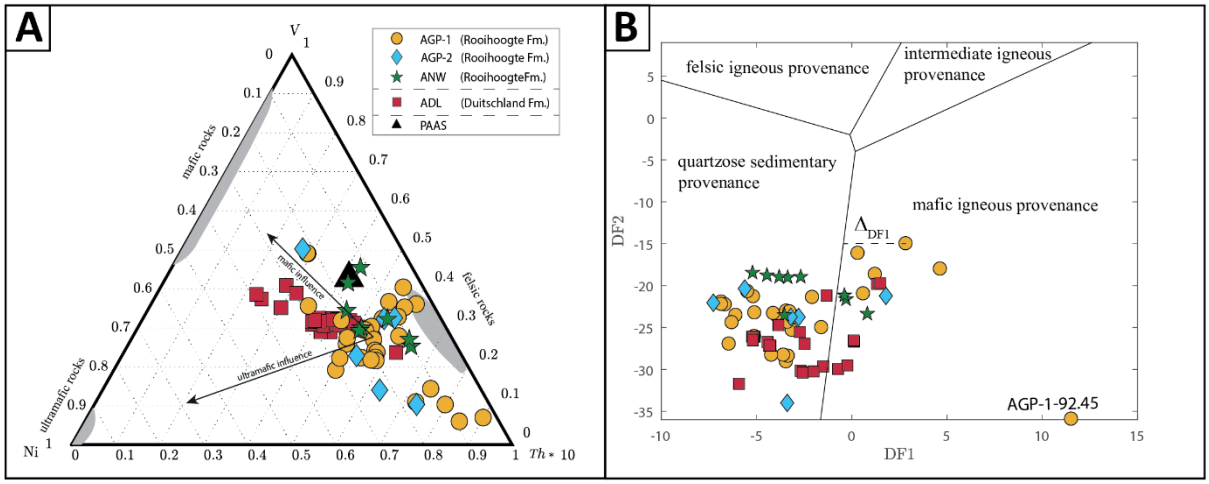

Figure 3.10. **(A)** *V-Ni-Th*10 ternary diagram for fine-grained siliciclastic samples (fine sand to shale) of the four geochemically analyzed drill cores.* The shaded areas represent approximate compositions of felsic, mafic and ultramafic rocks. The composition of PAAS is

shown as reference. **(B)** *Discrimination function diagram for sedimentary provenance from Roser and Korsch (1988)*. Discrimination function 1 (DF1) = (−1.773 TiO_2) + (0.607 Al_2O_3) + (0.760 Fe_2O_3) + (−1.500 MgO) + (0.616 CaO) + (0.509 Na_2O) +(−1.224 K_2O) + (−9.090) and discrimination Function 2 (DF2) = (0.445 TiO_2) + (0.070 Al_2O_3) + (−0.250 Fe_2O_3) + (−1.142 MgO) + (0.438 CaO) + (1.475 Na_2O) + (−1.426 K_2O) + (-6.861). Sample AGP-1-92.45 deviates from the general sample population due to its high iron content ($Fe_2O_{3(t)}$ = 14.37 wt.%). The stippled line, named Δ_{DF1}, marks an example of the deviation from the line separating the quartzose sedimentary provenance field and the mafic provenance field that are plotted in stratigraphic order in figure 9, column 4.

Chemostratigraphic data for the complete Duitschland and Rooihoogte succession continuing into the lower Timeball Hill Formation is only available in the Gopane area (AGP-1 and 2 drill cores combined, Fig. 3.9A). At this locality there is a gradual increase in detrital input (TiO_2/Al_2O_3) in the lower sequence corresponding to the upward-coarsening regressive succession (Fig. 3.9A, column 1). This is combined with a rather poorly defined increase in sediment maturity (decreasing Yb/Zr), constant CIA index (around 75-78) and indications of a quartzose-dominated provenance (Fig. 3.9A, columns 2 through 4). Above the Langbaken conglomerate, detrital input, sediment maturity and the CIA index drop, whereas quartzose sedimentary provenance increases (Fig. 3.9A, column 4). Following that, there is an increase in mafic provenance supply in the upper part of the Rooihoogte Formation. All parameters are relatively constant in the distal prodelta shales of the Timeball Hill Formation (Fig. 3.9A, columns 1 through 5).

Erosion at the base of the upper sequence marks a clear change in deposition. The grain size-controlled sudden decrease in TiO_2/Al_2O_3 and the increase in Yb/Zr indicate an increasing distance from the paleoshoreline in sediments from the individual cores and, thus, a decrease in continental input (lower TiO_2/Al_2O_3) and an increase in pelagic sedimentation (higher Yb/Zr). The provenance changes from a felsic provenance with components of mafic material in the *Middle D/R* to a predominantly felsic provenance in the lower parts of the *Upper D/R*. The *Upper D/R* is present in all cores and has a generally stable sediment input (Al_2O_3/TiO_2) but shows an increasing proportion of mafic material towards the transition to the Timeball Hill Formation. The trend is most pronounced in AGP-1 and AGP-2 (Fig. 3.9A), which suggests that the mafic component to the Transvaal Basin came from the subordinate northwestern provenance reported for this part of the basin (Coetzee, 2001). This also complies

with the slightly larger range observed in $\varepsilon Nd_{2.42Ga}$ data in these two drill cores (Table 3.6). Likewise, the CIA values have an upward increasing trend in the *Upper D/R* interval, suggesting a change in weathering patterns. The black shales of the lower Timeball Hill Formation were deposited under stable conditions with only minor fluctuations in relative sea level change and provenance. Geochemically, the transition to the *Lower TBH* is best visible in the CIA index and Yb/Zr ratios that gradually and slightly decrease around the transition (Fig. 3.9A and B, columns 2 and 3), supporting a transitional sedimentary change from the Rooihoogte and Duitschland formations to the Timeball Hill Formation, as opposed to an unconformable contact.

3.8.3 Tectonic Setting and Provenance

The geochemical composition of siliciclastic sediments mirrors the cumulative effects of provenance, weathering, hydrographic sorting and post-depositional events (Nesbitt et al., 1997). The binary discrimination between Zr and TiO_2 (Table 3.2–3.5) shows that most samples display TiO_2/Zr ratios below 55, which is indicative for the preponderance of felsic components with only subordinated intermediate and rare to absent mafic components (Cao et al., 2018). This finding is supported by the ternary V-Ni-Th discrimination diagram (Fig. 3.10A), where most samples plot close to the felsic field, although some samples from all cores show some influence of mafic and/or ultramafic components. Both the Duitschland and Rooihoogte formations thus show similar geochemical signatures and seem to be derived primarily from a felsic source. The majority of samples from all cores plot within the quartzose sedimentary provenance field in figure 3.11B and with no visible difference between the cores when applying discrimination functions designed to distinguish between mafic, intermediate, felsic and quartzose sedimentary (recycled) provenances (Murali et al., 1983). Further, a quartzose sedimentary provenance indicates that the Duitschland and Rooihoogte formations have undergone at least one sedimentary cycle. This sedimentary recycling occurred fast, since the youngest measured ages of detrital zircon grains in the Duitschland and Rooihoogte formations are 2342±18 Ma and 2353±18 Ma, respectively (Zeh et al., 2020) and Re-Os pyrite geochronology yields a depositional age of 2316±7 Ma (Hannah et al., 2004) for the black shales in the lowermost parts of overlying lower Timeball Hill Formation. These dates also constrain the initiation of the GOE to an interval having a duration between 62 and 12 million years, depending on measurement uncertainties on the ages.

Discrimination function systematics specifically targeted towards distinguishing between different tectonic terranes for Precambrian rocks (Verma & Armstrong-Altrin, 2013) were used to evaluate the tectonic setting of the Duitschland and Rooihoogte formations (Fig. 3.11). Samples are divided into a high (> 63 wt% SiO_2) and a low (< 63 wt% SiO_2) silica suite after volatile free adjustment following the method described in Gill and Fitton (2022). All samples in the high silica sample suite and most samples in the low silica group plot in the field representing a collision zone setting, with a few samples in the latter group lying in the undefined transition zone between a collision and a rift setting with no observable differences between Rooihoogte and Duitschland formations (Fig. 3.11). In addition, zircon age populations from both the Duitschland and Rooihoogte formations are also practically identical (Fig. 3.12) and resemble distribution patterns associated with deposition in a forearc basin (Barham et al., 2022).

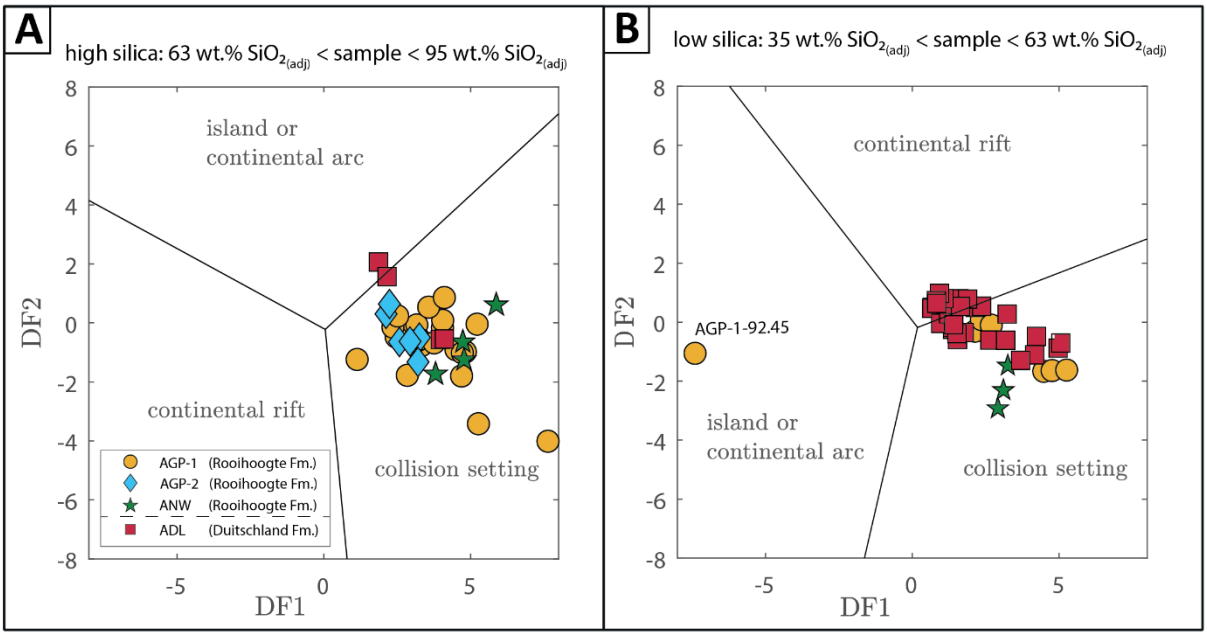

Figure 3.11. *Discrimination function diagram to distinguish between arc, continental rift and collision settings specifically calibrated for Precambrian rocks* (Verma and Armstrong-Altrin, 2013). Samples are divided into a high and a low silicate suite after volatile free adjustment (adj) of major element oxides. **(A)** high silica group samples (63 wt.% $SiO_{2\ (adj)}$ < sample < 95 wt.% $SiO_{2\ (adj)}$) and **(B)** low silica group samples (35 wt.% $SiO_{2\ (adj)}$ < sample < 63 wt.% $SiO_{2\ (adj)}$). Sample AGP-1 92.45 deviates from the general sample population due to its high $Fe_2O_{3(t)}$ content of 14.37 wt.% before volatile free adjustment.

Zeh et al. (2020) propose a generic model of the tectonic setting during the time interval from 2618 to 2342 Ma, which covers the depositional interval from the Malmani Subgroup to the Duitschland and Rooihoogte formations based on U-Pb-Hf isotope systematics of detrital zircon grains. Their preferred model suggests an amalgamation of three terranes: a 2570–2450 Ma juvenile Neoarchean terrane (JUNAT), a 2550–2450 Ma Neoarchean to Paleoproterozoic higher evolved continental arc terrane (NPCAT) and a 2650–3500 Ma composite Archean terrane (CAT), which all must have been attached to the Kaapvaal Craton prior to the deposition of the Duitschland and Rooihoogte formations. While zircon $\varepsilon Hf_{(t)}$ values of the Rooihoogte and Duitschland formations published by Zeh et al. (2020) show a largely bimodal distribution that these authors defined as the JUNAT ($\varepsilon Hf_{(t)} > 0$) and NPCAT ($\varepsilon Hf_{(t)} < 0$) with some minor data indicating sediment sourcing from an even older terrane (i.e., CAT) , bulk sediment $T_{DM}(Nd)$ data from this study only delineate values corresponding to the older proposed NPCAT $T_{DM}(Hf)$ ages (Fig. 3.12, Table 3.6) with no trace of the proposed JUNAT with $T_{DM}(Nd) < 2.9$ Ga. This is most likely due to the differences between Lu-Hf and Sm-Nd isotope systematics in relation to zircon $\varepsilon Hf_{(t)}$ versus bulk sediment $\varepsilon Nd_{2.42Ga}$ data, respectively. The $\varepsilon Hf_{(t)}$ data from detrital zircons tend to overrepresent felsic over (zircon-poor to free) mafic source components in any given tectonic environment. The overall Sm-Nd budget of the sediments, however, might be largely controlled by weathering of mafic minerals such as pyroxenes and amphiboles with generally high concentrations of REE, overwhelming the much lower REE concentrations delivered from resistant minerals associated with felsic rocks (e.g., zircons, feldspars). As such, the zircon $\varepsilon Hf_{(t)}$ data of Zeh et al. (2020) and the bulk sediment $\varepsilon Nd_{2.42Ga}$ data of this study do not contradict but rather complement each other regarding relative proportions of felsic and mafic source components. Given that Sm-Nd isotope systematics remain largely unaffected during erosion, weathering, sedimentation and metamorphism (Tripathy et al., 2012; Walter et al., 2000), the generally less than 5 unit spread in $\varepsilon Nd_{2.42Ga}$ values reported in this study, (Table 3.6; Fig. 3.12), may indicate that sediments of the Duitschland and Rooihoogte formations were sourced from the same provenance(s).

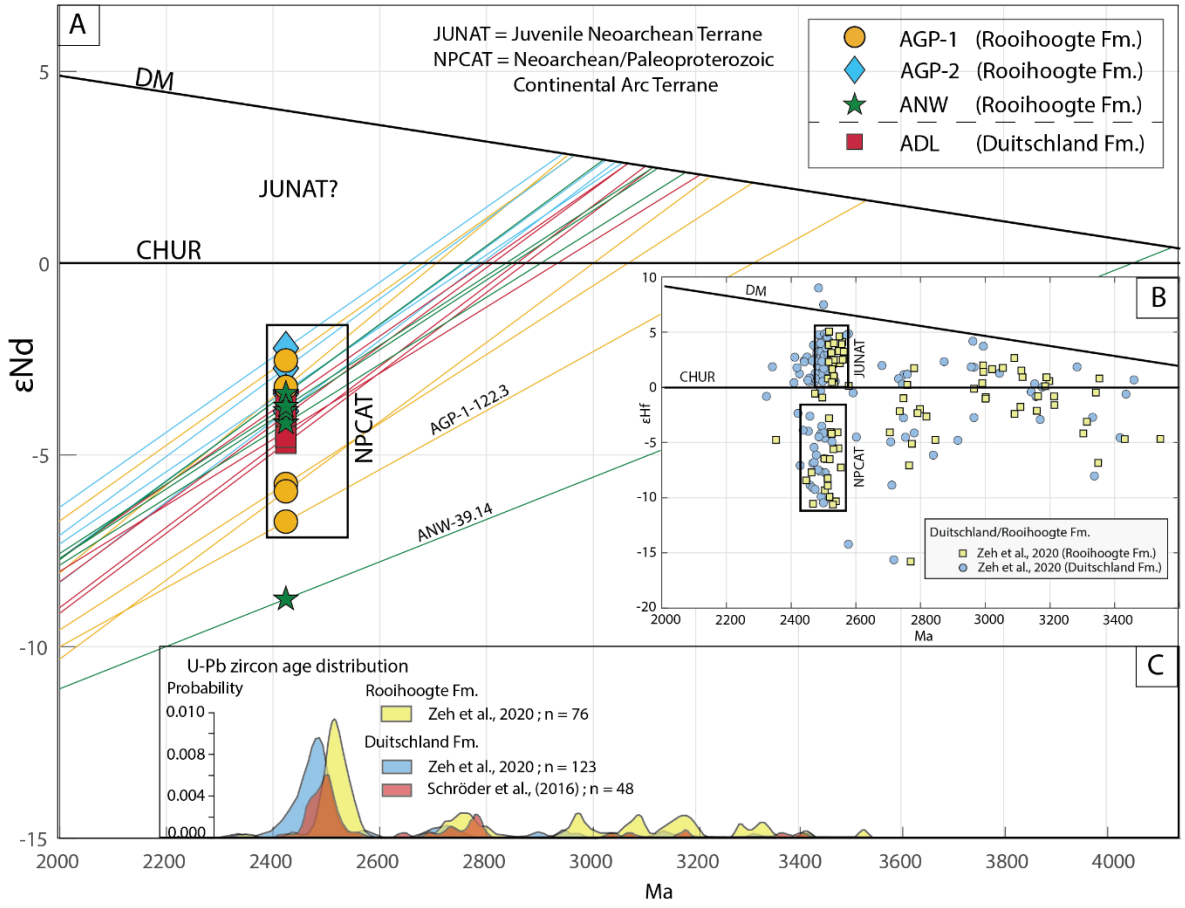

Figure 3.12. **(A)** *Bulk sediment Sm-Nd isotope evolution diagram of the fine-grained siliciclastic components from the drill cores* and **(B)** published Lu-Hf isotope systematics of detrital zircons from the Duitschland and Rooihoogte formations (Zeh, et al., 2020). **(C)** Literature U-Pb age distribution patterns of detrital zircons from the Duitschland and Rooihoogte formations (Schröder et al., 2016; Zeh et al., 2020).

One of the major conundrums about the zircon populations in the Duitschland and Rooihoogte formations and the Pretoria Group as a whole, is the dominance of a ~2.50 Ga zircon peak for which there are no known sources on the Kaapvaal Craton or immediate surroundings (Schröder et al., 2016; Zeh et al., 2020). In a global tectonic context, the deposition of the Transvaal Supergroup coincides with the tectono-thermal evolution of Archean-Paleoproterozoic cratons regarded as part of the Rae cratonic family, describing a common group of cratons with a contemporaneous record of generally collisional orogens (MacQuoid orogeny in Rae family, ~2.55 to 2.50 Ga) and largely peripheral orogens (Arrowsmith orogeny in Rae Family, ~2.50–2.30 Ga) (Pehrsson et al., 2013). Interestingly, bulk sediment $\varepsilon Nd_{2.42Ga}$ data from this study and zircon $\varepsilon Hf_{(t)}$ data from Zeh et al. (2020) resemble those reported in

Pehrsson et al. (2013) for Rae-type cratons and compare well to the JUNAT and NPCAT. Thus, a Rae-type craton potentially amalgamated with the Kaapvaal Craton around 2.55–2.50 Ga, which sourced the ~2.50 Ga zircon peak to the Koegas subgroup and Makganyene Formation (GWB) and corresponded to MacQuoid and early Arrowsmith stages (Ngobeli, 2019). Subsequently, around 2.40 to 2.32 Ga, late Arrowsmith tectonics resulted in uplift and erosion that created the unconformity which forms the base of the Pretoria Group. This event additionally introduced the earliest ~2.35 Ga zircons that became progressively more abundant and reached their maximum abundance in the upper Timeball Hill Formation (Zeh et al., 2020). Since the main provenance for most of the siliciclastics to the Pretoria Group was sourced from the north of the Kaapvaal Craton (Coetzee, 2001), a potential tectonic model, in agreement with the general concept by Zeh et al. (2020), but with appropriate craton configuration relative to sedimentary provenance is conceptualized in figure 3.13 following a concept developed by Ngobeli (2019).

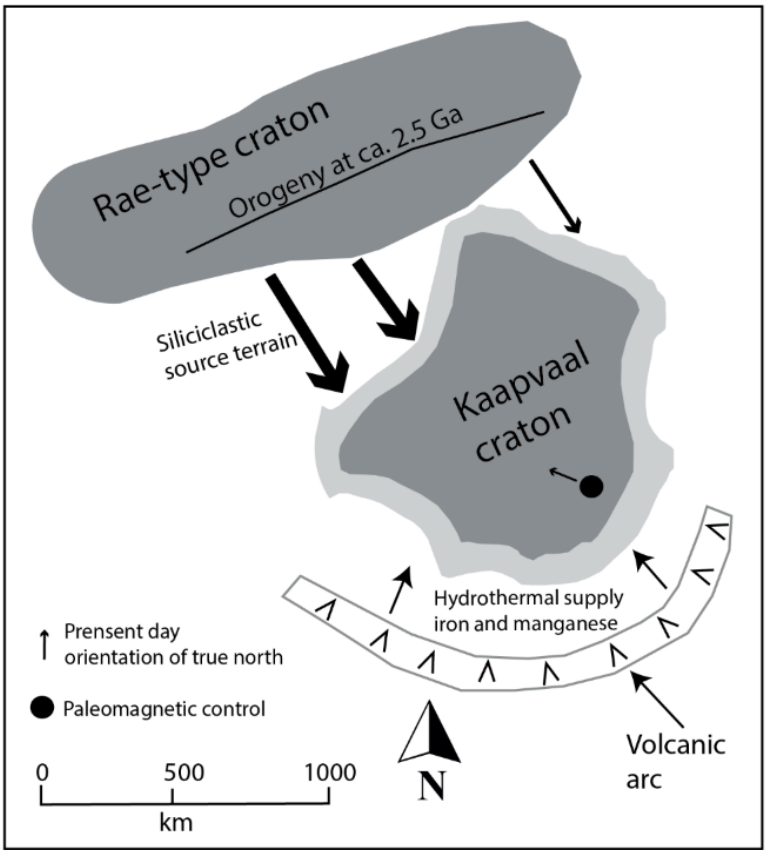

Figure 3.13. *Tectonic model of a potential collision between a Rae-type craton and the Kaapvaal* modified from Ngobeli (2019) with paleomagnetic correction adapted from Gumsley et al. (2017).

3.9 Implications for the GOE

Evidence from stratigraphy, chemostratigraphy, discrimination diagrams and functions, similarities in major element and trace element patterns, and Nd isotope systematics all indicate that the Duitschland and Rooihoogte formations are correlative. This conclusion is further supported by previously published zircon data and age distribution patterns (Schröder et al., 2016; Zeh et al., 2020) and Lu-Hf systematics (Zeh et al., 2020). Notably, neither of the arguments presented on their own exclude a decoupled deposition, but the accumulated body of evidence strongly indicates a contemporaneous deposition but at different distances to the paleoshoreline. A contemporaneous deposition of the two formations implies an abrupt loss of any undoubtedly atmospherically derived MIF-S signal in the Transvaal Basin (Izon et al., 2022) and thus a loss of MIF-S linked to a sudden pulse of oxygen. This correlation equally refutes the most convincing argument for a dynamic oxygenation pathway (Gumsley et al., 2017; Poulton et al., 2021). Notably, reports of MIF-S within the Timeball Hill Formation have been used to argue for younger regressions toward an oxygen-free atmospheric state (Poulton et al., 2021). However, the isolated and ephemeral nature of these rare instances of post-2.3 Ga MIF-S requires exceptionally short-term oscillations (Uveges et al., 2023) deserving further exploration (Izon et al., 2022)(Izon et al., 2022)(Izon et al., 2022). Whether an abrupt singular atmospheric change as observed in South Africa is representative of the global signal or whether an oscillating loss of MIF-S is recorded elsewhere, requires further investigation of global sedimentary correlations, the interaction of different isotopic sulfur pools, crustal MIF-S recycling, atmospheric modeling as well as a better understanding of the tipping points in the Earth system through biological, oceanic and geological feedback loops. However, the loss of any atmospheric MIF-S signal, a key indicator for early atmospheric oxygenation, is currently best constrained to 2434±6 Ma in Fennoscandia (Brasier et al., 2013), 2308±8 Ma in North America (Rasmussen et al., 2013) and 2316±7 Ma in South Africa (Hannah et al., 2004) (South Africa). This short time interval on Precambrian timescales could represent a turning point in the oxygenation of the Earth (Bekker et al., 2004; Guo et al., 2009; Luo et al., 2016; Warke et al., 2020). In fact, with both gas equilibration between the upper ocean and the atmosphere as well as the atmospheric mixing times being extremely fast on geological time scales, a rapid loss of MIF-S is expected to be roughly globally synchronous when accounting for differences in local exhaustion speeds of MIF-S from Archean weathering catchments, localized ‘oxygen oases’ and incomplete homogenization of the ocean isotopic sulfur pool. Considering an atmospheric mixing time of ~1 year (Jacob, 1999), it is difficult to maintain an atmosphere that

is not homogenized in either an oxic, neutral or anoxic state. Yet, while we argue that a singular oxygenation event is the most parsimonious explanation of the available data, we stress that most of our understanding of Earth's oxygenation has been gleaned from relatively few closely spaced and/or compromised sulfur isotope records. Consequently, as new exploratory and targeted work is conducted, both within the Transvaal Basin, and beyond, our perception of Earth's oxygenation is likely to evolve.

3.10 Summary and Conclusion

This study integrates sedimentological observations throughout the entire Transvaal area (South Africa) and the adjoining Kanye area (Botswana) with geochemical data from the four *CIMERA-Agouron GOE Drill Cores*, intersecting the Duitschland and Rooihoogte formations. This combined approach clarifies the stratigraphic relationship and depositional history of these formations while, at the same time, improving our understanding of the oxygen dynamics at the beginning of the GOE. The integrated picture of sedimentological observations from 11 stratigraphic sections combined with major and trace element data plus radiogenic Sr-Nd isotope compositions from four drill cores yields the following results:

- Continuous lateral marker beds (a basal conglomerate and diamictite, a mid-formational unconformity (MDU)) can be traced between 11 stratigraphic sections throughout the Transvaal Basin and the Kanye Basin (Botswana).
- The contacts between the Duitschland and Timeball Hill formations and the Rooihoogte and Timeball Hill formations are sharp and can be traced laterally across the Transvaal Basin. In the Duitschland area, however, the contact is locally developed as an intra-formational paleokarstic breccia formed during exposure and dissolution of carbonate beds. The contact likely represents a high-order sequence boundary and laterally correlative conformity with a relatively short time gap before Timeball Hill deposition. The base of both Rooihoogte and Duitschland formations is an unconformity and overlying chert conglomerate/diamictite pair that can be traced across much of the basin.
- Major and trace element compositions of all geochemically investigated drill cores are similar and suggest a predominantly felsic source of sediments within the Duitschland and Rooihoogte formations.
- Application of discrimination functions and comparison of zircon distribution patterns suggest that sediments from the Duitschland and Rooihoogte formations originated in a

collisional setting and have been recycled at least once. Neodymium and Hf isotope systematics implicate the amalgamation of a Rae-type craton and the Kaapvaal Craton.

- Most recent age constraints on the Duitschland and Rooihoogte formations limit the time interval for sedimentary redeposition. This brackets the loss of MIF-S signal in the Pretoria Group to a period between 62 and 12 million years.
- $\varepsilon Nd_{2.42Ga}$ values show very uniform patterns, which together with the interconnected distribution of samples from all cores suggest the same provenance.
- Highly radiogenic $^{87}Sr/^{86}Sr$ ratios yielding a regression age of 1996±86 Ma, indicating a resetting of the Rb-Sr system by the Bushveld intrusion. Consequently, Sr isotope systematics should be cautiously used in the Transvaal Basin.
- The integration of sedimentology, chemostratigraphy, bulk isotopic and geochemical similarities, discrimination diagrams as well as zircon ages and zircon distributions indicate that the Duitschland and Rooihoogte formations are correlative. Thus, the loss of MIF-S, as recorded within the Pretoria Group, occurred once, removing a key line of evidence used to argue for an oscillating atmospheric trajectory.

3.11 Acknowledgments

Elmar Reitter and Bernd Steinhilber are gratefully thanked for their technical support during laboratory work. Lucile Roué is thanked for her help during core sampling. The University of Johannesburg is acknowledged for providing facilities for core storage and helping with logistics during sampling. The CIMERA-Agouron GOE and Biomarker Drilling Project is gratefully thanked for providing scientific quality drill cores. Financial support was provided by the German Research Foundation (DFG) grant SCHO1071/12-1 to Ronny Schönberg as part of the DFG priority program SPP-1833 ‘Building a Habitable Earth’. Gareth Izon acknowledges support from the Simmons Collaboration on the Origin of Life and a joint MIT–UJ MISTI seed award.

3.12 Tables

Table 3.2. Major and trace element data for Agouron GOE Drill Core AGP-1

Sample depth	**47.66**	**48.14**	**48.42**	**50.07**	**50.28**	**51.055**	**53.185**	**54.06**	**54.79**	**57.73**[a]	**58.675**	**60.2**	**61.12**[a]	**62.04**[a]	**63.37**[a]	**65.19**	**67.34**[a]	**69.33**	**70.09**[a]	**70.84**[a]
RockType	**CS**	**CS**	**CS**	**Py CS**	**BIF**	**Py CS**	**Py CS**	**Py CS**	**Py CS**	**Py CS**	**Py CS**	**Py CS**	**Py CS**	**Py CS**	**Py CS**	**Shale**	**Shale**	**Shale**	**Shale**	**Shale**
Stratigraphic Zone	***Upper D/R***	***Upper D/R***	***Upper D/R***	***Upper D/R***	***Upper D/R***	***Upper D/R***	***Upper D/R***	***Upper D/R***	***Upper D/R***	***Upper D/R***	***Upper D/R***	***Upper D/R***	***Upper D/R***	***Upper D/R***	***Upper D/R***	***Upper D/R***	***Upper D/R***	***Upper D/R***	***Upper D/R***	***Upper D/R***
Major elements [wt.%]																				
SiO_2	59.8	65.8	63.9	58.5	66.2	61.3	60.2	62.6	63.9	59.5		62.7	63.8	62.7	63.9	71.7	70.7	71.8	72.6	68.4
Al_2O_3	16.5	17.0	15.1	18.3	8.49	14.0	19.3	17.4	16.3	16.2		15.6	15.7	15.4	15.2	12.7	11.8	13.3	13.4	14.6
TiO_2	0.601	0.582	0.564	0.615	0.270	0.481	0.654	0.602	0.578	0.590		0.610	0.650	0.710	0.590	0.371	0.320	0.347	0.250	0.700
Fe_2O_3	12.0	5.98	9.59	9.96	16.5	12.3	6.47	6.73	6.36	8.31		7.27	6.63	7.21	5.88	4.74	2.00	3.30	2.19	3.17
MnO	0.019	0.018	0.044	0.054	0.074	0.072	0.026	0.065	0.065	0.110		0.078	0.070	0.070	0.060	0.047	0.110	0.081	0.060	0.070
MgO	0.539	0.756	0.807	2.55	2.79	2.80	1.98	2.71	2.71	2.86		2.87	2.47	2.64	2.51	2.66	1.38	2.90	2.14	1.86
CaO	0.003	0.014	0.007	0.016	0.120	0.258	0.018	0.094	0.079	1.58		0.563	0.450	0.450	0.470	0.325	1.80	0.653	0.450	0.750
K2O	2.93	2.73	1.95	3.39	0.481	2.20	5.43	4.18	3.88	3.90		3.41	3.73	3.55	3.67	2.70	3.25	2.91	3.64	3.63
Na_2O	0.106	0.098	0.097	0.102	0.057	0.090	0.127	0.422	0.456	0.020		0.668	0.480	0.530	0.580	0.680	0.780	1.03	0.540	1.40
P_2O_5	0.036	0.051	0.041	0.076	0.181	0.219	0.060	0.066	0.063	0.070		0.077	0.090	0.090	0.080	0.059	0.060	0.068	0.030	0.090
LOI	7.29	6.27	7.76	6.18	3.55	4.37	4.54	4.54	4.08	5.87		5.59	5.84	6.62	6.14	2.69	6.45	2.71	3.77	4.63
Sum	99.8	99.2	99.9	99.7	98.8	98.1	98.8	99.4	98.5	99.0		99.4	99.8	99.9	99.0	98.6	98.7	99.1	99.0	99.3
Trace elements [µg/g]																				
Li	34.0	39.6	42.3	55.6	46.8	52.5	54.0	57.1	52.1	54.8	49.3	45.4	47.5	49.4	47.4	53.2	26.4	44.0	38.1	35.2
Be	4.10	3.69	3.05	4.27	1.66	3.14	4.80	3.58	3.33	3.60	3.84	3.03	3.50	3.62	3.82	3.31	3.18	2.68	3.07	3.27
Sc	22.5	22.2	20.7	23.5	11.1	16.1	25.1	21.6	21.1	19.0	20.0	9.94	19.5	18.7	15.7	20.4	10.5	12.0	5.32	13.9
Ti	3762	3795	3729	3741	1675	2845	3901	3662	3530	3369	3622	2255	3734	4029	3305	3745	1699	2042	1324	4065
V	129	121	135	161	105	104	136	116	112	106	114	47.1	109	114	95.6	107	31.6	28.4	16.6	69.4
Cr	141	140	118	59.4	73.7	100	151	136	130	131	136	61.9	135	139	122	132	46.5	27.1	12.8	67.8
Co	2.50	5.30	14.3	5.51	12.9	13.7	9.80	12.0	25.1	36.4	9.92	4.21	16.6	17.2	8.13	6.50	4.24	6.03	3.65	8.57
Ni	13.5	23.3	35.6	18.1	28.2	43.0	39.3	74.3	61.8	101	74.2	37.2	68.9	98.5	40.6	71.2	47.5	27.8	25.0	62.2
Cu	21.1	35.7	37.2	39.4	70.8	35.8	133	50.5	23.5	29.5	57.0	45.3	100	74.4	22.1	127	442	10.1	103	77.9
Zn	56.9	68.1	111	107	195	153	279	110	84.4	115	68.3	119	192	241	160	118	88.1	58.1	37.5	30.2
Ga	24.0	23.5	21.2	24.5	12.5	18.3	25.3	22.8	22.1	21.4	22.2	17.7	20.6	19.9	20.1	20.4	16.9	16.4	17.9	18.0
Rb	186	166	122	198	31.6	125	326	238	214	202	219	149	200	189	195	191	168	139	174	172
Sr	24.1	37.7	27.3	47.7	23.9	35.8	23.2	33.9	33.0	41.5	31.5	40.2	41.8	42.8	39.5	50.8	69.9	53.9	38.0	75.3
Y	21.5	20.9	27.7	31.8	32.9	35.4	26.0	30.0	31.0	23.9	33.2	29.1	29.6	35.7	26.0	37.3	19.4	31.4	24.5	21.5
Zr	148	144	201	105	69.8	146	159	160	150	136	153	203	152	172	168	155	171	191	157	182

Table continued on next page

Sample depth	**47.66**	**48.14**	**48.42**	**50.07**	**50.28**	**51.055**	**53.185**	**54.06**	**54.79**	**57.73[a]**	**58.675**	**60.2**	**61.12[a]**	**62.04[a]**	**63.37[a]**	**65.19**	**67.34[a]**	**69.33**	**70.09[a]**	**70.84[a]**
RockType	**CS**	**CS**	**CS**	**Py CS**	**BIF**	**Py CS**	**Py CS**	**Py CS**	**Py CS**	**Py CS**	**Py CS**	**Py CS**	**Py CS**	**Py CS**	**Py CS**	**Shale**	**Shale**	**Shale**	**Shale**	**Shale**
Stratigraphic Zone	***Upper D/R***	***Upper D/R***	***Upper D/R***	***Upper D/R***	***Upper D/R***	***Upper D/R***	***Upper D/R***	***Upper D/R***	***Upper D/R***	***Upper D/R***	***Upper D/R***	***Upper D/R***	***Upper D/R***	***Upper D/R***	***Upper D/R***	***Upper D/R***	***Upper D/R***	***Upper D/R***	***Upper D/R***	***Upper D/R***
Nb	15.0	13.1	13.0	13.6	6.17	11.3	13.9	13.5	11.9	12.5	13.0	15.9	11.4	12.8	13.8	13.8	12.0	13.6	10.8	14.4
Mo	0.481	1.13	0.533	6.24	1.94	1.33	0.343	0.285	0.496	0.707	0.319	0.095	0.340	0.511	0.440	0.335	0.150	0.859	0.414	1.75
Cd	0.060	0.050	0.061	0.051	0.034	0.055	1.41	0.068	0.064	0.084	0.064	0.146	0.292	0.386	0.252	0.124	0.128	0.070	0.070	0.088
Sn	6.52	6.17	4.29	6.58	0.962	4.85	8.11	5.53	5.60	5.61	5.60	6.39	5.31	5.12	5.11	4.77	6.66	7.09	6.97	6.13
Sb	1.49	1.44	1.80	2.35	1.90	1.78	2.56	3.39	1.32	2.26	1.21	0.884	1.72	2.95	1.65	2.85	0.581	0.566	0.520	2.06
Cs	8.79	7.86	5.83	9.91	1.49	5.86	17.8	12.7	10.6	10.0	11.3	5.56	9.54	9.09	8.98	9.66	5.88	5.52	6.38	6.38
Ba	1731	1538	1149	1860	304	1251	2666	2084	1960	1765	1940	1512	1867	1768	1912	1722	1669	1522	2023	2007
La	18.1	26.6	22.9	30.8	28.2	45.9	61.3	47.1	44.2	33.5	46.6	55.1	48.3	62.2	52.2	52.8	51.9	59.1	47.0	38.4
Ce	35.6	49.0	41.2	55.3	59.5	93.2	124	97.1	88.3	64.5	96.1	109	95.7	123	107	106	106	117	95.1	77.8
Pr	4.12	5.37	4.45	6.33	7.53	10.9	13.5	10.9	9.90	7.05	10.7	11.9	10.9	13.2	11.5	12.0	11.0	12.8	10.3	8.85
Nd	14.7	18.5	15.3	23.3	30.1	40.4	47.1	38.9	35.7	25.0	38.9	42.0	39.3	45.6	40.4	43.6	38.2	45.2	36.0	32.0
Sm	3.09	3.49	3.19	4.80	6.93	8.07	8.41	7.42	6.81	4.78	7.48	7.73	7.31	7.87	7.14	8.30	6.80	8.60	6.81	6.13
Eu	0.678	0.751	0.730	1.13	1.28	1.61	1.66	1.38	1.28	1.08	1.35	1.05	1.36	1.56	1.30	1.54	0.883	1.07	0.923	0.946
Tb	0.535	0.539	0.623	0.843	1.13	1.13	0.918	0.981	0.938	0.718	0.993	0.938	0.948	0.974	0.846	1.15	0.732	1.01	0.820	0.715
Gd	2.70	3.00	2.96	4.79	7.17	7.45	6.56	6.20	6.07	4.42	6.40	6.34	6.36	6.53	5.79	7.41	5.17	6.96	5.50	4.94
Dy	3.76	3.66	4.46	5.49	6.58	6.58	5.05	6.12	5.63	4.36	6.02	5.58	5.52	5.78	4.70	6.92	4.01	5.89	4.59	3.94
Ho	0.898	0.855	1.07	1.25	1.33	1.36	1.02	1.32	1.19	0.940	1.30	1.16	1.17	1.28	0.984	1.45	0.807	1.19	0.939	0.821
Er	2.90	2.74	3.39	3.86	3.65	3.88	2.99	3.83	3.44	2.75	3.75	3.29	3.41	3.78	2.86	4.09	2.29	3.28	2.69	2.36
Tm	0.492	0.458	0.564	0.634	0.543	0.596	0.490	0.596	0.542	0.439	0.577	0.513	0.537	0.537	0.537	0.630	0.350	0.492	0.411	0.358
Yb	3.46	3.27	3.86	4.32	3.47	3.92	3.43	3.92	3.61	2.93	3.74	3.31	3.59	3.76	2.97	4.09	2.23	3.08	2.59	2.30
Lu	0.559	0.530	0.594	0.684	0.534	0.600	0.565	0.609	0.568	0.454	0.572	0.498	0.465	0.465	0.465	0.639	0.331	0.446	0.381	0.353
Hf	4.25	3.89	3.90	4.01	1.85	3.94	4.41	4.45	3.90	3.73	4.01	5.61	3.93	4.53	4.20	4.22	4.42	5.30	4.49	4.58
Ta	1.31	1.20	1.21	1.29	0.549	1.08	1.35	1.25	1.08	1.22	1.24	1.39	1.10	1.20	1.25	1.26	1.12	1.36	1.19	1.14
W	4.93	3.90	3.73	5.28	1.18	2.76	8.13	3.03	3.04	3.08	5.61	4.66	3.38	4.66	5.05	3.31	3.66	2.54	1.00	5.67
pb	8.29	12.0	11.4	8.60	11.0	11.3	14.6	8.03	12.3	6.15	6.48	10.00	8.50	10.6	8.46	7.75	4.76	5.82	5.70	8.26
Th	21.6	19.9	19.8	22.0	9.96	17.6	23.9	22.7	19.5	20.2	19.8	24.4	19.3	20.3	20.7	21.8	21.0	22.0	23.6	17.6
U	4.96	4.98	4.46	8.43	4.33	5.91	5.65	5.51	4.62	4.71	4.86	7.03	5.79	5.80	5.64	5.95	7.67	7.95	9.52	6.04
∑REY	113	140	133	175	191	261	303	257	239	177	258	278	255	312	265	288	250	298	239	201
TiO_2/Zr	40.6	40.3	28.1	58.8	38.7	32.8	41.2	37.7	38.5	43.4	0.000	30.0	42.9	41.2	35.1	23.9	18.7	18.2	15.9	38.5

Table continued on next page

Sample depth	71.56[a]	73.16	74.8	75.1	75.59	86.70[a]	87.44[a]	89.18	90.45	92.45[a]	96.2	102.06[a]	105.16[a]	122.31	128.31	139.52	151	159.77	160.24	163.3
RockType	Py CS	Py CS	Py CS	Py CS	Py CS	Diabase	Diabase	Carb.	C. Strom	Silt	BIF	Silt	Silt	Silt	Silt	Carb. shale	Silt	BIF	C. BIF	BIF
Stratigraphic Zone	*Upper D/R*	*Upper D/R*	*Upper D/R*	*Upper D/R*	*Upper D/R*	*Upper D/R*	*Upper D/R*	*Upper D/R*	*Upper D/R*	*Upper D/R*	*Upper D/R*	*Middle D/R*	*Middle D/R*	*Middle D/R*	*Middle D/R*	*Middle D/R*	*Middle D/R*	*Penge Fm.*	*Penge Fm.*	*Penge Fm.*
Major elements [wt.%]																				
SiO_2	69.1		66.6	67.1	57.3	76.2	77.3	12.4		54.6	44.9	61.1	60.4	59.4	53.6	64.8	56.5	23.8	11.4	40.5
Al_2O_3	13.1		15.0	14.8	20.2	9.22	9.36	2.73		19.0	17.3	16.3	16.6	17.7	17.2	16.8	17.7	9.12	0.321	0.294
TiO_2	0.510		0.510	0.546	0.295	0.340	0.320	0.175		1.05	1.24	0.810	0.800	0.798	0.704	0.722	0.677	0.143	0.030	0.029
Fe_2O_3	3.45		2.38	2.46	2.36	3.49	1.40	2.67		14.4	18.6	8.35	8.53	8.72	8.80	4.12	10.5	40.8	45.7	37.2
MnO	0.040		0.051	0.044	0.027	0.160	0.110	37.2		0.270	2.01	0.100	0.100	0.078	0.057	0.043	0.150	0.771	1.05	0.437
MgO	1.66		2.39	2.37	2.38	2.51	1.30	2.89		1.46	2.36	3.28	3.40	4.02	4.08	2.08	3.50	6.55	4.84	2.15
CaO	0.280		0.525	0.351	0.157	0.760	0.800	9.86		0.090	0.584	0.370	0.460	0.365	0.180	0.453	1.07	0.919	9.08	1.56
K2O	3.20		3.77	3.77	6.15	2.22	2.85	0.837		0.170	4.44	4.14	4.18	4.16	4.36	5.32	4.51	0.000	0.000	0.000
Na_2O	1.06		0.518	0.499	0.153	0.000	0.000	0.083		4.66	0.238	1.15	0.980	0.837	0.684	0.115	0.115	0.000	0.061	0.083
P_2O_5	0.060		0.073	0.074	0.109	0.040	0.040	0.073		0.060	0.218	0.130	0.140	0.268	0.142	0.118	0.194	0.091	0.094	0.019
LOI	7.15		7.90	8.08	5.69	4.31	5.29	30.9		4.15	8.10	3.80	3.76	4.06	4.12	6.87	6.02	15.9	26.9	16.1
Sum	99.6		99.7	100	94.8	99.3	98.8	99.8		99.9	100	99.5	99.4	100	93.8	101	101	98.2	99.5	98.3
Trace elements [µg/g]																				
Li	31.1	69.3	52.6	44.4	54.7	31.9	18.3	14.0	43.0	46.8	48.1	40.4	41.5	48.4	53.2	49.2	54.8	12.9	3.07	1.35
Be	3.06	4.00	4.70	3.66	5.74	1.97	2.39	2.84	4.11	4.33	5.44	3.41	3.78	4.36	4.73	5.48	3.20	3.28	1.61	1.03
Sc	12.6	20.8	22.6	17.3	9.65	8.76	7.96	7.36	34.8	38.9	51.9	17.2	16.3	18.9	19.9	19.4	22.7	3.24	2.68	2.60
Ti	2798	3864	4065	3588	1795	1821	1686	1413	6009	6889	8305	4698	4676	4983	4490	4829	4405	1154	162	154
V	67.2	104	103	92.0	37.0	50.2	44.3	87.7	196	214	346	96.6	98.3	107	114	158	132	28.1	14.5	12.1
Cr	90.0	161	157	110	14.7	74.1	52.6	145	222	210	229	220	220	249	246	146	222	15.3	13.9	21.7
Co	2.12	2.93	1.01	0.936	0.732	8.31	79.4	78.8	29.1	31.9	40.1	27.1	25.1	33.9	28.0	127	28.3	18.1	8.47	4.15
Ni	52.9	82.3	164	116	16.7	93.9	116	152	87.4	95.5	70.5	85.7	91.8	111	111	126	94.7	14.2	9.28	10.4
Cu	89.8	84.1	118	241	4.27	65.8	14.0	449	14.8	11.2	36.2	23.7	30.4	35.7	13.2	466	33.9	1.04	26.6	3.10
Zn	506	62.7	35.5	59.4	35.7	42.6	19.9	322	114	128	82.0	84.5	79.2	85.9	88.1	52.9	78.5	66.7	30.2	23.3
Ga	16.6	25.8	25.5	20.3	27.5	12.7	12.2	7.73	22.4	24.4	23.5	21.7	22.4	23.2	25.7	22.5	24.4	18.6	1.32	1.20
Rb	144	195	242	196	304	77.6	105	69.3	216	236	236	208	209	202	230	298	239	0.963	5.09	10.5
Sr	46.5	39.4	54.7	55.8	23.0	25.7	23.9	195	48.1	53.3	66.6	94.4	95.1	86.9	74.8	72.3	101	12.0	19.6	8.80
Y	23.9	44.3	56.2	47.2	41.9	29.3	18.2	15.8	14.4	15.7	28.7	31.7	32.9	43.3	35.5	19.9	25.6	21.6	13.8	8.04
Zr	139	201	145	176	175	96.7	112	146	168	160	144	226	213	188	175	171	144	93.8	11.3	13.5
Nb	16.2	25.9	17.0	14.5	9.15	8.43	8.56	6.65	11.6	12.7	8.92	22.4	21.9	21.2	23.9	14.0	14.1	6.82	0.814	0.756
Mo	1.69	2.12	2.38	1.91	2.36	3.93	7.24	1.72	1.25	1.61	1.84	0.822	1.35	0.912	1.10	4.03	2.06	0.769	0.527	1.32
Cd	0.480	0.067	0.070	0.077	0.055	0.040	0.040	0.277	0.071	0.064	0.070	0.097	0.097	0.066	0.062	0.092	0.056	0.040	0.015	0.008
Sn	4.45	6.30	7.06	6.08	9.39	4.22	5.87	1.95	4.21	4.06	1.08	8.98	8.65	7.93	9.39	4.29	4.33	0.308	0.388	0.250

Table continued on next page

Sample depth	**71.56**[a]	**73.16**	**74.8**	**75.1**	**75.59**	**86.70**[a]	**87.44**[a]	**89.18**	**90.45**	**92.45**[a]	**96.2**	**102.06**[a]	**105.16**[a]	**122.31**	**128.31**	**139.52**	**151**	**159.77**	**160.24**	**163.3**
RockType	**Py CS**	**Py CS**	**Py CS**	**Py CS**	**Py CS**	**Diabase**	**Diabase**	**Carb.**	**C. Strom**	**Silt**	**BIF**	**Silt**	**Silt**	**Silt**	**Silt**	**Carb. shale**	**Silt**	**BIF**	**C. BIF**	**BIF**
Stratigraphic Zone	***Upper D/R***	***Upper D/R***	***Upper D/R***	***Upper D/R***	***Upper D/R***	***Upper D/R***	***Upper D/R***	***Upper D/R***	***Upper D/R***	***Upper D/R***	***Upper D/R***	***Middle D/R***	***Middle D/R***	***Middle D/R***	***Middle D/R***	***Middle D/R***	***Middle D/R***	***Penge Fm.***	***Penge Fm.***	***Penge Fm.***
Sb	3.54	2.27	5.59	2.26	0.846	0.600	1.89	3.39	0.430	0.759	1.16	1.05	1.17	1.05	1.19	2.53	0.811	0.287	1.15	0.472
Cs	6.42	8.82	10.3	8.69	11.8	3.32	3.61	2.51	12.9	14.0	16.9	14.9	14.3	14.0	15.2	19.4	16.2	3.36	4.65	9.10
Ba	1560	2011	2875	2305	3666	2592	2518	1843	1847	1992	1775	1057	1052	963	1004	1101	827	4.31	41.8	51.2
La	33.0	56.3	51.3	60.4	131	34.1	25.1	27.7	28.7	29.3	23.8	50.8	51.3	58.0	62.4	30.4	45.0	63.1	5.80	1.87
Ce	64.0	109	97.5	116	277	64.3	48.7	125	58.1	61.0	60.8	101	98.7	120	122	55.6	88.9	113	9.90	2.95
Pr	7.54	12.6	11.2	13.4	29.0	7.42	5.59	6.16	5.68	6.04	6.83	10.9	10.7	13.4	13.0	6.19	9.71	11.4	1.25	0.385
Nd	27.7	44.2	40.1	48.1	100.0	26.5	20.1	22.0	18.5	20.0	27.3	38.3	37.2	50.4	45.4	21.7	34.9	36.4	5.03	1.60
Sm	5.28	7.79	7.96	9.10	16.5	5.02	3.71	4.37	3.16	3.41	6.38	7.25	7.03	10.9	8.32	3.68	6.39	4.45	0.996	0.342
Eu	0.804	1.39	1.68	1.81	2.30	0.866	0.658	0.938	0.781	0.823	1.64	1.42	1.35	2.16	1.60	0.698	1.34	0.890	0.254	0.094
Tb	0.658	1.04	1.36	1.25	1.46	0.721	0.497	0.618	0.475	0.500	1.03	0.994	0.990	1.59	1.08	0.507	0.789	0.336	0.204	0.086
Gd	4.39	6.98	8.25	8.31	11.8	4.54	3.17	3.69	2.74	2.95	6.50	6.37	6.20	10.7	7.09	3.18	5.38	2.84	1.23	0.482
Dy	3.90	6.42	8.60	7.60	7.84	4.47	2.99	3.71	3.00	3.26	6.27	5.74	5.80	8.81	6.49	3.29	4.67	2.09	1.46	0.662
Ho	0.873	1.45	1.93	1.63	1.53	1.00	0.666	0.773	0.652	0.710	1.29	1.19	1.22	1.68	1.34	0.736	0.968	0.514	0.366	0.186
Er	2.67	4.44	5.67	4.68	4.14	2.97	2.03	2.21	1.99	2.13	3.60	3.38	3.51	4.31	3.77	2.20	2.73	1.69	1.14	0.662
Tm	0.439	0.731	0.876	0.723	0.610	0.465	0.329	0.349	0.333	0.355	0.569	0.524	0.541	0.620	0.579	0.353	0.418	0.282	0.179	0.118
Yb	2.98	5.12	5.77	4.71	3.73	3.02	2.24	2.23	2.27	2.45	3.80	3.34	3.43	3.81	3.68	2.34	2.68	1.95	1.18	0.869
Lu	0.503	0.854	0.908	0.741	0.542	0.481	0.367	0.322	0.344	0.375	0.566	0.489	0.505	0.544	0.539	0.355	0.400	0.338	0.185	0.151
Hf	3.73	5.23	5.72	4.74	5.61	2.50	2.46	2.32	4.22	4.55	3.96	5.70	5.51	5.16	4.84	4.65	3.92	2.70	0.194	0.198
Ta	1.08	1.86	1.74	1.31	1.44	0.771	0.600	0.467	1.01	1.12	0.711	2.30	2.28	2.15	2.48	1.28	1.28	0.563	0.048	0.035
W	3.47	5.88	6.70	4.43	2.10	3.33	1.87	7.42	2.03	2.51	4.50	3.71	4.07	4.91	5.53	5.30	6.67	0.399	2.29	0.391
pb	8.52	7.35	211	92.5	5.97	3.68	3.91	14.9	2.67	2.97	4.15	17.5	12.7	13.8	9.22	12.9	5.46	1.98	2.23	0.954
Th	15.8	25.1	27.1	20.6	47.9	12.3	9.54	6.54	11.6	12.6	7.00	24.9	26.6	26.2	29.9	16.0	18.8	15.0	0.776	0.515
U	6.36	9.78	8.92	6.96	15.3	5.92	4.49	1.25	2.32	2.48	4.37	6.67	6.81	6.59	6.89	6.70	5.75	3.18	0.347	0.170
∑REY	179	303	299	326	629	185	134	216	141	149	179	264	261	330	312	151	230	261	43.0	18.5
TiO_2/Zr	36.6	0.000	35.3	31.0	16.8	35.2	28.6	12.0		65.7	86.1	35.9	37.6	42.5	40.1	42.3	47.0	15.2	26.4	21.5

[a] Major and trace elements from Rou´e, et al., (2021)

[b] Abbreviations: CS = carbonaceous shale, Py. CS = pyritic carbonaceous shale, Carb. = carbonate, C. Strom = stromatolitic carbonate, BIF = banded iron formation, C. BIF = carbonaceous banded iron formation

Table 3.3. Major and trace element data for Agouron GOE Drill Core AGP-2

Sample depth	**59.125**	**60.2**	**62.30**[a]	**63.21**[a]	**64.045**	**66.17**[a]	**67.45**[a]	**68.08**	**73.67**	**76.08**[a]	**77.175**	**83.14**[a]	**83.88**[a]	**86.88**[a]	**87.40**[a]	**89.16**	**92.67**[a]	**95.21**	**102.15**	**108.21**	**122.75**	**128.35**
RockType	**GS**	**GS**	**Shale**	**Shale**	**Shale**	**Shale**	**Shale**	**Shale**	**Shale**	**Shale**	**Shale**	**CS**	**Carb.**	**CS**	**C. BIF**	**CS**	**CS**	**CS**	**CS**	**CS**	**Silt**	**BIF**
Stratigraphic Zone	***Lower TBH***	***Lower TBH***	***Lower TBH***	***Lower TBH***	***Lower TBH***	***Lower TBH***	***Lower TBH***	***Lower TBH***	***Lower TBH***	***Lower TBH***	***Lower TBH***	***Lower TBH***	***Lower TBH***	***Lower TBH***	***Lower TBH***	***Lower TBH***	***Upper D/R***	***Upper D/R***	***Upper D/R***	***Upper D/R***	***Upper D/R***	***Upper D/R***
Major elements [wt.%]																						
SiO_2	61.6	61.1	61.1	57.3	61.1	65.3	64.6	60.9	62.9	59.5	61.7	63.6	47.0	62.4	48.0	61.2	62.2	63.0	73.0	59.0	61.7	55.8
Al_2O_3	17.5	18.0	17.2	16.1	16.5	15.8	16.4	16.0	16.2	16.3	16.0	15.9	7.52	17.6	6.47	14.6	16.4	15.9	12.4	13.5	18.4	15.7
TiO_2	0.635	0.687	0.690	0.590	0.663	0.660	0.620	0.650	0.729	0.640	0.620	0.570	0.242	0.700	0.240	0.550	0.590	0.604	0.300	0.530	0.708	0.975
Fe_2O_3	8.08	7.05	7.16	12.9	6.12	5.94	5.21	7.94	7.08	9.16	8.48	7.64	11.9	6.40	17.5	12.4	7.66	6.97	4.30	2.57	4.58	17.1
MnO	0.042	0.031	0.030	0.060	0.030	0.030	0.030	0.038	0.042	0.060	0.048	0.030	0.196	0.030	0.220	0.070	0.060	0.069	0.041	0.030	0.147	0.363
MgO	2.74	2.28	2.10	2.40	2.12	1.91	1.94	2.49	2.59	2.77	2.87	2.18	3.00	2.14	2.18	2.46	2.51	2.59	2.23	1.82	3.70	2.24
CaO	0.229	0.052	0.110	0.090	0.119	0.130	0.140	0.193	0.131	1.26	0.431	0.120	14.2	0.100	13.7	0.360	0.110	0.295	0.316	0.210	0.541	0.307
K2O	3.29	4.09	3.88	3.13	3.67	3.96	4.07	3.98	3.83	3.45	3.21	3.59	0.495	4.15	0.000	2.58	4.02	3.73	3.14	4.06	3.15	2.74
Na_2O	0.840	0.398	0.490	0.540	0.476	0.330	0.650	0.493	0.614	0.640	0.806	0.820	0.185	0.360	0.000	0.470	0.390	0.568	0.381	0.400	2.71	0.347
P_2O_5	0.157	0.062	0.070	0.060	0.058	0.060	0.070	0.079	0.068	0.070	0.056	0.070	0.385	0.060	1.04	0.150	0.060	0.073	0.047	0.050	0.268	0.141
LOI	4.66	6.18	7.02	6.79	7.33	5.36	5.83	6.88	5.11	5.96	5.47	4.87	12.8	4.98	10.3	4.86	5.21	5.33	3.65	17.6	3.70	4.07
Sum	99.8	100.0	99.9	100.0	98.2	99.5	99.5	99.6	99.3	99.8	99.7	99.4	98.1	98.9	99.6	99.7	99.2	99.1	99.9	99.7	99.5	99.8
Trace elements [µg/g]																						
Li	51.4	44.3	36.3	37.4	43.7	35.8	36.0	45.2	45.2	48.6	50.8	46.1	49.2	52.0	20.6	49.7	52.9	46.7	55.2	38.8	55.5	12.0
Be	2.81	3.06	2.43	2.94	3.46	3.21	3.14	3.31	3.07	2.85	3.06	3.98	4.24	4.27	0.529	4.07	3.38	3.34	3.35	3.19	3.37	1.30
Sc	24.4	23.2	21.2	21.6	24.8	18.8	16.5	20.2	21.2	18.3	20.1	16.6	17.8	19.8	8.00	16.8	19.7	12.8	15.6	13.8	36.4	28.0
Ti	4250	4685	3909	3920	4713	3776	3587	4036	4490	3646	3817	3337	3421	3494	1178	3228	3417	1836	4444	2981	6451	6368
V	154	143	127	131	145	96.1	93.9	119	105	109	119	98.4	103	115	78.4	101	103	36.5	45.6	72.6	231	206
Cr	168	184	156	154	171	117	123	143	131	129	139	118	120	135	52.4	115	126	42.5	30.3	89.9	262	62.6
Co	19.5	22.6	18.7	22.9	20.8	14.8	8.17	26.9	39.5	18.7	21.1	8.14	9.30	22.9	12.0	17.5	3.97	19.1	50.1	1.71	52.9	33.1
Ni	48.9	68.2	60.1	65.7	86.4	56.5	28.5	101	106	50.4	55.4	27.1	29.0	56.8	27.4	40.5	33.2	58.5	75.2	76.0	103	49.1
Cu	35.5	133	80.1	41.9	280	71.8	24.4	159	26.7	44.7	39.1	35.9	38.4	110	91.8	36.5	17.3	47.6	5.37	86.7	17.8	81.0
Zn	122	126	111	87.5	88.0	83.3	58.3	77.3	82.4	123	122	83.0	84.9	122	321	290	62.5	171	72.7	180	142	81.8
Ga	24.6	25.9	21.9	22.7	25.2	20.8	20.1	21.7	21.9	20.7	21.1	20.4	20.9	20.9	8.99	19.1	21.9	18.6	19.3	17.4	22.0	18.6
Rb	184	223	198	212	220	205	207	207	190	188	176	209	206	181	0.444	148	224	174	108	196	131	39.2
Sr	37.6	47.0	34.8	34.5	39.3	30.6	44.5	23.6	50.6	68.3	55.8	43.9	47.1	35.5	267	35.3	32.6	23.1	116	37.0	44.1	388
Y	37.0	41.2	38.0	36.4	36.3	30.7	25.4	38.6	30.5	30.8	32.3	32.7	34.4	26.2	46.3	29.9	25.9	32.9	55.0	36.0	19.7	19.7
Zr	137	161	147	144	172	171	162	157	160	133	128	136	135	131	55.4	179	152	201	301	151	170	149
Nb	12.9	16.3	12.7	13.2	15.4	12.8	11.8	12.9	12.0	11.1	12.2	11.8	12.7	12.2	4.57	12.2	10.7	17.4	21.5	12.0	11.1	10.1
Mo	0.873	6.44	1.51	0.507	1.19	1.21	0.265	2.68	0.941	1.42	1.48	0.944	1.21	2.06	1.33	0.805	0.510	1.04	129	1.68	2.21	1.17

Table continued on next page

Sample depth	**59.125**	**60.2**	**62.30**[a]	**63.21**[a]	**64.045**	**66.17**[a]	**67.45**[a]	**68.08**	**73.67**	**76.08**[a]	**77.175**	**83.14**[a]	**83.88**[a]	**86.88**[a]	**87.40**[a]	**89.16**	**92.67**[a]	**95.21**	**102.15**	**108.21**	**122.75**	**128.35**
RockType	**GS**	**GS**	**Shale**	**Shale**	**Shale**	**Shale**	**Shale**	**Shale**	**Shale**	**Shale**	**Shale**	**CS**	**Carb.**	**CS**	**C. BIF**	**CS**	**CS**	**CS**	**CS**	**CS**	**Silt**	**BIF**
Stratigraphic Zone	***Lower TBH***	***Lower TBH***	***Lower TBH***	***Lower TBH***	***Lower TBH***	***Lower TBH***	***Lower TBH***	***Lower TBH***	***Lower TBH***	***Lower TBH***	***Lower TBH***	***Lower TBH***	***Lower TBH***	***Lower TBH***	***Lower TBH***	***Lower TBH***	***Upper D/R***	***Upper D/R***	***Upper D/R***	***Upper D/R***	***Upper D/R***	***Upper D/R***
Cd	0.071	0.089	0.080	0.080	0.180	0.073	0.069	0.071	0.073	0.146	0.138	0.122	0.127	0.064	0.065	0.094	0.094	0.214	0.043	0.175	0.071	0.099
Sn	4.15	6.27	5.34	5.84	6.53	6.02	5.35	5.24	5.26	4.63	4.33	5.66	5.99	5.89	0.093	5.81	5.59	7.38	7.74	4.76	0.882	2.18
Sb	1.23	2.04	2.73	1.78	3.08	2.67	0.899	1.91	1.61	1.02	2.51	1.83	1.77	1.77	1.35	2.07	0.804	1.36	2.70	2.70	1.07	0.651
Cs	7.36	9.26	7.94	8.17	8.55	7.00	7.46	7.55	10.4	8.74	9.49	9.49	10.1	8.85	0.503	7.06	11.7	7.33	5.96	11.5	8.16	1.02
Ba	1303	1570	1370	1548	1603	1635	1686	1703	1492	1581	1613	2033	2028	1645	14.3	1460	2070	1624	3836	1527	1400	570
La	55.4	58.0	52.9	42.0	52.4	59.1	9.52	44.6	27.9	41.1	71.0	61.9	62.8	31.0	26.5	36.4	24.5	62.9	56.6	34.1	35.5	21.9
Ce	107	117	108	82.7	98.2	118	19.9	82.7	54.0	80.5	134	131	129	63.1	55.4	72.7	49.9	124	116	66.4	77.2	42.9
Pr	12.4	13.7	11.8	9.51	11.5	12.6	2.41	9.89	6.55	9.08	14.9	14.4	15.3	7.28	7.17	8.33	5.67	14.0	13.9	7.84	8.43	5.31
Nd	44.5	49.3	43.1	34.6	41.0	44.2	9.04	36.1	24.1	32.8	51.5	52.5	55.7	26.3	29.4	30.4	20.5	49.5	50.8	28.5	30.7	20.5
Sm	8.68	9.50	8.27	6.73	8.09	8.11	2.00	7.28	4.98	6.20	9.03	9.77	10.5	5.03	6.77	6.00	4.10	9.25	10.1	5.43	6.03	4.27
Eu	1.89	1.73	1.66	1.17	1.72	2.03	0.513	1.91	0.966	1.22	1.94	1.86	1.99	1.08	1.69	1.36	0.846	1.25	1.72	0.929	1.37	1.33
Tb	1.18	1.27	1.16	1.02	1.19	0.974	0.518	1.12	0.828	0.909	1.12	1.18	1.23	0.738	1.28	0.916	0.696	1.09	1.43	0.868	0.753	0.637
Gd	7.82	8.41	7.57	6.34	7.59	6.67	2.65	6.98	4.96	5.65	7.66	8.22	8.76	4.38	8.31	5.56	3.91	7.50	9.23	5.25	4.95	4.14
Dy	6.90	7.52	6.73	6.18	7.08	5.37	3.64	6.95	5.20	5.48	6.31	6.34	6.81	4.69	7.50	5.51	4.54	6.36	8.93	5.46	4.34	3.76
Ho	1.43	1.56	1.42	1.36	1.44	1.14	0.897	1.49	1.13	1.18	1.25	1.29	1.38	1.06	1.58	1.19	1.04	1.34	1.93	1.24	0.902	0.782
Er	4.02	4.38	4.06	3.98	4.08	3.37	2.73	4.28	3.32	3.42	3.40	3.61	3.81	3.27	4.30	3.56	3.17	3.77	5.70	3.76	2.53	2.15
Tm	0.616	0.663	0.619	0.619	0.631	0.535	0.535	0.653	0.522	0.519	0.503	0.544	0.575	0.533	0.620	0.572	0.508	0.590	0.876	0.595	0.402	0.310
Yb	3.98	4.20	3.94	3.90	4.16	3.48	2.79	4.24	3.54	3.30	3.15	3.48	3.76	3.53	3.72	3.74	3.41	3.81	5.64	3.91	2.66	1.94
Lu	0.597	0.627	0.600	0.600	0.643	0.545	0.545	0.661	0.579	0.500	0.468	0.550	0.587	0.564	0.542	0.583	0.541	0.569	0.885	0.642	0.396	0.289
Hf	3.82	4.50	3.84	3.70	4.71	4.21	3.80	4.32	4.40	3.45	3.53	3.62	3.85	3.38	1.40	4.31	3.87	5.86	7.96	3.96	4.65	3.72
Ta	1.31	1.58	1.22	1.20	1.47	1.13	1.08	1.28	1.21	1.09	1.14	1.09	1.22	1.20	0.415	1.08	0.967	1.60	1.61	1.07	1.02	0.630
W	3.45	4.88	4.29	3.54	4.53	4.15	3.53	3.18	3.19	2.82	3.45	2.93	3.35	3.12	0.792	2.67	2.80	3.92	10.6	4.10	2.30	0.369
Tl	1.60	2.16	0.000	0.000	2.03	0.000	0.000	1.91	1.94	0.000	1.85	0.000	2.43	0.000	0.000	0.000	0.000	2.15	1.17	0.000	0.760	0.171
pb	8.92	13.4	18.6	21.0	36.0	12.5	5.22	9.73	8.04	7.83	11.0	11.6	12.5	12.3	7.96	11.7	3.84	37.5	12.3	16.8	2.94	9.51
Th	20.9	21.9	18.8	18.8	20.3	16.2	17.1	18.4	17.2	16.7	18.1	18.7	19.7	17.7	7.09	17.2	18.1	25.9	20.5	16.9	12.6	3.75
U	5.58	6.31	5.58	6.46	6.36	4.45	4.90	5.56	5.39	4.76	4.05	7.51	8.01	4.51	3.45	5.83	4.75	8.63	9.62	5.95	2.33	1.10
ΣREE+Y	294	320	289	237	276	297	83.1	247	169	223	339	329	336	179	201	207	149	319	339	201	196	130
TiO_2/Zr	46.5	42.7	47.1	41.0	38.6	38.7	38.3	41.5	45.6	48.1	48.4	41.9	17.9	53.5	43.3	30.7	38.9	30.0	10.0	35.1	41.7	65.6

[a] Major and trace elements from Rou´e, et al. (2021)

[b] Abbreviations: CS = carbonaceous shale, Carb. = carbonate, BIF = banded iron formation, C. BIF = carbonate rich banded iron formation, GS = grey shale

Table 3.4. Major and trace element data for Agouron GOE Drill Core ANW

Sample depth	**27.31**	**29.77**	**30.51**	**31.76**	**32.56**	**33.15**	**36.47**	**37.3**	**38.28**	**39.12**	**40.05**	**41.44**	**41.7**	**43.12**	**43.7**	**44.76**	**45.13**
RockType	**CS**	**CS**	**CS**	**CS**	**CS**	**CS**	**CS**	**CS**	**CS**	**CS**	**CS**	**Ch. BIF**	**Chert**	**GS**	**GS**	**GS**	**GS**
Stratigraphic Zone	***Lower TBH***	***Lower TBH***	***Lower TBH***	***Lower TBH***	***Lower TBH***	***Lower TBH***	***Upper D/R***	***Upper D/R***	***Upper D/R***	***Upper D/R***	***Upper D/R***	***Upper D/R***	***Upper D/R***	***Upper D/R***	***Upper D/R***	***Upper D/R***	***Upper D/R***
Major [wt.%]																	
SiO_2	64.4	67.0	63.0	67.9	70.2	62.2	69.1	66.2	60.6	63.2	65.4	46.7	76.2	57.1	61.2	55.5	60.1
Al_2O_3	16.3	13.7	17.1	18.5	15.1	13.5	15.1	14.9	14.2	14.9	15.3	4.99	13.4	19.9	19.1	22.1	21.8
TiO_2	0.624	0.625	0.573	0.643	0.587	0.591	0.520	0.561	0.501	0.577	0.574	0.243	0.474	1.51	0.997	1.11	1.98
Fe_2O_3	3.23	3.48	4.40	1.71	3.24	5.61	2.12	3.70	6.41	5.65	4.02	21.6	0.723	8.53	7.45	8.28	4.94
MnO	0.026	0.034	0.053	0.021	0.043	0.085	0.058	0.072	0.080	0.103	0.061	0.063	0.016	0.262	0.235	0.254	0.137
MgO	1.24	1.53	2.11	1.14	1.68	2.68	1.47	1.71	1.80	2.10	1.43	0.444	0.564	1.60	1.47	1.70	1.15
CaO	0.058	0.000	0.000	0.007	0.000	0.010	0.042	0.065	0.065	0.066	0.064	0.030	0.036	0.226	0.107	0.178	0.179
K2O	0.246	0.187	0.230	0.283	0.301	0.178	0.270	0.257	0.229	0.231	0.253	0.486	0.255	0.262	0.265	0.306	0.301
Na_2O	3.85	2.86	3.67	4.44	3.25	2.47	3.24	3.14	2.96	2.96	3.31	1.05	3.04	4.05	3.92	4.54	5.25
P_2O_5	0.050	0.039	0.055	0.051	0.030	0.049	0.053	0.070	0.068	0.069	0.072	0.040	0.046	0.190	0.109	0.178	0.160
LOI	5.83	10.2	8.43	3.75	5.30	7.79	8.17	8.65	10.8	8.80	7.61	22.5	3.30	3.52	3.43	3.37	3.00
Sum	95.8	99.6	99.6	98.4	99.7	95.2	100	99.3	97.7	98.7	98.0	98.2	98.1	97.2	98.2	97.5	99.0
Trace elements [µg/g]																	
Li	28.5	47.3	61.2	25.6	43.8	80.8	42.0	48.9	55.2	62.4	41.0	13.4	12.8	49.8	46.1	52.8	33.3
Be	3.91	3.74	4.44	3.00	2.80	2.76	4.44	4.38	4.46	4.12	4.00	4.32	1.65	3.46	3.31	3.38	3.77
Sc	22.3	20.0	23.6	19.4	19.8	17.4	19.4	21.2	21.4	23.1	23.2	12.6	13.6	30.6	27.6	27.4	33.4
Ti	4265	4824	4206	4294	4089	4250	3808	4187	4084	4257	4112	3869	1978	10226	6755	7326	12757
V	118	218	677	124	151	100	94.3	115	123	126	164	109	55.6	213	160	142	247
Cr	151	183	186	166	162	146	127	144	143	160	156	105	62.4	187	197	119	200
Co	3.60	5.50	1.09	0.307	2.76	1.34	0.460	7.85	21.8	20.6	19.4	0.339	272	18.6	10.4	13.8	7.40
Ni	67.6	90.3	80.4	18.6	26.2	129	38.7	43.4	79.4	86.0	97.1	46.1	829	84.7	60.3	51.7	63.6
Cu	125	49.8	145	32.7	20.0	181	67.7	24.9	59.2	121	87.2	12.3	266	3.43	9.90	17.1	243
Zn	152	109	166	65.8	55.7	119	57.2	71.3	115	86.2	84.3	24.8	30.3	113	87.7	94.6	73.0
Ga	24.7	22.3	26.7	27.8	22.0	21.8	24.3	24.2	25.0	24.1	24.5	25.9	8.77	29.3	26.8	31.8	31.2
Rb	212	182	223	232	176	139	187	183	195	180	191	181	73.1	192	181	203	221
Sr	72.6	62.3	59.9	80.4	60.1	58.8	72.1	59.4	58.5	55.7	64.2	78.8	29.4	61.7	58.8	69.7	73.6
Y	43.2	52.0	35.7	31.1	37.2	39.1	49.8	44.0	49.8	60.2	53.3	23.8	20.9	34.5	31.9	53.9	37.8
Zr	187	202	177	206	169	219	208	175	196	203	189	193	108	264	261	418	311
Nb	16.5	18.7	21.1	18.3	16.4	16.5	17.3	15.0	17.0	16.5	16.5	16.1	8.99	21.9	24.5	31.9	27.1
Mo	0.636	22.8	15.6	1.06	2.61	1.16	1.96	2.33	2.59	2.63	5.48	0.649	48.9	0.505	0.791	0.701	1.16
Cd	0.115	0.093	0.100	0.097	0.074	0.125	0.139	0.147	0.199	0.126	0.134	0.112	0.060	0.197	0.261	0.190	0.229

Table continued on next page

Sample depth	**27.31**	**29.77**	**30.51**	**31.76**	**32.56**	**33.15**	**36.47**	**37.3**	**38.28**	**39.12**	**40.05**	**41.44**	**41.7**	**43.12**	**43.7**	**44.76**	**45.13**
RockType	**CS**	**CS**	**CS**	**CS**	**CS**	**CS**	**CS**	**CS**	**CS**	**CS**	**CS**	**Ch. BIF**	**Chert**	**GS**	**GS**	**GS**	**GS**
Stratigraphic Zone	***Lower TBH***	***Lower TBH***	***Lower TBH***	***Lower TBH***	***Lower TBH***	***Lower TBH***	***Upper D/R***	***Upper D/R***	***Upper D/R***	***Upper D/R***	***Upper D/R***	***Upper D/R***	***Upper D/R***	***Upper D/R***	***Upper D/R***	***Upper D/R***	***Upper D/R***
Sn	6.24	6.14	7.01	7.11	5.52	4.55	6.43	6.04	5.77	5.91	6.40	6.56	0.443	5.24	5.36	5.93	7.56
Sb	0.927	3.08	1.70	0.602	1.56	0.999	0.640	5.30	18.0	9.58	13.0	1.98	284	0.777	0.589	0.779	1.74
Cs	11.3	11.2	13.8	12.1	9.65	8.59	12.7	12.4	13.3	12.3	13.1	10.4	5.07	10.4	9.83	11.1	11.0
Ba	3119	2702	3446	3928	3028	2574	5489	5081	5302	4984	5486	7393	2099	2842	2795	3013	3447
La	51.0	80.2	69.9	42.8	50.5	48.6	32.7	33.3	31.9	22.1	43.1	20.7	16.1	50.2	56.8	96.8	58.6
Ce	92.7	149	131	79.6	95.3	89.2	63.9	60.7	60.2	42.4	81.5	42.4	30.1	106	115	219	125
Pr	11.9	18.4	16.5	9.54	11.5	10.7	8.23	7.76	7.72	5.38	10.3	4.81	3.47	12.1	12.5	24.9	14.6
Nd	44.4	66.1	60.5	34.1	41.5	38.7	30.3	28.6	28.8	20.8	38.6	16.7	12.2	44.1	43.6	90.5	54.4
Sm	8.81	12.4	11.6	6.44	8.23	7.37	6.31	5.76	6.03	5.06	7.92	3.29	2.53	9.02	8.36	16.5	11.1
Eu	1.79	2.41	2.18	1.41	1.69	1.57	1.39	1.24	1.41	1.32	1.66	0.972	0.725	2.18	2.00	3.47	2.48
Tb	1.21	1.57	1.21	0.863	1.10	1.08	1.21	1.09	1.22	1.40	1.38	0.556	0.493	1.23	1.07	1.84	1.37
Gd	7.89	10.8	9.04	5.51	7.33	6.97	6.71	6.29	6.97	7.47	8.10	3.15	2.70	8.22	6.99	12.4	9.24
Dy	7.36	9.17	6.68	5.39	6.44	6.68	8.23	7.23	8.03	9.57	8.96	3.76	3.41	7.07	6.41	11.3	8.02
Ho	1.59	1.92	1.34	1.17	1.36	1.45	1.89	1.66	1.86	2.22	2.00	0.894	0.808	1.43	1.33	2.38	1.64
Er	4.62	5.37	3.84	3.44	3.86	4.23	5.67	4.97	5.58	6.66	5.93	2.92	2.57	3.98	3.82	6.79	4.62
Tm	0.722	0.803	0.601	0.547	0.595	0.666	0.895	0.782	0.882	1.03	0.929	0.519	0.431	0.604	0.598	1.05	0.724
Yb	4.75	5.03	4.01	3.65	3.85	4.41	5.83	5.11	5.83	6.75	6.14	3.76	3.06	3.89	3.98	6.76	4.81
Lu	0.753	0.743	0.625	0.561	0.578	0.690	0.898	0.798	0.918	1.05	0.964	0.601	0.502	0.573	0.592	0.988	0.716
Hf	5.34	5.63	5.37	6.14	4.61	5.85	5.63	4.77	5.24	5.35	5.17	5.26	2.84	7.30	7.08	11.6	8.41
Ta	1.62	1.84	2.09	1.99	1.60	1.57	1.62	1.40	1.56	1.55	1.51	1.59	0.630	1.92	2.13	2.55	2.21
W	3.57	4.35	3.34	3.47	3.08	4.03	2.99	3.29	3.47	4.35	4.32	4.34	3.06	6.10	3.97	3.43	4.39
Tl	3.01	3.12	4.37	3.96	2.99	2.36	3.13	3.07	3.71	3.48	4.37	4.29	3.03	1.96	1.81	1.92	2.10
pb	21.5	15.0	11.6	7.04	10.00	11.2	11.7	18.7	33.4	20.4	25.4	6.43	201	5.45	4.01	5.92	7.92
Th	23.5	23.6	27.9	29.2	21.6	21.2	24.1	20.1	21.0	21.7	21.5	23.7	5.09	21.5	27.6	33.1	23.2
U	7.44	13.1	14.0	6.57	6.24	7.37	8.16	5.64	6.89	7.83	7.84	12.8	4.70	1.81	2.76	2.04	2.37
ΣREE+Y	283	416	355	226	271	261	224	209	217	194	271	129	100	285	295	548	335
TiO_2/Zr	33.3	30.9	32.3	31.1	34.8	27	25	32	25.5	28.5	30.4	12.6	43.9	57.3	38.3	26.5	63.8

a Abbreviations: CS = carbonaceous shale, Ch. BIF = cherty banded iron formation, GS = grey shale

Table 3.5. Major and trace element data for Agouron GOE Drill Core ADL

Sample depth	**78.3**	**80.25**	**132.08**	**136.38**	**142.12**	**151.365**	**153.2**	**154.87**	**157.21**	**167.54**	**169.85**	**170.845**	**177.5**	**189.45**	**193.39**	**197.695**	**199.1**	**204.08**	**207.61**	**212.235**	**212.7**	**214.85**
RockType	**Shale**	**Shale**	**Shale**	**Shale**	**FS**	**CS**	**Shale**	**Shale**	**Shale**	**Silt**	**Silt**	**Silt**	**Silt**	**Silt**	**Silt**	**FS**	**Silt**	**Silt**	**FS**	**Silt**	**Silt**	**FS**
Stratigraphic Zone	***Upper D/R***	***Upper D/R***	***Upper D/R***	***Upper D/R***	***Upper D/R***	***Upper D/R***	***Upper D/R***	***Upper D/R***	***Upper D/R***	***Upper D/R***	***Upper D/R***	***Upper D/R***	***Upper D/R***	***Upper D/R***	***Upper D/R***	***Upper D/R***	***Upper D/R***	***Upper D/R***	***Upper D/R***	***Upper D/R***	***Upper D/R***	***Upper D/R***
Major elements [wt.%]																						
SiO_2	54.0	51.1	49.3	58.6	56.0	55.1	53.3	56.3	52.3	56.3	63.6	61.6	54.0	54.8	55.0	56.7	54.1	54.9	53.9	56.0	55.8	53.4
Al_2O_3	20.2	19.2	13.2	17.2	15.4	17.7	19.1	19.8	19.1	18.1	14.2	15.8	18.3	18.4	18.4	17.8	17.9	18.3	18.1	17.3	17.5	18.2
TiO_2	0.773	0.755	0.917	0.964	0.956	0.666	0.728	0.840	0.688	0.733	0.638	0.669	0.721	0.711	0.697	0.693	0.743	0.752	0.758	0.783	0.781	0.889
Fe_2O_3	11.8	12.2	12.6	10.4	11.5	12.0	11.9	8.50	12.9	9.14	8.35	8.04	12.3	11.8	11.4	11.1	12.3	12.1	12.4	11.9	11.8	12.7
MnO	0.110	0.109	0.135	0.053	0.068	0.118	0.104	0.097	0.106	0.064	0.078	0.081	0.067	0.067	0.065	0.058	0.078	0.069	0.066	0.069	0.071	0.096
MgO	4.97	4.86	5.80	5.04	5.88	4.83	4.84	4.17	4.73	4.13	4.35	3.93	4.75	4.45	4.37	4.28	4.77	4.67	4.71	4.64	4.69	5.12
CaO	0.392	0.737	6.57	0.234	1.16	0.395	0.447	0.523	0.374	0.325	0.520	0.443	0.349	0.338	0.418	0.280	0.316	0.316	0.317	0.403	0.406	0.279
K2O	3.12	3.20	1.07	2.61	1.98	3.27	3.81	4.21	3.85	3.54	2.32	2.83	3.87	4.04	4.31	3.85	4.08	3.50	3.50	2.76	2.78	3.39
Na_2O	0.761	0.760	0.803	1.12	1.01	1.29	1.17	1.23	1.25	1.49	2.40	1.92	1.28	0.908	0.872	1.08	1.27	1.55	1.77	1.53	1.50	1.13
P_2O_5	0.191	0.173	0.658	0.074	0.086	0.181	0.201	0.168	0.213	0.212	0.157	0.132	0.195	0.179	0.175	0.185	0.183	0.194	0.187	0.178	0.175	0.176
LOI	4.50	5.31	8.68	4.40	5.14	4.22	4.30	4.20	4.30	3.80	3.30	3.44	4.00	4.10	4.10	3.86	4.00	3.50	4.00	4.28	4.30	4.30
Sum	101	98.3	99.7	101	99.2	99.8	99.8	100.0	99.8	97.9	99.9	98.8	99.8	99.8	99.8	99.8	99.8	99.8	99.8	99.8	99.8	99.8
Trace elements [µg/g]																						
Li	109	107	102	91.0	107	80.6	81.7	65.6	86.7	59.3	66.3	59.9	94.5	72.0	62.5	66.7	74.8	81.6	74.8	84.4	85.8	90.6
Be	4.06	3.93	1.84	2.95	2.43	3.20	3.35	3.75	3.83	3.67	2.59	2.95	4.54	3.54	3.38	3.66	3.66	3.79	3.62	3.03	3.13	3.28
Sc	29.2	27.7	24.8	27.0	26.2	22.6	25.2	26.6	25.0	23.9	14.0	15.7	30.1	23.3	21.1	22.7	23.9	24.7	23.4	22.0	22.5	26.6
Ti	4957	4591	5768	6077	5724	3888	4476	5213	4155	4603	3720	3943	5453	4321	3852	4065	4426	4725	4518	4661	4937	5480
V	157	145	157	176	164	127	148	155	144	130	84.6	91.8	165	130	118	122	135	141	137	129	133	148
Cr	273	261	333	350	238	241	260	249	240	225	148	161	285	229	202	208	226	237	227	222	232	291
Co	46.7	43.7	40.5	33.0	33.1	23.0	42.4	86.2	47.7	32.1	22.2	24.9	43.2	33.8	30.2	27.2	32.2	33.6	29.9	28.5	31.4	30.7
Ni	142	135	160	134	124	127	144	145	129	95.5	59.3	69.6	129	103	92.3	92.4	100	104	101	98.5	105	130
Cu	2.01	2.12	169	65.4	472	3.32	15.8	95.1	26.8	40.6	61.9	92.8	19.8	1.41	1.54	13.4	55.5	60.1	43.5	34.3	74.7	88.8
Zn	114	112	107	88.4	93.2	86.4	87.8	71.4	99.1	79.4	73.2	72.0	120	86.7	78.4	80.6	88.4	91.2	88.4	92.3	97.9	108
Ga	28.6	27.0	17.9	22.8	20.5	24.7	27.1	27.1	27.2	25.4	17.6	20.1	33.0	25.8	23.4	24.3	25.8	26.9	25.9	24.0	24.8	26.3
Rb	201	202	59.7	137	107	152	180	217	173	174	119	152	226	208	212	205	190	172	153	135	141	159
Sr	94.0	91.1	56.2	27.2	27.5	39.2	40.7	48.5	51.0	60.4	66.9	60.6	65.2	46.2	49.7	44.5	48.0	57.7	56.3	49.5	49.5	44.0
Y	29.0	28.4	56.4	16.6	17.9	24.6	29.4	21.3	28.7	28.0	19.8	18.5	33.3	25.7	24.6	24.8	25.7	28.2	26.8	24.4	26.4	28.9
Zr	141	137	127	152	132	136	146	155	144	153	126	119	177	139	125	139	142	148	142	138	142	157
Nb	16.3	16.3	11.3	13.9	12.8	12.3	13.8	15.1	13.2	14.2	12.1	13.1	17.2	14.1	12.0	13.9	13.5	14.9	13.9	13.5	13.9	14.4
Mo	1.03	0.742	0.455	0.480	0.932	1.41	4.66	1.58	1.55	9.12	18.3	1.19	5.51	1.16	1.19	1.87	2.24	2.07	1.80	1.56	1.52	1.04

Table continued on next page

Sample depth	**78.3**	**80.25**	**132.08**	**136.38**	**142.12**	**151.365**	**153.2**	**154.87**	**157.21**	**167.54**	**169.85**	**170.845**	**177.5**	**189.45**	**193.39**	**197.695**	**199.1**	**204.08**	**207.61**	**212.235**	**212.7**	**214.85**
RockType	**Shale**	**Shale**	**Shale**	**Shale**	**FS**	**CS**	**Shale**	**Shale**	**Shale**	**Silt**	**Silt**	**Silt**	**Silt**	**Silt**	**Silt**	**FS**	**Silt**	**Silt**	**FS**	**Silt**	**Silt**	**FS**
Stratigraphic Zone	***Upper D/R***	***Upper D/R***	***Upper D/R***	***Upper D/R***	***Upper D/R***	***Upper D/R***	***Upper D/R***	***Upper D/R***	***Upper D/R***	***Upper D/R***	***Upper D/R***	***Upper D/R***	***Upper D/R***	***Upper D/R***	***Upper D/R***	***Upper D/R***	***Upper D/R***	***Upper D/R***	***Upper D/R***	***Upper D/R***	***Upper D/R***	***Upper D/R***
Cd	0.048	0.059	0.062	0.059	0.066	0.055	0.052	0.058	0.052	0.056	0.050	0.056	0.068	0.053	0.046	0.065	0.059	0.058	0.054	0.060	0.063	0.062
Sn	6.00	5.33	1.90	3.63	1.19	3.93	4.64	5.21	4.47	4.80	3.14	3.62	5.51	4.69	4.09	2.55	4.34	4.68	4.44	1.23	4.13	4.86
Sb	1.49	1.30	0.626	0.722	1.13	1.89	1.03	1.68	0.909	0.727	0.542	0.617	0.793	0.651	0.723	0.790	1.01	0.883	0.804	0.766	0.772	1.00
Cs	12.1	12.4	2.56	5.80	4.73	6.84	7.88	9.39	9.00	8.56	8.97	9.62	11.0	9.78	13.0	11.9	10.5	9.50	7.06	5.85	6.25	6.44
Ba	442	456	192	439	365	575	627	784	630	597	306	450	782	755	698	687	652	581	526	469	485	587
La	52.2	59.4	78.2	33.8	24.0	43.1	43.9	37.9	37.9	49.0	30.7	36.2	61.9	49.9	52.6	50.5	44.3	54.7	47.6	41.5	50.8	53.5
Ce	99.0	116	158	66.0	49.3	81.6	83.8	68.2	72.3	91.9	63.7	73.6	116	93.0	100	99.6	83.6	106	92.1	78.1	98.3	106
Pr	11.2	12.9	19.5	7.15	5.70	9.25	9.57	7.39	8.27	10.5	7.49	8.63	12.8	10.2	11.1	11.0	9.45	12.0	10.4	8.63	10.9	11.6
Nd	40.2	46.0	74.9	24.9	21.1	33.1	34.8	26.0	30.0	37.7	27.4	31.1	44.8	35.9	38.6	38.7	33.6	42.2	37.0	30.9	38.7	41.5
Sm	7.64	8.63	15.6	4.36	4.15	6.17	6.63	4.65	5.90	7.23	5.18	5.53	8.25	6.52	6.78	6.96	6.33	7.73	6.92	5.83	7.12	7.89
Eu	1.46	1.68	3.02	1.19	1.01	1.53	1.40	1.18	1.47	1.56	1.07	1.05	1.88	1.40	1.39	1.45	1.35	1.90	1.43	1.28	1.45	1.72
Tb	0.977	1.02	2.12	0.555	0.583	0.783	0.896	0.625	0.836	0.915	0.650	0.630	1.10	0.853	0.837	0.844	0.840	0.965	0.885	0.786	0.909	1.01
Gd	6.74	7.08	14.6	3.64	3.63	5.26	5.74	4.00	5.28	6.15	4.36	4.33	7.22	5.59	5.58	5.70	5.53	6.49	5.88	5.16	6.11	6.86
Dy	5.61	5.79	11.7	3.22	3.52	4.59	5.44	3.81	5.13	5.33	3.75	3.63	6.50	4.95	4.80	4.85	4.94	5.53	5.10	4.64	5.19	5.67
Ho	1.13	1.15	2.25	0.659	0.730	0.950	1.14	0.813	1.09	1.09	0.754	0.732	1.32	1.01	0.969	0.984	1.01	1.11	1.04	0.955	1.04	1.14
Er	3.13	3.13	5.67	1.85	2.10	2.67	3.19	2.38	3.13	3.03	2.07	2.02	3.64	2.82	2.65	2.73	2.81	3.05	2.87	2.67	2.87	3.11
Tm	0.477	0.476	0.747	0.293	0.326	0.402	0.482	0.378	0.471	0.459	0.312	0.302	0.544	0.427	0.393	0.416	0.423	0.455	0.428	0.404	0.427	0.461
Yb	3.09	3.06	4.19	1.96	2.15	2.58	3.06	2.52	3.03	2.93	1.98	1.92	3.49	2.72	2.48	2.65	2.70	2.89	2.73	2.57	2.68	2.88
Lu	0.455	0.455	0.559	0.297	0.325	0.388	0.447	0.378	0.444	0.429	0.287	0.284	0.506	0.397	0.358	0.393	0.398	0.420	0.396	0.378	0.392	0.418
Hf	3.82	3.86	3.50	4.10	3.68	3.84	4.03	4.32	3.96	4.22	3.43	3.35	4.85	3.83	3.47	3.91	3.90	4.07	3.89	3.85	3.93	4.27
Ta	1.51	1.54	0.915	1.23	1.04	1.14	1.28	1.38	1.21	1.32	1.13	1.25	1.59	1.31	1.04	1.26	1.24	1.36	1.27	1.25	1.25	1.27
W	4.80	5.25	2.28	3.08	3.20	4.81	5.39	5.20	5.12	4.53	3.33	3.60	6.37	5.03	3.99	4.05	4.72	5.24	5.20	5.21	4.69	5.05
Tl	0.840	0.866	0.241	0.533	0.455	0.642	0.616	0.801	0.616	0.603	0.483	0.600	0.786	0.725	0.871	0.773	0.700	0.640	0.543	0.488	0.504	0.581
Pb	10.4	9.36	9.91	11.1	9.49	6.64	7.49	8.05	6.74	10.1	12.3	13.6	8.81	10.4	8.85	16.9	12.3	10.1	11.7	11.4	15.0	8.57
Th	21.6	22.2	10.3	14.3	11.3	18.4	18.8	19.1	19.7	19.5	12.5	12.2	23.9	18.8	17.6	19.2	18.6	19.6	18.8	18.0	18.0	18.9
U	5.31	6.63	3.11	3.57	3.03	4.64	4.64	5.85	5.14	5.25	3.53	3.91	6.17	4.62	4.43	5.01	5.01	5.31	5.21	4.94	4.88	4.64
ΣREE+Y	262	295	448	167	137	217	230	181	204	246	169	189	303	241	253	252	223	274	242	208	253	272
TiO_2/Zr	54.7	55.0	72.5	63.4	72.3	49.0	49.9	54.2	47.9	47.9	50.7	56.2	40.8	51.3	56.0	49.9	52.4	50.9	53.4	56.8	55.0	56.6

Table continued on next page

Sample depth	**218.815**	**223.8**	**226.72**	**233.88**	**234.9**	**238.69**	**239.85**	**256.87**	**263.87**	**267.14**
RockType	**Fs**	**FS**	**FS**	**Shale**	**Shale**	**FS**	**FS**	**Shale**	**Shale**	**Shale**
Stratigraphic Zone	***Upper D/R***	***Upper D/R***	***Upper D/R***	***Upper D/R***	***Upper D/R***	***Upper D/R***	***Upper D/R***	***Upper D/R***	***Upper D/R***	***Upper D/R***
Major elements [wt.%]										
SiO_2	61.2	61.1	59.1	55.6	55.7	58.6	55.4	56.6	55.1	57.0
Al_2O_3	17.2	18.0	18.7	17.4	14.2	18.2	18.8	18.1	19.7	20.2
TiO_2	0.764	0.752	0.762	0.558	0.508	0.716	1.15	0.989	0.844	0.746
Fe_2O_3	7.42	6.96	7.22	10.1	14.5	8.02	8.80	9.34	8.95	8.14
MnO	0.047	0.040	0.033	0.055	0.094	0.037	0.064	0.069	0.038	0.031
MgO	3.95	4.07	4.28	5.29	6.80	4.35	4.92	5.04	4.58	4.26
CaO	0.190	0.173	0.167	0.174	1.04	0.208	0.172	0.547	0.154	0.133
K2O	4.23	4.24	4.46	3.45	1.25	5.47	4.15	3.84	4.80	5.00
Na_2O	0.455	0.448	0.289	0.184	0.192	0.736	0.355	0.514	0.181	0.174
P_2O_5	0.135	0.135	0.137	0.115	0.258	0.119	0.143	0.163	0.127	0.122
LOI	4.23	4.00	4.00	4.70	5.60	3.50	4.90	4.70	4.70	4.30
Sum	99.8	99.9	99.2	97.6	100	100.0	98.9	99.9	99.2	100
Trace elements [µg/g]										
Li	52.1	58.9	56.6	73.2	94.2	61.8	57.3	61.0	57.0	53.6
Be	2.87	3.10	3.46	2.84	1.56	5.66	3.70	3.32	4.36	4.32
Sc	17.3	18.4	20.0	16.0	17.3	18.5	27.2	23.6	23.9	21.8
Ti	4524	4490	4884	3601	3216	4431	7303	5965	5064	4712
V	116	122	130	119	113	140	199	166	159	147
Cr	190	193	213	190	196	217	455	314	247	218
Co	29.5	24.4	30.0	15.6	31.5	30.4	61.2	37.5	32.3	29.6
Ni	74.5	75.0	89.6	77.6	103	86.3	198	142	112	95.5
Cu	54.5	96.6	106	36.6	101	9.66	52.3	55.0	64.5	53.6
Zn	62.7	63.2	63.0	77.4	112	44.3	48.8	54.3	44.3	43.0
Ga	21.9	22.9	24.7	23.4	19.4	24.2	26.5	24.4	26.2	26.7
Rb	167	172	184	128	61.9	317	164	162	197	204
Sr	36.2	35.0	34.9	25.2	29.1	47.5	30.1	38.5	31.4	33.2
Y	23.4	25.4	28.6	22.3	38.3	33.8	33.2	30.5	31.9	29.3
Zr	157	153	161	126	108	136	182	165	153	147
Nb	16.0	15.9	16.6	11.8	8.66	17.6	16.8	16.5	16.6	16.4
Mo	3.56	3.07	6.09	6.14	5.21	4.04	2.64	2.61	3.17	3.23
Cd	0.075	0.072	0.067	0.052	0.059	0.050	0.071	0.071	0.065	0.055
Sn	5.44	5.27	5.20	4.52	2.01	5.39	5.24	3.13	6.02	5.88
Sb	3.83	1.26	1.20	0.761	1.39	1.01	1.11	0.674	0.736	0.791

Table continued on next page

Sample depth	**218.815**	**223.8**	**226.72**	**233.88**	**234.9**	**238.69**	**239.85**	**256.87**	**263.87**	**267.14**
RockType	**Fs**	**FS**	**FS**	**Shale**	**Shale**	**FS**	**FS**	**Shale**	**Shale**	**Shale**
Stratigraphic Zone	***Upper D/R***	***Upper D/R***	***Upper D/R***	***Upper D/R***	***Upper D/R***	***Upper D/R***	***Upper D/R***	***Upper D/R***	***Upper D/R***	***Upper D/R***
Cs	8.98	9.31	9.69	7.01	2.91	62.7	7.97	7.59	9.71	10.1
Ba	481	482	509	465	189	541	565	528	620	611
La	49.0	49.1	50.5	31.3	51.6	73.0	34.7	52.7	54.3	54.0
Ce	92.1	90.3	95.4	60.8	98.0	144	59.9	101	105	101
Pr	10.2	9.90	10.7	6.36	11.3	16.8	6.33	11.4	11.7	11.1
Nd	35.6	34.8	37.7	22.0	41.9	62.8	21.9	40.6	41.7	38.9
Sm	6.32	6.33	7.00	4.02	9.37	11.9	4.21	7.49	7.68	7.19
Eu	1.43	1.34	1.61	1.23	2.33	2.77	1.17	1.73	1.69	1.48
Tb	0.745	0.798	0.910	0.621	1.48	1.20	0.882	0.991	1.01	0.940
Gd	4.99	5.31	5.92	3.77	10.4	8.41	4.90	6.58	6.60	6.06
Dy	4.43	4.74	5.36	3.88	7.71	6.71	5.75	5.84	6.07	5.54
Ho	0.923	0.993	1.10	0.844	1.44	1.30	1.25	1.20	1.26	1.13
Er	2.63	2.81	3.11	2.50	3.60	3.47	3.64	3.31	3.47	3.14
Tm	0.404	0.429	0.470	0.397	0.497	0.506	0.554	0.492	0.513	0.471
Yb	2.61	2.76	2.98	2.56	3.00	3.15	3.49	3.08	3.24	2.98
Lu	0.388	0.408	0.437	0.377	0.435	0.462	0.516	0.453	0.472	0.438
Hf	4.43	4.29	4.45	3.46	2.88	3.73	4.84	4.60	4.34	4.06
Ta	1.63	1.60	1.62	1.13	0.800	1.41	1.48	1.61	1.69	1.57
W	5.17	5.22	6.04	4.65	3.52	4.98	4.94	4.60	5.38	5.18
Tl	0.802	0.801	0.816	0.661	0.359	2.16	0.788	0.747	0.874	0.851
Pb	16.8	9.61	14.3	7.58	17.2	9.63	11.4	8.46	10.6	11.2
Th	20.3	20.6	22.1	17.6	14.0	36.7	17.0	20.5	23.9	22.7
U	6.76	6.57	7.06	4.77	4.10	7.16	5.41	6.16	7.05	6.78
ΣREE+Y	235	235	252	163	281	370	182	268	276	263
TiO_2*/Zr*	48.5	49.3	47.2	44.4	47.0	52.8	63.2	60.0	55.2	50.7

[a] Abbreviations: CS = carbonaceous shale, FS = fine-grained sand

Table 3.6. Sr and Nd isotopic data for bulk sediments of the Agouron GOE Drill Cores

Core	Depth (Sample ID)	Rb [µg/g]	Sr [µg/g]	$^{87}Rb/^{86}Sr$	$^{87}Sr/^{86}Sr$[a]	$^{87}Sr/^{86}Sr$[b] 1.96 Ga	Sm [µg/g]	Nd [µg/g]	$^{147}Sm/^{144}Nd$	$^{143}Nd/^{144}Nd$[a]	ε(0)[c]	$T_{DM}^{b;c;f}$ GA	$T_{DM}^{b;d;f}$ GA	ε(Nd)[b; e] 2.42 Ga
AGP-1														
	50.07	202	48.8	11.56	1.064224±10	0.73741	4.51	22.0	0.1268	0.511227±10	-27.5	3.34	3.19	-5.8
	69.4	127	54.2	6.515	0.930173±10	0.74592	7.23	36.0	0.1199	0.511281±10	-26.5	3.01	2.85	-2.5
	105.21	209	97.9	5.965	0.903883±10	0.73518	7.15	37.9	0.1163	0.51105±10	-31.0	3.25	3.11	-5.9
	122.3	212	86.7	6.823	0.930759±10	0.73780	9.64	43.5	0.1367	0.511336±10	-25.4	3.55	3.41	-6.7
	139.5	271	70.5	10.72	1.038897±10	0.73560	3.07	17.6	0.1077	0.511051±10	-31.0	2.99	2.85	-3.2
AGP-2														
	66.17	209	32.4	18.00	1.242168±10	0.73298	7.79	41.9	0.1148	0.511132±10	-29.4	3.08	2.93	-3.9
	83.88	209	45.8	12.77	1.093455±10	0.73239	9.58	50.6	0.1167	0.511221±10	-27.6	3.00	2.85	-2.7
	95.21	206	42.7	13.46	1.116812±10	0.73606	6.51	34.1	0.1178	0.511204±10	-28.0	3.06	2.91	-3.4
	108.4	226	43.7	14.43	1.128280±10	0.72032	5.24	26.8	0.1206	0.511309±10	-25.9	2.99	2.83	-2.2
	128.4	123	40.0	8.597	0.973659±10	0.73052	4.90	24.5	0.1234	0.511296±10	-26.2	3.10	2.94	-3.3
ANW														
	29.79	160	52.2	8.533	0.958878±10	0.71754	8.98	47.3	0.1171	0.511193±10	-28.2	3.06	2.91	-3.4
	36.47	169	62.1	7.617	0.933121±10	0.71769	5.00	24.0	0.1287	0.51134±10	-25.3	3.21	3.05	-4.2
	39.14	141	41.1	9.547	0.985244±10	0.71525	3.59	14.4	0.1536	0.511503±10	-22.1	4.12	4.15	-8.8
	43.14	178	54.7	9.095	0.985686±10	0.72845	7.27	35.6	0.1260	0.511313±10	-25.9	3.16	3.00	-3.9
	45.17	180	66.7	7.541	0.976666±10	0.76338	9.14	44.7	0.1262	0.511322±10	-25.7	3.15	2.99	-3.7
ADL														
	80.25	209	90.5	6.434	0.910023±10	0.72806	7.96	42.6	0.1153	0.511098±10	-30.0	3.15	3.00	-4.7
	132.08	58.7	53.4	3.065	0.813528±10	0.72684	13.0	62.0	0.1296	0.511343±10	-25.3	3.24	3.08	-4.4
	142.12	110	27.1	11.35	1.051792±10	0.73071	3.67	18.6	0.1214	0.511251±10	-27.0	3.11	2.95	-3.6
	212.14	138	49.2	7.850	0.956411±10	0.73440	5.20	27.4	0.1170	0.511162±10	-28.8	3.10	2.95	-4.0
	256.87	136	30.9	12.23	1.091456±10	0.74571	5.09	27.3	0.1151	0.511103±10	-30.0	3.13	2.99	-4.5

[a] In-run precision given as 2 standard error in the last decimal places
[b] Calculated with a $\lambda(^{87}Rb)$ of $1.42 \cdot 10^{-11}$ year^{-1} or with a $\lambda(^{147}Sm)$ of $6.54 \cdot 10^{-12}$ year^{-1}, respectively
[c] DM linear evolution model is calcuated from Peucat et al., (1989)
[d] DM polynomial evolution model is calculated from Nägler and Kramers (1998)
[e] CHUR parameters from Bouvier et al., (2008); $^{147}Sm/^{144}Nd = 0.1960$ and $^{143}Nd/^{144}Nd = 0.512630$
[f] DM parameters from Peucat et al., (1989); $^{147}Sm/^{144}Nd = 0.2137$ and $^{143}Nd/^{144}Nd = 0.51315$

3.13 References

Albut, G., Babechuk, M. G., Kleinhanns, I. C., Benger, M., Beukes, N. J., Steinhilber, B., Smith, A. J., Kruger, S. J., & Schoenberg, R. (2018). Modern rather than Mesoarchaean oxidative weathering responsible for the heavy stable Cr isotopic signatures of the 2.95 Ga old Ijzermijn iron formation (South Africa). *Geochimica et Cosmochimica Acta*, *228*, 157-189.

Anbar, A. D., Duan, Y., Lyons, T. W., Arnold, G. L., Kendall, B., Creaser, R. A., Kaufman, A. J., Gordon, G. W., Scott, C., & Garvin, J. (2007). A whiff of oxygen before the great oxidation event? *Science*, *317*(5846), 1903-1906.

Barham, M., Kirkland, C., & Handoko, A. (2022). Understanding ancient tectonic settings through detrital zircon analysis. *Earth and Planetary Science Letters*, *583*, 117425.

Bekker, A., Holland, H., Wang, P.-L., Rumble Iii, D., Stein, H., Hannah, J., Coetzee, L., & Beukes, N. (2004). Dating the rise of atmospheric oxygen. *Nature*, *427*(6970), 117.

Bekker, A., Kaufman, A. J., Karhu, J. A., Beukes, N. J., Swart, Q. D., Coetzee, L. L., & Eriksson, K. A. (2001). Chemostratigraphy of the Paleoproterozoic Duitschland Formation, South Africa: implications for coupled climate change and carbon cycling. *American Journal of Science*, *301*(3), 261-285.

Bekker, A., Krapež, B., & Karhu, J. A. (2020). Correlation of the stratigraphic cover of the Pilbara and Kaapvaal cratons recording the lead up to Paleoproterozoic Icehouse and the GOE. *Earth-Science Reviews*, *211*. https://doi.org/10.1016/j.earscirev.2020.103389

Beukes, N. (1983). Palaeoenvironmental setting of iron-formations in the depositional basin of the Transvaal Supergroup, South Africa. In *Developments in Precambrian Geology* (Vol. 6, pp. 131-198). Elsevier.

Beukes, N. (1986). The Transvaal sequence in Griqualand west. Mineral deposits of southern Africa,

Birch, A. (2016). *Agouron GOE Project*

Blankenship, R. E., & Hartman, H. (1998). The origin and evolution of oxygenic photosynthesis. *Trends in biochemical sciences*, *23*(3), 94-97.

Body, J. (1982, 13-14 Sep. 1982). *Sedimentology applied to exploration mining, engineering and environmental studies* Third Symposium of the sedimentological Division of the Geological Society of South Africa, South Africa.

Brasier, A., Martin, A., Melezhik, V., Prave, A., Condon, D., Fallick, A., & Scientists, F.-D. (2013). Earth's earliest global glaciation? Carbonate geochemistry and geochronology of the Polisarka Sedimentary Formation, Kola Peninsula, Russia. *Precambrian Research*, *235*, 278-294.

Brocks, J. J., Logan, G. A., Buick, R., & Summons, R. E. (1999). Archean molecular fossils and the early rise of eukaryotes. *Science*, *285*(5430), 1033-1036.

Button, A. (1973). *A regional study of the stratigraphy and development of the Transvaal Basin in the eastern and northeastern Transvaal* University of The Witwatersrand, 1973 Library Has Copy On Microfiche.].

Button, A. (1986). The Transvaal sub-basin of the Transvaal Sequence. Mineral deposits of southern Africa,

Cao, H., Huang, Y., Li, G., Zhang, L., Wu, J., Dong, L., Dai, Z., & Lu, L. (2018). Late Triassic sedimentary records in the northern Tethyan Himalaya: Tectonic link with Greater India. *Geoscience Frontiers*, *9*(1), 273-291.

Catling, D. C., Zahnle, K. J., & McKay, C. P. (2001). Biogenic methane, hydrogen escape, and the irreversible oxidation of early Earth. *Science*, *293*(5531), 839-843.

Catuneanu, O., & Eriksson, P. G. (2002). Sequence stratigraphy of the Precambrian Rooihoogte–Timeball Hill rift succession, Transvaal Basin, South Africa. *Sedimentary Geology*, *147*(1-2), 71-88.

Chandler, F. W. (1980). Proterozoic redbed sequences of Canada.

Chen, H.-F., Yeh, P.-Y., Song, S.-R., Hsu, S.-C., Yang, T.-N., Wang, Y., Chi, Z., Lee, T.-Q., Chen, M.-T., Cheng, C.-L., Zou, J., & Chang, Y.-P. (2013). The Ti/Al molar ratio as a new proxy for tracing sediment transportation processes and its application in aeolian events and sea level change in East Asia. *Journal of Asian Earth Sciences*, *73*, 31-38. https://doi.org/10.1016/j.jseaes.2013.04.017

Cheney, E. S., & Winter, H. d. l. R. (1995). The late Archean to Mesoproterozoic major unconformity-bounded units of the Kaapvaal Province of Southern Africa. *Precambrian Research*, *74*(4), 203-223.

Coetzee, L., Beukes, N. J., Gutzmer, J., & Kakegawa, T. (2006). Links of organic carbon cycling and burial to depositional depth gradients and establishment of a snowball Earth at 2.3 Ga. Evidence from the Timeball Hill Formation, Transvaal Supergroup, South Africa. *South African Journal of Geology*, *109*(1-2), 109-122.

Coetzee, L. L. (2001). *Genetic stratigraphy of the Paleoproterozoic Pretoria Group in the western Transvaal* University of Johannesburg, M.Sc. thesis (unpublished), 210 p.].

Eickmann, B., Hofmann, A., Wille, M., Bui, T. H., Wing, B. A., & Schoenberg, R. (2018). Isotopic evidence for oxygenated Mesoarchaean shallow oceans. *Nature Geoscience*, *11*(2), 133-138.

Eriksson, P., Altermann, W., Catuneanu, O., Van der Merwe, R., & Bumby, A. (2001). Major influences on the evolution of the 2.67–2.1 Ga Transvaal basin, Kaapvaal craton. *Sedimentary Geology*, *141*, 205-231.

Eriksson, P., Hattingh, P., & Altermann, W. (1995). An overview of the geology of the Transvaal Sequence and Bushveld Complex, South Africa. *Mineralium Deposita*, *30*, 98-111.

Eriksson, P., Schweitzer, J., Bosch, P., Schereiber, U., Van Deventer, J., & Hatton, C. (1993). The Transvaal sequence: an overview. *Journal of African Earth Sciences (and the Middle East)*, *16*(1-2), 25-51.

Eroglu, S., van Zuilen, M. A., Taubald, H., Drost, K., Wille, M., Swanner, E. D., Beukes, N. J., & Schoenberg, R. (2017). Depth-dependent δ13C trends in platform and slope settings of the Campbellrand-Malmani carbonate platform and possible implications for Early Earth oxygenation. *Precambrian Research*, *302*, 122-139.

Falcón, L. I., Magallón, S., & Castillo, A. (2010). Dating the cyanobacterial ancestor of the chloroplast. *The Multidisciplinary Journal of Microbial Ecology Journal*, *4*(6), 777-783.

Farquhar, J., Bao, H., & Thiemens, M. (2000). Atmospheric influence of Earth's earliest sulfur cycle. *Science*, *289*(5480), 756-758.

Fedo, C. M., Wayne Nesbitt, H., & Young, G. M. (1995). Unraveling the effects of potassium metasomatism in sedimentary rocks and paleosols, with implications for paleoweathering conditions and provenance. *Geology*, *23*(10), 921-924.

Franchi, F. (2018). Petrographic and geochemical characterization of the Lower Transvaal Supergroup stromatolitic dolostones (Kanye Basin, Botswana). *Precambrian Research*, *310*, 93-113.

Franchi, F., & Mapeo, R. B. M. (2019). Evolution of an Archaean intracratonic basin: A review of the Transvaal Supergroup lithostratigraphy in Botswana. *Earth-Science Reviews*, *191*, 273-290.

Gill, R., & Fitton, G. (2022). *Igneous rocks and processes: a practical guide*. John Wiley & Sons.

Gumsley, A. P., Chamberlain, K. R., Bleeker, W., Söderlund, U., de Kock, M. O., Larsson, E. R., & Bekker, A. (2017). Timing and tempo of the Great Oxidation Event. *Proceedings of the National Academy of Sciences*, *114*(8), 1811-1816.

Guo, Q., Strauss, H., Kaufman, A. J., Schröder, S., Gutzmer, J., Wing, B., Baker, M. A., Bekker, A., Jin, Q., & Kim, S.-T. (2009). Reconstructing Earth's surface oxidation across the Archean-Proterozoic transition. *Geology*, *37*(5), 399-402.

Hannah, J. L., Bekker, A., Stein, H. J., Markey, R. J., & Holland, H. D. (2004). Primitive Os and 2316 Ma age for marine shale: implications for Paleoproterozoic glacial events and the rise of atmospheric oxygen. *Earth and Planetary Science Letters*, *225*(1-2), 43-52.

Hartzer, F. J. (2000). Geology of Transvaal inliers in the Bushveld Complex. *Memoir-geological Survey (Pretoria)*.

Hoffman, P. F. (2013). The Great Oxidation and a Siderian snowball Earth: MIF-S based correlation of Paleoproterozoic glacial epochs. *Chemical Geology*, *362*, 143-156.

Holland, H. D. (2002). Volcanic gases, black smokers, and the Great Oxidation Event. *Geochimica et Cosmochimica Acta*, *66*(21), 3811-3826.

Imai, N., TERASHIMA, S., ITOH, S., & ANDO, A. (1995). 1994 compilation of analytical data for minor and trace elements in seventeen GSJ geochemical reference samples,"Igneous rock series". *Geostandards Newsletter*, *19*(2), 135-213.

Izon, G., Luo, G., Uveges, B. T., Beukes, N., Kitajima, K., Ono, S., Valley, J. W., Ma, X., & Summons, R. E. (2022). Bulk and grain-scale minor sulfur isotope data reveal complexities in the dynamics of Earth's oxygenation. *Proceedings of the National Academy of Sciences*, *119*(13), e2025606119.

Jacob, D. J. (1999). Introduction to atmospheric chemistry. In *Introduction to Atmospheric Chemistry*. Princeton University Press.

Kane, J. S. (2004). Report of the international association of geoanalysts on the certification of Penrhyn Slate, OU-6. *Geostandards and Geoanalytical Research*, *28*(1), 53-80.

Kendall, B., Reinhard, C. T., Lyons, T. W., Kaufman, A. J., Poulton, S. W., & Anbar, A. D. (2010). Pervasive oxygenation along late Archaean ocean margins. *Nature Geoscience*, *3*(9), 647-652.

Kump, L. R., & Barley, M. E. (2007). Increased subaerial volcanism and the rise of atmospheric oxygen 2.5 billion years ago. *Nature*, *448*(7157), 1033-1036.

Kurzweil, F., Wille, M., Schoenberg, R., Taubald, H., & Van Kranendonk, M. J. (2015). Continuously increasing δ98Mo values in Neoarchean black shales and iron formations from the Hamersley Basin. *Geochimica et Cosmochimica Acta*, *164*, 523-542.

Lenhardt, N., Eriksson, P. G., Catuneanu, O., & Bumby, A. J. (2012). Nature of and controls on volcanism in the ca. 2.32–2.06 Ga Pretoria Group, Transvaal Supergroup, Kaapvaal craton, South Africa. *Precambrian Research*, *214*, 106-123.

Li, C.-F., Chen, F., & Li, X.-H. (2007). Precise isotopic measurements of sub-nanogram Nd of standard reference material by thermal ionization mass spectrometry using the NdO+ technique. *International Journal of Mass Spectrometry*, *266*(1-3), 34-41. https://doi.org/10.1016/j.ijms.2007.06.013

Luo, G., Ono, S., Beukes, N. J., Wang, D. T., Xie, S., & Summons, R. E. (2016). Rapid oxygenation of Earth's atmosphere 2.33 billion years ago. *Science advances*, *2*(5), e1600134.

Luo, J., Long, X., Bowyer, F. T., Mills, B. J. W., Li, J., Xiong, Y., Zhu, X., Zhang, K., & Poulton, S. W. (2021). Pulsed oxygenation events drove progressive oxygenation of the early Mesoproterozoic ocean. *Earth and Planetary Science Letters*, *559*. https://doi.org/10.1016/j.epsl.2021.116754

Mapeo, R., Armstrong, R., Kampunzu, A. B., Modisi, M., Ramokate, L., & Modie, B. (2006). A ca. 200 Ma hiatus between the Lower and Upper Transvaal Groups of southern Africa: SHRIMP U–Pb detrital zircon evidence from the Segwagwa Group, Botswana: implications for Palaeoproterozoic glaciations. *Earth and Planetary Science Letters*, *244*(1-2), 113-132.

Martini, J. E. J. (1979). A copper-bearing bed in the Pretoria Group in northeastern Transvaal.

McCarthy, T. S., Corner, B., Lombard, H., Beukes, N., Armstrong, R., & Cawthorn, R. G. (2018). The pre-Karoo geology of the southern portion of the Kaapvaal Craton, South Africa. *South African Journal of Geology 2018*, *121*(1), 1-22.

McLennan, S., Hemming, S., McDaniel, D., & Hanson, G. (1993). Geochemical approaches to sedimentation, provenance, and tectonics. *Special Papers-Geological Society of America*, 21-21.

Miyazaki, T., & Shuto, K. (1998). Sr and Nd isotope ratios of twelve GSJ rock reference samples. *Geochemical Journal*, *32*(5), 345-350.

Moore, J. M., Polteau, S., Armstrong, R., Corfu, F., & Tsikos, H. (2012). The age and correlation of the Postmasburg Group, southern Africa: Constraints from detrital zircon grains. *Journal of African Earth Sciences*, *64*, 9-19.

Moore, J. M., Tsikos, H., & Polteau, S. (2001). Deconstructing the Transvaal Supergroup, south Africa: implications for Palaeoproterozoic palaeoclimate models. *Journal of African Earth Sciences*, *33*(3-4), 437-444.

Murali, A., Parthasarathy, R., Mahadevan, T., & Das, M. S. (1983). Trace element characteristics, REE patterns and partition coefficients of zircons from different geological environments—a case study on Indian zircons. *Geochimica et Cosmochimica Acta*, *47*(11), 2047-2052.

Nägler, T. F., & Kramers, J. D. (1998). Nd isotopic evolution of the upper mantle during the Precambrian: models, data and the uncertainty of both. *Precambrian Research*, *91*(3-4), 233-252.

Nesbitt, H., & Young, G. (1982). Early Proterozoic climates and plate motions inferred from major element chemistry of lutites. *Nature*, *299*(5885), 715-717.

Nesbitt, H. W., Fedo, C. M., & Young, G. M. (1997). Quartz and feldspar stability, steady and non-steady-state weathering, and petrogenesis of siliciclastic sands and muds. *The Journal of Geology*, *105*(2), 173-192.

Ngobeli, R. (2019). *A comparison between detrital zircon age populations of the Koegas Subgroup of the Ghaap Group and overlying Makganyene Diamictite of the Postmasburg Group, Transvaal Supergroup, Griqualand West Area.* University of Johannesburg]. https://ujcontent.uj.ac.za/esploro/outputs/graduate/A-comparison-between-detrital-zircon-age/9912005607691?institution=27UOJ_INST

Ossa Ossa, F., Hofmann, A., Wille, M., Spangenberg, J. E., Bekker, A., Poulton, S. W., Eickmann, B., & Schoenberg, R. (2018). Aerobic iron and manganese cycling in a redox-stratified Mesoarchean epicontinental sea. *Earth and Planetary Science Letters*, *500*, 28-40.

Pehrsson, S. J., Berman, R. G., Eglington, B., & Rainbird, R. (2013). Two Neoarchean supercontinents revisited: The case for a Rae family of cratons. *Precambrian Research*, *232*, 27-43.

Peucat, J., Vidal, P., Bernard-Griffiths, J., & Condie, K. (1989). Sr, Nd, and Pb isotopic systematics in the Archean low-to high-grade transition zone of southern India: syn-accretion vs. post-accretion granulites. *The Journal of Geology*, *97*(5), 537-549.

Philippot, P., Ávila, J. N., Killingsworth, B. A., Tessalina, S., Baton, F., Caquineau, T., Muller, E., Pecoits, E., Cartigny, P., & Lalonde, S. V. (2018). Globally asynchronous sulphur isotope signals require re-definition of the Great Oxidation Event. *Nature communications*, *9*(1), Article #: 2245.

Planavsky, N. J., Asael, D., Hofmann, A., Reinhard, C. T., Lalonde, S. V., Knudsen, A., Wang, X., Ossa, F. O., Pecoits, E., & Smith, A. J. (2014). Evidence for oxygenic photosynthesis half a billion years before the Great Oxidation Event. *Nature Geoscience*, *7*(4), 283-286.

Playter, T., Corlett, H., Konhauser, K., Robbins, L., Rohais, S., Crombez, V., Maccormack, K., Rokosh, D., Prenoslo, D., & Furlong, C. M. (2018). Clinoform identification and correlation in fine-grained sediments: a case study using the Triassic Montney Formation. *Sedimentology*, *65*(1), 263-302.

Poulton, S. W., Bekker, A., Cumming, V. M., Zerkle, A. L., Canfield, D. E., & Johnston, D. T. (2021). A 200-million-year delay in permanent atmospheric oxygenation. *Nature*, *592*(7853), 232-236. https://doi.org/10.1038/s41586-021-03393-7

Rasmussen, B., Bekker, A., & Fletcher, I. R. (2013). Correlation of Paleoproterozoic glaciations based on U–Pb zircon ages for tuff beds in the Transvaal and Huronian Supergroups. *Earth and Planetary Science Letters*, *382*, 173-180. https://doi.org/10.1016/j.epsl.2013.08.037

Roscoe, S. (1976). *Huronian rocks and uraniferous conglomerates in the Canadian Shield*.

Rosing, M. T., & Frei, R. (2004). U-rich Archaean sea-floor sediments from Greenland–indications of> 3700 Ma oxygenic photosynthesis. *Earth and Planetary Science Letters*, *217*(3-4), 237-244.

Roué, L., Kurzweil, F., Wille, M., Wegwerth, A., Dellwig, O., Münker, C., & Schoenberg, R. (2021). Stable W and Mo isotopic evidence for increasing redox-potentials from the Paleoarchean towards the Paleoproterozoic deep ocean. *Geochimica et Cosmochimica Acta*, *309*, 366-387.

Schröder, S., Beukes, N. J., & Armstrong, R. A. (2016). Detrital zircon constraints on the tectonostratigraphy of the Paleoproterozoic Pretoria Group, South Africa. *Precambrian Research*, *278*, 362-393.

Scoates, J. S., & Friedman, R. M. (2008). Precise age of the platiniferous Merensky Reef, Bushveld Complex, South Africa, by the U-Pb zircon chemical abrasion ID-TIMS technique. *Economic Geology*, *103*(3), 465-471.

Swart, Q. D. (1999). *Carbonate rocks of the Paleoproterozoic Pretoria and Postmasburg Groups, Transvaal Supergroup* University of Johannesburg].

Taylor, S. R., & McLennan, S. M. (1985). *The continental crust: its composition and evolution*. Blackwell Scientific Publications.

Taylor, S. R., & McLennan, S. M. (1995). The geochemical evolution of the continental crust. *Reviews of geophysics*, *33*(2), 241-265.

Tripathy, G. R., Singh, S. K., & Krishnaswami, S. (2012). Sr and Nd Isotopes as Tracers of Chemical and Physical Erosion. In *Handbook of Environmental Isotope Geochemistry* (pp. 521-552). https://doi.org/10.1007/978-3-642-10637-8_26

Uveges, B. T., Izon, G., Ono, S., Beukes, N. J., & Summons, R. E. (2023). Reconciling discrepant minor sulfur isotope records of the Great Oxidation Event. *Nature communications*, *14*(1), Article #: 279.

Verma, S. P., & Armstrong-Altrin, J. S. (2013). New multi-dimensional diagrams for tectonic discrimination of siliciclastic sediments and their application to Precambrian basins. *Chemical Geology*, *355*, 117-133.

Walter, H., Hegner, E., Diekmann, B., & Kuhn, G. (2000). Provenance and transport of terrigenous sediment in the South Atlantic Ocean and their relations to glacial and interglacial cycles: Nd and Sr isotopic evidence. *Geochimica et Cosmochimica Acta*, *64*(22), 3813-3827.

Warke, M. R., Di Rocco, T., Zerkle, A. L., Lepland, A., Prave, A. R., Martin, A. P., Ueno, Y., Condon, D. J., & Claire, M. W. (2020). The Great Oxidation Event preceded a Paleoproterozoic "snowball Earth". *Proceedings of the National Academy of Sciences*, *117*(24), 13314-13320.

Warke, M. R., & Schröder, S. (2018). Synsedimentary fault control on the deposition of the Duitschland Formation (South Africa): Implications for depositional settings, Paleoproterozoic stratigraphic correlations, and the GOE. *Precambrian Research*, *310*, 348-364.

Wille, M., Kramers, J. D., Nägler, T. F., Beukes, N., Schröder, S., Meisel, T., Lacassie, J., & Voegelin, A. (2007). Evidence for a gradual rise of oxygen between 2.6 and 2.5 Ga from Mo isotopes and Re-PGE signatures in shales. *Geochimica et Cosmochimica Acta*, *71*(10), 2417-2435.

Zeh, A., Wilson, A. H., & Gerdes, A. (2020). Zircon U-Pb-Hf isotope systematics of Transvaal Supergroup – Constraints for the geodynamic evolution of the Kaapvaal Craton and its hinterland between 2.65 and 2.06 Ga. *Precambrian Research*, *345*, doi.org/10.1016/j.precamres.2020.105760. https://doi.org/10.1016/j.precamres.2020.105760

3.14 Supplementary Material

3.14.1 Core Descriptions

ADL (Duitschland Formation): The ADL core is the most proximal of the studied cores (Fig. 2C) and the most heterogeneous in terms of lithology. The lowermost part of the core covers a 24 meters thick interval consisting of interbedded sandstone, shale and dolostone in m-thick beds. With a sharp contact, interpreted as the MDU, it is overlain by 7 meters of conglomeratic sandstone, which forms the base of the upper Duitschland Formation. It is followed by 7 meters of interbedded silt/shale and fine sandstone. Henceforth comes a 4 meters thick fining-upward diamictite with an erosive base, overlain by 20 meters of dark grey shale. The next 20 meters consist of cross-bedded erosive sandstones in m-thick beds, interbedded with shale. This sandstone-dominated package is overlain by another 19 meters of dark grey shale. The next depositional sequence starts with 1m erosive conglomerate and sandstone, followed by 45 meters of laminated shale with siltstone interbeds, before coarsening upwards to a massive sandstone (7m thick) with planar and trough cross-bedding. This is followed by 72 meters of interbedded dark grey shale and siltstone with cm-thick conglomeratic unit in the lower part. Meter- to dm-thick limestone beds become more frequent towards the top of this package. Above follows 5 meters of stromatolitic limestone, overlain by 5 meters of grey shale that transition into 6 meters of banded iron formation. The next unit consists of 20 meters of interbedded shale, siltstone and sandstone. The uppermost 45 meters mainly contain m- and dm-thick stromatolitic limestones interbedded with m-thick grey shale.

ANW (Rooihoogte Formation): The ANW core is ~ 23 meters long and covers the entire Rooihoogte Formation as well as the lower part of the overlying Timeball Hill Formation. Its location is the most distal of the drill cores in this study. The lowermost part of the ANW core is a 13 meters thick diamictite and chert breccia-diamictite/chert breccia, which is followed by 4 meters of well-bedded mudstone. They are overlain by a meter of stromatolitic limestone capped by a thin massive chert layer. Above follows a 6 meters-thick unit of pyrite-rich carbonaceous shale with a 1.5 meters-thick tuff layer on top that potentially marks the conformable transition from the Rooihoogte Formation to the Timeball Hill Formation. The lower Timeball Hill Formation consists of pyritic carbonaceous shale with decreasing pyrite content up section of which the first c. 7 meters are archived in the core.

AGP-1 (Rooihoogte Formation): The AGP-1 core records almost the entire Rooihoogte Formation and is located within the foreland trough, but less proximal than the ADL drill core. At the base, it contains 6m of banded iron stones belonging to the Penge Iron Formation. A 3.5 meters thick chert conglomerate with an erosive base that marks the beginning of the Rooihoogte Formation. It is followed by 58 meters of interbedded shale, siltstone and rare fine sandstones. This unit ends at an erosive surface, which is assumed to represent the MDU. Above follow 6 meters of dm-thick sandstone beds, in turn overlain by a 3.5 meters thick dolostone with stromatolites and grainstone textures. It is overlain by a 1m-thick pyritic carbonaceous shale layer. Next comes a 10 meters thick massive highly altered diabase, which veins upward into the lower part of an 18 meters thick pyritic carbonaceous black shale interbedded with cm-thick graded intervals of siltstone and sandstone. The next unit is a 3m-thick quartzite followed by 3 meters of very pyrite-rich carbonaceous shale and another 1m-thick quartzite. The uppermost 10 meters consist of pyrite- and chert-rich carbonaceous shale, which transitions into a Fe-rich lutite at the top.

AGP-2 (Rooihoogte Formation; distal foreland trough): Drill core AGP-2 shares the location with AGP-1 but covers most of the upper part of the Rooihoogte Formation and the lower part of the Timeball Hill Formation. The lowermost part of the core is a 2.5 meters thick unit of interbedded shale, siltstone, and graded sandstone, sharply overlain by 2 meters of a peloidal and stromatolitic limestone. On top lies a 2 meters thick carbonate-rich shale, which is sharply overlain by 9 meters of highly altered diabase. The core continues with 21 meters of cherty-pyritic carbonaceous shale interbedded with graded silt- and sandstones, cm-thick limestone beds, and capped by half a meter of chert, marking the conformable contact to the Timeball Hill Formation. The upper part of the core consists of two units of carbonaceous shale, 16 and 15 meters thick, respectively, with a 4 meters thick diabase. On the very top lies another diabase with a thickness of 31 meters.

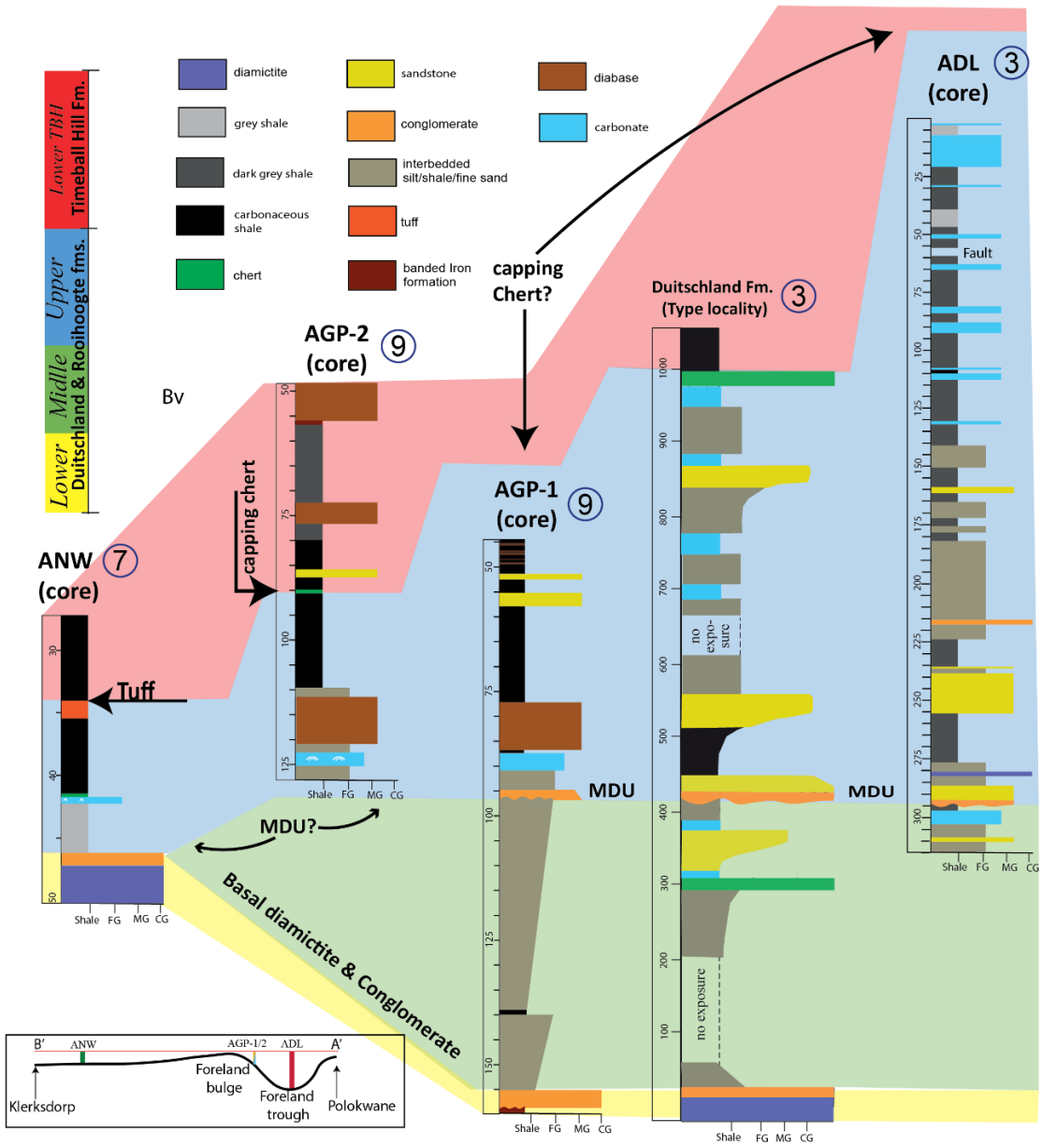

Figure 3.S1. *Stratigraphic correlation of the four geochemically analyzed drill cores.* The Duitschland and Rooihoogte formations are divided into three zones with a yellow (*Lower D/R*), green (*Middle D/R*) and blue (*Upper D/R*) color coding, while the Timeball Hill Formation is shown in red color (*Lower TBH*). The main marker horizons (basal diamictite and conglomerate, MDU, capping chert breccia) are marked between the investigated drill cores in stippled lines, and if **a marker horizon is inferred outside the range of a drill core, it is marked with a question mark.** The stratigraphy of the Duitschland Formation at the type locality (Duitschland Farm) is added for comparison and is modified from Schröder et al. (2016). Note that the large differences in stratigraphic thickness are due to the deposition in a foreland bulge basin. The numbers to the right of each drill core name refer to the geographical position in Fig. 2.

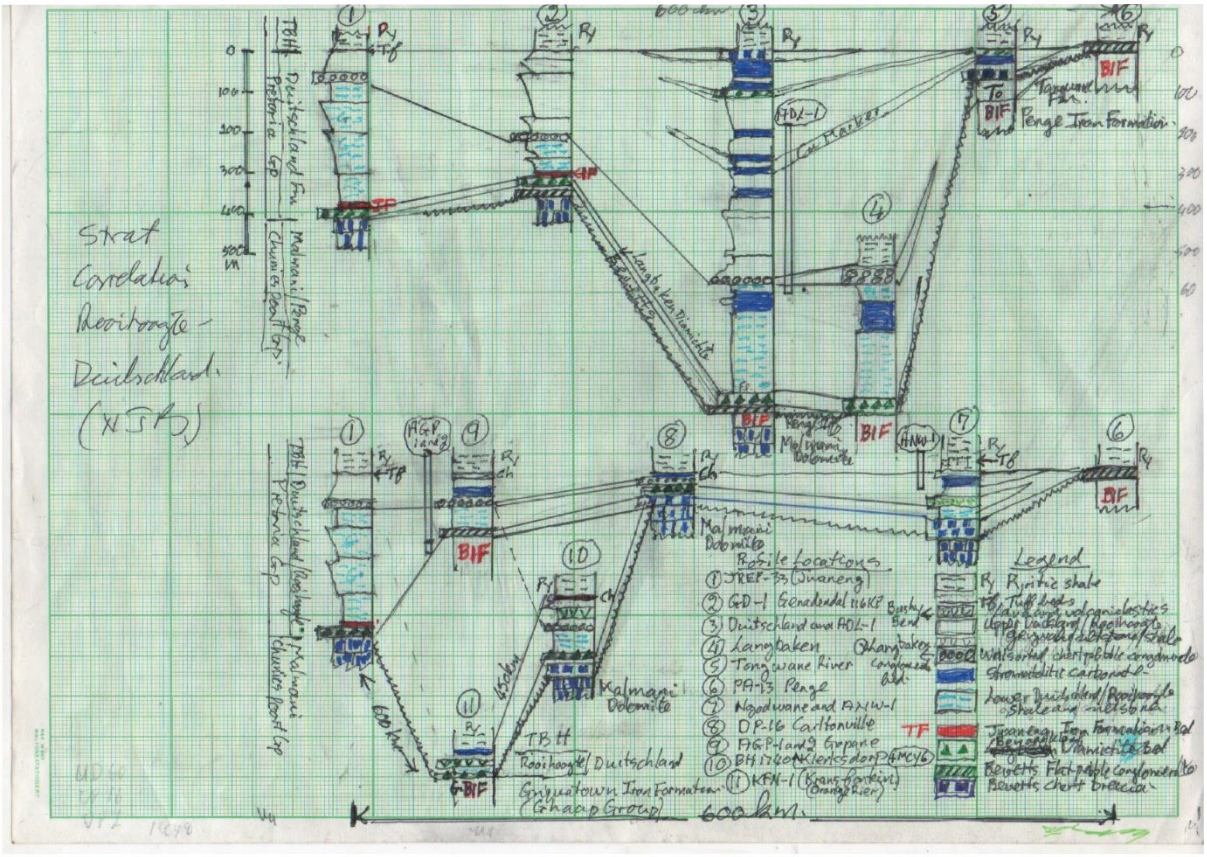

Figure 3.S2. *Initial sketch from Nic Beukes field book correlating the eleven profiles across the Kapvaal Craton* (figure 4 in the manuscript). Nic Beukes tragically passed away before this manuscript was published, but the authors have included this sketch in loving memory of a close friend and colleague and as a tribute to his outstanding skills in field geology.

Table 3.S1A: Comparison of OU-6 vs GeoRem assigned values

Wt. %	OU-6[a]	GeoREM[b]	This study/GeoRem
SiO_2	56.05	57.35	0.98
TiO2	0.98	0.99	0.98
Al_2O_3	20.22	20.45	0.99
Fe_2O_3 (T)	8.75	8.94	0.98
MnO	0.29	0.28	1.04
MgO	2.55	2.41	1.06
CaO	0.72	0.74	0.97
Na_2O	1.88	1.76	1.07
K2O	3.07	3.03	1.01
P_2O_5	0.12	0.12	0.99
LOI	2.88	3.62	0.80
Sum	98.83	101.0	0.98

[a]Preparation: 1 ; Analyses: 1
[b]GeoRem preferred values ; Potts and Kane 2005

Table 3.S1B. Comparison of JB-2 vs GeoRem assigned values

Wt. %	JB-2[a]	Jochum et al. (2016)[b]	This study/GeoRem
SiO_2	51.85	53.14	0.98
TiO2	1.18	1.17	1.01
Al_2O_3	14.34	14.62	0.98
Fe_2O_3 (T)	14.87	14.28	1.04
MnO	0.24	0.21	1.12
MgO	4.80	4.43	1.08
CaO	10.16	9.85	1.03
Na_2O	2.41	2.05	1.17
K2O	0.41	0.42	0.97
P_2O_5	0.10	0.10	1.01
LOI	0.26		
Sum	100.68	100.28	1.00

[a]Preparations: 2; Analyses: 2
[b]GeoRem preferred values ; Jochum et al. (2016)

Table 3.S2A: Comparison of AGV-2 vs the UT longterm avarage and GeoRem values

AGV-2	W-2a calibration value	Average[a] (UT)	± % RSD	UT[b]	This study/UT	GeoReM[c]	This study/ GeoReM
		ng/g		ng/g		ng/g	
Li	9,158	10,671	0.7	10,745	0.99	10,800	0.99
Be	617	2,099	0.7	2,158	0.97	2,209	0.95
Sc	36,074	13,181	2.8	13,000	1.01	13,110	1.01
Ti	6,354,611	6,222,285	3.3	6,333,018	0.98	6,301,000	0.99
V	261,597	114,093	0.9	114,945	0.99	118,500	0.96
Cr	92,791	15,679	1.0	15,787	0.99	16,220	0.97
Co	44,526	15,657	0.7	15,676	1.00	15,460	1.01
Ni	69,993	17,867	0.6	17,981	0.99	18,870	0.95
Cu	103,000	48,397	0.8	49,123	0.99	51,510	0.94
Zn	77,000	87,267	1.1	88,789	0.98	86,700	1.01
Ga	17,424	19,561	0.8	19,813	0.99	20,420	0.96
Rb	19,803	67,026	0.7	67,171	1.00	67,790	0.99
Sr	194,828	648,259	1.8	658,828	0.98	659,500	0.98
Y	20,113	18,268	0.7	18,382	0.99	19,140	0.95
Zr	87,866	226,300	1.1	224,683	1.01	232,000	0.98
Nb	7,275	13,944	0.9	14,015	0.99	14,120	0.99
Mo	423	1,976	1.0	1,980	1.00	2,000	0.99
Cd	77	121	7.3	118	1.03	184	0.66
Sn	1,950	2,244	10.1	2,241	1.00	1,830	1.23
Sb	800	513	9.2	475	1.08	458	1.12
Cs	888	1,151	0.2	1,147	1.00	1,173	0.98
Ba	169,680	1,129,884	1.9	1,150,793	0.98	1,134,000	1.00
La	10,521	37,632	0.8	37,276	1.01	38,210	0.98
Ce	23,216	68,878	2.1	69,715	0.99	69,430	0.99
Pr	3,025	8,222	0.4	8,153	1.01	8,165	1.01
Nd	12,911	30,345	0.3	30,133	1.01	30,490	1.00
Sm	3,266	5,481	0.3	5,458	1.00	5,509	0.99
Eu	1,094	1,517	0.4	1,501	1.01	1,553	0.98
Tb	615	623	0.4	628	0.99	4,678	0.13
Gd	3,708	4,530	1.0	4,493	1.01	651	6.96
Dy	3,808	3,441	0.3	3,427	1.00	3,549	0.97
Ho	803	678	0.4	673	1.01	682	0.99
Er	2,222	1,799	0.3	1,806	1.00	1,825	0.99
Tm	327	260	0.5	262	0.99	262	0.99

Table continued on next page

AGV-2	W-2a calibration value	Average[a] (UT)	± % RSD	UT[b]	This study/UT	GeoReM[c]	This study/ GeoReM
		ng/g		ng/g		ng/g	
Yb	2,058	1,620	0.5	1,626	1.00	1,653	0.98
Lu	301	245	0.2	245	1.00	251	0.98
Hf	2,356	5,025	1.3	5,003	1.00	5,137	0.98
Ta	454	834	0.4	830	1.00	865	0.96
W	260	534	20.9	471	1.13	553	0.97
Tl	94	272	1.3	274	0.99	275	0.99
Pb	7,528	12,806	2.1	12,651	1.01	13,140	0.97
Th	2,104	5,984	1.8	6,010	1.00	6,174	0.97
U	505	1,902	1.6	1,887	1.01	1,885	1.01

[a]Digestions: 5 ; Analyses: 5
[b]n UT = University of Tuebingen long term average ; n= 219
[c]GeoRem preferred values ; Jochum et al. (2016)

Table 3.S2B. Comparison of Ou-6 vs the UT longterm avarage and GeoRem values

OU-6	W-2a calibration values	Average[a]	± % RSD	UT[b]	This study/UT	GeoReM[c]	This study/ GeoReM
		ng/g		ng/g		ng/g	
Li	9,158	103,417	1.96	102,626	1.01		
Be	617	2,508	1.98	2,511	1.00		
Sc	36,074	25,425	2.34	24,729	1.03	22,790	1.12
Ti	6,354,611	6,255,114	3.43	6,169,705	1.01		
V	261,597	127,413	2.53	124,319	1.02	125,700	1.01
Cr	92,791	75,051	2.46	73,214	1.03	70,020	1.07
Co	44,526	29,990	2.24	29,236	1.03	28,560	1.05
Ni	69,993	40,407	2.31	39,502	1.02	39,920	1.01
Cu	103,000	44,301	8.83	44,005	1.01	44,620	0.99
Zn	77,000	112,956	2.02	111,173	1.02		
Ga	17,424	24,287	2.22	23,842	1.02	24,570	0.99
Rb	19,803	125,911	2.44	124,740	1.01	120,700	1.04
Sr	194,828	136,588	2.23	133,823	1.02	132,900	1.03
Y	20,113	26,940	2.45	26,631	1.01		
Zr	87,866	143,698	8.76	150,621	0.95		
Nb	7,275	15,570	2.36	15,263	1.02	14,620	1.07
Mo	423	668	21.48	529	1.26		
Cd	77	68	4.49	65	1.04		

Table continued on next page

OU-6	W-2a calibration values	Average[a]	± % RSD	UT[b]	This study/UT	GeoReM[c]	This study/ GeoReM
		ng/g		ng/g		ng/g	
Sn	1,950	2,720	13.44	2,705	1.01	2,525	1.08
Sb	800	613	8.36	590	1.04		
Cs	888	8,478	2.35	8,334	1.02	8,092	1.05
Ba	169,680	499,142	2.12	488,567	1.02	480,700	1.04
La	10,521	35,084	2.32	34,097	1.03	33,840	1.04
Ce	23,216	82,814	2.56	81,600	1.01	78,530	1.05
Pr	3,025	8,600	2.37	8,369	1.03	8,097	1.06
Nd	12,911	31,876	2.45	31,080	1.03	30,400	1.05
Sm	3,266	6,312	2.61	6,165	1.02	6,091	1.04
Eu	1,094	1,408	2.96	1,366	1.03	1,409	1.00
Tb	615	865	2.44	851	1.02	870	0.99
Gd	3,708	5,530	2.57	5,386	1.03	5,550	1.00
Dy	3,808	5,178	2.48	5,064	1.02	5,110	1.01
Ho	803	1,078	2.31	1,054	1.02	1,028	1.05
Er	2,222	3,046	2.44	3,036	1.00	2,989	1.02
Tm	327	468	2.65	470	1.00	451	1.04
Yb	2,058	3,061	2.64	3,062	1.00	3,011	1.02
Lu	301	458	3.33	461	0.99	461	0.99
Hf	2,356	3,949	7.36	4,167	0.95	4,762	0.83
Ta	454	1,000	2.41	975	1.03	991	1.01
W	260	1,616	16.57	1,312	1.23	1,313	1.23
Tl	94	577	4.59	558	1.03	506	1.14
Pb	7,528	28,498	2.16	27,748	1.03	28,210	1.01
Th	2,104	11,418	3.34	11,259	1.01	11,560	0.99
U	505	1,991	3.69	1,973	1.01	1,973	1.01

[a]Digestions: 5 ; Analyses: 5
[b]UT = University of Tuebingen long term average; n = 128
[c]GeoRem preferred values ; Kane (2004)

Chapter 4

Atmospheric Oxygenation at the Onset of Earth's Great Oxidation Forced Enhanced Marine Anoxia

4.1 Abstract

Capturing the loss of mass-independent sulphur isotope fractionation (MIF-S), the correlative South African Duitschland and Rooihoogte formations are widely held to bear the isotopic fingerprint of the first atmospheric oxygenation at the onset of the so-called Great Oxidation Event (GOE). Surprisingly, however, while the multiple sulphur isotope systematics of these formations remain central to our understanding of the GOE, until now, comparatively little work has been done to elucidate the repercussions within the marine realm. Here we present chemostratigraphic records from four drill cores covering a large area of the Transvaal Basin, transcending these crucial units and continuing into the overlying Timeball Hill Formation, that document the immediate, yet counterintuitive, marine response to atmospheric oxygenation. Specifically, irrespective of the interpretative framework employed, our basin-wide redox-sensitive trace element data document an environmental change from oxic/suboxic conditions within the lower and middle parts of the Duitschland and Rooihoogte formations to suboxic/anoxic conditions within their upper reaches. Interestingly, in concert with a ~35 ‰ negative $\delta^{34}S$ excursion that implicates increased sulphate availability and bacterial sulphate reduction, $\delta^{98/95}Mo_{3134+0.25}$ values increase by ~1.0 to 1.5 ‰. Combining these observations with increased Fe/Mn ratios, elevated total sulphur and carbon contents and a trend towards lower $\delta^{13}C_{org}$ values imply a shift toward less oxygenated conditions across the Transvaal Basin. The combined observations in the mentioned parameters expose a geobiological feedback-driven causality between the earliest oxygenation of the atmosphere and decreased redox potentials of medium to deep marine environments, at least within the Transvaal Basin.

4.2 Introduction

Treated as a biosignature in the search for life, free molecular oxygen is typically considered a prerequisite to sustain widespread eukaryotic life (Nursall, 1959). Nevertheless, despite oxygen comprising 21% of Earth's contemporary atmosphere, this life-sustaining gas was

conspicuously absent for half of our planet's existence. In its broadest sense, the oxygenation of Earth's atmosphere occurred via two key steps around the transition from the Archaean to the Palaeoproterozoic, commonly referred to as Great Oxidation Event (GOE) (e.g., Holland, 2002, 2006) and again at the end of the Neoproterozoic, known as Neoproterozoic Oxidation Event (NOE) (e.g., Och & Shields-Zhou, 2012). The oxygenation of the Earth most probably originated as a consequence of the evolution of oxygenic phototrophs and perturbations in the oxygen source-sink balance of the planet (Brocks et al., 1999; Catling et al., 2001; Holland, 2002; Kump & Barley, 2007). Interestingly, signs of marine oxygenation occur much earlier than atmospheric oxygenation with heavy stable isotope systems (e.g., Fe, Cr, Mo, U, Tl) and redox-sensitive trace element systematics disclosing small to medium scale marine oxygenation in so-called 'oxygen oases' up to several hundred million years prior to the GOE (Albut et al., 2019; Brocks et al., 1999; Duan et al., 2010; Eickmann et al., 2018; Eroglu et al., 2017; Falcón et al., 2010; Kurzweil et al., 2015; Ossa Ossa et al., 2018; Ostrander, Nielsen, et al., 2019; Planavsky et al., 2014; Rosing & Frei, 2004; Roué et al., 2021; Wille et al., 2007). A key indicator for atmospheric O_2 evolution is the transition from mass-independent fractionation of sulphur isotopes (MIF-S) to mass-dependent fractionation of sulphur isotopes (MDF-S), which occurs once pO_2 concentrations reach a threshold value of 10^{-5}–10^{-6} of the present atmospheric levels (PAL) (Farquhar et al., 2000; Zahnle et al., 2006). This is currently best constrained to have occurred for the first time between ~2.45 Ga and 2.32 Ga in the global geological record (Philippot et al., 2018; Warke et al., 2020), but a deeper understanding of improved stratigraphic correlations and more absolute age constraints within sedimentary basins and between cratons are still needed. Two fundamental formations in this respect are the stratigraphically correlative Duitschland and Rooihoogte formations of the Transvaal Supergroup (South Africa), which both record some of the most prominent and abrupt MIF-S to MDF-S transitions in the global geological record (Guo et al., 2009; Izon et al., 2022; Luo et al., 2016; Poulton et al., 2021). Thus, these two formations have been studied intensively in order to understand atmospheric oxygen dynamics during the early stages of the GOE. However, the contemporary marine realm has received comparatively less attention during these two formations' deposition. Hence, we measured a series of geochemical environmental tracers, including total sulphur (TS) and organic matter (TOC) concentrations as well as trace element data, and stable isotope redox proxies (Mo, U, V, $\delta^{34}S$, $\delta^{98/95}Mo_{3134+0.25}$, Fe^{3+}/Fe_{tot}) on four drill cores intersecting the Duitschland and Rooihoogte formations. Hereby, we aim to improve the current knowledge of the temporal redox evolution in the marine ecosystem at this

critical junction in Earth's history and understand the interaction between atmospheric and marine redox change during the onset of the GOE.

4.3 Geological Setting

4.3.1 Overview

The Transvaal Supergroup, (South Africa), is preserved within two main structural basins—the Griqualand West Area (GWA) and the Transvaal Area (TA)—covering an area of about 500,000 km^2 (Beukes, 1987; Beukes et al., 2002; Coetzee, 2001). Representing remnants of a single marine basin that once covered the entire Kaapvaal Craton, the GWA and TA capture principally slope- and platform-type sedimentation, respectively. The TA features three unconformity-bound sedimentary packages (Fig. 4.1) that start with the predominantly siliciclastic Wolkeberg Group (Beukes, 1987; Sumner & Beukes, 2006), overlain by transgressive–regressive chemical sedimentation of the Chuniespoort Group (Beukes, 1984; Beukes, 1987; Sumner & Beukes, 2006) that, itself, yields to the largely siliciclastic Pretoria Group (Coetzee, 2001; Eriksson & Botha, 1988; Schröder et al., 2016). In the GWA, the Schmidtsdrift Subgroup and Ghaap Group represent respective equivalents of the Wolkberg and Chuniespoort groups of the TA (Beukes, 1984; Beukes, 1987). The Postmasburg Group (GWA) has no preserved correlative in the TA and consists of various lithologies, ranging from glacial diamictite, volcanic rocks and chemical precipitates in ascending order. It is unconformably deposited on the Ghaap Group (GWA) and chronostratigraphically appears before the Pretoria Group (TA) (Gumsley et al., 2017; Moore et al., 2012) (Fig. 4.1).

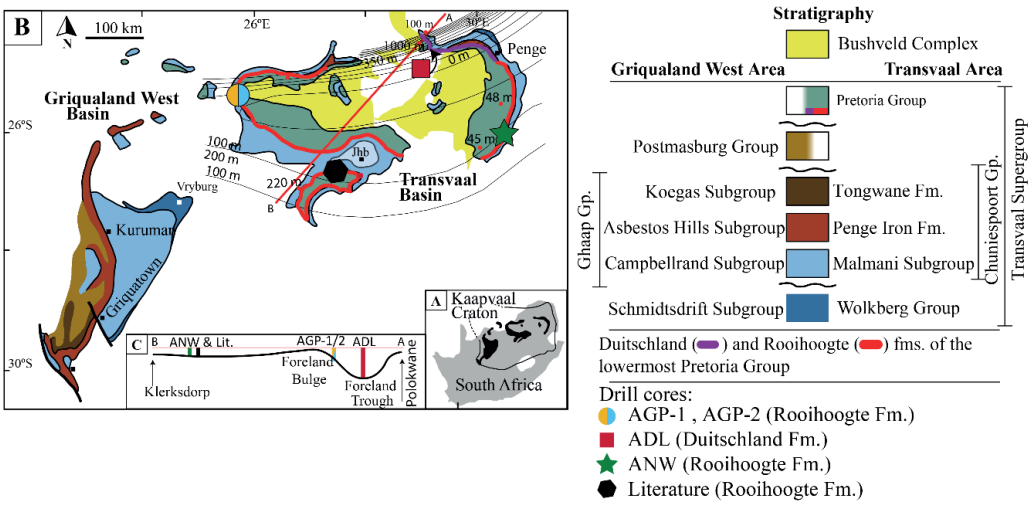

Figure 4.1. *Simplified geological map and bathymetric cross-section locating the studied cores (AGP-1, AGP-2, ADL and ANW) within the Transvaal Supergroup*. The isopach lines are

modified from Coetzee (2001) and denote the approximate thickness of the strata in the Duitschland and Rooihoogte formations. The black hexagon signals the Carletonville area where the demise of S-MIF has been captured within the Rooihoogte Formation in several continuous core expressions (EBA-1, EBA-2, EBA-4, KEA-4; Luo et al., 2016; Poulton et al., 2021; Izon et al., 2022; Uveges et al., 2023). Johannesburg is abbreviated Jhb.

4.3.2 The Duitschland and Rooihoogte Formations

The Duitschland and Rooihoogte formations mark the onset of the Pretoria Group within the TA, consisting of two lobes that are referred to as the eastern (ETA) and western (WTA) Transvaal areas that are separated by the Bushveld Igneous Complex (Fig. 4.1). The Duitschland formation is geographically limited to the northernmost part of the eastern lobe. In contrast, the Rooihoogte Formation spans the remainder of the eastern and western lobes (Fig. 4.1). Despite having different lithostratigraphic names, we consider the Duitschland and Rooihoogte formations to be different environmental expressions of the same sedimentary formation deposited at different distances to the Palaeo-shoreline, based on arguments lined out in Havsteen et al. (2023). The strongest argument for stratigraphic equivalence between the Duitschland and Rooihoogte formations is their remarkably consistent internal stratigraphy, which is generally traceable throughout the entire Transvaal Basin. Specifically, both formations entail a basal conglomerate and diamictite, a mid-formational unconformity and a capping chert breccia that is locally karstified. Additionally, there are no discernable differences in the major and trace element compositions, U–Pb distribution patterns of detrital zircon, or radiogenic Sr–Nd-Hf isotope compositions of materials from the two formations (Coetzee, 2001; Schröder et al., 2016; Zeh et al., 2020; Havsteen et al., 2023). However, we note that other researchers regard each formation as a distinct sedimentary package, placing the Duitschland Formation depositionally before the Rooihoogte Formation (Bekker, 2015; Gumsley et al., 2017; Moore et al., 2012; Poulton et al., 2021; Senger et al., 2023). This view especially arises from not regarding the uppermost chert contact as a locally karstified surface, but rather as an erosional contact between the Duitschland and the Timeball Hill formations and a sharp conformable contact between the Rooihoogte and the Timeball Hill formations (Gumsley et al., 2017). Furthermore, an ongoing debate surrounds the interpretation of the maximum depositional age of the Duitschland Formation inferred from U-Pb dating of detrital zircons, as opposed to the well-constrained and undisputed depositional age at the transition between the uppermost Rooihoogte Formation and lowermost Timeball Hill Formation of 2316 ± 7 Ma by Re-Os dating of black shales (Hannah et al., 2004). Zeh et al.

(2020) originally interpreted the maximum depositional age of the Duitschland Formation to be 2342 ± 18 Ma, based on the U-Pb date of the youngest, singular detrital zircon of their data set, and thus similar to the age of the Rooihoogte Formation. However, Senger et al. (2023) reinterpreted the maximum depositional age of the Duitschland Formation to be 2427 ± 18 Ma based on the youngest reproducible zircon cluster from the data set of Zeh et al. (2020), and thus placing the Duitschland Formation to be significantly older than the Rooihoogte Formation.

Both formations are composed of argillite, arenite and interbedded conglomerate with subordinate chert and carbonate beds, sharply overlain by the pyritic black shales of the lower Timeball Hill Formation (Coetzee, 2001). The Duitschland and Rooihoogte formations can be divided into three intervals (Coetzee, 2001; Havsteen et al., 2023; Warke & Schröder, 2018): (1) the *lower D/R* interval, represented by a basal glacial diamictite and a chert pebble conglomerate (sometimes breccia) known as the Bevets conglomerate; (2) the *middle D/R* interval consisting of two upward coarsening deltaic sequences terminated by the mid-Duitschland unconformity (MDU), and (3) the *upper D/R* interval, comprising interbedded argillites and carbonates that overall represents a shallowing of the system. Above lies the deep water pyrite-rich black shales of the lower Timeball Hill Formation (*lower TBH* Fm.), commonly with a chert layer marking the transition.

4.4 Materials and Methods

4.4.1 Sample Selection

This study leverages samples from four scientific drill cores obtained during the *CIMERA-Agouron GOE and Biomarker Drilling Project*. All major and trace element analyses, detailed core descriptions, and sample positions are reported in Havsteen et al. (2023), while this work only provides a condensed summary of the core descriptions. The Rooihoogte Formation is captured in three cores, two obtained near Gopane (AGP-1 and AGP-2; 25°17.359S, 25°44.493E) and the remainder near Ngodwana (ANW; 25°36.239S, 30°37.002E). Except for the transition to the Timeball Hill Formation, AGP-1 captures almost the entire Rooihoogte Formation, while AGP-2 transects the upper Rooihoogte Formation and the lower Timeball Hill Formation. The ANW core transects the upper Rooihoogte Formation and lower Timeball Hill Formation, while the Duitschland Formation is represented within the ADL core, obtained near the Duitschland Farm KS95 type-area (24°17.268S, 29°07.491E) in the northeastern ETA. The ADL drill core intersects the upper part of the middle Duitschland and most of the upper interval

of the Duitschland Formation. Fine-grained siliciclastic lithologies (shale–silt) were targeted for sampling, taking care to avoid veining and secondary mineralisation.

4.4.2 Molybdenum Isotope Measurements

Depending on the samples Mo contents, between 100 and 300 mg of powdered sample were weighed into Savillex PFA beakers along with an appropriate amount of a ^{97}Mo-^{100}Mo double-spike tracer to achieve the desired 1:1 sample–spike ratio. A 2:5 mixture of 28M HF and 14M HNO_3 was added to the sample powders, and sample digestion and spike equilibration were achieved via closed vessel heating atop a hot plate at 100 °C for three days with intermittent treatments in an ultrasonic bath. After overnight drying at 80 °C, the fluoride complexes that formed during the initial digestion step were dissolved by a three-day reflux with 2 mL of 6M HCl at 120 °C, leaving a clear, residue-free digestate. Finally, after dissolution in 2 mL 3M HCl, molybdenum was purified via the one-step anion exchange chromatographic protocol described in Willbold et al. (2016), using 7mL columns filled with 2 mL of Eichrom AG1-X8 (100–200 mesh) resin.

Molybdenum isotope measurements were made using the ThermoFisher© Scientific NeptunePlus multi-collector inductively coupled plasma mass spectrometer (MC-ICP-MS) housed within the Isotope Geochemistry Group at the University of Tuebingen, Germany. Purified Mo was introduced to the MC-ICP-MS as 25 ppb solutions in 0.3M HNO_3 via a CETAC Aridus II™ desolvating nebuliser system. Static measurements comprising 90 cycles with 4.2 second cycle integration times were performed in low-resolution mode. Collectors were arranged so that potential isobaric interferences from Ru could be monitored via the ^{99}Ru ion beam, allowing hypothetical correction to the ^{98}Mo and ^{100}Mo signals. All samples, standards and procedural blanks were bracketed by measurements of the carrier solution 0.3M HNO_3, allowing on-peak-zero background subtraction. Double spike deconvolution was performed assuming compliance with exponential mass fractionation law, effectively correcting for any mass-dependent fractionation induced through purification and analysis (Rudge et al., 2009).

All data are reported in δ-notation relative to the international reference material, NIST-SRM-3134 (NIST 3134; Eq. 1), and expressed in per mille by multiplication with a factor of 1000.

$$\delta^{98/95}Mo_{3134} = \left(\frac{^{98}Mo/^{95}Mo_{sample}}{^{98}Mo/^{95}Mo_{3134}} - 1\right) \times 1000 \quad (1)$$

To facilitate comparison to earlier studies that leveraged a Johnson Matthey (JM) Bern standard, however, a 0.25 ‰ offset was applied to compensate for the isotopic differences between the JM-Bern standard and NIST SRM3134 reference material (Nägler et al., 2014) as employed for example by Craig (1957) for O isotopes and, and also recently applied for Zn isotopes by Rosca et al. (2021).

$$\delta^{98/95}Mo_{3134+\,0.25} = 1.00025 \times \delta^{98/95}Mo_{3134} + 0.25 \quad (2)$$

Inclusive of unknowns, duplicates, reference materials and blanks, a total of 96 Mo isotope measurements were made over four analytical sessions. Throughout the study, the NIST-3134 and the JM-Bern standard solution yielded respective average $\delta^{98/95}Mo_{3134}$ values of 0.000 ± 0.044 ‰ (2SD, n = 58) and -0.277 ± 0.051 ‰ (2SDσ, n = 43), in accordance with published values (Goldberg et al., 2013; Greber et al., 2012; Kurzweil et al., 2016; Ossa Ossa et al., 2018) and, indeed, the Tuebingen lab long-term offset ($\Delta^{98}Mo_{(JM\text{-}NIST\ 3134)}$ = -0.274 ± 0.056 ‰ (2SD, n = 223). In Table 4.1–4.4, we report both $\delta^{98/95}Mo_{3134}$ and $\delta^{98/95}Mo_{3134+0.25}$ values, but we use $\delta^{98/95}Mo_{3134+0.25}$ values in all figures and the text, as suggested by Nägler et al. (2014). Repeated processing of the reference material, JB-2 (Geological Survey of Japan), yielded an average $\delta^{98/95}Mo_{3134+0.25}$ value of 0.279 ± 0.059 ‰ (2SD; n = 6, digests = 4), which is indistinguishable from the compiled reported average (0.298 ± 0.033 ‰ (2SD, n=51) (Casalini et al., 2019; Chen et al., 2019; Freymuth et al., 2015; Villalobos-Orchard et al., 2020; Willbold et al., 2016; Zhao et al., 2016) and the long-term in-house average (0.284 ± 0.046 ‰, 2SD, n = 34). Total procedural Mo blanks were below 0.5 ng, with one outlier at 2.7 ng. However, when compared to $\delta^{98/95}Mo_{3134+0.25}$ of duplicate digests of the same samples measured in different batches, the values were identical (Table 4.4), and thus no isotopic blank correction was performed.

4.4.3 Sulphur Isotope Analysis

Following the protocol outlined in Izon et al. (2022), major sulphur isotope data were generated by fluorination within the Geobiology Laboratory at the Massachusetts Institute of Technology, USA. Briefly, aliquots of powdered sample were boiled with acidified ethanoic chromous chloride, allowing their sulphide-sulphur inventories to be captured as zinc sulphide. Dropwise addition of silver sulphide then displaced zinc, leaving silver sulphide precipitates that were washed and captured. Thereafter, 3 mg aliquots of dry silver sulphide were converted to sulphur hexafluoride (SF_6) via overnight reaction at 300 °C with fluorine gas. Finally, the analyte was cryogenically separated from residual F_2 and impurities before preparative-gas-chromatography, which ultimately yielded pure SF_6 for mass spectrometric analysis.

Monitoring SF^{5+} ion beams at mass/charge ratios (m/z) of 127 and 129, $^{34}S/^{32}S$ isotope ratios of samples were expressed in conventional delta-notation (i.e., $\delta^{34}S$) relative to the international reference standard, Vienna Canyon Diablo Troilite (VCDT).

4.4.4 Iron Speciation

Following the Pratt Method (Maxwell, 1968), the proportion of ferrous to ferric iron in selected samples from the AGP-1 drill core was determined via rapid acid digestion and subsequent colorimetric redox-titration. Depending on iron content, two doublets of sample powder of either 150–200 or 200–250 mg were digested for 12 min at 170 °C in a mixture of 27.5 M HF (5 mL), 18.0 M H_2SO_4 (5 mL) and water (5 mL) in a teflon liner. The samples were then immediately transferred to an Erlenmeyer flask containing 50 mL of previously boiled and still warm milli-Q18.2 MΩ · cm H_2O, 30 mL of saturated H_3BO_3 solution and 6 mL of 14.6 M H_3PO_4 and diluted with a further ~140 mL of warm 18.2 MΩ · cm H_2O, and titrated directly against a $KMnO_4$ solution.

Calibration of 0.1 M $KMnO_4$ against 0.1 M oxalic acid was performed daily and used for the titration. Each measurement session was initiated with two blank measurements, followed by four rock reference materials (BIR-1a and OU-6) before sample measurements were instigated. In the rare instance where the FeO content of the duplicate digestions deviated by more than 0.5 wt.%, an additional measurement was performed. Processed alongside our unknowns, replicate analyses of USGS BIR-1a yielded a mean FeO content of 8.75 ± 0.61 wt.% (1SD; n = 16), in agreement with published estimates (Babechuk et al., 2019; Saikkonen & Rautiainen, 1993; Schuessler et al., 2008); Likewise, OU-6 (IAG) was processed 24 times, returning a mean FeO content of 1.87 ± 0.23 (1SD), inseparable from its assigned value (1.65 ± 0.019 wt.%; Kane (2004)).

4.4.5 Carbon, Nitrogen, and Sulphur Content

Total carbon, nitrogen, and sulphur concentrations were determined by flash combustion using the Elementar VARIO EL III analyzer within the Soil Science and Geomorphology Group, University of Tuebingen, Germany. Approximately 40 mg of sample was wrapped into tin foil capsules and analysed using oxidative heat combustion at 1150 °C with tungsten trioxide as a catalyst. Triplicates of the organic-rich reference material, OAS IVA 33802150, were measured every 30 samples to test accuracy and precision of the method. The long-term (n>2000) internal relative standard deviations (1rsd) are 1.3%, 2.5% and 2.4% for total carbon,

nitrogen and sulphur determinations, respectively. These numbers are adapted as an estimate of method precision.

4.4.6 Organic Carbon Content and Isotopic Composition

Carbonate-carbon was removed from 20 mg aliquots of powdered samples via multiple treatments with 5% HCl. The residues were washed with 18.2 MΩ cm H_2O and dried at 60 °C for subsequent mass spectrometric analyses. Dependent on their carbon contents, 0.05–1.3 mg of decarbonated residue was wrapped in Sn-foil and loaded into the autosampler of a Carlo-Erba (NC 2500) elemental analyzer interfaced with a Finnigan Delta Plus XL isotope ratio mass spectrometer. Samples were combusted at 1050 °C in an oxygen stream and the combustible component was swept through the oxidation–reduction furnace, and the resultant CO_2 was ultimately cleaned by gas chromatography before admittance into the isotope ratio mass spectrometer (IRMS). The sample CO_2 is measured and evaluated relative to an internal laboratory tank gas standard calibrated against internal and international standards (Acetanilide). All $\delta^{13}C_{org}$ values are given in permille relative to Vienna Pee Dee Belemnite (VPDB), and the external precision calculated over 10 to 15 standards is typically in the range of 0.1 ‰.

4.5 Results

4.5.1 Authigenic Enrichment of Redox-Sensitive Trace Elements

The authigenic components of the samples' redox-sensitive trace elements (RSTE) molybdenum, uranium and vanadium were determined by correcting their detrital background with two different methods. The first method (model 1; Algeo & Tribovillard, 2009) corrects for any detrital background components by normalising to aluminium (Al), under the assumption that all Al is detrital and the siliciclastic portion of the sediments resembles the composition of the Post Archaean Average Shale (PAAS) (Taylor & McLennan, 1985). By using modern restricted basins as analogues, covariations in U and Mo enrichment factors were subsequently utilized to differentiate marine redox environments in the geological record (Fig. 4.2). Enrichment factors (EF) for U and Mo were calculated according to equation 3.

$$X_{EF} = \frac{(X/Al)_{sample}}{(X/Al)_{PAAS}} \quad (3)$$

Where Al and X are the weight concentration of Al in wt.% and element 'X' in µg/g in the sample and the selected normalisation material. Most samples from all drill cores plot within the suboxic field, with a few samples extending towards an anoxic or particulate shuttling

environment (Fig. 4.2). It is important to note that some samples fall below 1 in Mo and/or U enrichment factors and can thus not be distinguished from detrital background levels.

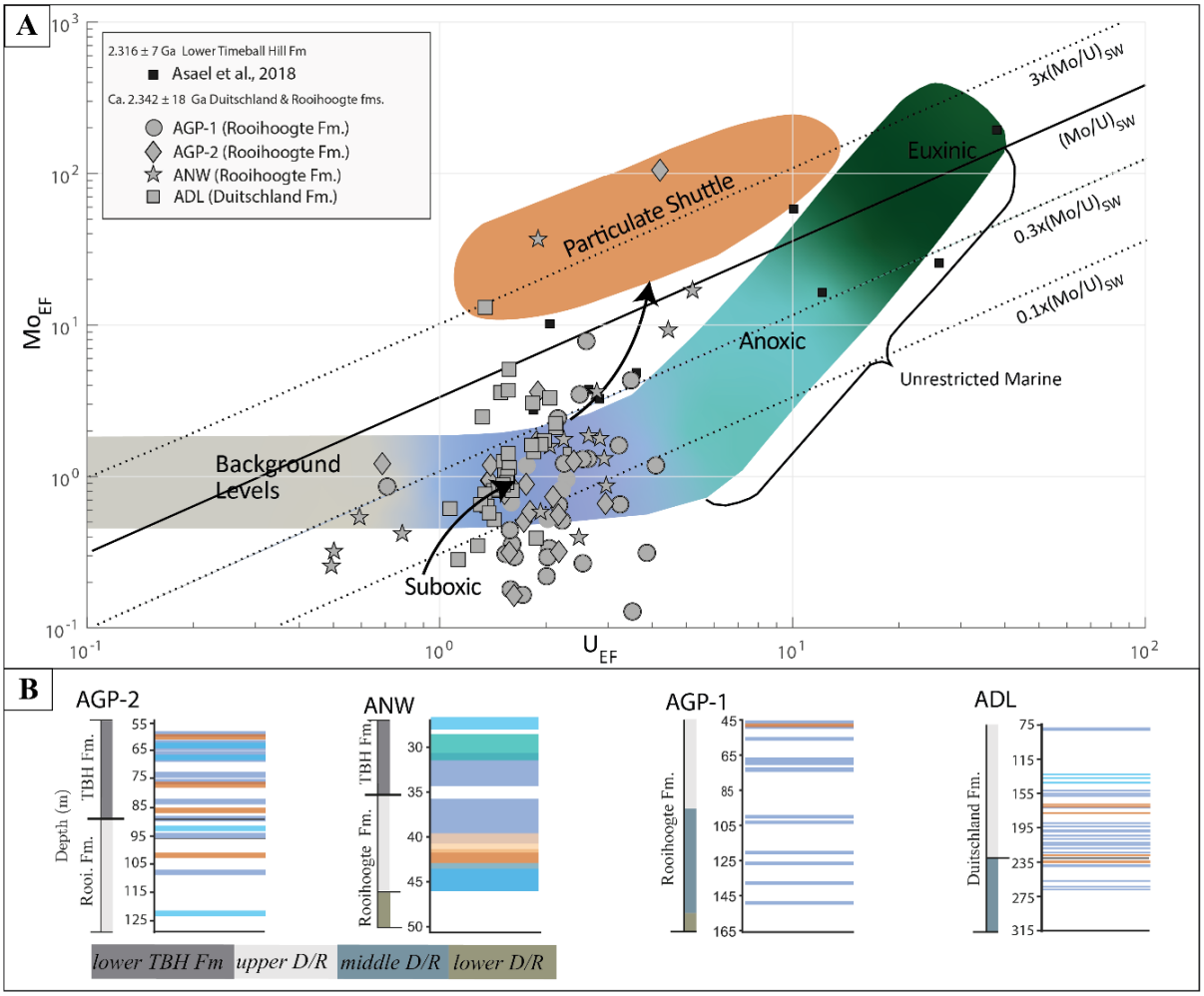

Figure 4.2. *Molybdenum and uranium covariation within the lower Pretoria Group.* Within panel **A**, data are expressed as enrichment factors (Eq. 3), allowing empirically detected redox regimes to be identified (Algeo and Tribovillard, 2009). Here, shape separates the data by core, while the present-day molar Mo/U ratio of seawater $(Mo/U)_{SW}$, and associated scale are illustrated as solid and dashed lines, respectively. For reference, published data from the Timeball Hill Formation (EBA-2; Asael et al., 2018) are included as black squares. The inferred redox setting is visualized in a stratigraphic context **(B)**. Centering each sample ± 0.5 meters of strata, however, leaves the apparent coverage as a function of core length.

The second method (model 2; Bennett & Canfield, 2020) used to determine the authigenic enrichment of redox-sensitive trace elements is avoiding normalisation to a crustal average (e.g., PAAS or UCC), which may not be a good representative for the particular terrigenous input source and speed of the Transvaal sediments. Instead, this model uses receiver operating characteristic curve analysis to quantitively determine enrichment factor thresholds, allowing differentiation between various marine settings with equal weight on minimising false positives and negatives (Bennett & Canfield, 2020). Enrichments are calculated using equation 4.

$$X_E = \left(\frac{X\ (\mu g/g)}{Al\ (wt.\%)}\right) \quad (4)$$

Where X_E is the enrichment of element X (V, Mo, Re, U) and Al and X are the concentration of Al and element X in the sample. The threshold values between different redox settings are defined in Bennett and Canfield (2020). Most samples from all cores plot in the oxic field regardless of tracer system used (V/Al vs. U/Al or V/Al vs. Mo/Al; Fig. 4.3). However, some samples plot in the 'beneath perennial-oxygen minimum zone' (beneath P-OMZ), indicative of oxic bottom waters. This is especially true for samples from AGP-1 and ANW drill cores.

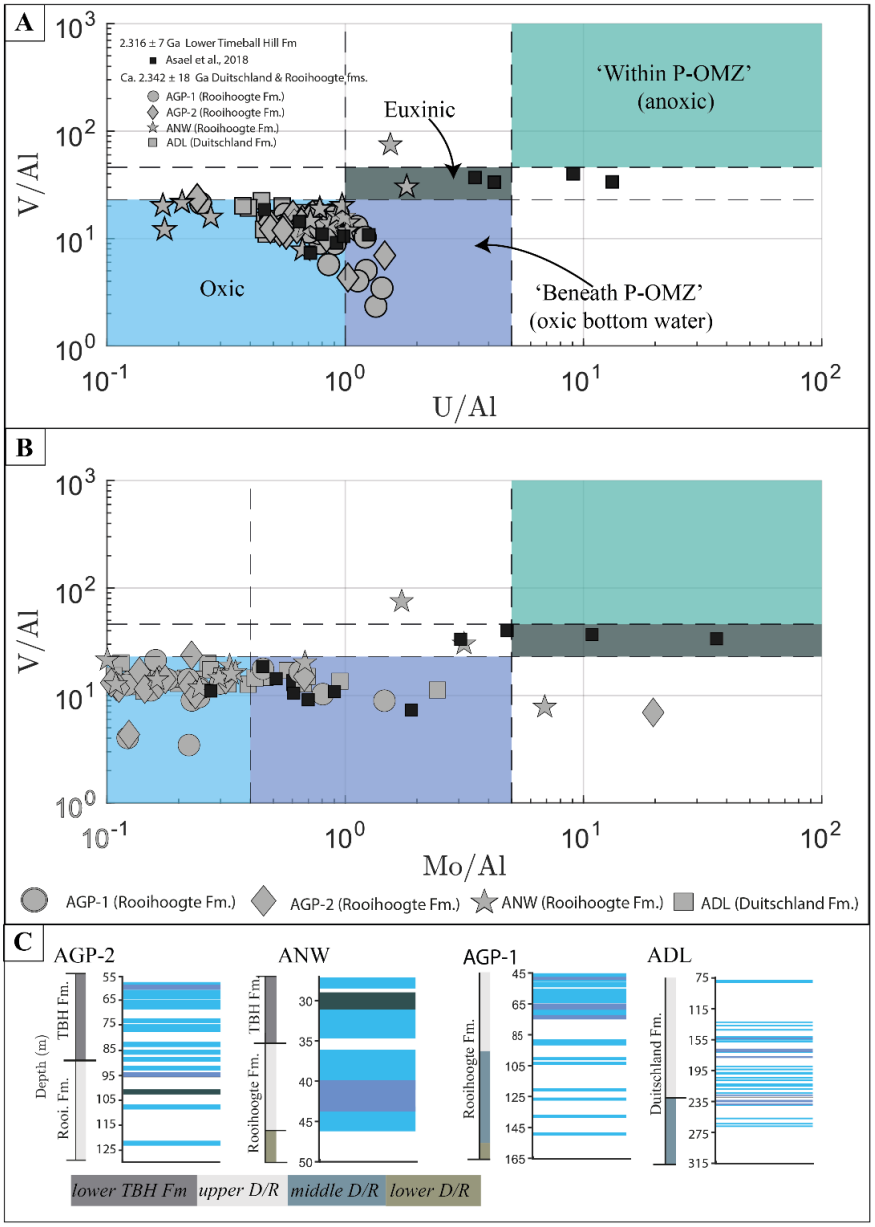

Figure 4.3. *Aluminum-normalised V, U and Mo systematics of the lower Pretoria Group.* New data are augmented with published data from the Timeball Hill Formation (EBA-2; Asael et al., 2018), using shape to separate between cores. In V/Al vs. U/Al **(A)** and V/Al vs. Mo/Al-space **(B)**, contemporary observations have been used to delineate fields that typify deposition within oxic and euxinic basins, as well as beneath perennial oxygen minimum zones (OMZ) with differing basal water oxygen regimes (Bennett and Canfield, 2020). These inferences are transposed stratigraphically in panel C, where each data point encompasses ±0.5 meters of strata from the data point.

4.5.2 Stratigraphic Trends

The entire Duitschland and Rooihoogte succession extending into the lowermost Timeball Hill Formation is only captured by combination of drill cores AGP-1 and -2 (Fig. 4.4A). The m*iddle D/R* and *upper D/R* intervals display decreasing trends in $\delta^{34}S$ and $\delta^{13}C$ from approximately +15 ‰ to -20 ‰ and approximately -30‰ to -35‰, respectively (AGP-1, 151 to 48 m; Fig. 4.4A, columns 2 and 6). In concert with this isotopic decrease, sulphur contents rise from levels typically below the limit of detection (LOD) to concentrations as high as 0.6 wt.% in the *upper D/R* interval. Likewise, TOC shows stable values with an average of 0.59 wt. % in the *lower D/R* interval (AGP-1, 151 to 105 m) that increases to as much as 5.9 wt.% in the *upper D/R* interval (AGP-1, 92 to 70 m; Fig. 4.4A, column 5). Over the same stratigraphic section, $\delta^{98/95}Mo_{3134+0.25}$ values also increase from -0.657 ‰ to as much as 1.072 ‰, while Fe/Mn ratios overall gradually increase throughout the *upper D/R* interval (AGP-1, 92 to 47 m; Fig. 4.4A, columns 1 and 3). The transition from the *upper D/R* interval into the *lower TBH* Formation (AGP-2, 102 to 82 m) records low and stable $\delta^{34}S$ and $\delta^{13}C$ values around -23 ‰ and -37 ‰, respectively (Fig. 4.4A, columns 2 and 6). Over the same stratigraphic section, TS and TOC values stabilise, with average concentrations of 0.370 wt.% and 1.507 wt.%, respectively, while Fe/Mn ratios steadily increase (AGP-2, 95 to 83 m) before stabilising around 77 meters and upwards (Fig. 4.4A, columns 3, 4 and 5). From 108–83 m in AGP-2, $\delta^{98/95}Mo_{3134+0.25}$ values display a generally negative trend from 0.788 to approximately -0.057 ‰ before embarking on an oscillatory trend between 83 and 59 meters.

The trends observed in cores ANW (Fig. 4.4B) and ADL (Fig. 4.4C) show good agreement with those derived from the complete succession captured by the AGP cores. This is most evident in ANW, which records the transition from the *upper D/R* interval into the *lower TBH* Formation. Like the AGP drill cores, the ANW captures a decrease in $\delta^{34}S$ and $\delta^{13}C$ values that manifest as respective approximately 30 ‰ and 35 ‰ negative excursions within the *upper D/R* interval (ANW, 49 to 37 m) before stabilising in the *lower TBH* Formation (Fig. 4.4B, columns 2 and 6). This isotopic decrease corresponds with an increase in TS and TOC, with values rising abruptly at 41 m in the *upper D/R* interval, accompanied by a steady increase in Fe/Mn ratios and increasing $\delta^{98/95}Mo_{3134+0.25}$ values from -0.727 to 0.672 ‰ at the stratigraphic level from approximately 43 to 38 (Fig. 4.4B, columns 1 and 3). In the upper part of the *upper D/R* interval (ANW, 38 to 32 m), TS, Fe/Mn ratios and $\delta^{98/95}Mo_{3134+0.25}$ values steadily decrease to 0.156 wt.%, 20 and 0.089 ‰, respectively, while $\delta^{34}S$, $\delta^{13}C$ and TOC stay relatively constant with means of -34.9 ‰, -23.3 ‰ and 5.3 wt.% (Fig. 4.4B, columns 1 through 6). In the *lower*

TBH Formation, $\delta^{98/95}Mo_{3134+0.25}$ values gradually become more positive, peaking at 0.740 ‰ at 30 m core depth before decreasing to -0.352 ‰ in the topmost sample (Fig. 4.4B, column 1). $\delta^{34}S$ and $\delta^{13}C$ values are low and stable throughout the *lower TBH* Formation with average values of -22.2 ‰ and -35.4 ‰, respectively, while Fe/Mn and TS increase from 35 and 0.434 wt.% to 67 and 0.677 wt.%, (Fig. 4.4B, columns 2, 3, 4 and 6). TOC shows an oscillatory trajectory, starting at 5 wt.% in the *upper D/R* interval and lowermost *TBH* Formation (ANW, 36 to 33 m), whereafter values drop to 1.5 wt.% (31 m) and shortly after peaking at 7.7 wt.% at 29 meters core depth, (Fig. 4.4B, column 5).

The ADL drill core almost solely records the *upper D/R* interval till below the Timeball Hill Formation. $\delta^{34}S$ values are relatively stable between 0 and 10 ‰ with a slightly increasing trend in a parabolic fashion between 270 to 109 meters core depth, while $\delta^{13}C$ values oscillate between -31 and -23 ‰ over the same interval (Fig. 4.4C, columns 2 and 6). Both TS and TOC show low and stable values in the *upper D/R* interval (ADL, 267 to 78 m) with average concentrations of 0.1708 (LOD values omitted, see Table 4.4) and 0.085 wt.%, respectively, while Fe/Mn have an average of 85 and show no particular trend, (Fig. 4.4C, column 3, 4 and 5 and 6). The $\delta^{98/95}Mo_{3134+0.25}$ compositions gradually decrease from 0.393 to -0.088 ‰ between 270 to 109 m, with the lowest value (-0.794 ‰) at 80 meters core depth (Fig. 4.4C, column 1).

An important feature between the drill cores is the trends observed in Fe/Mn ratios, which increase with stratigraphic height in the AGP-1, AGP-2 and ANW drill cores but with subtle differences in the relative increase (Fig. 4.4A-B, column 3). The Fe/Mn ratios range from 30 to 200 (AGP-1), 25 to 230 (AGP-2) and 20 to 60 (ANW), while no particular trend is observed in the ADL drill, which ranges in values from 80 to 240 (ADL), (Fig. 4.4C, column 3). Additionally, the AGP-1 drill core has two outliers of 300 (AGP-1 48.14 m) and 578 (AGP-1 47.66 m) (Fig. 4.4A, column 3). It is important to note that the same trend is observed in the drill cores throughout the basin in the *upper D/R* interval and that the increasing Mn/Fe ratios seem to reflect an increasing iron content with stratigraphic height while Mn displays consistently low and stable concentrations. The exceptions are the lower part of the *upper D/R* interval in the ANW drill core (45 to 43 m) and the upper part of the *middle D/R* and lowermost *upper D/R* intervals in the AGP-1 drill core (105 to 86 m) (Fig. 4.4A-B, column 3). Concerning the interval in the ANW drill core (back bulge), MnO concentrations display a mean of 0.22 wt.% (n=4), which is significantly higher than background levels (PAAS = 0.06 wt.%; UCC = 0.08 wt.%), (Fig. 4.4B, column 3). For the AGP-1 drill core, the lower part of the *middle D/R* interval (151 to 122 m) MnO

concentrations display a low average of 0.08 (n = 4), which is similar to the UCC and PAAS, whereas the upper part of the *middle D/R* interval (105 to 92 m) display MnO content above average crustal concentrations with a mean MnO content of 0. 0.15 wt.% (n = 5), (Fig. 4.4A, column 3).

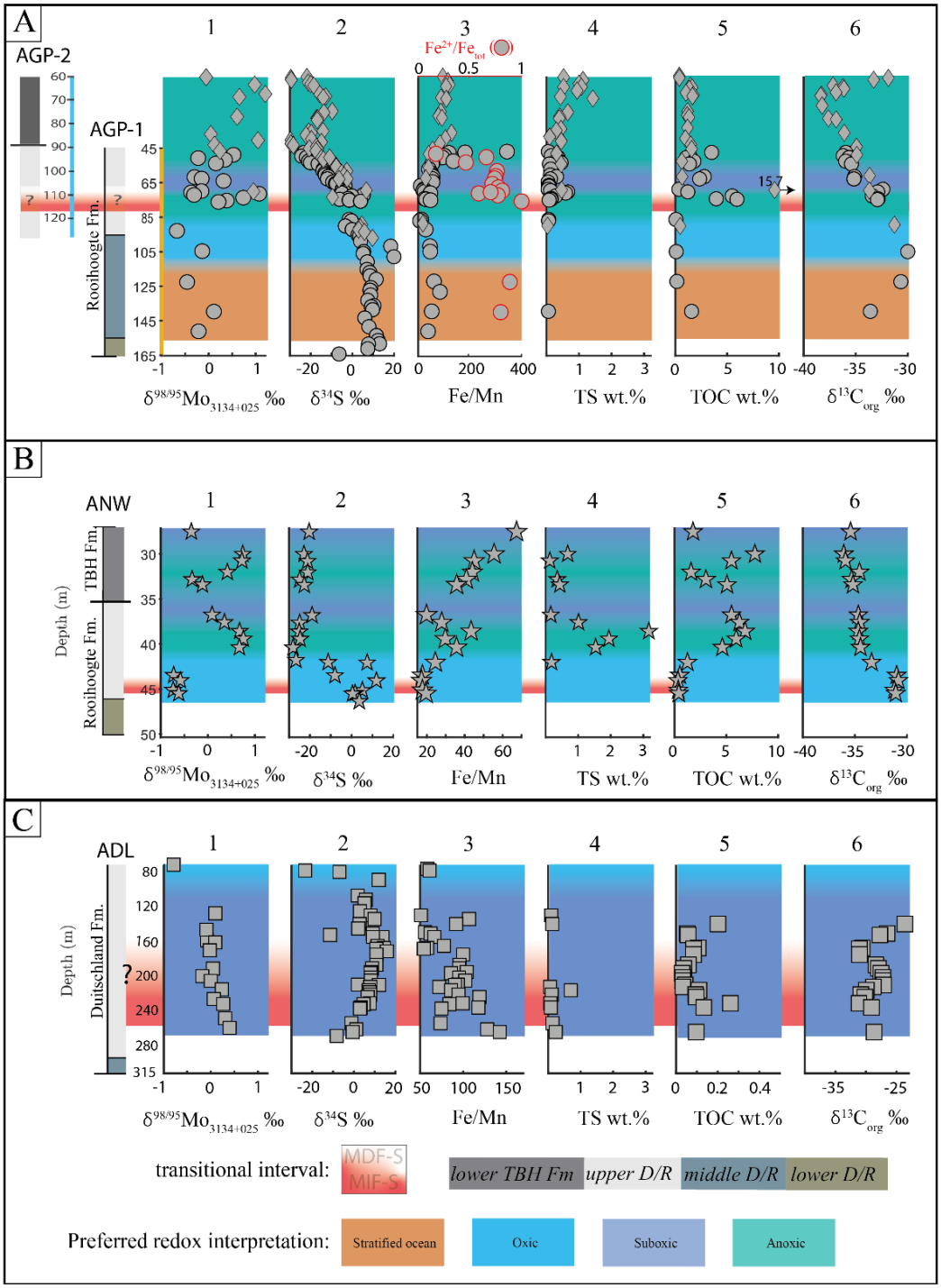

Figure 4.4. *Isotopic and elemental data from the lower Pretoria Group examined in cores AGP-1 and -2* ***(A)****, ANW* ***(B)*** *and ADL* ***(C)***. The colored boxes represent the inferred redox

condition at a given stratigraphic level based on the combined redox information extracted from all measured parameters. The approximate loss of MIF-S is positioned by recalling the documented loss of MIF-S within several cores from the Carletonville area (Poulton et al., 2021; Izon et al., 2022; Uveges et al., 2023) and available data from the Duitschland area (Guo et al., 2009).

4.6 Discussion

4.6.1 Sedimentological Considerations for the Interpretation of Geochemical Redox Signals

Starting with the most distal core, ANW, the transition to the Timeball Hill Formation is not marked by a change in grain size; rather, the transition is recorded as a change from grey to black shale. This might suggest that the observed redox change is not predominantly sea-level controlled, although sea-level shifts in mudstones can, at times, manifest as solely compositional changes without significant alteration in grain size (Dinelli et al., 2007). Similarly, the ANW core captures a change in redox at 43–40 meters core depth, which is also not accompanied by a change in grain size (Fig. 4.4B). In the AGP-1 (*middle* – and *upper D/R* intervals), a coarsening-upwards regressive system tract (RST) is succeeded by several minor TSS. However, the change in redox parameters registered in the lower to middle part of the *upper D/R* interval (AGP-1, 75–100m) post-dates the MDU by several meters of strata (Fig. 4.4A). Thus, the observed changes in geochemical redox proxies seem to predominantly reflect redox changes in the basin that are not controlled by relative sea level change.

4.6.2 Integrated Assessment of the Marine Redox State

Given that trace element cycling was likely significantly different during the Palaeoproterozoic (Anbar, 2008; Da Silva & Williams, 2001; Robbins et al., 2016), direct transfer of proxies from modern ocean settings should be applied carefully to the ancient sedimentary rock record. Additionally, knowing that post-depositional diagenetic effects, microbial activity and hydrothermal activity all have the potential to perturb the elemental and isotopic budgets of ancient records, these processes must also be considered carefully (Johnson et al., 2013; Morford et al., 2005). To avoid these pitfalls, herein, we cross-calibrated and validated our RSTE-based inferences with additional well-established environmental and redox-sensitive proxies ($\delta^{98/95}Mo_{3134+0.25}$, Fe/Mn, $\delta^{34}S$, TS, TOC, $\delta^{13}C_{org}$). While we concede that these proxies

are also affected by post-depositional effects, combining several independent redox proxies with differing sensitivities to alteration helps to identify compromised data and to fortify our inferences.

Both RSTE models are in broad agreement, although subtle differences are apparent. Principally suboxic conditions were identified by *model 1* (Fig. 4.2) with transient shifts toward anoxic and oxic deposition, as well as intervals influenced by Mn-shuttling. *Model 2* (Fig. 4.3), however, fingerprints a predominantly oxygenated depositional setting with the episodic development of euxinic conditions or intervals reminiscent of those that resemble deposition beneath P-OMZ. Comparatively, *model 1* exposes relatively few instances of fully oxygenated conditions (e.g., ANW, 45–43 m; AGP-1, oscillatory above 70 m). Against a modern oxygenated environment, deposition 'beneath P-OMZ' (*model 2)* identifies a setting with oxygenated bottom waters. In a Palaeoproterozoic context, with lower elemental seawater inventories, we adopt a more conservative 'suboxic' category for these samples. Some sections classified as 'oxic' in *model 2* are considered 'particulate influenced' in *model 1*. In reality, both categories indicate significant amounts of O_2 in the water column, with particulate shuttling inferring a stratified water column where Mo is shuttled across the chemocline in association with soluble Fe-Mn(oxyhydrogen)oxides (Algeo & Tribovillard, 2009; Kurzweil et al., 2021; Kurzweil et al., 2022; Smrzka et al., 2019). Thus, areas identified as those influenced by 'shuttle processes' in *model 1* and 'oxic' in *model 2* both point to the presence of significant amounts of oxygen in the water column.

The most significant discrepancies in Palaeoenvironmental reconstruction are between the layers classified as 'particulate shuttle influenced' in *model 1* and 'euxinic' in *model 2* (i.e., ANW, 29.77–30.55 m). Here, $\delta^{98/95}Mo_{3134+0.25}$ values evolve from -0.335 to 0.741 ‰, which is inconsistent with particulate shuttling because of the lack of the significant negative fractionation that accompanies this process between MoO_4^{2-} in seawater and precipitated Fe-Mn-(hydro)oxides (Barling & Anbar, 2004; Wasylenki et al., 2008). A similar conclusion is reached concerning the discrepancy seen at ~41–44 m (ANW), where *model 1* indicates particulate shuttling while *model 2* identifies deposition within a suboxic/anoxic oxygen minimum zone (OMZ). In this interval, $\delta^{98/95}Mo_{3134+0.25}$ values increase from -0.728 to 0.754 ‰, again providing strong evidence against the operation of Mn-shuttling. Instead, the positive shifts in $\delta^{98/95}Mo_{3134+0.25}$ compositions rather fit with an environmental transition from oxic to suboxic/anoxic conditions as indicated by *model 2.* In sediments deposited in anoxic to mildly

oxygenated bottom waters (O_2< 10 µM), capable of reducing both Mn-oxides and sulphate, there are two main drivers controlling the $\delta^{98/95}Mo_{3134+0.25}$ composition of the sediments. Firstly, the relative amount of Fe vs Mn drawdown with (oxyhydr)oxides and secondly, the aqueous H_2S concentration of the sediment pore and bottom waters (Goldberg et al., 2009; Poulson et al., 2009). Under ferruginous conditions, a larger proportion of Mo adsorbs onto Fe- rather than Mn-(oxyhydr)oxides, reducing the isotopic offset between Mo in seawater and the authigenic particles in the sediments. That is due to the smaller isotopic fractionation between the solid and solution ($\Delta^{98}Mo$) for Fe-(oxyhydr)oxides and seawater (e.g., $\Delta^{98}Mo_{solution\text{-}ferrihydrite}$ = ~1.11 ± 0.15 ‰; Goldberg et al. (2009)), relative to Mn-(oxyhydr)oxides and seawater of $\Delta^{98}Mo_{solution–MnOx}$ = ~2.4 to 2.9 ± 0.1 ‰ (Barling & Anbar, 2004; Wasylenki et al., 2008). Similarly, in sediments deposited under high H_2S porewater conditions (but not sulfidic; H_2S > 11 µM), the Mo isotopic offset between seawater molybdate (MoO_4^{2-}) and sediment tetrathiomolybdate (MoS_4^{2-}) is controlled by incomplete transformation of intermediate thiomolybdate species (e.g., MoO_3S^{2-}, $MoO_2S_2^{2-}$, $MoOS_3^{2-}$). Accumulatively viewed incomplete thiolation induces a moderate offset from seawater of approximately -0.6 to -1.00 ‰ in $\delta^{98/95}Mo_{3134+0.25}$ (Kendall et al., 2017), although the fractionation associated with a specific thiolation step may be significant (Kerl et al., 2017; Nägler et al., 2011). The development of ferruginous water conditions and/or H_2S-rich pore or bottom waters could hence independently or collectively, lower the isotopic offset between authigenic Mo and its isotopically heavier seawater precursor. Evidence for the development of such conditions at ~41–44 and ~**29–30 m** core depth in the ANW is indicated by increasing Fe/Mn ratios and decreasing $\delta^{34}S$ compositions coupled with high TS concentrations, respectively. Consequently, the observed shift in $\delta^{98/95}Mo_{3134+0.25}$ is likely a combination of these environmental conditions. Furthermore, genuinely euxinic conditions (anoxic and sulfidic) probably only developed for short periods, as indicated by the intervals with high TS concentrations and increasing $\delta^{98/95}Mo_{3134+0.25}$ compositions (e.g., ANW (40–43 m)). Assimilated, the water column within the Transvaal Basin during the deposition of the upper Duitschland and Rooihoogte formations and lower Timeball Hill Formation was, to a large extent, oxygen-poor (sub- to anoxic). and Fe-rich (Mn-poor). This interpretation is reinforced by literature $\delta^{98/95}Mo_{3134+0.25}$ values and Fe_{HR}/Fe_T data from core EBA-2 that reveals an oscillating and largely anoxic background with isolated instances of euxinia (Asael et al., 2018).

Within the lower part of the *middle D/R* interval (122–151 m), the relatively low $\delta^{98/95}Mo_{3134+0.25}$ values seen in core AGP-1 coupled with moderate Mo enrichments and MnO contents that approximate those seen in UCC and PAAS, fingerprint particulate shuttling where reductive Mn dissolution supplies Mo oxygen-poor bottom waters where it can be fixed within the sediments. In contrast, the lower part of the upper Rooihoogte Formation in cores AGP-1 (86–105 m) ANW (42–45 m) features up to two-fold MnO enrichments when compared to PAAS, implying the preservation of Mn oxides to at least some extent, and thus molecular oxygen within the water column (Fig. 4.5). This inference is supported by low $\delta^{98/95}Mo_{3134+0.25}$ values (-0.738 to -0.123 ‰), generally non-detectable sulphur contents and low TOC (approximately 0.4 wt.%; Fig. 4.5, Table. 4.1).

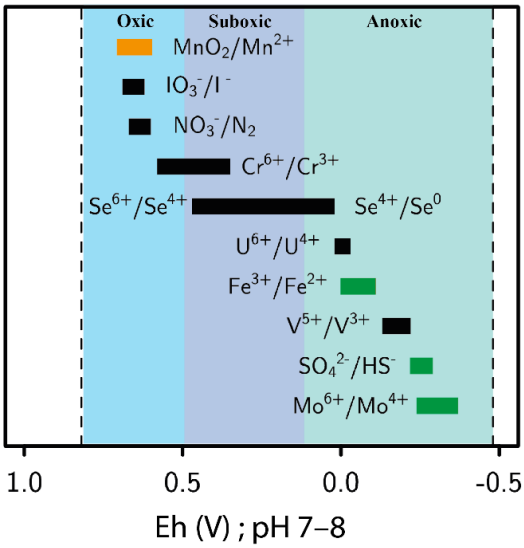

Figure 4.5. *Redox potentials (Eh) of commonly used paleoenvironmental redox couples after Kipp et al. (2020).* Green coloration signals a change observed throughout, while orange indicates changes only observed over restricted stratigraphic intervals. Black bars denote unused redox couples that are included as a reference.

In summary, the marine oxygenation state likely evolved from a stratified ocean in the lower reaches of the *middle D/R* interval into a fully oxygenated ocean in the upper part of the interval and the overlying lowermost segment of the *upper D/R* interval. In the middle and upper reaches of the *upper D/R* interval, however, the marine oxygenation state transitioned into a suboxic to anoxic state, with the episodic development of euxinia. This marine oxygenation state, predominantly in the suboxic to anoxic realm, stabilised and continued during the deposition of the lower Timeball Hill Formation.

4.6.3 Linking Atmospheric Oxygenation to Marine Deoxygenation

Comparison of the CIMERA-Agouron GOE drill cores (Havsteen et al., 2023) with several drill cores that capture the loss of MIF-S (EBA-2, EBA-4 and KEA-4 drill cores) within the Rooihoogte Formation (Izon et al., 2022; Luo et al., 2016) and outcrop samples from the Duitschland Formation (Guo et al., 2009), suggest that the shift towards less oxygenated marine conditions is causally linked to atmospheric oxygenation. Importantly, this argument is valid regardless of whether our preferred correlation of the Duitschland and Rooihoogte formations is adapted or not. The pronounced shift toward negative $\delta^{34}S$ values seen in the Carletonville area (EBA-2, EBA-4 and KEA drill cores) in the immediate aftermath of the initial demise of MIF-S provides a convenient chemostratigraphic marker to examine our data.

While it is important to note that the *upper D/R* interval captures a basinal deepening (Coetzee, 2001; Havsteen et al., 2023), it is clear that the redox shift post-dates the mid-formational unconformity several meters of strata above the sedimentological transition from the *middle D/R* to the *upper D/R* interval. Moreover, sea level high stands are usually associated with negative $\delta^{98/95}Mo_{3134+0.25}$ values as such episodes typically expose more sediments in the basin to H_2S poor conditions (Ostrander, Sahoo, et al., 2019). Thus, this rather counterintuitive trend of marine deoxygenation in response to atmospheric oxygenation, is best explained by geobiological feedbacks. A slightly oxygenated atmosphere, as expressed by the loss of MIF-S, drives oxidative weathering on the continents and elevates nutrient input to the oceans, resulting in increased primary productivity and increased oxygen demand within the deep waters (Fig. 4.6). The conceptualisation of this idea has been suggested by Canfield (1998), but is geochemically rarely demonstrated as clearly and rapidly after the initial loss of MIF-S, as documented in this study. Especially the initiation of microbial sulphate reduction, as illustrated by the low $\delta^{34}S$ of approximately -25 ‰, highlights the connection between the build-up of sulphate levels (expressed as an increase in TS) in the marine realm and terrestrial pyrite oxidation. The negative $\delta^{34}S$ values (approximately -25 ‰) succeeding the loss of MIF-S strengthens this interpretation of increasing marine sulphate concentrations far above 200 µM, since marine sulphate reducers usually produce a low isotopic offset of less than 5 ‰ when sulphate concentrations are less than 200 µM (Habicht & Canfield, 2001). This threshold value for sulphate concentrations is much higher than the inferred sulphate concentration of approximately 2.5 µM in the Archaean ocean (Crowe et al., 2014), and thus only a minute offset between sulphate and sulphide is expected before a substantial marine sulphate pool is established. Higher marine sulphate concentrations would further dampen atmospheric methane

fluxes to the atmosphere, since the accumulation of a marine sulphate pool perturbs the balance between sulphate reducers and methanogens, leaving less organic matter for methanogenesis (Canfield, 1993). Furthermore, an ocean rich in sulphate would increase anaerobic methane oxidation, allowing less methane to escape the sediments and reach the atmosphere, thereby perturbing the atmospheric source-sink balance in favour of O_2 accumulation (Catling et al., 2007). Likewise, the observed increase in TOC and decrease in $\delta^{13}C$ values imply enhanced photosynthetic activity and carbon burial, leading to a net O_2 gain to the atmosphere. The integrated framework of presented data thus exposes a geobiological feedback-driven causality between the earliest atmospheric oxygenation and marine deoxygenation, controlled by the interplay between O_2 production by cyanobacteria in the shallow marine realm and perturbations of the sulphur cycle.

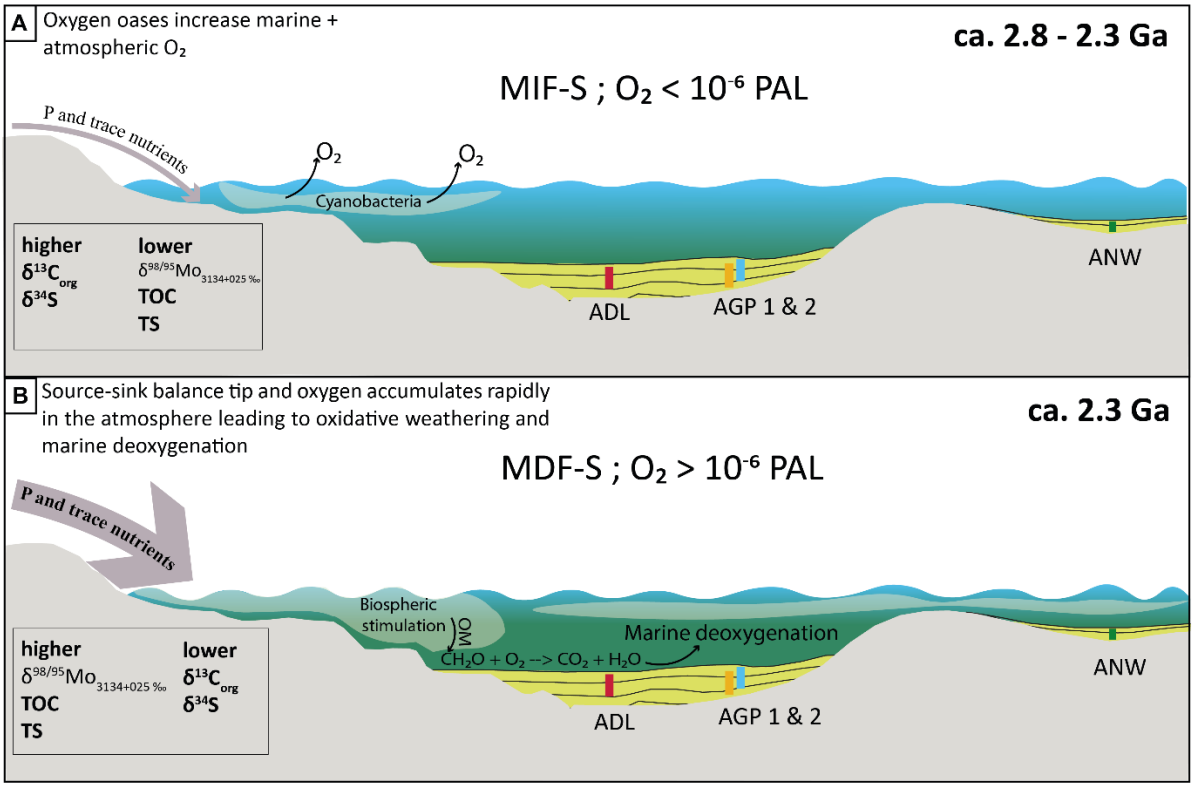

Figure 4.6. *Model explaining the observed redox changes in the aftermath of the GOE.* Before the loss of MIF-S **(A)**, low levels of atmospheric oxygen regulated oxidative weathering, limiting marine nutrient availability and, thus, the size of the biosphere. Atmospheric oxygenation at 2.3 Ga **(B)**, however, overcame this limitation, fueling oxidative weathering that, in turn, increased nutrient fluxes to the marine realm. Such oxygen-driven eutrophication would have elevated primary production, strengthening degradative oxygen demands and, thus, marine deoxygenation.

4.7 Conclusion

This study integrates several environmental and redox-sensitive proxies ($\delta^{98/95}Mo_{3134+0.25}$, $\delta^{34}S$, $\delta^{13}C_{org}$, TS, TOC, Fe/Mn and RSTE) from four drill cores, intersecting the correlative Duitschland and Rooihoogte formations, both recording the loss of MIF-S, in order to understand the temporal marine redox evolution in response to the earliest atmospheric oxygenation.

- Two independent RSTE models suggest an oxic-suboxic marine environment preceding the loss of MIF-S, which transitions into suboxic/anoxic conditions in the immediate aftermath of atmospheric oxygenation. This conclusion is further supported by increasing trends in $\delta^{98/95}Mo_{3134+0.25}$, TS, and TOC and decreasing trends in $\delta^{34}S$, $\delta^{13}C_{org}$ and Fe/Mn. The initiation of oxidative continental weathering increased nutrient delivery to the oceans, triggered cyanobacteria blooms in the surface oceans and ultimately marine deoxygenation. This is expressed biogeochemically in the decrease of $\delta^{34}S$ and $\delta^{13}C_{org}$ values in concert with elevated TS and TOC contents, signalling non-limiting microbial sulphate reduction and the ingrowth of the seawater sulphate reservoir. The positive shift in $\delta^{98/95}Mo_{3134+0.25}$ values can thus be linked to decreased fractionation from ambient seawater driven by increased sulphur and ferrous iron in the bottom waters.
- Combined Fe/Mn, MnO, and $\delta^{98/95}Mo_{3134+0.25}$ systematics disclose oxygenated shallow oceans predating the loss of MIF-S signals. However, on a basin-wide scale, the Eh potential of the water column was high enough to oxidize Mo, S and Fe but not high enough to significantly oxidize Mn in most cases, except in the uppermost part of the *middle D/R* and lowermost *upper D/R* intervals.
- Based on the combination of multiple geochemical redox-sensitive proxies, the shallow marine realm likely evolved from a stratified state into oxic-suboxic conditions before the loss of MIF-S, whereafter, the marine redox state transitioned to anoxic-suboxic conditions. Our data implies a geobiological feedback-driven relationship linking early atmospheric oxygenation to a decline in the marine oxygenation state. Yet, it remains to be determined whether this trend is constrained to the Transvaal Basin or represents a global phenomenon.

4.8 Acknowledgements

Sampling assistance from Lucile Roué and laboratory support from Elmar Reitter and Bernd Steinhilber are gratefully recognised. The Agouron Institute funded the drilling campaign that yielded the material analysed herein, while the University of Johannesburg provided invaluable logistical support and access to the cores. Financial support, thereafter, was provided by the German Research Foundation (DFG) grant SCHO1071/12-1 to Ronny Schoenberg as part of the DFG priority program SPP-1833 'Building a Habitable Earth'. Gareth Izon gratefully recognises his MISTI Seed Award as well as long-standing financial support from the Simons Collaboration (#290361FY18) and the National Science Foundation (#2148916) via respective awards to Roger Summons and Edward Boyle at MIT. Gareth is indebted to Shadrack Tshivhiahuvhi and Lucig Khoza, who aided his initial sampling campaign. We thank two anonymous reviewers for their careful and constructive feedback on this manuscript, which significantly improved its quality.

4.9 Tables

Table 4.1. Geochemical redox parameters in the AGP-1 drill core

Depth (m)	Lithology	Lithostrat'	MnO	V	Mo	U	Fe/ Mn	Fe^{2+}/Fe_T	δ^{98}Mo (‰)		2SE	N_T	S_T	C_T	TOC	$\delta^{13}C$	$\delta^{34}S$	Inferred Redox State	
			wt.%	[µg/g]					NIST 3134	NIST 3134+ 0.25‰		Wt.%				‰ VDPB	‰ VCDT	Algeo & Tribovillard, 2009	Bennett & Canfield, 2020
47.66	Carb. shale	Upper D/R	0.019	129	0.481	4.96	568					0.074	0.057	1.51				Oxic	Oxic
48.14	Carb. shale	Upper D/R	0.018	121	1.13	4.98	300	0.180	0.282	0.532	0.018	0.067	0.074	1.54	3.50	-36.0	-23.2	Suboxic	Oxic
48.14	Carb. shale	Upper D/R							0.271	0.521	0.025	*BDL*	*BDL*	*BDL*					
48.42	Carb. shale	Upper D/R	0.044	135	0.533	4.46	197		0.511	0.761	0.022				1.38	-36.2		Oxic	Oxic
50.07	Py. carb. shale	Upper D/R	0.054	161	6.24	8.43	167	0.678	-0.461	-0.211	0.021	0.095	0.147	1.27	1.07	-35.6		Shuttle influenced	BOMZ
50.31	BIF	Upper D/R	0.074	105	1.94	4.33	202		-0.087	0.163	0.019	*BDL*	0.878	0.317	0.852		-24.4	n/a	n/a
51.06	Py. carb. shale	Upper D/R	0.072	104	1.33	5.91	154		0.102	0.352	0.025	0.056	0.357	1.01	1.79	-36.0	-22.1	Suboxic	Oxic
51.06	Py. carb. shale	Upper D/R							0.097	0.347	0.023	*BDL*	*BDL*	*BDL*					
53.25	Py. carb. shale	Upper D/R	0.026	136	0.343	5.65	225	0.472	0.422	0.672	0.024	0.133	0.401	1.65			-21.1	Oxic	Oxic
54.06	Py. carb. shale	Upper D/R	0.065	116	0.285	5.51	93.5					0.106	0.450	1.78	1.35	-35.4		Oxic	Oxic
54.79	Py. carb. shale	Upper D/R	0.065	112	0.496	4.62	88.4					0.096	0.090	1.41			-16.5	Oxic	Oxic
57.74	Py. carb. shale	Upper D/R	0.110	106	0.707	4.71	68.2	0.779				0.094	0.131	1.03			-14.0	Suboxic	Oxic
58.68	Py. carb. shale	Upper D/R		114	0.319	4.86											-14.2	Oxic	Oxic
60.20	Py. carb. shale	Upper D/R	0.078	47.1	0.095	7.03	84.1										-13.3	Oxic	Oxic
61.12	Py. carb. shale	Upper D/R	0.070	109	0.340	5.79	85.5	0.763	-0.538	-0.288	0.021	0.099	0.121	2.42			-13.0	Oxic	Oxic
62.04	Py. carb. shale	Upper D/R	0.070	114	0.511	5.8	93.0	0.757	-0.388	-0.138	0.022	0.105	0.309	2.63	2.79	-35.1	-11.7	Oxic	Oxic
63.37	Py. carb. shale	Upper D/R	0.060	95.6	0.440	5.64	88.5	0.742	0.073	0.323	0.025	0.110	0.124	2.41	2.34	-35.2	-12.0	Oxic	Oxic
65.19	Shale	Upper D/R	0.047	107	0.335	5.95	91.1					0.072	*BDL*	0.776			-9.46	Oxic	Oxic
67.34	Shale	Upper D/R	0.110	31.6	0.150	7.67	16.4	0.800				0.088	0.079	1.56			-3.61	Oxic	BOMZ
69.33	Shale	Upper D/R	0.081	28.4	0.859	7.95	36.8	0.830	-0.392	-0.142	0.02	0.063	0.050	0.546	0.34	-32.4	-4.90	Suboxic	BOMZ
69.33	Shale	Upper D/R							-0.415	-0.165	0.021	*BDL*	*BDL*	*BDL*					
70.09	Shale	Upper D/R	0.060	16.6	0.414	9.52	33.0	0.719	-0.610	-0.360	0.023	0.079	0.126	0.693			-5.03	Oxic	Oxic
70.84	Shale	Upper D/R	0.070	69.4	1.75	6.04	40.9	0.599	0.822	1.07	0.02	0.081	0.655	1.26	1.20	-32.9	-3.92	Suboxic	Oxic

Table continued on next page

Depth (m)	Lithology	Lithostrat'	MnO	V	Mo	U	Fe/ Mn	Fe^{2+}/Fe_T	δ^{98}Mo (‰)		2SE	N_T	S_T	C_T	TOC	$\delta^{13}C$	$\delta^{34}S$	Inferred Redox State	
			wt.%	[µg/g]					NIST 3134	NIST 3134+ 0.25‰		Wt.%				‰ VDPB	‰ VCDT	Algeo & Tribovillard, 2009	Bennett & Canfield, 2020
71.56	Py. carb. shale	Upper D/R	0.040	67.2	1.69	6.36	77.9	0.788	-0.547	-0.297	0.024	0.081	0.588	3.77			-4.96	Suboxic	Oxic
73.16	Py. carb. shale	Upper D/R		104	2.12	9.78			0.489	0.739	0.021	0.091	0.285	4.35	5.48	-33.4	-0.234	Oxic	Oxic
74.80	Py. carb. shale	Upper D/R	0.051	103	2.38	8.92	42.1		0.141	0.391	0.024	0.090	0.136	4.21	3.95	-32.9	-2.11	Suboxic	BOMZ
75.10	Py. carb. shale	Upper D/R	0.044	92.0	1.91	6.96	50.5					*BDL*	0.133	5.45	5.94	-32.9	-6.14	Suboxic	Oxic
75.59	Py. carb. shale	Upper D/R	0.027	37.0	2.36	15.3	78.9	1.02	-0.103	0.147	0.022	0.135	0.082	3.52			-1.49	Suboxic	BOMZ
75.59	Py. carb. shale	Upper D/R							-0.033	0.217	0.012	*BDL*	*BDL*	*BDL*					
89.18	Stromatolitic Carb.	Upper D/R	37.2	87.7	1.72	1.25	0.065		-0.730	-0.480	0.022	*BDL*	9.36	0.095	7.25			n/a	n/a
90.45	Stromatolitic Carb.	Upper D/R		196	1.25	2.32											-3.40		Oxic
92.45	Siltstone	Upper D/R	0.270	214	1.61	2.48	48.1		-0.908	-0.658	0.015	0.043	*BDL*	0.267			-0.099	oxic	Oxic
92.45	Siltstone	Upper D/R							-0.836	-0.586	0.023	*BDL*	*BDL*	*BDL*					
102.06	Siltstone	Middle D/R	0.100	96.6	0.822	6.67	75.4			0.25							18.3	Suboxic	Oxic
105.16	Siltstone	Middle D/R	0.100	98.3	1.35	6.81	77.0		-0.373	-0.123	0.022	*BDL*	*BDL*	0.216	0.078	-30.0	5.42	Suboxic	Oxic
122.31	Siltstone	Middle D/R	0.078	107	0.912	6.59	101	0.909	-0.694	-0.444	0.021	0.031	*BDL*	0.172	0.143	-30.7		Suboxic	Oxic
128.31	Siltstone	Middle D/R	0.057	114	1.10	6.89	139											Suboxic	Oxic
139.52	Siltstone	Middle D/R	0.043	158	4.03	6.70	86.4	0.818	-0.130	0.120	0.024	0.049	0.059	1.77	1.56	-33.6		Suboxic	Oxic
151.00	Siltstone	Middle D/R	0.150	132	2.06	5.75	63.3		-0.451	-0.201	0.021	0.036	*BDL*	0.828				Suboxic	Oxic
162.00	BIF	Penge	0.437	12.1	1.32	0.170	76.9	0.824	0.498	0.748	0.02	*BDL*	5.743	*BDL*	5.41			n/a	n/a

Measurements marked '*BDL'* were below the limit of detection: $N_t < 0.003$, $S_t < 0.05$, $C_t < 0.10$

Blank fields indicate that no data exists for that particular entry

Table 4.2. Geochemical redox parameters in the AGP-2 drill core

Depth (m)	Lithology	Lithostrat'	MnO	V	Mo	U	Fe/ Mn	δ^{98}Mo (‰)			N_T	S_T	C_T	TOC	δ^{13}C	δ^{34}S	Inferred redox state	
			wt.%	[µg/g]				NIST 3134	NIST 3134+ 0.25‰	2SE	Wt.%				‰ VDPB	‰ VCDT	Algeo & Tribovillard, 2009	Bennett & Canfield, 2020
59.13	Grey shale	Lower TBH	0.042	154	0.873	5.58	174	-0.393	-0.143	0.022	0.061	0.496	0.168	0.167	-31.8	-22.6	Suboxic	Oxic
60.20	Grey shale	Lower TBH	0.031	143	6.44	6.31	205				0.066	1.10	0.154	0.175	-33.2		Shuttle influenced	BOMZ
62.30	Grey shale	Lower TBH	0.030	127	1.51	5.58	216	0.555	0.805	0.022	0.078	0.992	1.70	2.08	-37.4	-22.1	Suboxic	Oxic
63.21	Grey shale	Lower TBH	0.060	131	0.507	6.46	194				0.085	0.512	1.90	2.31	-36.5	-21.0	Oxic	Oxic
64.05	Grey shale	Lower TBH	0.030	145	1.19	6.36	184				0.082	1.05	1.75	1.93	-36.5	-19.8	Suboxic	Oxic
66.17	Grey shale	Lower TBH	0.030	96.1	1.21	4.45	179	0.808	1.06	0.026	0.080	0.939	1.51	1.47	-37.1	-15.7	Suboxic	Oxic
67.45	Grey shale	Lower TBH	0.030	93.9	0.265	4.90	157	0.261	0.511	0.03	0.090	0.427	2.12	2.49	-38.3	-13.2	Oxic	Oxic
68.08	Grey shale	Lower TBH	0.038	119	2.68	5.56	189				0.084	1.42	2.16	2.37	-38.4	-14.3	Suboxic	Oxic
73.67	Grey shale	Lower TBH	0.042	105	0.941	5.39	152				0.077	0.600	1.65	1.51	-38.3	-10.2	Suboxic	Oxic
76.08	Grey shale	Lower TBH	0.060	109	1.42	4.76	138	0.213	0.463	0.025	0.090	0.382	1.65	1.44	-37.8	-17.3	Suboxic	Oxic
77.18	Grey shale	Lower TBH	0.048	119	1.48	4.05	159				0.093	0.374	1.71	1.7	-37.0	-17.1	Shuttle influenced	Oxic
83.14	Carb. shale	Lower TBH	0.030	98.4	0.944	7.51	230	-0.307	-0.057	0.023	0.104	0.419	1.39	1.5	-36.2	-21.5	Suboxic	Oxic
86.26	Carb. shale	Lower TBH	0.030	115	2.06	4.51	193	0.620	0.870	0.025						-23.6	Shuttle influenced	Oxic
89.16	Carb. shale	Lower TBH	0.070	101	0.805	5.83	159	-0.247	0.003	0.025	0.066	0.305	1.26	1.21	-34.9	-23.7	Suboxic	Oxic
92.67	Carb. shale	Upper D/R	0.060	103	0.510	4.75	115	-0.156	0.094	0.017	0.100	0.130	1.61	1.94	-34.9	-21.2	Oxic	Oxic
95.21	Carb. shale	Upper D/R	0.069	36.5	1.04	8.63	91.2				0.099	0.438	1.93	2.05	-35.3	-16.2	Suboxic	BOMZ
102.15	Carb. shale	Upper D/R	0.041	45.6	129	9.62	94.8				0.084	0.314	0.771	0.714	-33.8	-11.6	Particulate shuttle	Euxinic
108.20	Carb. shale	Upper D/R	0.030	72.6	1.68	5.95	77.4	0.538	0.788	0.026	0.176	0.436	14.2	15.7	-33.7	-4.08	Suboxic	Oxic
122.75	Siltstone	Upper D/R	0.147	231	2.21	2.33	28.1				0.034	0.061	0.347	0.257	-31.3	3.86	Oxic	Oxic

Blank fields indicate that no data exists for that particular entry

Table 4.3. Geochemical redox parameters in the ANW drill core

Depth (m)	Lithology	Lithostrat'	MnO	V	Mo	U	Fe/ Mn	δ^{98}Mo (‰)		2SE	N_T	S_T	C_T	TOC	δ^{13}C	δ^{34}S	Inferred redox state	
			wt.%	[µg/g]				NIST 3134	NIST 3134+ 0.25‰		Wt.%				‰ VDPB	‰ VCDT	Algeo & Tribovillard, 2009	Bennett & Canfield, 2020
27.31	Carb. shale	Lower TBH	0.026	118	0.636	7.44	112	-0.602	-0.352	0.022	0.170	*BDL*	1.81	1.78	-35.4	-20.4	Oxic	Oxic
29.77	Carb. shale	Lower TBH	0.034	218	22.8	13.1	92.5	0.491	0.741	0.024	0.153	0.678	7.36	7.76	-36.1	-22.9	Anoxic	Euxinic
30.51	Carb. shale	Lower TBH	0.053	677	15.6	14.0	74.9	0.474	0.724	0.028	0.187	0.127	5.47	5.49	-35.9	-21.2	Anoxic	Euxinic
31.76	Carb. shale	Lower TBH	0.021	124	1.06	6.57	73.4	0.163	0.413	0.018	0.235	*BDL*	1.74	1.59	-34.6	-21.0	Suboxic	Oxic
32.56	Carb. shale	Lower TBH	0.043	151	2.61	6.24	68.1	-0.585	-0.335	0.019	0.153	0.355	3.04	3.03	-35.3	-24.9	Suboxic	Oxic
33.15	Carb. shale	Lower TBH	0.085	100	1.16	7.37	59.6	-0.366	-0.116	0.018	0.129	0.434	4.71	5.07	-35.2	-22.7	Suboxic	BOMZ
36.47	Carb. shale	Upper D/R	0.058	94.3	1.96	8.16	33.0	-0.161	0.089	0.024	0.163	0.157	5.37	5.50	-34.7	-19.0	Suboxic	BOMZ
37.30	Carb. shale	Upper D/R	0.072	115	2.33	5.64	46.4	0.102	0.352	0.025	0.143	1.01	6.23	6.27	-34.5	-24.9	Suboxic	Oxic
38.28	Carb. shale	Upper D/R	0.080	123	2.59	6.89	72.3	0.423	0.673	0.021	0.151	3.17	6.50	6.82	-34.7	-25.2	Suboxic	Oxic
39.12	Carb. shale	Upper D/R	0.103	126	2.63	7.83	49.5	0.504	0.754	0.026	0.149	1.94	5.73	5.95	-34.6	-24.7	Suboxic	Oxic
40.05	Carb. shale	Upper D/R	0.061	164	5.48	7.84	59.5	0.419	0.669	0.023	0.163	1.53	4.66	4.61	-34.5	-28.1	Shuttle influenced	BOMZ
41.70	Chert	Middle D/R	0.016	55.6	48.9	4.70	40.8				0.113	0.180	1.17	1.24	-33.4		Particulate shuttle	BOMZ
43.12	Shale	Middle D/R	0.262	213	0.505	1.81	29.4	-0.978	-0.728	0.027	0.131	*BDL*	0.462	0.508	-31.0	-8.01	Oxic	Oxic
43.70	Shale	Middle D/R	0.235	160	0.791	2.76	28.6	-0.835	-0.585	0.023	0.129	*BDL*	0.363	0.327	-30.8	11.9	Suboxic	Oxic
44.76	Shale	Middle D/R	0.254	142	0.701	2.04	29.4	-0.988	-0.738	0.023	0.151	*BDL*	0.358	0.355	-31.2	5.14	Oxic	Oxic
45.13	Shale	Middle D/R	0.137	247	1.16	2.37	32.6	-0.869	-0.619	0.023	0.159	*BDL*	0.464	0.404	-31.1	0.417	Suboxic	Oxic

Measurements marked '*BDL'* were below the limit of detection: $N_t < 0.003$, $S_t < 0.05$, $C_t < 0.10$
Blank fields indicate that no data exists for that particular entry

Table 4.4. Geochemical redox parameters in the ADL drill core

Depth (m)	Lithology	Lithostrat'	MnO	V	Mo	U	Fe/ Mn	δ^{98}Mo (‰)			N_T	S_T	C_T	TOC	δ^{13}C	δ^{34}S	Inferred Redox State	
			wt.%	[µg/g]				NIST 3134	NIST 3134+ 0.25‰	2SE	Wt.%				‰ VDPB	‰ VCDT	Algeo & Tribovillard, 2009	Bennett & Canfield, 2020
78.3	Shale	Upper D/R	0.110	157	1.03	5.31	96.6										Suboxic	Oxic
80.3	Shale	Upper D/R	0.109	145	0.742	6.63	101	-1.05	-0.795	0.025						-23.5	Suboxic	Oxic
132.1	Shale	Upper D/R	0.135	157	0.455	3.11	84.4				*BDL*	0.087	1.42	–		7.90	Oxic	Oxic
136.4	Shale	Upper D/R	0.053	176	0.48	3.57	178	-0.162	0.088	0.029						9.81	Oxic	Oxic
142.1	F. sandstone	Upper D/R	0.068	164	0.932	3.03	153				*BDL*	0.117	0.423	0.199	-23.7	2.64	Oxic	Oxic
151.4	Carb. shale	Upper D/R	0.118	127	1.41	4.64	92.0									-40.4	Suboxic	Oxic
153.2	Shale	Upper D/R	0.104	148	4.66	4.64	103				*BDL*	*BDL*	*BDL*	0.052	-26.6	8.92	Shuttle influenced	BOMZ
154.9	Shale	Upper D/R	0.097	155	1.58	5.85	79.1	-0.338	-0.088	0.02	*BDL*	*BDL*	0.122	0.056	-27.8	-11.6	Suboxic	Oxic
157.2	Shale	Upper D/R	0.106	144	1.55	5.14	110				*BDL*	*BDL*	*BDL*			13.6	Suboxic	Oxic
167.5	Siltstone	Upper D/R	0.064	130	9.12	5.25	129	-0.315	-0.065	0.024	*BDL*	*BDL*	0.104			11.2	Shuttle influenced	BOMZ
169.9	Siltstone	Upper D/R	0.078	84.6	18.3	3.53	96.6	-0.190	0.060	0.017	*BDL*	*BDL*	0.135	0.104	-30.6	14.3	Particulate shuttle	BOMZ
170.8	Siltstone	Upper D/R	0.081	91.8	1.19	3.91	89.7				*BDL*	*BDL*	0.126	0.082	-31.1	10.7	Suboxic	Oxic
177.5	Siltstone	Upper D/R	0.067	165	5.51	6.17	166	-0.278	-0.028	0.022	*BDL*	*BDL*	*BDL*	0.082	-31.1	10.7	Shuttle influenced	BOMZ
189.5	Siltstone	Upper D/R	0.067	130	1.16	4.62	159				*BDL*	*BDL*	*BDL*	0.058	-28.4	10.7	Suboxic	Oxic
193.4	Siltstone	Upper D/R	0.065	118	1.19	4.43	158				*BDL*	*BDL*	*BDL*	0.035	-28.0	8.63	Suboxic	Oxic
197.7	F. sandstone	Upper D/R	0.058	122	1.87	5.01	173				*BDL*	*BDL*	*BDL*			7.98	Suboxic	Oxic
199.1	Siltstone	Upper D/R	0.078	135	2.24	5.01	142	-0.217	0.033	0.023	*BDL*	*BDL*	*BDL*	0.027	-27.6	7.91	Suboxic	Oxic
204.1	Siltstone	Upper D/R	0.069	141	2.07	5.31	158				*BDL*	*BDL*	*BDL*	0.030	-27.3	8.02	Suboxic	Oxic
207.6	F. sandstone	Upper D/R	0.066	137	1.80	5.21	170	-0.408	-0.158	0.024	*BDL*	*BDL*	*BDL*	0.030	-27.3	8.04	Suboxic	Oxic
212.2	Siltstone	Upper D/R	0.069	129	1.56	4.94	156	-0.256	-0.006	0.022						1.76	Suboxic	Oxic

Table continued on next page

Depth (m)	Lithology	Lithostrat'	MnO	V	Mo	U	Fe/ Mn	δ^{98}Mo (‰)			N_T	S_T	C_T	TOC	$\delta^{13}C$	$\delta^{34}S$	Inferred Redox State	
			wt.%	[µg/g]				NIST 3134	NIST 3134+ 0.25‰	2SE	Wt.%				‰ VDPB	‰ VCDT	Algeo & Tribovillard, 2009	Bennett & Canfield, 2020
212.7	Siltstone	Upper D/R	0.071	133	1.52	4.88	150				*BDL*	*BDL*	*BDL*	0.043	-27.2	12.0	Suboxic	Oxic
214.9	F. sandstone	Upper D/R	0.096	148	1.04	4.64	120				*BDL*	0.050	*BDL*	0.031	-28.8	7.73	Suboxic	Oxic
218.8	F. sandstone	Upper D/R	0.047	116	3.56	6.76	143				*BDL*	0.689	0.131	0.108	-30.0	6.99	Suboxic	Oxic
223.8	F. sandstone	Upper D/R	0.040	122	3.07	6.57	157	-0.033	0.217	0.029	*BDL*	0.104	0.114	0.092	-30.9	7.68	Suboxic	Oxic
226.7	F. sandstone	Upper D/R	0.033	130	6.09	7.06	198				*BDL*	*BDL*	0.142	0.095	-30.2	6.48	Shuttle influenced	BOMZ
233.9	Shale	Upper D/R	0.055	119	6.14	4.77	165	-0.190	0.060	0.02	*BDL*	0.062	0.219	0.259	-31.2	7.45	Shuttle influenced	BOMZ
234.9	Shale	Upper D/R	0.094	113	5.21	4.10	139									4.57	Shuttle influenced	BOMZ
238.7	F. sandstone	Upper D/R	0.037	140	4.04	7.16	196				*BDL*	0.076	0.120	0.132	-29.1	3.16	Suboxic	BOMZ
239.9	F. sandstone	Upper D/R	0.064	199	2.64	5.41	124	-0.011	0.239	0.019						2.96	Suboxic	Oxic
256.9	Shale	Upper D/R	0.069	166	2.61	6.16	122	0.060	0.310	0.023	*BDL*	0.126	0.274			-1.30	Suboxic	Oxic
263.9	Shale	Upper D/R	0.038	159	3.17	7.05	213									1.06	Suboxic	Oxic
267.1	Shale	Upper D/R	0.031	147	3.23	6.78	237	0.143	0.393	0.033	*BDL*	0.225	0.154	0.095	-28.7	-0.701	Suboxic	Oxic

Measurements marked '*BDL'* were below the limit of detection: $N_t < 0.003$, $S_t < 0.05$, $C_t < 0.10$

Blank fields indicate that no data exists for that particular entry

4.10 References

Albut, G., Kamber, B. S., Brüske, A., Beukes, N. J., Smith, A. J., & Schoenberg, R. (2019). Modern weathering in outcrop samples versus ancient paleoredox information in drill core samples from a Mesoarchaean marine oxygen oasis in Pongola Supergroup, South Africa. *Geochimica et Cosmochimica Acta*, *265*, 330-353.

Algeo, T. J., & Tribovillard, N. (2009). Environmental analysis of paleoceanographic systems based on molybdenum–uranium covariation. *Chemical Geology*, *268*(3-4), 211-225.

Anbar, A. D. (2008). Elements and Evolution. *Science*, *322*, 1481-1483.

Asael, D., Rouxel, O., Poulton, S. W., Lyons, T. W., & Bekker, A. (2018). Molybdenum record from black shales indicates oscillating atmospheric oxygen levels in the early Paleoproterozoic. *American Journal of Science*, *318*(3), 275-299.

Babechuk, M. G., Weimar, N. E., Kleinhanns, I. C., Eroglu, S., Swanner, E. D., Kenny, G. G., Kamber, B. S., & Schoenberg, R. (2019). Pervasively anoxic surface conditions at the onset of the Great Oxidation Event: New multi-proxy constraints from the Cooper Lake paleosol. *Precambrian Research*, *323*, 126-163.

Barling, J., & Anbar, A. (2004). Molybdenum isotope fractionation during adsorption by manganese oxides. *Earth and Planetary Science Letters*, *217*(3-4), 315-329.

Bekker, A. (2015). Huronian glaciation. *Encyclopedia of Astrobiology*, 1128-1135.

Bennett, W. W., & Canfield, D. E. (2020). Redox-sensitive trace metals as paleoredox proxies: A review and analysis of data from modern sediments. *Earth-Science Reviews*, *204*, 103175.

Beukes, N. (1984). Sedimentology of the Kuruman and Griquatown iron-formations, Transvaal Supergroup, Griqualand West, South Africa. *Precambrian Research*, *24*(1), 47-84.

Beukes, N. J. (1987). Facies relations, depositional environments and diagenesis in a major early Proterozoic stromatolitic carbonate platform to basinal sequence, Campbellrand Subgroup, Transvaal Supergroup, Southern Africa. *Sedimentary Geology*, *54*(1-2), 1-46.

Beukes, N. J., Dorland, H., Gutzmer, J., Nedachi, M., & Ohmoto, H. (2002). Tropical laterites, life on land, and the history of atmospheric oxygen in the Paleoproterozoic. *Geology*, *30*(6), 491-494.

Brocks, J. J., Logan, G. A., Buick, R., & Summons, R. E. (1999). Archean molecular fossils and the early rise of eukaryotes. *Science*, *285*(5430), 1033-1036.

Canfield, D. E. (1993). *Organic matter oxidation in marine sediments*. Springer.

Canfield, D. E. (1998). A New Model for Proterozoic Ocean Chemistry. *Nature*, *396*, 451-453.

Casalini, M., Avanzinelli, R., Tommasini, S., Elliott, T., & Conticelli, S. (2019). Ce/Mo and molybdenum isotope systematics in subduction-related orogenic potassic magmas of Central-Southern Italy. *Geochemistry, Geophysics, Geosystems*, *20*(6), 2753-2768.

Catling, D., Claire, M., & Zahnle, K. (2007). Anaerobic methanotrophy and the rise of atmospheric oxygen. *Philosophical Transactions of the Royal Society A: Mathematical, Physical and Engineering Sciences*, *365*(1856), 1867-1888.

Catling, D. C., Zahnle, K. J., & McKay, C. P. (2001). Biogenic methane, hydrogen escape, and the irreversible oxidation of early Earth. *Science*, *293*(5531), 839-843.

Chen, S., Hin, R. C., John, T., Brooker, R., Bryan, B., Niu, Y., & Elliott, T. (2019). Molybdenum systematics of subducted crust record reactive fluid flow from underlying slab serpentine dehydration. *Nature communications*, *10*(1), 1-9.

Coetzee, L. L. (2001). *Genetic stratigraphy of the Paleoproterozoic Pretoria Group in the western Transvaal* University of Johannesburg, M.Sc. thesis (unpublished), 210 p.].

Craig, H. (1957). Isotopic standards for carbon and oxygen and correction factors for mass-spectrometric analysis of carbon dioxide. *Geochimica et Cosmochimica Acta*, *12*(1-2), 133-149.

Crowe, S. A., Paris, G., Katsev, S., Jones, C., Kim, S.-T., Zerkle, A. L., Nomosatryo, S., Fowle, D. A., Adkins, J. F., & Sessions, A. L. (2014). Sulfate was a trace constituent of Archean seawater. *Science*, *346*(6210), 735-739.

Da Silva, J. F., & Williams, R. J. P. (2001). *The biological chemistry of the elements: the inorganic chemistry of life*. Oxford University Press.

Dinelli, E., Tateo, F., & Summa, V. (2007). Geochemical and mineralogical proxies for grain size in mudstones and siltstones from the Pleistocene and Holocene of the Po River alluvial plain, Italy. *Geological Society of America Special Papers*, *420*, 25-36.

Duan, Y., Anbar, A. D., Arnold, G. L., Lyons, T. W., Gordon, G. W., & Kendall, B. (2010). Molybdenum isotope evidence for mild environmental oxygenation before the Great Oxidation Event. *Geochimica et Cosmochimica Acta*, *74*(23), 6655-6668.

Eickmann, B., Hofmann, A., Wille, M., Bui, T. H., Wing, B. A., & Schoenberg, R. (2018). Isotopic evidence for oxygenated Mesoarchaean shallow oceans. *Nature Geoscience*, *11*(2), 133-138.

Eriksson, P., Meyer, R., & Botha, W. (1988). A hypothesis on the nature of the Pretoria Group basin. *South African Journal of Geology*, *91*(4), 490-497.

Eroglu, S., van Zuilen, M. A., Taubald, H., Drost, K., Wille, M., Swanner, E. D., Beukes, N. J., & Schoenberg, R. (2017). Depth-dependent δ13C trends in platform and slope settings of the Campbellrand-Malmani carbonate platform and possible implications for Early Earth oxygenation. *Precambrian Research*, *302*, 122-139.

Falcón, L. I., Magallón, S., & Castillo, A. (2010). Dating the cyanobacterial ancestor of the chloroplast. *The Multidisciplinary Journal of Microbial Ecology Journal*, *4*(6), 777-783.

Farquhar, J., Bao, H., & Thiemens, M. (2000). Atmospheric influence of Earth's earliest sulfur cycle. *Science*, *289*(5480), 756-758.

Freymuth, H., Vils, F., Willbold, M., Taylor, R. N., & Elliott, T. (2015). Molybdenum mobility and isotopic fractionation during subduction at the Mariana arc. *Earth and Planetary Science Letters*, *432*, 176-186.

Goldberg, T., Archer, C., Vance, D., & Poulton, S. W. (2009). Mo isotope fractionation during adsorption to Fe (oxyhydr) oxides. *Geochimica et Cosmochimica Acta*, *73*(21), 6502-6516.

Goldberg, T., Gordon, G., Izon, G., Archer, C., Pearce, C. R., McManus, J., Anbar, A. D., & Rehkämper, M. (2013). Resolution of inter-laboratory discrepancies in Mo isotope data: an intercalibration. *Journal of Analytical Atomic Spectrometry*, *28*(5), 724-735.

Greber, N. D., Siebert, C., Nägler, T. F., & Pettke, T. (2012). δ98/95Mo values and molybdenum concentration data for NIST SRM 610, 612 and 3134: Towards a common protocol for reporting Mo data. *Geostandards and Geoanalytical Research*, *36*(3), 291-300.

Gumsley, A. P., Chamberlain, K. R., Bleeker, W., Soderlund, U., de Kock, M. O., Larsson, E. R., & Bekker, A. (2017). Timing and tempo of the Great Oxidation Event. *Proceedings of the National Academy of Sciences*, *114*(8), 1811-1816. https://doi.org/10.1073/pnas.1608824114

Guo, Q., Strauss, H., Kaufman, A. J., Schröder, S., Gutzmer, J., Wing, B., Baker, M. A., Bekker, A., Jin, Q., & Kim, S.-T. (2009). Reconstructing Earth's surface oxidation across the Archean-Proterozoic transition. *Geology*, *37*(5), 399-402.

Habicht, K. S., & Canfield, D. E. (2001). Isotope fractionation by sulfate-reducing natural populations and the isotopic composition of sulfide in marine sediments. *Geology*, *29*(6), 555-558.

Hannah, J. L., Bekker, A., Stein, H. J., Markey, R. J., & Holland, H. D. (2004). Primitive Os and 2316 Ma age for marine shale: implications for Paleoproterozoic glacial events and the rise of atmospheric oxygen. *Earth and Planetary Science Letters*, *225*(1-2), 43-52.

Havsteen, J. C., Kleinhanns, I. C., Schröder, S., Eickmann, B., Izon, G., Gogouvitis, M. D., Ngobeli, R., Beukes, N. J., & Schoenberg, R. (2023). Evidence for contemporaneous deposition of the Duitschland and Rooihoogte formations (Transvaal Supergroup): Implications for tempo and mode of Earth's Great Oxidation. *Precambrian Research*, *391*, doi.org/10.1016/j.precamres.2023.107055.

Holland, H. D. (2002). Volcanic gases, black smokers, and the Great Oxidation Event. *Geochimica et Cosmochimica Acta*, *66*(21), 3811-3826.

Holland, H. D. (2006). The oxygenation of the atmosphere and oceans. *Philosophical Transactions of the Royal Society B: Biological Sciences*, *361*(1470), 903-915.

Izon, G., Luo, G., Uveges, B. T., Beukes, N., Kitajima, K., Ono, S., Valley, J. W., Ma, X., & Summons, R. E. (2022). Bulk and grain-scale minor sulfur isotope data reveal complexities in the dynamics of Earth's oxygenation. *Proceedings of the National Academy of Sciences*, *119*(13), e2025606119.

Johnson, C. M., Ludois, J. M., Beard, B. L., Beukes, N. J., & Heimann, A. (2013). Iron formation carbonates: Paleoceanographic proxy or recorder of microbial diagenesis? *Geology*, *41*(11), 1147-1150.

Kane, J. S. (2004). Report of the international association of geoanalysts on the certification of Penrhyn Slate, OU-6. *Geostandards and Geoanalytical Research*, *28*(1), 53-80.

Kendall, B., Dahl, T. W., & Anbar, A. D. (2017). The stable isotope geochemistry of molybdenum. *Reviews in Mineralogy and Geochemistry*, *82*(1), 683-732.

Kerl, C. F., Lohmayer, R., Bura-Nakic, E., Vance, D., & Planer-Friedrich, B. (2017). Experimental confirmation of isotope fractionation in thiomolybdates using ion chromatographic separation and detection by multicollector ICPMS. *Analytical Chemistry*, *89*(5), 3123-3129.

Kump, L. R., & Barley, M. E. (2007). Increased subaerial volcanism and the rise of atmospheric oxygen 2.5 billion years ago. *Nature*, *448*(7157), 1033-1036.

Kurzweil, F., Archer, C., Wille, M., Schoenberg, R., Münker, C., & Dellwig, O. (2021). Redox control on the tungsten isotope composition of seawater. *Proceedings of the National Academy of Sciences*, *118*(18), e2023544118.

Kurzweil, F., Dellwig, O., Wille, M., Schoenberg, R., Arz, H. W., & Muenker, C. (2022). The stable tungsten isotope composition of sapropels and manganese-rich sediments from the Baltic Sea. *Earth and Planetary Science Letters*, *578*, 117-303.

Kurzweil, F., Wille, M., Gantert, N., Beukes, N. J., & Schoenberg, R. (2016). Manganese oxide shuttling in pre-GOE oceans–evidence from molybdenum and iron isotopes. *Earth and Planetary Science Letters*, *452*, 69-78.

Kurzweil, F., Wille, M., Schoenberg, R., Taubald, H., & Van Kranendonk, M. J. (2015). Continuously increasing δ98Mo values in Neoarchean black shales and iron formations from the Hamersley Basin. *Geochimica et Cosmochimica Acta*, *164*, 523-542.

Luo, G., Ono, S., Beukes, N. J., Wang, D. T., Xie, S., & Summons, R. E. (2016). Rapid oxygenation of Earth's atmosphere 2.33 billion years ago. *Science advances*, *2*(5), e1600134.

Maxwell, J. A. (1968). *Rock and mineral analysis*. John Wiley & Sons.

Moore, J. M., Polteau, S., Armstrong, R., Corfu, F., & Tsikos, H. (2012). The age and correlation of the Postmasburg Group, southern Africa: Constraints from detrital zircon grains. *Journal of African Earth Sciences*, *64*, 9-19.

Morford, J. L., Emerson, S., Breckel, E. J., & Kim, S. H. (2005). Diagenesis of oxyanions (V, U, Re, and Mo) in pore waters and sediments from a continental margin. *Geochimica et Cosmochimica Acta*, *69*, 5021–5032. https://doi.org/10.1016/j.gca.2005.05.015

Nägler, T., Neubert, N., Böttcher, M., Dellwig, O., & Schnetger, B. (2011). Molybdenum isotope fractionation in pelagic euxinia: Evidence from the modern Black and Baltic Seas. *Chemical Geology*, *289*(1-2), 1-11.

Nägler, T. F., Anbar, A. D., Archer, C., Goldberg, T., Gordon, G. W., Greber, N. D., Siebert, C., Sohrin, Y., & Vance, D. (2014). Proposal for an international molybdenum isotope measurement standard and data representation. *Geostandards and Geoanalytical Research*, *38*(2), 149-151.

Nursall, J. (1959). Oxygen as a prerequisite to the origin of the Metazoa. *Nature*, *183*, 1170-1172.

Och, L., & Shields-Zhou, G. A. (2012). The Neoproterozoic oxygenation event: Environmental perturbations and biogeochemical cycling. *Earth-Science Reviews*, *110*, 26–57. https://doi.org/10.1016/j.earscirev.2011.09.004

Ossa Ossa, F., Hofmann, A., Wille, M., Spangenberg, J. E., Bekker, A., Poulton, S. W., Eickmann, B., & Schoenberg, R. (2018). Aerobic iron and manganese cycling in a redox-stratified Mesoarchean epicontinental sea. *Earth and Planetary Science Letters*, *500*, 28-40.

Ostrander, C. M., Nielsen, S. G., Owens, J. D., Kendall, B., Gordon, G. W., Romaniello, S. J., & Anbar, A. D. (2019). Fully oxygenated water columns over continental shelves before the Great Oxidation Event. *Nature Geoscience*, *12*(3), 186–191.

Ostrander, C. M., Sahoo, S. K., Kendall, B., Jiang, G., Planavsky, N. J., Lyons, T. W., Nielsen, S. G., Owens, J. D., Gordon, G. W., & Romaniello, S. J. (2019). Multiple negative molybdenum isotope excursions in the Doushantuo Formation (South China) fingerprint complex redox-related processes in the Ediacaran Nanhua Basin. *Geochimica et Cosmochimica Acta*, *261*, 191-209.

Philippot, P., Ávila, J. N., Killingsworth, B. A., Tessalina, S., Baton, F., Caquineau, T., Muller, E., Pecoits, E., Cartigny, P., & Lalonde, S. V. (2018). Globally asynchronous sulphur isotope signals require re-definition of the Great Oxidation Event. *Nature communications*, *9*(1), Article #: 2245.

Planavsky, N. J., Asael, D., Hofmann, A., Reinhard, C. T., Lalonde, S. V., Knudsen, A., Wang, X., Ossa, F. O., Pecoits, E., & Smith, A. J. (2014). Evidence for oxygenic photosynthesis half a billion years before the Great Oxidation Event. *Nature Geoscience*, *7*(4), 283-286.

Poulson, R. L., McManus, J., Severmann, S., & Berelson, W. M. (2009). Molybdenum behavior during early diagenesis: Insights from Mo isotopes. *Geochemistry, Geophysics, Geosystems*, *10*(6), doi.org/10.1029/2008GC002180.

Poulton, S. W., Bekker, A., Cumming, V. M., Zerkle, A. L., Canfield, D. E., & Johnston, D. T. (2021). A 200-million-year delay in permanent atmospheric oxygenation. *Nature*, *592*(7853), 232-236. https://doi.org/10.1038/s41586-021-03393-7

Robbins, L. J., Lalonde, S. V., Planavsky, N. J., Partin, C. A., Reinhard, C. T., Kendall, B., Scott, C., Hardisty, D. S., Gill, B. C., & Alessi, D. S. (2016). Trace elements at the intersection of marine biological and geochemical evolution. *Earth-Science Reviews*, *163*, 323-348.

Rosca, C., König, S., Pons, M.-L., & Schoenberg, R. (2021). Improved protocols for Zn purification and MC-ICP-MS analyses enable determination of small-scale Zn isotope variations. *Chemical Geology*, *586*, doi.org/10.1016/j.chemgeo.2021.120440.

Rosing, M. T., & Frei, R. (2004). U-rich Archaean sea-floor sediments from Greenland–indications of> 3700 Ma oxygenic photosynthesis. *Earth and Planetary Science Letters*, *217*(3-4), 237-244.

Roué, L., Kurzweil, F., Wille, M., Wegwerth, A., Dellwig, O., Münker, C., & Schoenberg, R. (2021). Stable W and Mo isotopic evidence for increasing redox-potentials from the Paleoarchean towards the Paleoproterozoic deep ocean. *Geochimica et Cosmochimica Acta*, *309*, 366-387.

Rudge, J. F., Reynolds, B. C., & Bourdon, B. (2009). The double spike toolbox. *Chemical Geology*, *265*(3-4), 420-431. https://doi.org/10.1016/j.chemgeo.2009.05.010

Saikkonen, R. J., & Rautiainen, I. A. (1993). Determination of ferrous iron in rock and mineral samples by three volumetric methods. *Bulletin of the Geological Society of Finland*, *65*, 59-63.

Schröder, S., Beukes, N. J., & Armstrong, R. A. (2016). Detrital zircon constraints on the tectonostratigraphy of the Paleoproterozoic Pretoria Group, South Africa. *Precambrian Research*, *278*, 362-393.

Schuessler, J. A., Botcharnikov, R. E., Behrens, H., Misiti, V., & Freda, C. (2008). Amorphous materials: properties, structure, and durability: oxidation state of iron in hydrous phono-tephritic melts. *American Mineralogist*, *93*(10), 1493-1504.

Senger, M., Davies, J., Ovtcharova, M., Beukes, N., Gumsley, A., Gaynor, S., Ulianov, A., Ngobeli, R., & Schaltegger, U. (2023). Improving the chronostratigraphic framework of the Transvaal Supergroup (South Africa) through in-situ and high-precision U-Pb geochronology. *Precambrian Research*, *392*, doi.org/10.1016/j.precamres.2023.107070.

Smrzka, D., Zwicker, J., Bach, W., Feng, D., Himmler, T., Chen, D., & Peckmann, J. (2019). The behavior of trace elements in seawater, sedimentary pore water, and their incorporation into carbonate minerals: A review. *Facies*, *65*(4), 1-47.

Sumner, D. Y., & Beukes, N. J. (2006). Sequence stratigraphic development of the Neoarchean Transvaal carbonate platform, Kaapvaal Craton, South Africa. *South African Journal of Geology*, *109*(1-2), 11-22.

Taylor, S. R., & McLennan, S. M. (1985). *The continental crust: its composition and evolution*. Blackwell Scientific Publications.

Uveges, B. T., Izon, G., Ono, S., Beukes, N. J., & Summons, R. E. (2023). Reconciling discrepant minor sulfur isotope records of the Great Oxidation Event. *Nature communications*, *14*(1), Article #: 279.

Villalobos-Orchard, J., Freymuth, H., O'Driscoll, B., Elliott, T., Williams, H., Casalini, M., & Willbold, M. (2020). Molybdenum isotope ratios in Izu arc basalts: the control of subduction zone fluids on compositional variations in arc volcanic systems. *Geochimica et Cosmochimica Acta*, *288*, 68-82.

Warke, M. R., Di Rocco, T., Zerkle, A. L., Lepland, A., Prave, A. R., Martin, A. P., Ueno, Y., Condon, D. J., & Claire, M. W. (2020). The Great Oxidation Event preceded a Paleoproterozoic "snowball Earth". *Proceedings of the National Academy of Sciences*, *117*(24), 13314-13320.

Warke, M. R., & Schröder, S. (2018). Synsedimentary fault control on the deposition of the Duitschland Formation (South Africa): Implications for depositional settings, Paleoproterozoic stratigraphic correlations, and the GOE. *Precambrian Research*, *310*, 348-364.

Wasylenki, L. E., Rolfe, B. A., Weeks, C. L., Spiro, T. G., & Anbar, A. D. (2008). Experimental investigation of the effects of temperature and ionic strength on Mo isotope fractionation during adsorption to manganese oxides. *Geochimica et Cosmochimica Acta*, *72*(24), 5997-6005.

Willbold, M., Hibbert, K., Lai, Y. J., Freymuth, H., Hin, R. C., Coath, C., Vils, F., & Elliott, T. (2016). High-precision mass-dependent molybdenum isotope variations in magmatic rocks determined by double-spike MC-ICP-MS. *Geostandards and Geoanalytical Research*, *40*(3), 389-403.

Wille, M., Kramers, J. D., Nägler, T. F., Beukes, N., Schröder, S., Meisel, T., Lacassie, J., & Voegelin, A. (2007). Evidence for a gradual rise of oxygen between 2.6 and 2.5 Ga from Mo isotopes and Re-PGE signatures in shales. *Geochimica et Cosmochimica Acta*, *71*(10), 2417-2435.

Zahnle, K., Claire, M., & Catling, D. (2006). The loss of mass-independent fractionation in sulfur due to a Palaeoproterozoic collapse of atmospheric methane. *Geobiology*, *4*(4), 271-283.

Zeh, A., Wilson, A. H., & Gerdes, A. (2020). Zircon U-Pb-Hf isotope systematics of Transvaal Supergroup – Constraints for the geodynamic evolution of the Kaapvaal Craton and its hinterland between 2.65 and 2.06 Ga. *Precambrian Research*, *345*, doi.org/10.1016/j.precamres.2020.105760. https://doi.org/10.1016/j.precamres.2020.105760

Zhao, P. P., Li, J., Zhang, L., Wang, Z. B., Kong, D. X., Ma, J. L., Wei, G. J., & Xu, J. F. (2016). Molybdenum mass fractions and isotopic compositions of international geological reference materials. *Geostandards and Geoanalytical Research*, *40*(2), 217-226.

4.11 Supplementary Material

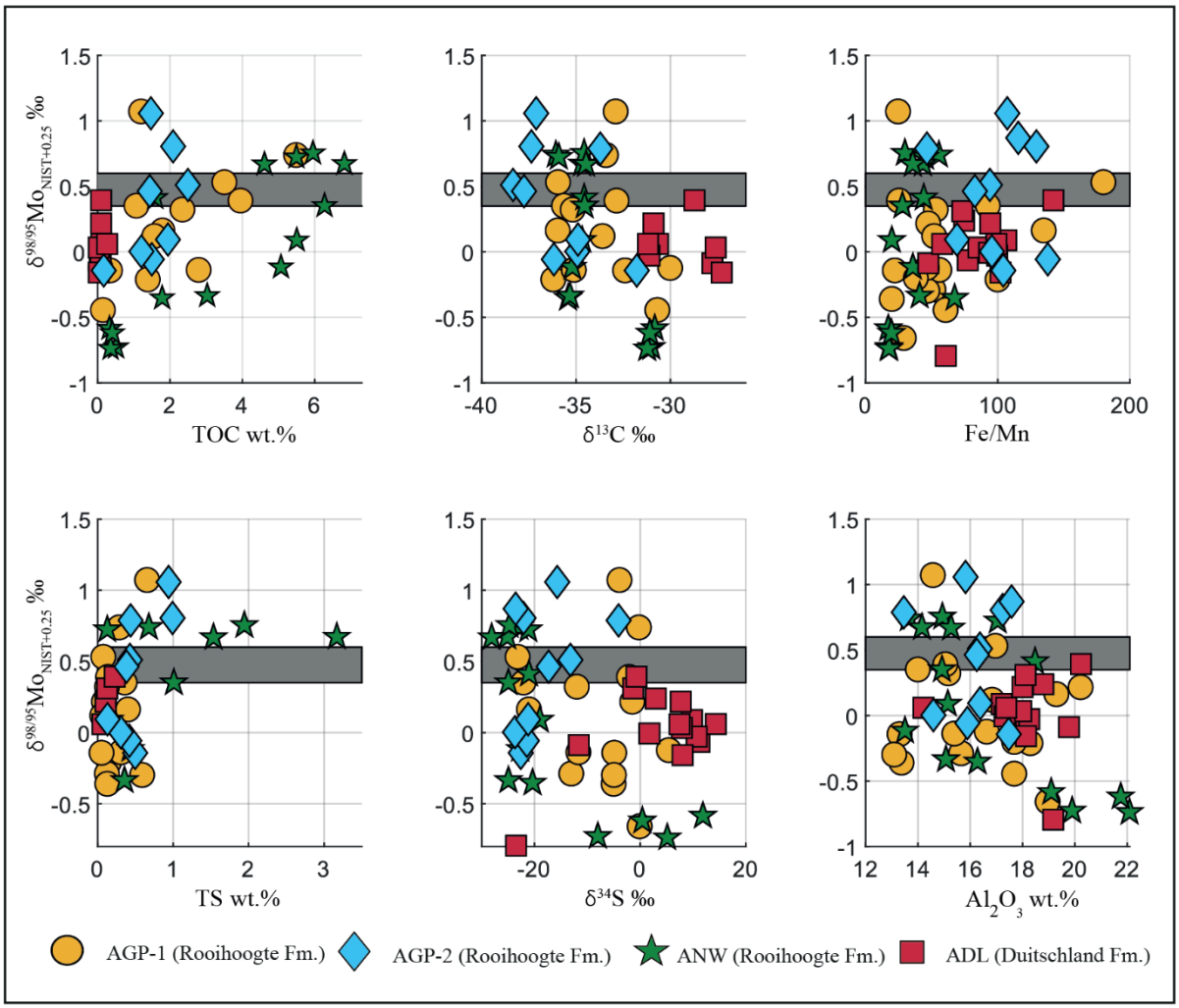

Figure 4.S1. *Scatter plots illustrating the relationship between Mo isotope systematics ($\delta^{98/95}Mo_{NIST+0.25}$) and selected isotopic and elemental proxies within the lower Pretoria Group.* The grey box represents the estimated Mo isotope composition of bulk continental crust (Willbold and Elliott, 2017).

Chapter 5

The Hotazel Formation: Unraveling the Interplay between Bioproductivity, Oxygen Minimum Zones and Archean Marine Redox Evolution

5.1 Introduction

The Neoarchean to Paleoproterozoic Eras signify a critical change in Earth's surface redox-conditions. During this time period, substantial amounts of O_2 accumulated in the shallow marine realm and subsequently in the atmosphere (e.g. Olson et al., 2013; Wille et al., 2007), culminating in the ~2.45–2.32 billion years (Ga) Great Oxidation Event (GOE) (Hannah et al., 2004; Holland, 2006; Luo et al., 2016), and arguably representing one of the most pronounced geobiological changes ever recorded in the Earth system. Sediments from the 2.65 to 2.06 Ga Transvaal Supergroup (South Africa) play an instrumental role in deciphering the tempo and mode of the GOE. Yet, the lack of direct sediment deposition ages has led to discrepancies in stratigraphic correlation within the Transvaal Supergroup, ultimately triggering conflicting interpretations of the trajectory for the GOE (Coetzee et al., 2006; Gumsley et al., 2017; Guo et al., 2009; Havsteen et al., 2023; Luo et al., 2016; Poulton et al., 2021). In this respect, improved U-Pb ages on baddeleyite (ZrO_2) grains in dykes from the Ongeluk large igneous province of 2426 ± 3 Ma (Gumsley et al., 2017) stand in contrast to the previously inferred Pb-Pb age of 2222 ± 13 Ma (Cornell et al., 1996) and correlation with the ≤2,250–2,240 Ma Hekpoort Formation of the Transvaal Area (TA) (Cornell et al., 1996; Schröder et al., 2016). These findings convincingly resolved some of the stratigraphic issues and forced a fundamental reinterpretation of the stratigraphy in the Transvaal Supergroup. Specifically, the Posmasburg Group in the Griqualand West Area (GWA) now holds a geochronological position preceding the Pretoria Group in the (TA) (Fig. 5.1A), which contrasts with the previously inferred correlative deposition (Beukes et al., 2002; Cornell et al., 1996; Eriksson et al., 2006; Eriksson & Cheney, 1992). In this context, a crucial aspect for our understanding of the oxygen evolution in the atmosphere-ocean system is the Hotazel Formation within the Postmasburg Group, with its revised inferred depositional age of about 2400 Ma now being about 200 million years (Gumsley et al., 2017) older than it was believed to be before.

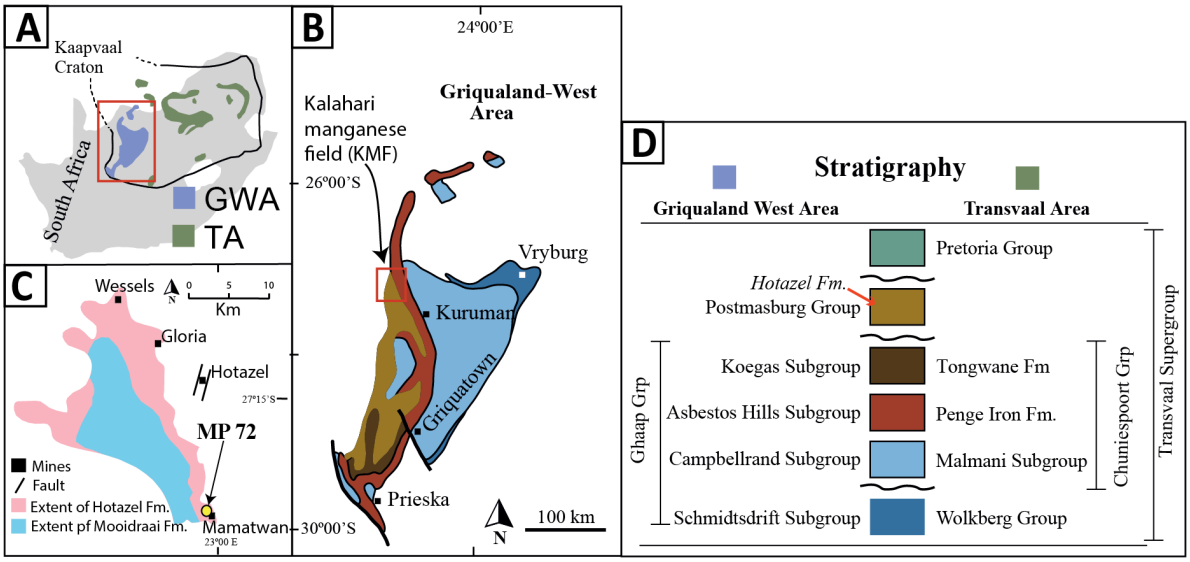

Figure 5.1. **(A):** *Overview of the Transvaal Supergroup outcrop strata on the Kaapvaal Craton* **(B)** Detailed view of the Griqualand West Area (GWA) of the Transvaal supergroup. **(C)** Zoom in on the Kalahari Manganese Field (KMF) of the Postmasburg Group. **(D)** Simple stratigraphic model showcasing correlative groups between the GWA and the Transvaal Area (TA).

The Hotazel Formation is a banded iron formation (BIF) interspersed with bands exceptionally rich in manganese (up to >50 wt.%), compared to the roughly 1 wt.% in a typical BIF (Mhlanga et al., 2023). Such large-scale quantities of Manganese in chemical sediments require the oxidation of dissolved Mn(II) to insoluble Mn(III,IV) (hydr)oxides, which can be achieved by either abiotic oxidation of Mn(II) in the presence of O_2 or similar reactive oxygen species or by Mn-oxidizing photosynthesis (Johnson et al., 2013b; Tebo et al., 2004). The Hotazel Formation, therefore, offers a critical window for deciphering the temporal oxygen evolution of the atmosphere-ocean system across the Neoarchean-Paleoproterozoic boundary at the onset of the GOE, and simultaneously gives insights into its potential links to the biosphere. Integrated within the stratigraphic framework by Gumsley et al. (2017), the Hotazel Formation was deposited before the loss of mass-independent fractionation of sulfur isotopes (MIF-S), a key indicator for atmospheric O_2, in the Transvaal Supergroup. This observation reinforces previous geochemical interpretations indicating a mildly oxygenated to oxygenated shallow marine realm preceding the accumulation of O_2 in the atmosphere (Anbar et al., 2007; Eroglu et al., 2017; Kendall et al., 2010; Kurzweil et al., 2016; Ostrander et al., 2019; Wille et al., 2007).

Here we present coupled Fe and Mo stable isotope and trace element systematics to explore the interplay between abiotic and biochemical redox processes during the deposition of the Hotazel Formation and investigate various proposed depositional models from a sedimentological and geochemical perspective.

5.2 Geological Setting

5.2.1 The Transvaal Supergroup

The Transvaal Supergroup represents a mix of predominantly chemical and siliciclastic sediments deposited on the Kaapvaal Craton between 2.65 and 2.05 Ga (Moore et al., 2001). It is exposed in two geographically distinct locations referred to as the Griqualand West Area (GWA) and the Transvaal Area (TA). However, initial sedimentation most probably spanned the entire Kaapvaal Craton based on the uniformity between the TA and GWA (Beukes, 1986). This is further supported by correlative strata identified in Botswana (Franchi and Mapeo, 2019) and in the Free State Province of South Africa, about 200–300 km south of the Transvaal Area (McCarthy et al., 2018). Globally the Transvaal Supergroup potentially constitutes one lithospheric fragment, which, combined with the Pilbara Province (Australia) and the Grunehogna Province (Antarctica), jointly formed the ~3.05 to 1.5 Vaalbara Craton (Mhlanga et al., 2023).

This work focuses on the Hotazel Formation of the upper Postmasburg Group (GWA), and thus, the reader is referred to other studies for a comprehensive review of the stratigraphy of the entire Transvaal Supergroup (e.g., Beukes, 1983, 1986; Gumsley et al., 2017; Moore et al., 2012; Moore et al., 2001). In brief, the GWA consists of two sedimentary groups, the lower Ghaap Group, representing a transgressive-regressive cycle of predominantly carbonates and BIFs, and the upper Postmasburg Group, which encompasses a variety of lithologies ranging from a basal glacial diamictite overlain by volcanic rocks and lastly precipitation of BIF and carbonates. The Postmasburg Group ends the Transvaal Supergroup in the GWA with a major erosional unconformity. While subgroups and formations of the Ghaap Group in the GWA are correlative to subgroups and formations of the Chuniespoort Group in the TA, the equivalent of the Postmasburg Group in the GWA is notably absent in the TA (Fig. 5.1D). As such, strata of the Transvaal Supergroup in the TA exhibit a significant gap in the sedimentary record right before the GOE, which has been pinpointed to the Duitschland and Rooihoogte formations of

the lowermost Pretoria Group (TA), based on the first unquestionable disappearance of MIF-S. Consequently, the upper Postmasburg Group, including the Hotazel Formation, become critical targets for investigating Earth's atmospheric oxygen evolution just prior to the loss of MIF-S. In contrast, strata of the Transvaal Supergroup in the GWA miss an equivalent to the Pretoria Group (Fig. 5.1D), thereby lacking sedimentary records that could detail the GOE, marked by the demise of MIF-S, (Gumsley et al., 2017).

5.2.2 The Hotazel Formation

The Hotazel Formation, dated to ~2.4 Ga and first defined by Rogers (1906), is part of the upper Postmasburg Group, which unconformably overlies the Ghaap Group. Anchoring the Postmasburg Group is the glacial diamictite-dominated Makganyene Formation (Polteau et al., 2006). The Makganyene Formation is overlain by the Ongeluk Formation, a massive volcanic sequence, mainly comprised of basalts and andesites. Conformably succeeding the Ongeluk Formation are the BIF and Mn-rich layers of the Hotazel Formation, which is again conformably overlain by the Mooidraai Formation. The latter consists of various carbonate lithologies (limestones and dolostones) and constitutes the uppermost formation of the Postmasburg Group (Tsikos et al., 2001).

Geochronologically, the depositional age of the Hotazel Formation is bracketed by the overlying Mooidraai Formation and the underlying Ongeluk Formation. The Mooidraai Formation is dated to 2394 ± 26 Ma (Bau et al., 1999) and 2392 ± 23 Ma (Fairey et al., 2013) using Pb-Pb and U-Pb dating, respectively. Conversely, the 2424 ± 23 Ma U-Pb date from the Ongeluk Formation (Gumsley et al., 2017) establishes a maximum age constraint.

The Hotazel Formation has a thickness of 100-150 meters and is one of five erosional relicts (Kalahari, Avontuur, Leinster, Langdon and Hotazel) that combined comprise the Kalahari Manganese Field (KMF) (Beukes et al., 2016), (Fig. 5.1B). The Hotazel Formation in the area of drillcore MP-72 near the Middelplaats mine is characterized by four BIF units (BIF-1, BIF-2, BIF-3, BIF-4) interrupted by three manganese layers, a lower (MnF-1), a middle (MnF-2) and an upper manganese bed (MnF-3), figure 5.2 (Beukes et al., 2016). The manganese layers vary in thickness, but MnF-1 is the most significant and reaches a maximum thickness of 45 meters at the Mamatwan Mine, while the thickness of MnF-2 and MnF-3 are typically less than 2 and 1 meters, respectively, although very variable. Mineralogically the lower BIF layers overlying the Ongeluk Formation are mainly composed of jaspilite and hematite, whereas

stratigraphically higher BIFs are predominantly comprised of magnetite-hematite, magnetite-carbonate and magnetite-silicate facies (Gutzmer and Beukes, 1996; Tsikos and Moore, 1997). The manganese layers display a cyclical relationship with the BIF at the top and the bottom. These contacts from BIF to manganese bands gradually transition from chert-rich BIF to bands of hematite-lutite, followed by a zone of jacobsite and lastly, the Mn-layers comprised of braunite-lutite bands (Fig. 5.2). (Gutzmer and Beukes, 1996; Tsikos et al., 2010).

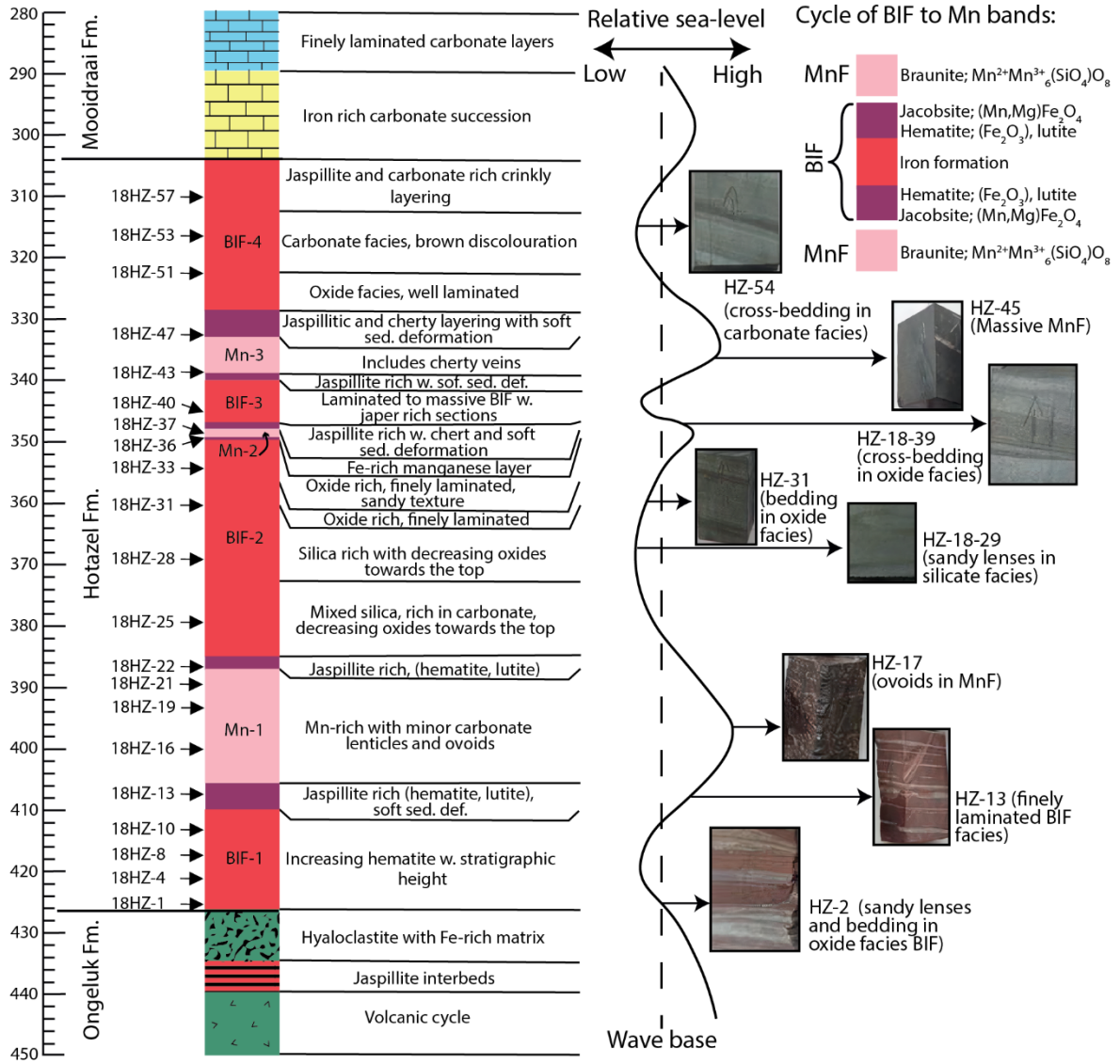

Figure 5.2. *Detailed sedimentary log of MP-72 drill* core intersecting the upper Ongeluk, Hotazel and lower Mooidraai formations. The figure also includes a relative sea-level curve linking sedimentary variations to environmental change. Note the cyclic nature of the Manganese and BIF (cherty BIF → hematite, lutite → jacobsite → braunite). The figure is modified from Fitton (2022)

5.3 Current Depositional Models for the Hotazel Formation

The genesis of the Hotazel Formation is a vigorously debated topic (Beukes, 1983, 1986; Cairncross & Beukes, 2013; Cornell & Schütte, 1995; Mhlanga et al., 2023; Tsikos & Moore, 1997). One prevalent and classical model for Mn-rich BIF deposition suggests that iron and manganese precipitate from reduced waters during upwelling (Beukes et al., 2016; Smith et al., 2013; Yin et al., 2023). In the *Upwelling Model,* hydrothermal fluids enriched in Fe(II) and Mn(II) are transported onto an oxygenated shelf environment in an otherwise stratified ocean, where these elements are oxidized and precipitated as insoluble Fe(III)- and Mn(III/IV)-(hydr)oxides onto the ocean floor (Fig. 5.3A). In this scenario, Fe is deposited more distal than Mn since Fe-oxidation occurs at a lower redox potential Eh relative to Mn-oxidation (Spinks et al., 2023). However, the Fe-beds of the Hotazel Formation contain tiny wave-ripple cross-lamination, pointing to deposition above the storm wave base, a sedimentological feature that is not found in the Mn-layers (Cairncross and Beukes, 2013). The Mn-layers thus appear to have been deposited in deeper waters, below storm wave base, relative to a shallower deposition of the Fe-beds (Cairncross and Beukes, 2013), contradicting the *Upwelling Model*, which is based on redox dynamics. In addition, the Hotazel Formation features interfingering of Mn-layers with granular jasper, lavas and tuffaceous beds, indicating a deposition nearer to a vent source (Beukes et al., 2016). However, at the same time, geochemical indicators for at least high-temperature hydrothermal activity (e.g., a positive Eu anomaly) are absent or, at best very weak in the Hotazel Formation (Tsikos and Moore, 1997). To account for these observations, a second model for Mn-rich BIF deposition suggests the influence of a low-temperature (<250 °C) hydrothermal plume, related to volcanic activity in a back-arc basinal setting, that intrudes into a fully oxygenated water column. In this *Hydrothermal Plume Model*, iron precipitates in shallower waters closer to the thermally uplifted vent of the evolving volcanic arc, while manganese sedimentation occurs in deeper waters at the distal end of the hydrothermal plume (Fig. 5.3B). The problem with this model is, that the distance of Fe- and Mn-precipitation from the plume source does not change with transgression and regression cycles, unless the plume activity is depending on water depth, which is very unlikely.

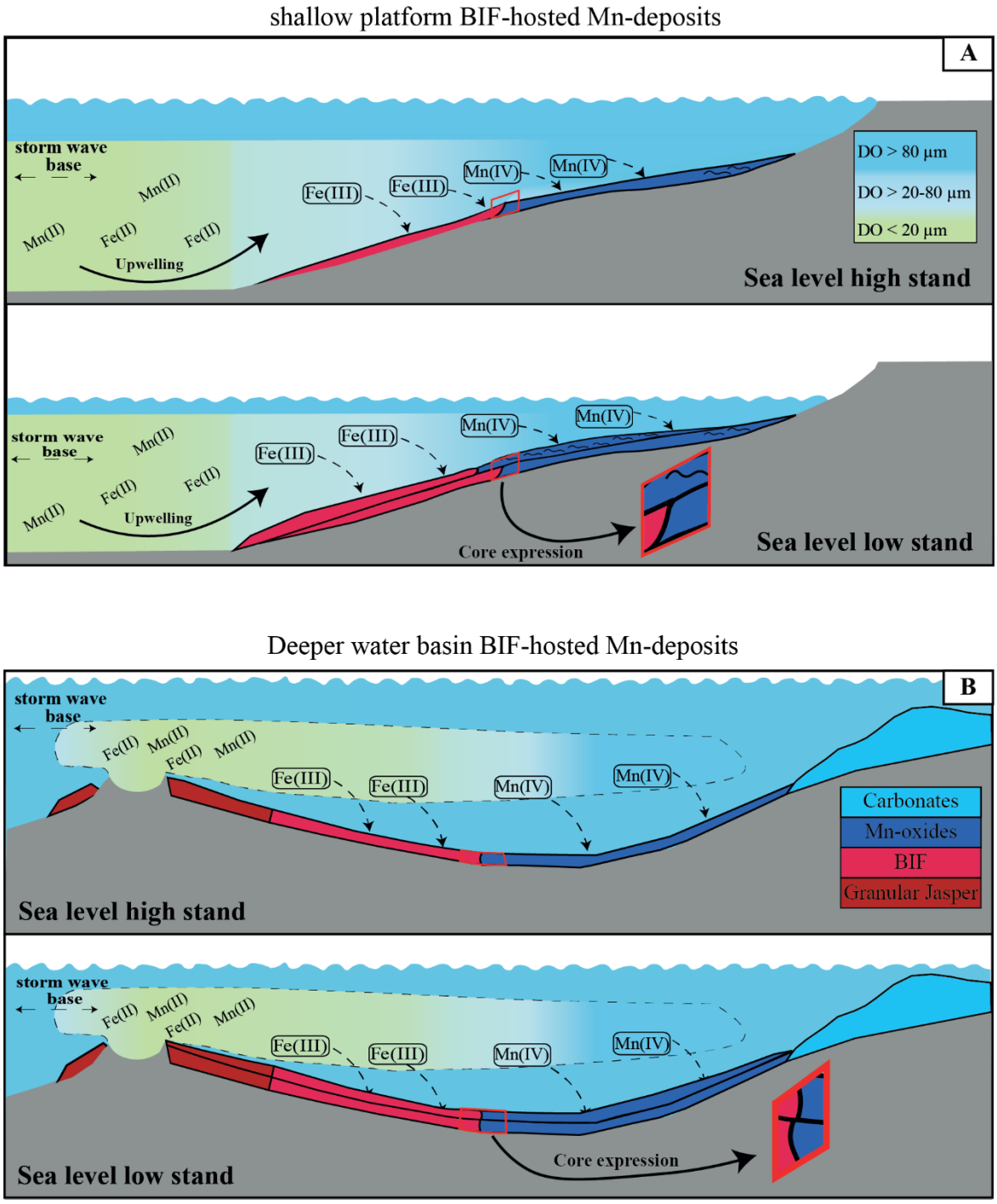

Figure 5.3. *Illustration of the two predominant models for the genesis of the Hotazel Formation.* **Model A** (*Upwelling Model*) describes a scenario where upwelling deep waters enriched in reduced Fe and Mn that traverse a chemocline in an upwelling zone, leading to deposition of Fe distal and Mn more proximal to the shoreline. **Model B (***Hydrothermal Plume Model)* suggests a low-temperature hydrothermal plume supplying reduced Fe and Mn to a restricted back-arc basin within a fully oxygenated water column. This dynamic facilitates BIF deposition in relatively shallow waters (closer to the vent) and Mn sedimentation in deeper water, more distal to the vent, where the Fe-supply is exhausted.

5.4 Methods

5.4.1 Major Elements and Trace Elements

Major and trace element analyses were performed in the Isotope Geochemistry Group within the Department of Geosciences at the University of Tuebingen and reported in Fitton (2022) following the analytical method described in detail in Albut et al. (2018).

5.4.2 Molybdenum Isotopes

Depending on the Mo concentration of the respective sample, between 100 and 600 mg of powdered sample were weighed into 30 mL Savillex Teflon beakers, and an adequate amount of ^{97}Mo-^{100}Mo double spike was added, aiming for a spike-sample Mo ratio of 1:1. Subsequently, the samples were digested in a 2.5:1 mixture ratio of 28M HF and 14M HNO_3 for seven days at 100 °C with frequent ultrasonication. Next, samples were dried down and redissolved in 6M HCl two times in cycles of 3 days at 120 °C, applying frequent ultrasonic treatments in order to redissolve any fluoride complexes that formed during the initial digestion step. For chromatographic separation of Mo, the samples were dissolved in 1.8 mL 3M HCl. They were then purified using 7mL columns containing 2 mL of the anion exchange resin Eichrom AG1-X8 (100-200 mesh), employing a single-step chromatographic separation procedure following the method developed by Willbold et al. (2016). Measurements of Mo isotope ratios were performed on the ThermoFisher© Scientific NeptunePlus multi-collector inductively-coupled plasma mass spectrometer (MC-ICP-MS) connected to a CETAC© Aridus II™ sample introduction system housed at Isotope Geochemistry Laboratory, University of Tuebingen. Isobaric interferences on the ^{98}Mo and ^{100}Mo-ion signals by ^{98}Ru and ^{100}Ru were accounted for by monitoring the ^{99}Ru signal and calculating signal intensities of the Ru interference isotopes using instrumental mass-bias adjusted natural abundances. Background signals were corrected by on-peak-zero subtraction of pure analyte acids. Samples and standards were measured in low resolution and static mode encompassing 90 cycles, each with a 4.2 second integration time. The double-spike correction was done using exponential mass fractionation law, ensuring adequate correction for both the instrumental mass bias and any mass-dependent fractionation processes during the purification steps. Data are reported using delta notation relative to the international reference material NIST-SRM-3134 (NIST 3134), as shown in equation 1. To facilitate inter-laboratory data comparison, an offset of 0.25 ‰ was applied to all data to account for the isotopic difference between the standard Johnson Matthey

(JM) and the NIST 3134 (Goldberg et al., 2013; Nägler et al., 2014), according to equation 2 (see, for example, Craig, 1957).

$$\delta^{98/95}Mo_{3134} = \left(\frac{^{98}Mo/^{95}Mo_{sample}}{^{98}Mo/^{95}Mo_{3134}} - 1\right) \times 1000 \quad (1)$$

$$\delta^{98/95}Mo_{3134+0.25} = 1.00025 \times \delta^{98/95}Mo_{3134} + 0.25 \quad (2)$$

The NIST 3134 and the JM reference solutions displayed mean values of $\delta^{98/95}Mo_{3134}$ at 0.000-±-0.024 ‰ (2SD, n = 16) and -0.260 ± 0.087 ‰ (2SD, n = 10), respectively. This matches both literature values (e.g., Greber et al., 2012; Goldberg et al., 2013; Kurzweil et al., 2016; Ossa Ossa et al., 2018) and the long-term reproducibility of the Isotope Geochemistry Laboratory in Tuebingen, yielding an offset between NIST 3134 and the JM ($\Delta^{98}Mo_{(JM- NIST 3134)}$) of -0.274 ± 0.056 ‰ (2SD, n = 223). The basalt rock reference material JB-2 (Geological Survey of Japan) determined analytical session during course of this study gave a $\delta^{98/95}Mo_{3134+0.25}$ value of 0.270 ± 0.032 ‰ (2SE, n = 1), which aligns with both the compiled literature average reporting a mean of $\delta^{98/95}Mo_{3134+0.25-}$=-0.298-± 0.033 ‰ (2SD, n = 51) (Casalini et al., 2019; Chen et al., 2019; Freymuth et al., 2015; Villalobos-Orchard et al., 2020; Willbold et al., 2016; Zhao et al., 2016) and the long-term Tuebingen Laboratory reproducibility of $\delta^{98/95}Mo_{3134+0.25}$ = 0.284 ± 0.046 ‰ (2SD, n = 38). The full procedural blanks contained 0.7 ng Mo, which is negligible relative to the amount of Mo separated from the samples, and thus, no blank correction was performed.

5.4.3 Iron Isotopes

For Fe isotope analysis, approximately 15 mg of sample powder was added to 7 mL Savillex beakers. The digestion followed the same method as for Mo (section 5.4.2), but without adding the (^{57}Fe-^{58}Fe) double-spike tracer solution. After digestion, the samples were redissolved in 3mL 6 M HCl, and an aliquot containing ~15 µg Fe was doped with the ^{57}Fe-^{58}Fe double-spike tracer in a 1:1 sample-spike ratio. The Fe purification was performed using the anion exchange resin AG1-X8 (100–200 mesh), following the method described by Schoenberg and von Blanckenburg (2005). The samples were then dissolved in 0.3 M HNO_3 to a concentration of 2.5 µg/g Fe. Measurements were also conducted on ThermoFisher© Scientific NeptunePlus MC-ICP-MS housed at the Isotope Geochemistry Laboratory in Tuebingen, but coupled to the standard SSI dual cyclonic spray chamber. The instrument was set to measure in medium resolution mode to avoid polyatomic interferences from, for example, $^{40}Ar^{16}O^+$ on $^{56}Fe^+$ and

$^{40}Ar^{14}N^{+}$ on the $^{54}Fe^{+}$ signals (Weyer and Schwieters, 2003). The MC-ICP-MS was operated in static mode and $^{52}Cr^{+}$ and $^{60}Ni^{+}$ were simultaneously measured with Fe isotope beams for correction of isobaric interferences of $^{54}Cr^{+}$ on $^{54}Fe^{+}$ and $^{58}Ni+$ on $^{58}Fe^{+}$ signals through natural abundances of relevant isotopes, assuming identical instrumental mass bias fractionation between Cr, Ni and Fe during the measurements. Any background signal was corrected by subtracting the on-peak-zero signal of the 0.3M HNO_3 uptake solution before and after each sample measurement. Each measurement consisted of 90 integration cycles of 4.2 seconds. The double-spike deconvolution technique following the method by Compston and Oversby (1969) with exponential mass fractionation law allowed in-run correction of the instrumental bass-bias and mass-dependent isotope fractionation potentially occurring during Fe purification. Results are reported in δ-notation relative to the IRMM-014 and expressed as permille deviation by multiplication with 1000 (equation 3):

$$\delta^{56/54}Fe = \left(\frac{^{56}Fe/^{54}Fe_{sample}}{^{56}Fe/^{54}Fe_{IRMM\ 014}} - 1\right) \times 1000 \quad (3)$$

The IRMM 014 returned a $\delta^{56/54}Fe_{IRMM\ 014}$ value of 0.000 ± 0.020 ‰ (2SD, n = 13) in accordance with the long-term reproducibility of analytical sessions of 0.000 ± 0.034 ‰ (2SD, n = 313). The in-house Tueb-Fe standard yielded a value of -0.375 ± 0.027 ‰ (2SD, n = 8), complying well with other studies (Babechuk et al., 2019; Wagner et al., 2021; Wu et al., 2017) and the Tuebingen Laboratory's long-term reproducibility of -0.377 ± 0.038 ‰ (2SD, n = 103). The basalt rock reference material JB-2 (Geological Survey of Japan) returned a $\delta^{56/54}Fe_{IRMM\ 014}$ value of 0.076-±-0.023 ‰ (2SE, n = 1), which agrees well with the compiled literature values of 0.071 ± 0.021 ‰ (2SD, n = 23) (He et al., 2015; Millet et al., 2012; Schuth et al., 2015; Weyer & Ionov, 2007; Zhu et al., 2020). Similarly, the iron formation rock reference material IF-G (Centre de Recherches Petrographiques et Geochimiques) determined during the course of this study gave a $\delta^{56/54}Fe_{IRMM\ 014}$ value of 0.642 ± 0.022 ‰ (2SE, n = 1), which also aligns with our compilation of published values of 0.635 ± 0.041 ‰ (2SD, n = 5) (Albut et al., 2019; Busigny et al., 2018; Kurzweil et al., 2016; Mänd et al., 2021; Nie et al., 2017). The total procedural blank contained 30 ng Fe, which is negligible relative to the amount of iron in the samples.

5.5 Results

5.5.1 Geochemical Characterization

Following the general stratigraphy of the Hotazel Formation described in Beukes et al. (2016), the drill core samples are categorized into BIF-intervals (BIF-Group; BIF-1, BIF-2, BIF-3, BIF-4), Mn-intervals (Mn-Group; MnF-1, MnF-2, MnF-3) and Jasper-intervals (Jasper-group; Jasper-1, Jasper-2, Jasper-3 and Jasper-4), of which the BIF and manganese intervals cover the majority of the core (Fig. 5.2; Table 1). Indicators for detrital input (e.g., Al, Ti) display stable and low concentrations irrespective of lithotype and stratigraphic height. Specifically, the average Al and Ti contents are 0.131 wt.% and 0.0184 wt.%, respectively, considerably lower than values from the Post Archean Average Shale (PAAS) of 10.0 wt.% and 0.599 wt.%, respectively (Taylor and McLennan, 1985).

Neither BIF nor Mn samples show any contribution from high-temperature hydrothermal fluids (Fig. 5.4). There is also little indication of significant contribution from low-temperature hydrothermal fluids, as indicated by rare earth elements and PAAS normalized REE+Y patterns (Fig. 5.4). Some samples from BIF-1, Jasper-1 and BIF-2 display Y/Ho ratios resembling those of hydrothermal waters (~28–31; Men et al., 2020), but most samples have ratios more consistent with Paleoproterozoic surface seawater (~48–65; Men et al., 2020), as denoted in Table 1. The PAAS normalized REE+Y patterns resemble modern seawater, exhibiting relative enrichments in Heavy REE (slope: Mn-bands = 6.69, BIF-bands = 5.98) relative to light REE (slope: Mn-bands = 8.46, BIF-bands = 8.41). Additionally, the REE+Y patterns highlight a relative enrichment in Y, while Eu displays insignificant to no deviation from the general pattern (Fig. 5.4). Notably, although the enrichment in La gives the impression of a negative Ce anomaly, only a few samples demonstrate true negative cerium anomalies, and these are not associated with any specific lithotypes, nor are they uniform within layers (Fig. 5.5).

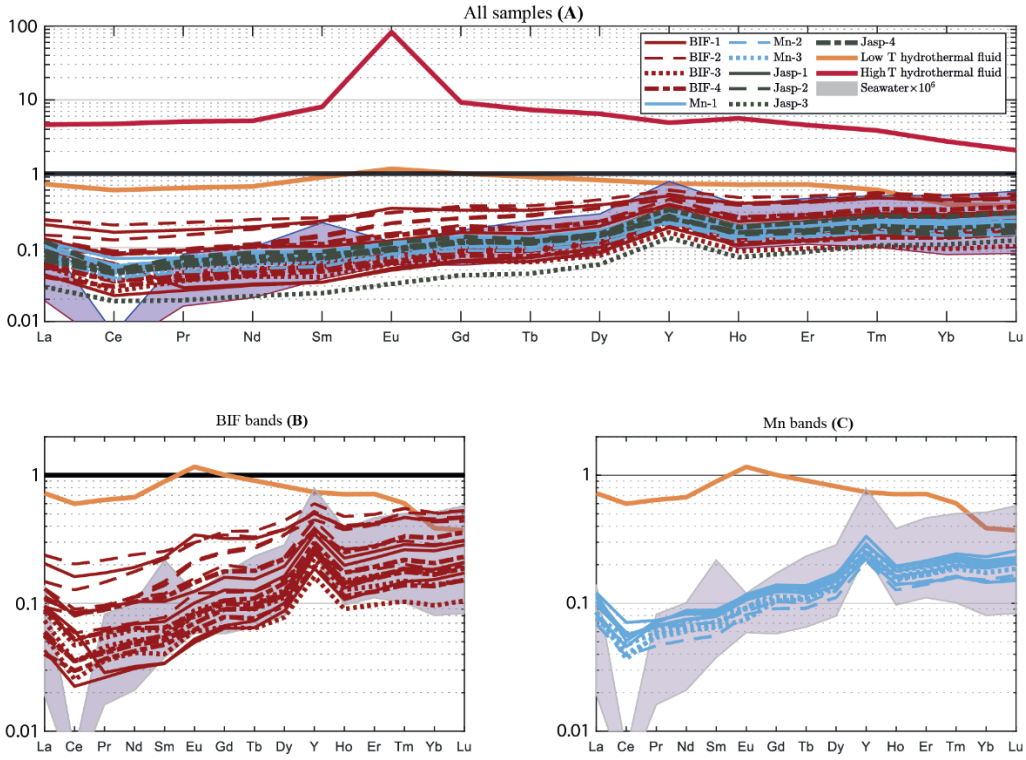

Figure 5.4. *PAAS normalized REE+Y patterns* of **(A)** all samples, **(B)** BIF bands and **(C)** Mn bands. Low and high-temperature hydrothermal fluid (Tchatchueng et al., 2021) and Seawater × 10^6 (Bolhar et al., 2004) are plotted for reference.

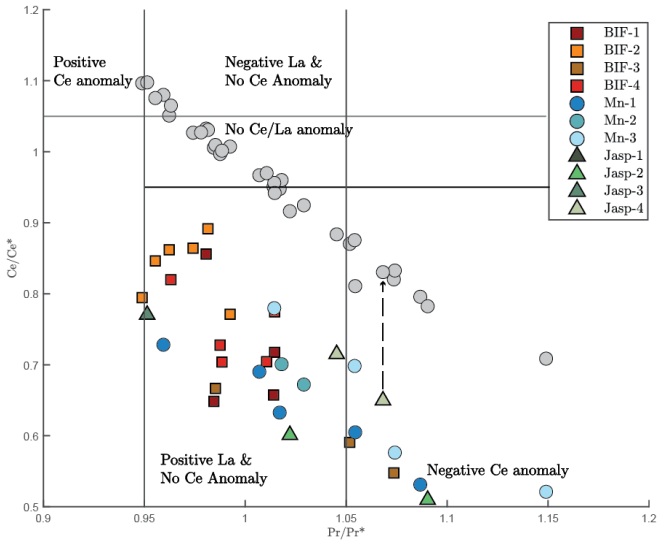

Figure 5.5. *True Ce-anomaly discrimination diagram* calculated after Bau and Dulski (1996) (colored points) and Lawrence and Kamber (2006) (grey points). Please note that while each data point has been shifted vertically, no samples within the negative Ce-anomaly field change discrimination box.

Contrary to typical Mo adsorption patterns, no discernible trend is observed between MnO content and Mo concentrations, while a weak trend is observed for most samples between Fe_2O_3 and Mo contents (R^2 = 0.54; Fig. 5.6A and B). All samples display a low Mo content irrespective of lithotype, with Mn-group ranging from 0.818–0.059 µg/g and the BIF-group from 0.078–0.968 µg/g. Iron isotopic compositions range from -2.95 to 0.497 ‰, with Jasper and Mn-layers returning lower $\delta^{56/54}Fe_{IRMM\ 014}$ values (-2.95 to -1.76 ‰) relative to BIF-layers (-1.53 to 0.497 ‰). Notably, three samples from BIF-1 align more with the Jasper and Mn-Group and are categorized as BIF-1-Subgroup (BIF-1-413.35; $\delta^{56/54}Fe_{IRMM\ 014}$ = -2.13 ‰, BIF-1-417.39; $\delta^{56/54}Fe_{IRMM\ 014}$ = -2.16 ‰). Samples classified as Jasper or MnF, in concert samples of the BIF-1-Subgroup, are jointly termed Group-1 (Fig. 5.6C and D). Molybdenum isotopes exhibit two distinct trends. The Group-1 samples has Fe/Mn<10 and display a moderate positive correlation with the Mo isotopic compositions (R^2 = 0.53; Fig. 5.6D). In contrast, the remainder BIF samples fall in a narrow Mo isotopic range ($\delta^{98/95}Mo_{3134+0.25}$ = 0.493–1.016 ‰) irrespective of the Fe/Mn ratio and with no apparent trend (Fig. 5.6D).

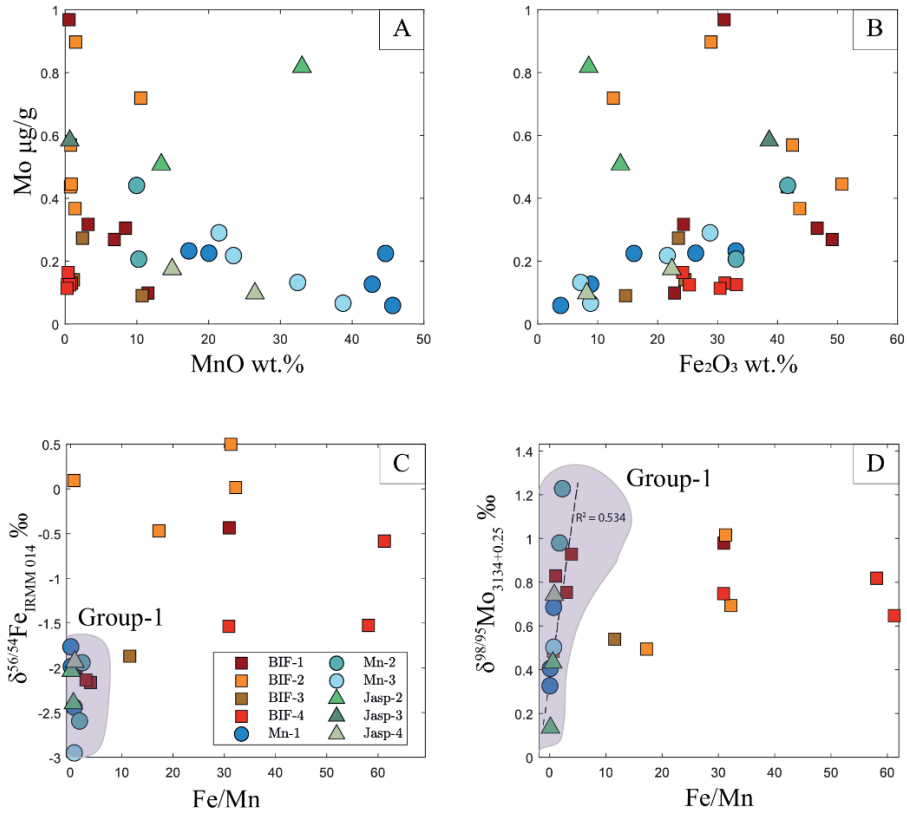

Figure 5.6. *Binary diagrams* showing Mo, $\delta^{56/54}Fe_{IRMM\ 014}$ and $\delta^{98/95}Mo_{3134+0.25}$ plotted against selected parameters (MnO, Fe_2O_3, Fe/Mn). Please note the anti-correlation between Mo and MnO in **(A)**. Group-1 samples, with a grey-colored background, can be identified in **(C)** and **(D)**, but are not as easily discernable in **(A)** and **(B)**, and therefore not defined.

5.5.2 Chemostratigraphic Trends

Starting from the lowermost sample belonging to the Hotazel Formation at 420 meters core depth (BIF-1), $\delta^{98/95}Mo_{3134+0.25}$ values display a continuous negative trend, declining from 0.828 ‰ to 0.134 ‰ by the top of MnF-1 (Fig. 5.7, column 5), while $\delta^{56/54}Fe_{IRMM\ 014}$ values remain relatively constant, ranging from -2.43 to -1.76 ‰ throughout the same interval (Fig. 5.7, column 6). The isotopic trends are accompanied by subtle decreases in Mo, Ce/Ce* and Y/Ho from 0.316 µg/g, 0.648, 50.3 to 0.126 µg/g, 0.531, 39.7, respectively (Fig. 5.7, columns 2–4).

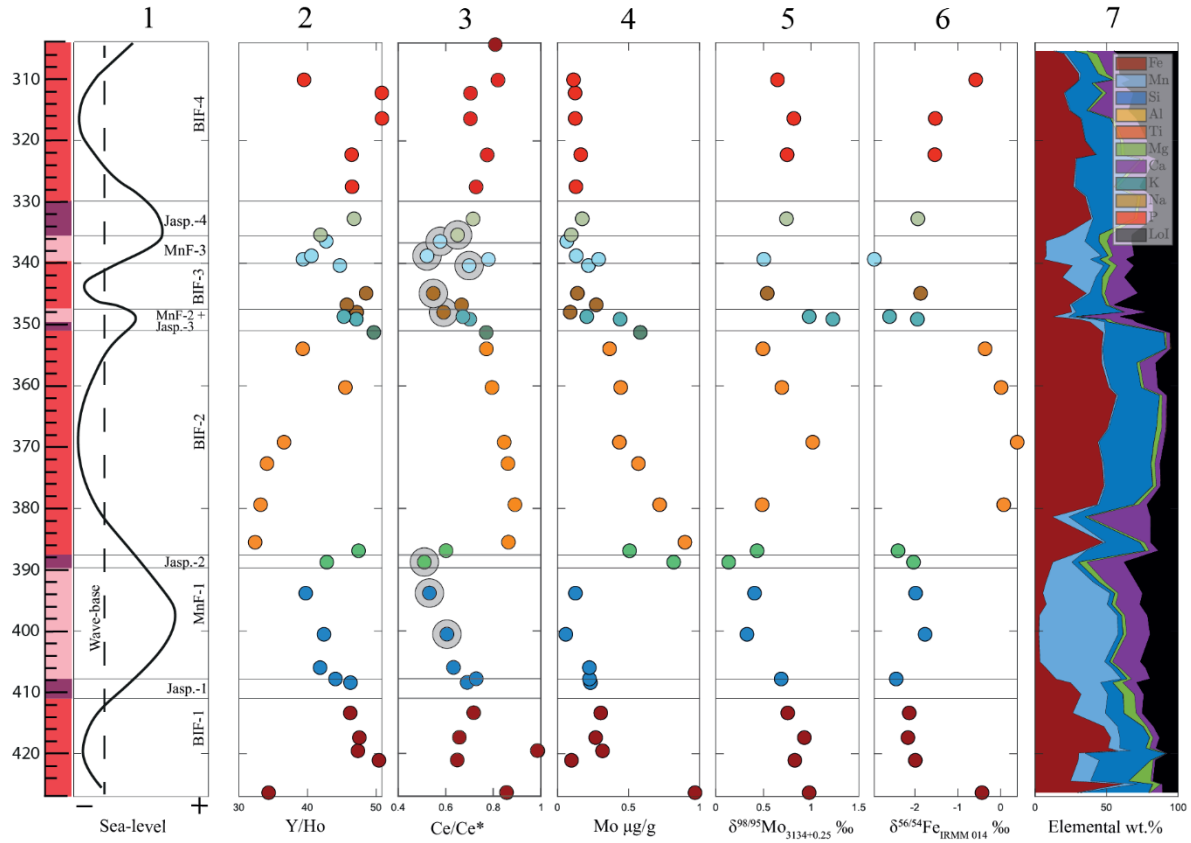

Figure 5.7. *Chemostratigraphic evolution* of selected geochemical parameters through drill core MP72. The sea-level curve is adapted from Fitton (2022), and the grey circles encircling some samples in column 3 represent samples exhibiting a true negative cerium anomaly, as determined in Figure 5.5.

In the Jasper-2 to lowermost BIF-2 intervals (388–379 m core depth), most geochemical parameters change abruptly following either a positive ($\delta^{56/54}Fe_{IRMM\ 014}$, Ce/Ce*, Mo) or negative (Y/Ho) change. Specifically, the shift results in a change from -2.40 ‰, 0.510, 0.82 µg/g and 42.8 to values of 0.09 ‰, 0.891, 0.72 µg/g, and 33.1 for $\delta^{56/54}Fe_{IRMM\ 014}$, Ce/Ce*, Mo

and Y/Ho, respectively. In contrast, the response in $\delta^{98/95}Mo_{3134+0.25}$ values from 0.43 ‰ in Jasp-2 to 1.02 ‰ only manifests about 10 meters higher in the core at 369 meters within the middle BIF-2 interval. The trend in $\delta^{98/95}Mo_{3134+0.25}$ is more gradual, signifying a continuous trend towards heavier Mo isotopic compositions. Following the abrupt shift, $\delta^{56/54}Fe_{IRMM\ 014}$ and Ce/Ce* remain relatively stable between 0.385 to -0.363 ‰ and 0.891 to 0.771 but display true negative values in the upper segments of MnF-1 and lower Jasper-2. In contrast, the remaining parameters follow either a continuous decreasing (Mo, $\delta^{98/95}Mo_{3134+0.25}$) or increasing (Y/Ho) trend, terminating at values of 0.366 µg/g, 0.493 ‰ and 39–45, respectively, at the top of BIF-2 (353 m). Progressing into MnF-2 and Jasper-3, $\delta^{98/95}Mo_{3134+0.25}$ and $\delta^{56/54}Fe_{IRMM\ 014}$ abruptly shift from 0.729 ‰ and -2.231 ‰ to 1.228 ‰ and -2.594 ‰, respectively, over approximately 5 m of strata. This shift is accompanied by scattered Mo concentrations ranging from 0.089 to 0.582, a slight increase in Y/Ho values to about 47, and a continuously decreasing Ce/Ce* anomaly ending at values of 0.672.

In BIF-3, starting at 348 m, both $\delta^{98/95}Mo_{3134+0.25}$ and $\delta^{56/54}Fe_{IRMM\ 014}$ rebound to values of 0.539 and -1.8 ‰, respectively, followed by an increasing trend to values of 0.647 and -0.583 at the top of BIF-4 (310m). An exception is sample MnF-3-339.35, which registers the lightest $\delta^{56/54}Fe_{IRMM\ 014}$ isotope value measured in this study of -2.951 ‰. Throughout the upper core segment (348–310 m), molybdenum concentrations and Y/Ho ratios remain stable, ranging from 0.065 µg/g to 0.289 µg/g and 39.4 to 50.8, respectively. The Ce/Ce* trend displays a smooth curve, reaching its minimum of 0.521 at the transition from BIF-3 to MnF-3, before rebounding and stabilizing at values ranging from 0.649–0.819 in Jasper-4 and BIF-4. In this core segment, the Ce/Ce* displays true negative anomalies that crosscut the sedimentary lithotypes (BIF-3, MNF-3 and Jasper 4).

5.6 Discussion

5.6.1 Iron Isotopes

Decoding the Light $\delta^{56/54}Fe_{IRMM\ 014}$ Values of the Hotazel Formation

Iron isotopes of BIFs are known to display a large range in Fe isotopic compositions with $\delta^{56/54}Fe_{IRMM\ 014}$ values extending several per mille positively and negatively. yet a peculiar aspect of the the Hotazel Formation is that it is characterized by predominantly negative $\delta^{56/54}Fe_{IRMM\ 014}$ values with Mn and Jasper layers as well as the BIF-1-Subgroup showing very low Fe isotopic compositions ranging from -1.77 ‰ to -2.95 ‰ (Fig. 5.7; Table 1). These

values cluster in the lowermost range of the natural variation in BIFs (~-2.5 to +1.5 ‰; Li et al., 2015) and, to our knowledge, include the lowest $\delta^{56/54}Fe_{IRMM\ 014}$ value ever measured in an iron (BIF and jaspilite) and Mn formations. Currently, no consensus exists to explain the large variation in iron isotopic compositions of BIFs; however, studies have proposed partial oxidation of hydrothermal ferrous iron (Bekker et al., 2010; Rouxel et al., 2005) and microbial dissimilatory iron reduction (DIR) in precursor Fe-(hydr)oxides sediments prior to lithification as potential pathways (Heimann et al., 2010; Johnson et al., 2008; C. M. Johnson et al., 2013). Addressing the 'progressive oxidation' hypothesis, the main problem is that only the last fraction of precipitated iron from an exhausted $Fe(II)_{aq}$ pool will inherit significantly negative Fe isotopic compositions, which does not fit for the Hotazel Formation with regards to the global open ocean BIF record (Li et al., 2015). Dissimilatory iron reduction produces a large negative offset in Fe isotopic compositions (~-1.3 to -2.6 ‰), but the 'DIR-hypothesis' is also problematic because it mainly applies to $\delta^{56/54}Fe$ variations over small areal scales. For Fe-recycling by DIR to explain stratigraphic scale $\delta^{56/54}Fe$ variations, a process capable of mixing large quantities of DIR-induced isotopically light $Fe(II)_{aq}$ on a basinal scale needs to be discovered (Li et al., 2015). Some estimates, however, indicate that up to 70 % of precipitated $Fe(III)_s$ in BIFs could be recycled back into the water column as $Fe(II)_{aq}$ under ideal conditions (Konhauser et al., 2005), but the extent of DIR is heavily dependent on the availability of organic carbon, which is challenging to constrain accurately for the Precambrian and thus limits model predictions.

Considering Archean seawater likely had a $\delta^{56/54}Fe_{IRMM\ 014}$ compositions between 0 and -0.5 ‰ (Beard et al., 2003) and considering that the complete oxidation process of $Fe(II)_{aq}$ to $Fe(III)_s$ induces a net positive isotopic offset of ~1.6–2.9 ‰ from seawater (Dauphas and Rouxel, 2006; Johnson et al., 2020 and references therein), a steady state system cannot produce the negative $\delta^{56/54}Fe_{IRMM\ 014}$ values observed. This suggests that the light $\delta^{56/54}Fe_{IRMM\ 014}$ values must be linked to either biological uptake or exhaustion of the marine ferrous iron pool or both. In the case of the Hotazel Formation, the combination of light $\delta^{56/54}Fe_{IRMM\ 014}$ values and Fe/Mn ratios typically below 4 indicate that exhaustion of the marine $Fe(II)_{aq}$ pool is at least partially responsible, if not the main driver. Given that Fe and Mn in many scenarios function as a redox couple, any oxidation of Mn(II) will be re-reduced by Fe(II) oxidation following equation 4 or 5 (Haese et al., 2000; Liu et al., 2022; Postma, 1985).

$$MnO_2 + 2Fe^{2+} + 2H_2O \rightarrow Mn^{2+} + 2FeOOH\ 2H + 2H^+ \quad (4)$$

$$Fe^{2+} + MnOOH \rightarrow FeOOH + Mn^{2+} \quad (5)$$

Based on the above equations, only when the marine iron pool is exhausted in $Fe(II)_{aq}$ does Mn start to oxidize and precipitate to any significant extent. The precipitation of Fe-(hydr)oxides from oxidation of $Fe(II)_{aq}$ follows a two-step process in which $Fe(II)_{aq}$ is first oxidized to $Fe(III)_{aq}$ by O_2 or Fe(II)-oxidizers that then precipitates as $Fe(III)_s$ (Dauphas and Rouxel, 2006), as shown in equation 6.

$$Fe(II)_{aq} \leftrightarrow Fe(III)_{aq} \rightarrow Fe(III)_s \quad 6$$

A Two-Stage Isotope Model Approach for the Hotazel Formation

In modeling the scenario of the Hotazel Formation, the process can be mathematically quantified using a two-stage open system isotopic model in which equilibrium fractionation is assumed between $Fe(II)_{aq}$ and $Fe(III)_{aq}$ and a Rayleigh fractionation for $Fe(III)_{aq}$ to $Fe(III)_s$ conversion (Anbar, 2004; Beard & Johnson, 2004; Dauphas & Rouxel, 2006; Johnson et al., 2004). This model is designed to simulate a scenario where iron is occasionally replenished and depleted in an ocean basin. The most widely applicable scenarios include (I) a (semi) restricted basin or (II) an upwelling zone onto a shallow continental shelf region, where replenishment of $Fe(II)_{aq}$ has intermittently ceased. In both cases, iron is systematically removed quantitatively from the system after replenishment. A key assumption behind the model is the open system approach, in the sense that any precipitated iron is considered permanently removed from the system and does not undergo reduction, dissolution and reincorporation into the aqueous iron pool. Given these assumptions, each sediment layer of iron oxide represents a fraction of precipitated iron from 0 to 1, which signifies the quantity of $Fe(III)_S$ removed from the system. Our measured samples $\delta^{56/54}Fe_{IRMM\ 014}$ compositions were then solved to match the instantaneous product function of the model (Fig. 5.8). A detailed explanation of the model assumptions, parameters and euqations used are given in the supplemenrary material (section 5.10).

To further independently verify the model's validity, we cross-validated the results using Fe/Mn ratios, following an approach similar to Tsikos et al. (2010). We assumed an initial aqueous Fe/Mn ratio of 70, slightly above the average oceanic crust (Qin and Humayun, 2008). Adapting the premise from Tsikos et al., 2010 that iron and manganese are removed at a constant rate of 100/1, the Fe/Mn ratio at any given time should reflect the amount of $Fe(III)_s$ removed from the reservoir at that specific time. This, in turn, provides an independent

validation of the relationship between the fraction of precipitated Fe^{3+}(f) and the isotopic composition in Figure 5.8A.

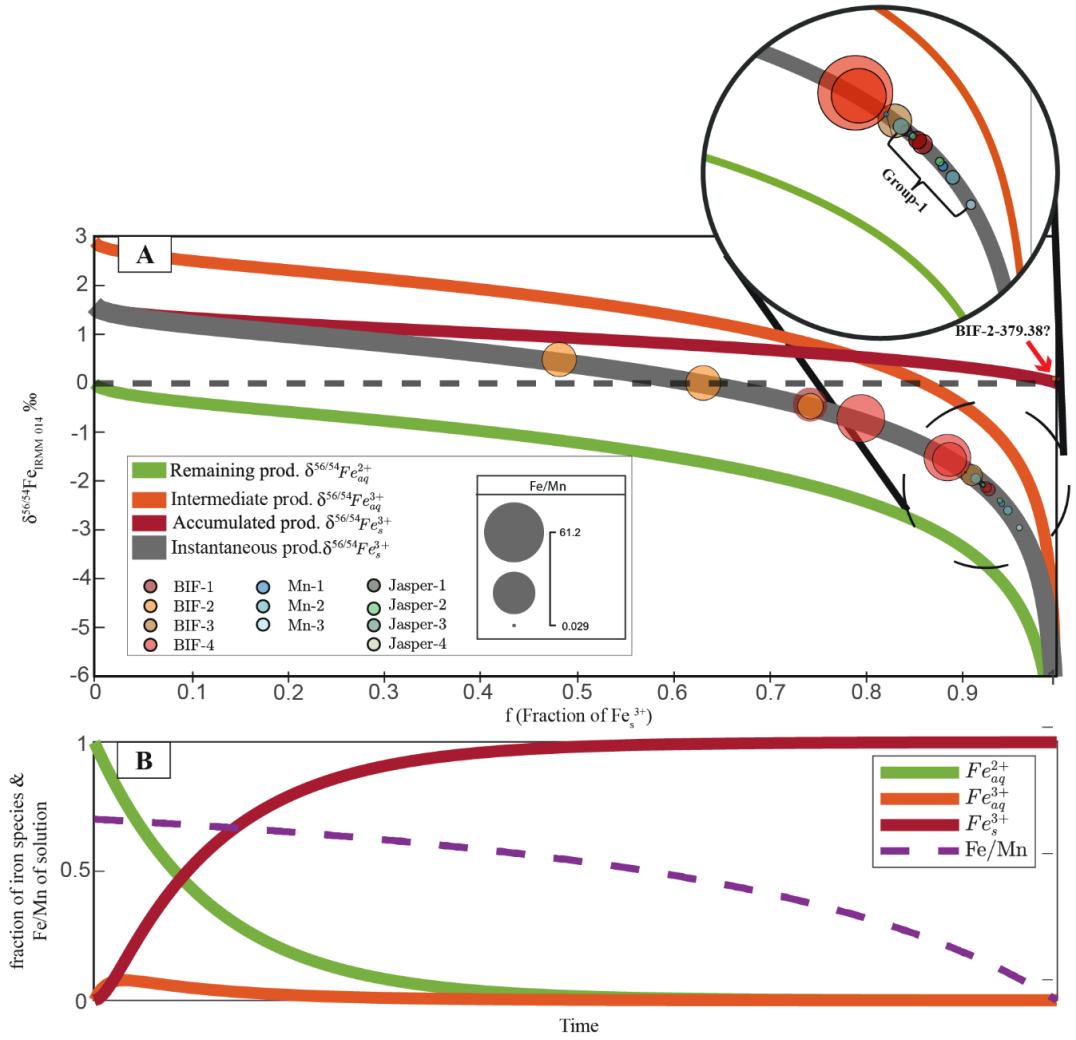

Figure 5.8. **(A)** *Isotopic evolution model of an open system without reactant replenishment, using a two-stage model approach*. Importantly, an 'open system' in this context implies that any precipitated iron leaves the system permanently. Yet, the system's input remains 'closed', meaning no $Fe(II)_{aq}$ is replenished. In the model, equilibrium fractionation is assumed between $Fe(II)_{aq}$ and $Fe(III)_{aq}$, while a Rayleigh condition is ascribed to the second stage, $Fe(III)_{aq}$ to $Fe(III)_{s}$, following the approach outlined in Dauphas and Rouxel (2006). The diameter of the circles represents the samples Fe/Mn ratio and the zoom-in illustrates an enhanced view of most of the samples. Panel **(B)** displays an evolution model for the proportion of iron species as a function of time since the system's closure. The model also integrates the evolution of the solution's Fe/Mn ratio, assuming an initial Fe/Mn ratio of 70 and maintaining a constant removal rate of 100/1. The supplementary information contains specific parameters and a detailed model explanation (section 5.10).

Modeled results show that negative $\delta^{56/54}Fe_{IRMM\ 014}$ values are only reached for the instantaneous product once about 60 % of the iron is precipitated from the water column (Fig. 5.8). Thus, the very low $\delta^{56/54}Fe_{IRMM\ 014}$ compositions observed in Group-1 indicate progressive depletion of aqueous ferrous iron content to about 90 %, based on comparison between the modeled results and measured $\delta^{56/54}Fe_{IRMM\ 014}$ values (Fig. 5.8A). Notably, the fact that samples from Group-1 also display the lowest Fe/Mn ratios substantiates the modeled outcomes. Yet, a seemingly contrasting observation is that samples with significantly higher Fe/Mn ratios (24–58) plot adjacent to Group-1 (Fig. 5.8A zoom-in). Therefore, the relationship between the quantity of iron removed and the Fe/Mn ratio of the samples appears relatively moderate and is likely influenced by additional processes such as DIR and diagenetic effects. In addition, from a stratigraphic perspective, a restricted basin scenario is plausible only if the isotopic composition of the samples gradually transitions towards lighter values until a replenishment occurs, returning Fe isotopic compositions close to that of Archean seawater (~0 ‰). Indications of such a dynamic are potentially visible in the lower segment of the drill core between 425 m and 380 m (Fig. 5.7, column 6). Interestingly, BIF-2-379.38, despite having one of the lowest Fe/Mn ratios of the sample set (0.648), exhibits a $\delta^{56/54}Fe_{IRMM\ 014}$ composition of 0.092 ‰. When modeling an open system by Rayleigh distillation, the very final fraction of precipitated iron is expected to mirror the isotopic composition of the initial reservoir. Considering the stratigraphic position of the BIF-2-379.38 at the transition between MnF-1 and BIF-2, the sample might encapsulate such a dynamic. The primary contention against an unreplenished open system scenario is that it fails to adequately explain the sedimentological observations of Mn deposition in deeper waters relative to Fe (Beukes et al., 2016; Fitton, 2022), which opposes typical marine redox dynamics.

5.6.2 Molybdenum Isotopes

Decoding the Heavy Mo Isotopic Compositions of the Hotazel Formation

The samples in Group-1, characterized by light $\delta^{56/54}Fe_{IRMM\ 014}$ values, display a large range in $\delta^{98/95}Mo_{3134+0.25}$, ranging from -0.115–0.978 ‰. That is unusually high $\delta^{98/95}Mo_{3134+0.25}$ isotopic compositions for samples consisting of several weight percent manganese, especially when considering that the largest known equilibrium isotopic fractionation of Mo in nature (~-3 ‰) occurs between Mn-oxides and dissolved molybdate MoO_4^{2-} (Barling and Anbar, 2004; Wasylenki et al., 2008). Based on the reasonable assumption that Mo adsorption to Mn-(hydr)oxides is the primary removal pathway for Mo in samples from Group-1, containing

about 5–35 wt.% Mn, and recognizing that all known processes fractionate Mo isotopes in a negative direction (Kendall et al., 2017), the $\delta^{98/95}Mo_{3134+0.25}$ values in the Mn layers imply that the $\delta^{98/95}Mo_{3134+0.25}$ composition of seawater was about 3–4 ‰. That is an exceptionally high Mo isotopic composition for a sedimentary formation deposited at the onset of the GOE in a significantly less oxygenated setting compared to the modern ocean, which registers a Mo signature of $\delta^{98/95}Mo_{3134+0.25} = 2.3 \pm 0.10$ ‰) (Barling et al., 2001; Siebert et al., 2003). Such high $\delta^{98/95}Mo_{3134+0.25}$ values in Mn-(hydr)oxides can almost only be reached by severe seawater Mo exhaustion of the marine molybdate inventory. However, elevated $\delta^{98/95}Mo_{3134+0.25}$ values of about 1 ‰ have previously been observed in BIFs and explained by deposition at different water depths (Kurzweil et al., 2016). In proximal environments, the adsorption of isotopically light and octahedrally coordinated Mo onto Mn-(hydr)oxides results in isotopically light sediments. Conversely, in distal settings, the diffusion of tetrahedrally coordinated and isotopically heavy seawater molybdate into the sediment porewaters generates heavy $\delta^{98/95}Mo_{3134+0.25}$ signatures (Kurzweil et al., 2016). However, in the context of current geological models for the genesis of the Hotazel Formation, this dynamic appears implausible, as the heaviest $\delta^{98/95}Mo_{3134+0.25}$ values sit in Mn-layers (Fig. 5.6D, Table 1). At the same time, Mo concentrations are generally lower in samples with high Mn content (Fig. 5.6A, Table 1), which is also peculiar since Mo adsorption affinity is higher for Mn-(hydr)oxides relative to Fe-(hydr)oxides (Smrzka et al., 2019). Likewise, the lower average of ΣREE+Y contents in Mn layers (ΣREE+Y = 19.2) relative to BIF layers (ΣREE+Y = 23.2) also indicate continuous depletion of marine metal inventories. Lastly, Molybdenum also has a reasonably high affinity to Fe-(hydr)oxides, and thus, the deposition of massive iron formation could exhaust the marine Mo inventory before deposition of the manganese-rich layers, potentially explaining the heavy $\delta^{98/95}Mo_{3134+0.25}$ compositions and low Mo concentrations in the Mn-layers.

Mo Adsorption and the Mn(III) Oxidation Hypothesis

An alternative hypothesis, proposed by Mhlanga et al. (2023), relates to the redox coupling of iron and manganese and the possibility of Mn deposition as Mn(III)-(hydr)oxides and not Mn(IV)-oxides, as is usually the case in the modern oxygenated ocean (J. E. Johnson et al., 2013; Tebo et al., 2004). In a less oxygenated ocean, at the onset of the GOE, Mn(II) oxidation possibly transformed to intermediate valence Mn(III)-(hydr)oxides, such as γ-MnOOH (manganite) at circumneutral to slightly alkaline pH as indicated experimentally (Murray et al., 1985). Chemically the reaction follows a single-step oxidation pathway to MnOOH as shown

in equation 7 (Morgan, 2005) and would fit mineralogical observations of no preserved Mn(IV)-oxides in the Hotazel Formation (Mhlanga et al., 2023).

$$4Mn^{2+}_{aq} + O_{2\,(aq)} + 6H_2O \rightarrow 4MnOOH + 8H^+ \quad (7)$$

Little work has been done on specific differences regarding metal adsorption rates onto Mn(III) relative to Mn(IV)-oxides. Generally, however, Mn(IV) compounds likely have higher adsorption rates compared to Mn(III) complexes, given that Mn(IV) has more unpaired electrons accessible for bonding and forming coordination complexes with other ions as well as a more negative surface charge (Tebo et al., 2004). These are all factors that enhance metal ion adsorption rates, although it should be noted that adsorption properties are heavily dependent on pH, other ligands and ions present in the environment and specific characteristics of the Mn-(hydr)oxide complex formed (e.g., surface area and charge, particle size, crystal structure) (Sun et al., 2019; Tebo et al., 2004). From a theoretical thermodynamic framework, γ-MnOOH has lower surface energies relative to MnO_2 (Sun et al., 2019) and could thus explain the trace element patterns observed in Mo and REE concentrations. Nevertheless, experimental work still needs to confirm whether the differences in Mn(III) vs. Mn(IV) adsorption rates would be significant enough to enforce an observable geochemical signal in sedimentary formations. Experimental data on molybdenum isotope fractionation factors between seawater and Mn-(hydr)oxides has focused on MnO_2 oxides (e.g., Barling & Anbar, 2004; Wasylenki et al., 2008) since it is the prevalent Mn-complex forming in modern oxygenated settings, but to the best of our knowledge, no experimental work has been carried out on other Mn(III)-(hydr)oxides species. For iron oxides and hydroxides, however, a range of fractionation factors are observed for Mo depending on the mineralogy, with $\delta^{98/95}Mo_{3134+0.25}$ values ranging from positive 0.83 to 2.19 ‰. Specifically, selected iron minerals show progressively increasing fractionation factors from magnetite to hematite: Magnetite (Fe_3O_4; $\Delta^{98}Mo = 0.83 \pm 0.60$ ‰), ferrihydrite ('$Fe(OH)_3 0.5H_2O$'; $\Delta^{98}Mo = 1.11 \pm 0.15$ ‰), goethite (FeO(OH), $\Delta^{98}Mo = 1.40 \pm 0.48$ ‰), hematite (Fe_2O_3, $\Delta^{98}Mo = 2.19 \pm 0.54$ ‰) (Kendall et al., 2017 and references therein). It is, therefore, reasonable to assume that a similar mechanism exists between different Mn-(hydr)oxides and could potentially explain the exceptionally high $\delta^{98/95}Mo_{3134+0.25}$ values observed in some manganese layers if the isotopic offset between seawater and MnOOH is smaller than that between seawater and MnO_2. Consequently, the Mn(III)-hypothesis could, at least partially, account for the heavy $\delta^{98/95}Mo_{3134+0.25}$ compositions in the Group-1.

5.6.3 Stratigraphic and Geochemical Framework

Current Depositional Models and Their Challenges

Both the *Upwelling Model* and *Hydrothermal Plume Model*, presented in section 5.3, fail to explain the sedimentological observations in the Hotazel Formation of tiny wave-ripple cross-lamination in its Fe-beds but not in the Mn-layers (Cairncross & Beukes, 2013). Counterintuitively to usual redox dynamics, this indicates deposition of the Mn-layers in deeper waters, below storm wave base, relative to a shallower deposition of the Fe-beds (Cairncross & Beukes, 2013). The *Upwelling Model* a (Model 1, Fig. 5.3A) satisfactorily explains most geochemical features, such as the light $\delta^{56/54}Fe_{IRMM\ 014}$ and heavy $\delta^{98/95}Mo_{3134+0.25}$ values and also the relative depletion of REE and Mo in manganese bands relative to iron layers by substantial marine metal depletion. The model would, however, require upwelling to cease for extended periods of time in order to deplete the heavily Fe(II) enriched Archean ocean in iron and initiate the deposition of manganese since significant Mn-deposition requires depletion of iron in the system (Spinks et al., 2023). From a chemostratigraphic perspective, the observed trends fit with overall lighter $\delta^{56/54}Fe_{IRMM\ 014}$ values during Mn deposition and renewal of iron and Mn to the system from replenishment events (likely upwelling). One clear and potentially two minor upwelling events are identified in the drill core (Fig. 5.7). That is based on the sudden positive shift in $\delta^{56/54}Fe_{IRMM\ 014}$ values and Y/Ho values that approximate hydrothermal sources (~28–30) rather than Paleoproterozoic waters (~48–65) (Men et al., 2020). The flaw of the model is that it fails to explain wave ripple cross-lamination in the iron beds and the absence of such textures in the Mn layers. Such features indicate that Mn deposition in the Hotazel Formation occurred in deeper waters relative to iron deposition, thus expressing an inversion of the marine redox gradient compared to typical marine redox dynamics.

For the *Hydrothermal Plume* scenario (model 2, Fig. 5.3B), iron is deposited in shallower waters closer to the thermally uplifted vent of the evolving volcanic arc, while manganese sedimentation occurs in deeper waters at the distal end of the hydrothermal plume. A prerequisite for the plume model is a fully oxygenated basin at the time of deposition, which is theoretically possible but unlikely, considering the deposition of the Hotazel Formation is ~2.4 Ga at the onset of the GOE. A supporting argument for the hypothesis is inferred shallow (<50 m) shelf environment depositional setting for the Ongeluk basaltic andesite, based on algal-laminae in dolomites succeeding the Mn ores (Beukes, 1983; Cornell & Schütte, 1995). Like the *Upwelling Model*, the *Hydrothermal Plume Model* also convincingly explains most geochemical trends through progressive metal depletion with distance from the plume. The

problems with this model are that few geochemical indications for hydrothermal activity are present in the Hotazel Formation, contradicting at least a high-temperature hydrothermal source, as evidenced from, for example, Eu anomalies (Schier et al., 2020; Tsikos & Moore, 1997) and Nd isotopes (Schier et al., 2020). Low-temperature hydrothermal sources (<250 °C) are difficult to identify geochemically (Bau & Dulski, 1996) and potentially could source the iron and manganese, especially contemplating that a marine origin of the $Fe(II)_{aq}$ and $Mn(II)_{aq}$ is almost unavoidable. The second and foremost problem with the *Hydrothermal Plume Model* is that the relative plume activity controls depositional changes from iron to manganese and vice versa, contradicting the apparent sea-level control of Fe and Mn layers based on sedimentological observations. The model can explain the sedimentological observations only if Mn deposition always occurs below and Fe deposition above the wave base. Since the distance from the core expression to the vent is fixed, this requires plume activity and relative sea-level changes to be intrinsically linked, which seems rather implausible.

The Bioproductivity Hypothesis

The Light Iron Isotope Signatures

As a third model proposed in this work, envisions a continental shelf setting where the deposition of Fe-Mn layers was controlled by the dynamic between primary productivity and dissolved O_2 in the water column. Primary productivity not only generates O_2 via oxygenic photosynthesis, but also synthesizes organic compounds (e.g., siderophores) and possesses the ability to oxidize Fe and Mn through anoxygenic photosynthesis (Knoll et al., 2012). Through changing levels of dissolved marine oxygen in the water column, this '*Bioproductivity hypothesis*' links sedimentological observation of deep-water Mn-deposits in the Hotazel Formation to both changes in relative sea-level and the interplay between primary productivity and respiration. Specifically, in periods with heightened primary productivity, the accumulation and subsequent decomposition of dead organic matter causes the expansion of the oxygen minimum zone (OMZ). In the modern ocean, OMZs display significant regional heterogeneity; however, a 'typical' OMZ is characterized by an O_2-depleted layer extending vertically from ~150 to 800 meters, in which dissolved O_2 concentration ranges between ~20–2 μmol/L. Importantly, while the central layer of most modern OMZs falls within this range, OMZs can start at depths as shallow as 10 meters and extend to depths exceeding 3500 meters (Fuenzalida et al., 2009; Karstensen et al., 2008; Paulmier & Ruiz-Pino, 2009). In addition to variations in the intensity of primary productivity, relative sea-level changes also move the

position of the OMZ accordingly (Moffitt et al., 2015). Any vertical displacement and/or expansion of the OMZ induces the dissolution of Fe-Mn-(hydr)oxides. These compounds were initially precipitated via either abiotic or biotic pathways in the overlying oxygenated waters; however, upon redissolution, they return to the aqueous solution as $Fe(II)_{aq}$ and $Mn(II)_{aq}$. At the oxidation front in the lower reaches of the OMZ, dissolved O_2 slowly starts to increase, and the dissolved $Fe(II)_{aq}$ and $Mn(II)_{aq}$ start to precipitate according to their redox potentials. Because $Fe(II)_{aq}$ requires less oxygen to be oxidized, iron precipitation happens earlier than $Mn(II)_{aq}$ oxidation at lower water depths. The concept is known as "oxygen minimum zone redirection" (Johnson et al., 1992; Klinkhammer & Bender, 1980) and has been empirically observed in Swiss lakes, sediments from the Indian Ocean and the Arabian Basin (Dickens & Owen, 1994; Schaller & Wehrli, 1996; Schenau et al., 2002).

During the final precipitation of Fe-(hydr)oxides from the water column, the precipitates will be enriched in $\delta^{56/54}Fe$ relative to seawater with an overall offset of about 1.6 to 2.9 ‰, depending on the specific pathway (Dauphas & Rouxel, 2006; Johnson et al., 2020). A critical aspect to highlight is that if iron replenishment is inhibited or absent, the iron precipitated becomes progressively lighter as the marine iron pool gets exhausted. After initial precipitation, the formed Fe and Mn precipitates face dissolution in the anoxic waters of the OMZ, mediated by DIR and dissimilatory manganese reduction (DMR), (Fig. 5.9). Due to the pronounced isotopic fractionation associated with DIR (~-1.3 to -2.6 ‰), the resulting $Fe(II)_{aq}$ pool is isotopically lighter than the Fe-Mn-(hydr)oxide counterparts, with the exact isotopic offset influenced by factors such as reaction rate, type of microbes, specific mineralogy, size of the precipitates, pH and temperature (Johnson et al., 2020). Subsequent to dissolution, this isotopically light iron and manganese pool is transported to the lower reaches of the OMZ, where it is reprecipitated (Fig. 5.9). During this phase, the dissolved Fe and Mn pool undergoes yet again oxidative reprecipitation, which induces a positive offset of about ~1.6–2.9 ‰ associated with Fe(II) oxidation (Dauphas & Rouxel, 2006; Johnson et al., 2020). Very importantly, this positive shift is imposed upon a previously established isotopically light Fe(II)aq pool caused predominantly through DIR and DMR in the OMZ and potentially further enhanced by limited $Fe(II)_{aq}$ replenishment to the basin. Consequently, the positive offset associated with the initial $Fe(II)_{aq}$ oxidation is surpassed by processes forcing the seawater Fe isotopic composition towards lighter values (e.g., DIR/DMR and basin restriction). Furthermore, as Fe conveys the OMZ, it potentially undergoes multiple precipitation-dissolution cycles, in what we term the 'DIR-engine', driving $\delta^{56/54}Fe$ signatures of $Fe(II)_{aq}$

increasingly lighter (Fig. 5.9). Finally, since Fe-(hydr)oxides precipitate out of solution prior to Mn-(hydr)oxides, dissolved $Fe(II)_{aq}$ in the OMZ inherits progressively lighter $\delta^{56/54}Fe$ compositions with ongoing iron precipitation. This mechanism explains the typically lighter $\delta^{56/54}Fe_{IRMM\ 014}$ values in Mn-layers relative to Fe-bands.

The Heavy Molybdenum Isotope Signatures

Molybdenum isotope compositions of the iron and manganese bands are decoupled from the oxygen minimum zone redirection process that controls the iron isotopes because Mo is immobilized in the anoxic sediment underlying the OMZ (Fig. 5.9). These sediments are enriched in Mo and carry isotopically light signatures. In contrast, the trace amounts of Mo that reach the final Mn-(hydr)oxide precipitates below the OMZ are remnants of isotopically heavy seawater molybdate that enter the deep-water sediments through direct transport from the water column, in a similar fashion to what is proposed in Kurzweil et al. (2016).

The Missing Cerium Anomaly

Typically, Mn-(hydr)oxides display positive Ce-anomalies due to the strong affinity of Ce to Mn-(hydr)oxides (Chester, 2009). However, an unusual feature of the Hotazel Formation is the observation of low Ce concentrations and true negative cerium anomalies in the Mn layers, which can potentially be attributed to the adsorption of Ce onto biogenic siderophores. These organic molecules are produced by microorganisms to sequester Fe(III) from the environment and compete with Mn-(hydr)oxides for cerium, which strongly limit the development of Ce anomalies in Mn-precipitates (Kraemer et al., 2017). As a result, Ce likely gets immobilized with biogenic siderophores in the anoxic sediments under the OMZ and, similar to Mo, is decoupled from further remobilization (Fig. 5.9). The observation that true negative Ce anomalies occur in the manganese layers of the Hotazel Formation (Fig. 5.7) suggests that the Ce(IV) that initially did adsorb to Fe-Mn-(hydr)oxides were subsequently re-released in the OMZ as Ce(III) alongside Fe(II) and Mn(II). Hereafter, the Ce was re-scavenged by Fe-(hydr)oxides before Mn-(hydr)oxide precipitation below the OMZ. The adsorption of Ce onto biogenic siderophores, as proposed by Kraemer et al. (2017), aligns with the *Bioproductivity Hypothesis*. This dynamic potentially explains the generally low Ce (and REE) concentration in the Hotazel Formation and provides a reason for the development of true negative Ce anomalies in the manganese layers.

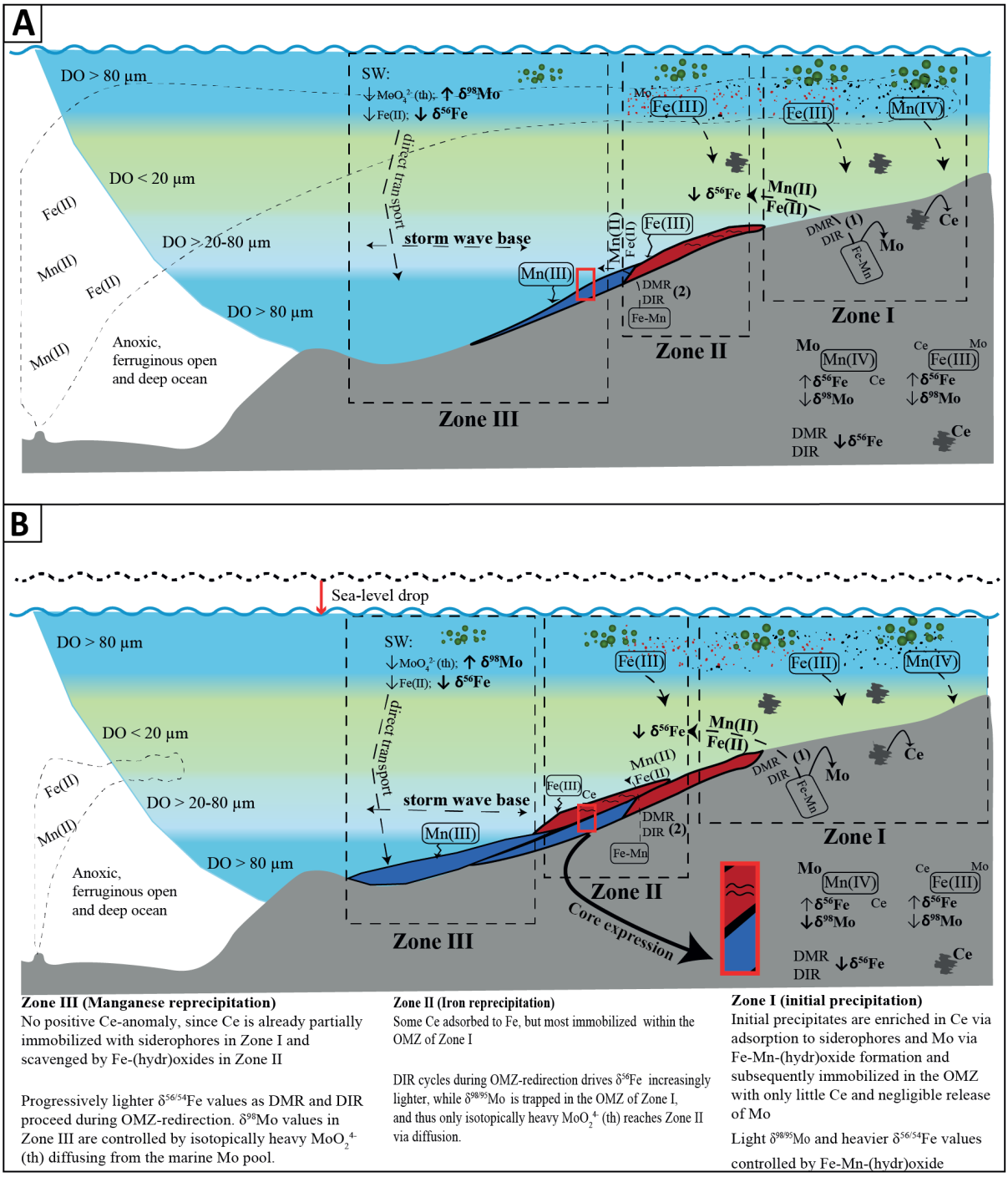

Figure 5.9. Conceptual model of the *Bioproducvity Hypothesis* for the deposition of the Hotazel Formation. In this model, reduced iron and manganese are brought to the continental shelf by upwelling and are oxidized according to their redox potentials, with Fe precipitating before Mn. High primary productivity leads to the formation of an OMZ, and within this zone, Fe and Mn undergo dissolution and are transported through this setting via OMZ-redirection. Once oxygen increases in the lower reaches of the OMZ, Fe and Mn re-precipitate out of solution, but in the inverse order. By introducing a relative sea-level drop, as illustrated between panels **(A)** and **(B)**, the model can adequately explain the unique sedimentary

dynamics of the Hotazel Formation, particularly the deposition of Mn at deeper water depths relative to Fe. The model also suggests a suitable solution for the exceptionally low $\delta^{56/54}Fe_{IRMM\ 014}$ by DIR cycling potentially coupled with semi-restricted basin conditions. Likewise, the model proposes that Mo is immobilized within the anoxic conditions of the OMZ. As a result, only a tiny fraction of isotopically heavy tetrahedrally coordinated molybdate reaches the final Mn-(hydr)oxide precipitates via direct transport. For a detailed discussion of the model, see section 5.6.3 in the text.

The Bioproductivity Hypothesis: Strengths and Weaknesses

The *Bioproductivity Hypothesis* adequately explains isotopic and concentration trends in the iron and manganese bands, while also accounting for sedimentological observations in the Hotazel Formation. The model's primary weak point is that it assumes oxygenated deep waters on the distal shelf, which contradicts the notion of a widespread ferruginous Archean deep ocean. However, in the modern ocean, surface mixing processes alone can oxygenate the uppermost 100 to 1000 meters (Chester, 2009). Therefore, it is not implausible to imagine an oxygenated shelf environment while maintaining a deep ferruginous ocean for a Neoarchean-Paleoproterozoic scenario.

Additionally, for this model to hold, the sediment porewaters must express an open system behavior for isotopically light $Fe(II)_{aq}$ to leave the pore waters following DIR/DMR reduction. Furthermore, the total production and redirection of $Fe(II)_{aq}$ and $Mn(II)_{aq}$ in the OMZ must be significant to account for the vast quantities of manganese and iron in the Hotazel Formation. A study on modern shelf environments indeed suggests that the Mn removal rate is comparable to the input rate and is mitigated through the OMZ via a series of dissolution and precipitation cycles (Johnson et al., 1992). The study also notes that the flux of Mn to the OMZ is small (~44 nmol/L/year) and primarily controlled by direct precipitation from the water column rather than sedimentary transport. However, in the context of early Earth, with different redox conditions and biogeochemical dynamics, conditions likely favored much larger quantities of Mn deposition directly from the water column, as evidenced by the unique deposition of Mn-rich BIFs, like the Hotazel Formation, in Precambrian rocks. Lastly, the Hotazel Formation is unique in that it indicates an inversed marine oxygen landscape based on its sedimentological features. Considering that few other Mn-rich BIFs are known to display similar sedimentological and geochemical characteristics in the geological record, it is plausible that one or more specific factors explicitly amplified the effect of the OMZ redirection process for

the Hotazel Formation. Such factors could be a Mn(II)-enriched Archean-Paleoproterozoic ocean, large blooms of primary productivity increasing the OMZ's extent or specific basinal structures promoting rapid water mixing. The extent of OMZ can be semi-quantified using nitrogen isotopes, as denitrification occurs in oxygen-depleted environments, such as the OMZ. The process of denitrification induces a large negative fractionation of ~25–35 ‰, which leaves the complementary and bioavailable marine nitrate reservoir comparatively enriched in $\delta^{15}N$ (Struck, 2011). Thus, for the *Bioproductivity Hypothesis* to be valid, we predict nitrogen isotopes from bulk rock to express a positive trend in sediments of the Hotazel Formation compared to Neoarchean-Paleoproterozoic seawater.

5.6.4 The Hotazel Formation in the Context of the GOE

If the *Bioproductivity Hypothesis* is correct, it implies that the marine biosphere was capable of producing a 'modern-like' oxygen profile in the shallow marine realm at the initiation of the GOE. This perspective lends support to the multiple geochemical and sedimentological indications of an oxygenated shallow marine realm prior to the loss of MIF-S in the Transvaal Basin (Eroglu et al., 2017; Franchi, 2018; Kendall et al., 2010; Kurzweil et al., 2016; Wille et al., 2007), and corroborates the idea of shallow marine 'Oxygen Oases' (Bau & Alexander, 2006; Kasting et al., 1992; Olson et al., 2013; Riding et al., 2014). The first unquestionable disappearance of MIF-S in the Transvaal Supergroup occurs in the correlative Duitschland and Rooihoogte formations, which are lithostratigraphically younger than the Hotazel Formation. Both the Duitschland and Rooihoogte formations were deposited in the Transvaal Area, while the Hotazel Formation was sedimented in the Griqualand West Area of. However, the entire sedimentary succession of the Transvaal Supergroup represents a rimmed shelf environment, with the Griqualand West Basin expressing the distal slope and the Transvaal Basin a proximal epeiric sea (Eroglu et al., 2015). Consequently, the integrated temporal redox evolution through these three formations indicates that already during the deposition of the Hotazel Formation, the marine redox state was oxygenated, which persisted until the first disappearance of MIF-S in the lower segments of the *Upper* Duitschland and Rooihoogte formations. Subsequently, atmospheric oxidative weathering intensified marine primary productivity through nutrient-driven feedback loops, culminating in marine deoxygenation in the wake of the GOE.

5.7 Summary and Conclusion

This study investigated iron and molybdenum isotopes from a drill core (MP72) intersecting the ~2.4 Ga Hotazel Formation. We aimed to develop a model for the deposition of the Hotazel Formation that integrates both sedimentological and geochemical observations. Furthermore, we explored the marine redox evolution of the Hotazel Formation in the context of the evolving marine redox landscape in the Transvaal Supergroup at the initiation of the GOE.

- The deposition of the Hotazel Formation is best explained by the development of an oxygen minimum zone. Within this zone, Fe and Mn are shuttled through the OMZ and underlying sediments via OMZ-redirection. This movement results in iterations of redox-induced dissolution and precipitation events, causing iron and manganese to settle in the more oxygenated water column beneath the OMZ, with Fe precipitating prior to Mn (Fig. 5.9).
- Multiple cycles of dissimilatory iron and manganese reduction in the OMZ work as a 'DIR-engine' that progressively drives Fe and Mo isotopic compositions towards increasingly light values.
- Our interpretations of the sedimentological and geochemical framework suggest that fully developed OMZs before the demise of MIF-S in the Transvaal Supergroup give precedence to the shallow marine 'oxygen oasis' hypothesis. Most notably, these findings imply that the marine shelf exhibited vertical oxygen profiles similar to those found in modern settings, were already established 2.4 billion years ago and were presumably driven by biomass production

5.8 Tables

Table 5.1. Fe and Mo isotopic values plus selected elements and ratios

Core Depth (m)	Subformation	$\delta^{56/54}Fe_{IRMM\ 014}$ ‰	2SE	$\delta^{98/95}Mo_{NIST3134+0.25}$ ‰	2SE	Mo (µg/g)	Fe_2O_3 (Wt.%)	MnO (Wt.%)	Fe/Mn	Ce/Ce*	Eu/Eu^t	Y/Ho
426.37	Ongeluk Fm	-0.44	0.03	0.98	0.03	0.97	31.1	0.544	31.0	0.856	1.32	34.3
424.95	BF1						24.6	1.54	8.63			
424.44	BF1						61.3	8.86	3.75			
421.09	BF1	-1.99	0.03	0.83	0.03	0.10	22.8	11.6	1.07	0.649	1.12	50.4
419.93	BF1						27.0	11.8	1.24			
419.55	BF1					0.32	24.3	3.21	4.10	0.986	1.12	47.3
419.07	BF1						55.8	7.49	4.04			
417.39	BF1	-2.16	0.02	0.93	0.03	0.27	49.1	6.86	3.88	0.657	1.12	47.5
415.55	BF1						49.8	5.32	5.07			
413.36	BF1	-2.13	0.02	0.75	0.02	0.30	46.6	8.41	3.00	0.718	1.03	46.2
410.31	BF1						26.9	20.9	0.699			
408.42	Jasp-1					0.23	33.1	17.3	1.04	0.690	1.11	46.2
407.81	MnF1	-2.44	0.02	0.69	0.03	0.23	26.3	20.0	0.712	0.728	1.12	44.1
405.97	MnF1					0.22	16.0	44.7	0.195	0.633	1.14	41.8
404.98	MnF1						8.35	45.8	0.099			
400.53	MnF1	-1.77	0.02	0.33	0.03	0.06	3.82	45.6	0.045	0.605	1.17	42.4
397.43	MnF1						3.04	54.9	0.030			
395.62	MnF1						3.45	54.6	0.034			
393.82	MnF1	-1.99	0.02	0.41	0.03	0.13	8.86	42.8	0.112	0.531	1.15	39.7
392.01	MnF1						6.19	47.3	0.071			
388.76	MnF1	-2.03	0.02	0.13	0.03	0.82	8.50	33.0	0.139	0.510	1.15	42.8
386.90	Jasp-2	-2.40	0.02	0.43	0.03	0.51	13.8	13.4	0.558	0.601	1.16	47.4
385.51	Jasp-2					0.90	28.9	1.46	10.7	0.864	1.14	32.3
381.37	BF2						44.9	1.44	16.9			
379.38	BF2	0.092	0.02	0.49	0.03	0.72	12.6	10.5	0.648	0.891	1.07	33.1
376.33	BF2						40.9	1.00	22.1			
372.68	BF2					0.57	42.5	0.777	29.6	0.862	1.10	34.1
369.19	BF2	0.50	0.03	1.02	0.03	0.44	41.6	0.721	31.3	0.846	1.18	36.6
367.02	BF2						37.8	0.533	38.4			
361.52	BF2						44.0	0.679	35.1			
360.25	BF2	0.01	0.03	0.69	0.02	0.44	50.7	0.853	32.2	0.795	1.11	45.5

Table continued on next page

Core Depth (m)	Subformation	$\delta^{56/54}Fe_{IRMM\ 014}$ ‰	2SE	$\delta^{98/95}Mo_{NIST3134+0.25}$ ‰	2SE	Mo (µg/g)	Fe_2O_3 (Wt.%)	MnO (Wt.%)	Fe/Mn	Ce/Ce*	Eu/Eu^t	Y/Ho
356.26	BF2						48.4	1.14	23.0			
353.95	BF2	-0.47	0.02	0.49	0.03	0.37	43.7	1.37	17.2	0.771	1.30	39.3
351.27	BF2					0.58	38.6	0.648	32.3	0.770	1.04	49.7
349.54	Jasp-3						40.1	1.07	20.3			
349.12	Jasp-3	-1.94	0.03	1.23	0.03	0.44	41.7	10.0	2.27	0.701	1.07	47.1
348.69	MnF2	-2.59	0.03	0.98	0.02	0.21	33.1	10.3	1.75	0.672	1.21	45.3
347.97	MnF2					0.09	14.6	10.7	0.739	0.591	1.21	47.2
346.77	BF3					0.27	23.5	2.42	5.3	0.667	1.19	45.7
344.90	BF3	-1.87	0.03	0.54	0.03	0.14	24.6	1.15	11.6	0.548	1.26	48.5
342.27	BF3						37.7	2.07	9.86			
340.36	MnF3					0.22	21.6	23.5	0.499	0.698	1.09	44.7
339.35	MnF3	-2.95	0.02	0.50	0.03	0.29	28.7	21.5	0.726	0.780	0.948	39.3
338.78	MnF3					0.13	7.16	32.4	0.120	0.521	0.940	40.6
336.40	MnF3					0.07	8.82	38.7	0.123	0.576	1.13	42.7
335.35	MnF3					0.10	8.17	26.5	0.167	0.650	1.04	41.9
332.73	Jasp-4	-1.93	0.03	0.74	0.02	0.17	22.4	14.9	0.812	0.715	1.04	46.8
329.07	Jasp-4						36.2	0.875	22.4			
327.51	BF4					0.13	31.2	0.879	19.2	0.728	1.10	46.5
322.94	BF4						25.6	0.904	15.3			
322.28	BF4	-1.54	0.02	0.75	0.03	0.16	24.2	0.424	30.9	0.774	1.09	46.4
319.99	BF4						41.7	0.536	42.1			
316.37	BF4	-1.53	0.02	0.82	0.03	0.12	33.2	0.309	58.1	0.704	1.09	50.8
315.04	BF4						31.5	0.404	42.3			
312.21	BF4					0.12	25.3	0.636	21.5	0.704	1.10	50.8
310.64	BF4						19.5	0.643	16.4			
310.06	BF4	-0.58	0.08	0.65	0.03	0.11	30.4	0.269	61.2	0.820	1.09	39.5
309.05	BF4						30.1	0.358	45.6			
305.81	BF4						32.4	1.35	13.0			
305.36	BF4						21.2	1.64	6.99			
304.26	BF4					0.08	14.0	1.31	5.80	0.809	1.18	49.2

Ce/Ce* after Bau et al., 1996
Eu/Eu^t after Bau et al., 1996

5.9 References

Albut, G., Babechuk, M. G., Kleinhanns, I. C., Benger, M., Beukes, N. J., Steinhilber, B., Smith, A. J., Kruger, S. J., & Schoenberg, R. (2018). Modern rather than Mesoarchaean oxidative weathering responsible for the heavy stable Cr isotopic signatures of the 2.95 Ga old Ijzermijn iron formation (South Africa). *Geochimica et Cosmochimica Acta*, *228*, 157-189.

Albut, G., Kamber, B. S., Brüske, A., Beukes, N. J., Smith, A. J., & Schoenberg, R. (2019). Modern weathering in outcrop samples versus ancient paleoredox information in drill core samples from a Mesoarchaean marine oxygen oasis in Pongola Supergroup, South Africa. *Geochimica et Cosmochimica Acta*, *265*, 330-353.

Anbar, A. (2004). Iron stable isotopes: beyond biosignatures. *Earth and Planetary Science Letters*, *217*(3-4), 223-236.

Anbar, A. D., Duan, Y., Lyons, T. W., Arnold, G. L., Kendall, B., Creaser, R. A., Kaufman, A. J., Gordon, G. W., Scott, C., & Garvin, J. (2007). A whiff of oxygen before the great oxidation event? *Science*, *317*(5846), 1903-1906.

Babechuk, M. G., Weimar, N. E., Kleinhanns, I. C., Eroglu, S., Swanner, E. D., Kenny, G. G., Kamber, B. S., & Schoenberg, R. (2019). Pervasively anoxic surface conditions at the onset of the Great Oxidation Event: New multi-proxy constraints from the Cooper Lake paleosol. *Precambrian Research*, *323*, 126-163.

Barling, J., & Anbar, A. (2004). Molybdenum isotope fractionation during adsorption by manganese oxides. *Earth and Planetary Science Letters*, *217*(3-4), 315-329.

Barling, J., Arnold, G. L., & Anbar, A. (2001). Natural mass-dependent variations in the isotopic composition of molybdenum. *Earth and Planetary Science Letters*, *193*(3-4), 447-457.

Bau, M., & Alexander, B. (2006). Preservation of Primary REE Patterns without Ce Anomaly during Dolomitization of Mid-Paleoproterozoic Limestone and the Potential Re-Establishment of Marine Anoxia Immediately after the 'Great Oxidation Event'. South African Journal of Geology, 109(1-2), 81-86.

Bau, M., & Dulski, P. (1996). Distribution of yttrium and rare-earth elements in the Penge and Kuruman iron-formations, Transvaal Supergroup, South Africa. *Precambrian Research*, *79*(1-2), 37-55.

Bau, M., Romer, R. L., Lüders, V., & Beukes, N. J. (1999). Pb, O, and C Isotopes in Silicified Mooidraai Dolomite (Transvaal Supergroup, South Africa): Implications for the Composition of Paleoproterozoic Seawater and 'Dating' the Increase of Oxygen in the Precambrian Atmosphere. Earth and Planetary Science Letters, 174(1-2), 43-57.

Beard, B. L., & Johnson, C. M. (2004). Fe isotope variations in the modern and ancient earth and other planetary bodies. *Reviews in Mineralogy and Geochemistry*, *55*(1), 319-357.

Beard, B. L., Johnson, C. M., Von Damm, K. L., & Poulson, R. L. (2003). Iron isotope constraints on Fe cycling and mass balance in oxygenated Earth oceans. *Geology*, *31*(7), 629-632.

Bekker, A., Slack, J. F., Planavsky, N., Krapez, B., Hofmann, A., Konhauser, K. O., & Rouxel, O. J. (2010). Iron formation: the sedimentary product of a complex interplay among mantle, tectonic, oceanic, and biospheric processes. *Economic Geology*, *105*(3), 467-508.

Beukes, N. (1983). Palaeoenvironmental setting of iron-formations in the depositional basin of the Transvaal Supergroup, South Africa. In *Developments in Precambrian Geology* (Vol. 6, pp. 131-198). Elsevier.

Beukes, N. (1986). The Transvaal sequence in Griqualand west. *Mineral deposits of southern Africa*, 819-828.

Beukes, N. J., Dorland, H., Gutzmer, J., Nedachi, M., & Ohmoto, H. (2002). Tropical laterites, life on land, and the history of atmospheric oxygen in the Paleoproterozoic. *Geology*, *30*(6), 491-494.

Beukes, N. J., Swindell, E. P., & Wabo, H. (2016). Manganese deposits of Africa. *Episodes Journal of International Geoscience*, *39*(2), 285-317.

Bolhar, R., Kamber, B. S., Moorbath, S., Fedo, C. M., & Whitehouse, M. J. (2004). Characterisation of early Archaean chemical sediments by trace element signatures. *Earth and Planetary Science Letters*, *222*(1), 43-60. https://doi.org/10.1016/j.epsl.2004.02.016

Busigny, V., Planavsky, N. J., Goldbaum, E., Lechte, M. A., Feng, L., & Lyons, T. W. (2018). Origin of the Neoproterozoic Fulu iron formation, South China: Insights from iron isotopes and rare earth element patterns. *Geochimica et Cosmochimica Acta*, *242*, 123-142.

Cairncross, B., & Beukes, N. J. (2013). *The Kalahari manganese field*. Random House Struik.

Casalini, M., Avanzinelli, R., Tommasini, S., Elliott, T., & Conticelli, S. (2019). Ce/Mo and molybdenum isotope systematics in subduction-related orogenic potassic magmas of Central-Southern Italy. *Geochemistry, Geophysics, Geosystems*, *20*(6), 2753-2768.

Chen, S., Hin, R. C., John, T., Brooker, R., Bryan, B., Niu, Y., & Elliott, T. (2019). Molybdenum systematics of subducted crust record reactive fluid flow from underlying slab serpentine dehydration. *Nature communications*, *10*(1), 1-9.

Chester, R. (2009). *Marine geochemistry*. John Wiley & Sons.

Coetzee, L., Beukes, N. J., Gutzmer, J., & Kakegawa, T. (2006). Links of organic carbon cycling and burial to depositional depth gradients and establishment of a snowball Earth at 2.3 Ga. Evidence from the Timeball Hill Formation, Transvaal Supergroup, South Africa. *South African Journal of Geology*, *109*(1-2), 109-122.

Compston, W., & Oversby, V. (1969). Lead isotopic analysis using a double spike. *Journal of Geophysical Research*, *74*(17), 4338-4348.

Cornell, D., & Schütte, S. (1995). A volcanic-exhalative origin for the world's largest (Kalahari) manganese field. *Mineralium Deposita*, *30*, 146-151.

Cornell, D., Schütte, S., & Eglington, B. (1996). The Ongeluk basaltic andesite formation in Griqualand West, South Africa: submarine alteration in a 2222 Ma Proterozoic sea. *Precambrian Research*, *79*(1-2), 101-123.

Craig, H. (1957). Isotopic standards for carbon and oxygen and correction factors for mass-spectrometric analysis of carbon dioxide. *Geochimica et Cosmochimica Acta*, *12*(1-2), 133-149.

Dauphas, N., & Rouxel, O. (2006). Mass spectrometry and natural variations of iron isotopes. *Mass Spectrometry Reviews*, *25*(4), 515-550.

Dickens, G. R., & Owen, R. M. (1994). Late Miocene-early Pliocene manganese redirection in the central Indian Ocean: Expansion of the intermediate water oxygen minimum zone. *Paleoceanography*, *9*(1), 169-181.

Eriksson, P., Altermann, W., Hartzer, F., Johnson, M., Anhaeusser, C., & Thomas, R. (2006). *The Transvaal Supergroup and its precursors* (A. C. Johnson MJ, Thomas RJ, Ed.). Geological Society of

South Africa/Council for Geoscience, Johannesburg.

Eriksson, P. G., & Cheney, E. S. (1992). Evidence for the transition to an oxygen-rich atmosphere during the evolution of red beds in the Lower Proterozoic sequences of southern Africa. *Precambrian Research*, *54*(2-4), 257-269.

Eroglu, S., Schoenberg, R., Wille, M., Beukes, N., & Taubald, H. (2015). Geochemical stratigraphy, sedimentology, and Mo isotope systematics of the ca. 2.58–2.50 Ga-old Transvaal Supergroup carbonate platform, South Africa. *Precambrian Research*, *266*, 27-46. https://doi.org/10.1016/j.precamres.2015.04.014

Eroglu, S., van Zuilen, M. A., Taubald, H., Drost, K., Wille, M., Swanner, E. D., Beukes, N. J., & Schoenberg, R. (2017). Depth-dependent δ13C trends in platform and slope settings of the Campbellrand-Malmani carbonate platform and possible implications for Early Earth oxygenation. *Precambrian Research*, *302*, 122-139.

Fairey, B., Tsikos, H., Corfu, F., & Polteau, S. (2013). U–Pb systematics in carbonates of the Postmasburg Group, Transvaal Supergroup, South Africa: primary versus metasomatic controls. *Precambrian Research*, *231*, 194-205.

Fitton, D. (2022). *A detailed stratigraphic, mineralogical and geochemical assessment of the Hotazel Formation at Middelplaats, Kalahari Mn Field, Northern Cape Province, South Africa* University of Johannesburg].

Franchi, F. (2018). Petrographic and geochemical characterization of the Lower Transvaal Supergroup stromatolitic dolostones (Kanye Basin, Botswana). *Precambrian Research*, *310*, 93-113.

Franchi, F., & Mapeo, R. B. M. (2019). Evolution of an Archaean intracratonic basin: A review of the Transvaal Supergroup lithostratigraphy in Botswana. *Earth-Science Reviews*, *191*, 273-290.

Freymuth, H., Vils, F., Willbold, M., Taylor, R. N., & Elliott, T. (2015). Molybdenum mobility and isotopic fractionation during subduction at the Mariana arc. *Earth and Planetary Science Letters*, *432*, 176-186.

Fuenzalida, R., Schneider, W., Garcés-Vargas, J., Bravo, L., & Lange, C. (2009). Vertical and horizontal extension of the oxygen minimum zone in the eastern South Pacific Ocean. *Deep Sea Research Part II: Topical Studies in Oceanography*, *56*(16), 992-1003.

Goldberg, T., Gordon, G., Izon, G., Archer, C., Pearce, C. R., McManus, J., Anbar, A. D., & Rehkämper, M. (2013). Resolution of inter-laboratory discrepancies in Mo isotope data: an intercalibration. *Journal of Analytical Atomic Spectrometry*, *28*(5), 724-735.

Greber, N. D., Siebert, C., Nägler, T. F., & Pettke, T. (2012). δ98/95Mo values and molybdenum concentration data for NIST SRM 610, 612 and 3134: Towards a common protocol for reporting Mo data. *Geostandards and Geoanalytical Research*, *36*(3), 291-300.

Gumsley, A. P., Chamberlain, K. R., Bleeker, W., Soderlund, U., de Kock, M. O., Larsson, E. R., & Bekker, A. (2017). Timing and tempo of the Great Oxidation Event. *Proc Natl Acad Sci U S A*, *114*(8), 1811-1816. https://doi.org/10.1073/pnas.1608824114

Guo, Q., Strauss, H., Kaufman, A. J., Schröder, S., Gutzmer, J., Wing, B., Baker, M. A., Bekker, A., Jin, Q., & Kim, S.-T. (2009). Reconstructing Earth's surface oxidation across the Archean-Proterozoic transition. *Geology*, *37*(5), 399-402.

Gutzmer, J., & Beukes, N. J. (1996). Mineral paragenesis of the Kalahari managanese field, South Africa. *Ore Geology Reviews*, *11*(6), 405-428.

Haese, R., Schramm, J., Rutgers Van Der Loeff, M., & Schulz, H. (2000). A comparative study of iron and manganese diagenesis in continental slope and deep sea basin sediments off Uruguay (SW Atlantic). *International Journal of Earth Sciences*, *88*, 619-629.

Hannah, J. L., Bekker, A., Stein, H. J., Markey, R. J., & Holland, H. D. (2004). Primitive Os and 2316 Ma age for marine shale: implications for Paleoproterozoic glacial events and the rise of atmospheric oxygen. *Earth and Planetary Science Letters*, *225*(1-2), 43-52.

Havsteen, J. C., Kleinhanns, I. C., Schröder, S., Eickmann, B., Izon, G., Gogouvitis, M. D., Ngobeli, R., Beukes, N. J., & Schoenberg, R. (2023). Evidence for contemporaneous deposition of the Duitschland and Rooihoogte formations (Transvaal Supergroup): Implications for tempo and mode of Earth's Great Oxidation. *Precambrian Research*, *391*, doi.org/10.1016/j.precamres.2023.107055.

He, Y., Ke, S., Teng, F. Z., Wang, T., Wu, H., Lu, Y., & Li, S. (2015). High-precision iron isotope analysis of geological reference materials by high-resolution MC-ICP-MS. *Geostandards and Geoanalytical Research*, *39*(3), 341-356.

Heimann, A., Johnson, C. M., Beard, B. L., Valley, J. W., Roden, E. E., Spicuzza, M. J., & Beukes, N. J. (2010). Fe, C, and O isotope compositions of banded iron formation carbonates demonstrate a major role for dissimilatory iron reduction in~ 2.5 Ga marine environments. *Earth and Planetary Science Letters*, *294*(1-2), 8-18.

Holland, H. D. (2006). The oxygenation of the atmosphere and oceans. *Philosophical Transactions of the Royal Society B: Biological Sciences*, *361*(1470), 903-915.

Johnson, C., Beard, B., & Weyer, S. (2020). *Iron geochemistry: an isotopic perspective*. Springer.

Johnson, C. M., Beard, B. L., & Roden, E. E. (2008). The iron isotope fingerprints of redox and biogeochemical cycling in modern and ancient Earth. *Annu. Rev. Earth Planet. Sci.*, *36*, 457-493.

Johnson, C. M., Beard, B. L., Roden, E. E., Newman, D. K., & Nealson, K. H. (2004). Isotopic constraints on biogeochemical cycling of Fe. *Reviews in Mineralogy and Geochemistry*, *55*(1), 359-408.

Johnson, C. M., Ludois, J. M., Beard, B. L., Beukes, N. J., & Heimann, A. (2013). Iron formation carbonates: Paleoceanographic proxy or recorder of microbial diagenesis? *Geology*, *41*(11), 1147-1150.

Johnson, J. E., Webb, S. M., Thomas, K., Ono, S., Kirschvink, J. L., & Fischer, W. W. (2013). Manganese-oxidizing photosynthesis before the rise of cyanobacteria. *Proceedings of the National Academy of Sciences*, *110*(28), 11238-11243.

Johnson, K. S., Berelson, W. M., Coale, K. H., Coley, T. L., Elrod, V. A., Fairey, W. R., Iams, H. D., Kilgore, T. E., & Nowicki, J. L. (1992). Manganese flux from continental margin sediments in a transect through the oxygen minimum. *Science*, *257*(5074), 1242-1245.

Karstensen, J., Stramma, L., & Visbeck, M. (2008). Oxygen minimum zones in the eastern tropical Atlantic and Pacific oceans. *Progress in Oceanography*, *77*(4), 331-350.

Kasting, J., Holland, H., & Kump, L. (1992). Atmospheric evolution: the rise of oxygen. *The Proterozoic Biosphere: A Multidisciplinary Study*, 1185-1188.

Kendall, B., Dahl, T. W., & Anbar, A. D. (2017). The stable isotope geochemistry of molybdenum. *Reviews in Mineralogy and Geochemistry*, *82*(1), 683-732.

Kendall, B., Reinhard, C. T., Lyons, T. W., Kaufman, A. J., Poulton, S. W., & Anbar, A. D. (2010). Pervasive oxygenation along late Archaean ocean margins. *Nature Geoscience*, *3*(9), 647-652.

Klinkhammer, G. P., & Bender, M. L. (1980). The distribution of manganese in the Pacific Ocean. *Earth and Planetary Science Letters*, *46*(3), 361-384.

Knoll, A. H., Canfield, D. E., & Konhauser, K. O. (2012). *Fundamentals of geobiology*. John Wiley & Sons.

Konhauser, K., Newman, D., & Kappler, A. (2005). The potential significance of microbial Fe (III) reduction during deposition of Precambrian banded iron formations. *Geobiology*, *3*(3), 167-177.

Kraemer, D., Tepe, N., Pourret, O., & Bau, M. (2017). Negative cerium anomalies in manganese (hydr) oxide precipitates due to cerium oxidation in the presence of dissolved siderophores. *Geochimica et Cosmochimica Acta*, *196*, 197-208.

Kurzweil, F., Wille, M., Gantert, N., Beukes, N. J., & Schoenberg, R. (2016). Manganese oxide shuttling in pre-GOE oceans–evidence from molybdenum and iron isotopes. *Earth and Planetary Science Letters*, *452*, 69-78.

Lawrence, M. G., & Kamber, B. S. (2006). The behaviour of the rare earth elements during estuarine mixing—revisited. *Marine Chemistry*, *100*(1-2), 147-161.

Li, W., Beard, B. L., & Johnson, C. M. (2015). Biologically recycled continental iron is a major component in banded iron formations. *Proceedings of the National Academy of Sciences*, *112*(27), 8193-8198.

Liu, J., Chen, Q., Yang, Y., Wei, H., Laipan, M., Zhu, R., He, H., & Hochella Jr, M. F. (2022). Coupled redox cycling of Fe and Mn in the environment: The complex interplay of solution species with Fe-and Mn-(oxyhydr) oxide crystallization and transformation. *Earth-Science Reviews*, *232*, 104105.

Luo, G., Ono, S., Beukes, N. J., Wang, D. T., Xie, S., & Summons, R. E. (2016). Rapid oxygenation of Earth's atmosphere 2.33 billion years ago. *Science advances*, *2*(5), e1600134.

Mänd, K., Lalonde, S. V., Paiste, K., Thoby, M., Lumiste, K., Robbins, L. J., Kreitsmann, T., Romashkin, A. E., Kirsimäe, K., & Lepland, A. (2021). Iron Isotopes Reveal a Benthic Iron Shuttle in the Palaeoproterozoic Zaonega Formation: Basinal Restriction, Euxinia, and the Effect on Global Palaeoredox Proxies. *Minerals*, *11*(4), 368.

McCarthy, T. S., Corner, B., Lombard, H., Beukes, N., Armstrong, R., & Cawthorn, R. G. (2018). The pre-Karoo geology of the southern portion of the Kaapvaal Craton, South Africa. *South African Journal of Geology 2018*, *121*(1), 1-22.

Men, Y., Wang, E., Fu, J., Jia, S., You, X., & He, Q. (2020). Geochemical constraints on the genesis of the Ekou banded iron formation, Shanxi Province, North China. *International Journal of Earth Sciences*, *109*, 2851-2868.

Mhlanga, X., Tsikos, H., Lee, B., Rouxel, O., Boyce, A., Harris, C., & Lyons, T. (2023). The Palaeoproterozoic Hotazel BIF-Mn Formation as an archive of Earth's earliest oxygenation. *Earth-Science Reviews*, 104389.

Millet, M.-A., Baker, J. A., & Payne, C. E. (2012). Ultra-precise stable Fe isotope measurements by high resolution multiple-collector inductively coupled plasma mass spectrometry with a 57Fe–58Fe double spike. *Chemical Geology*, *304*, 18-25.

Moffitt, S. E., Moffitt, R. A., Sauthoff, W., Davis, C. V., Hewett, K., & Hill, T. M. (2015). Paleoceanographic insights on recent oxygen minimum zone expansion: Lessons for modern oceanography. *PloS one*, *10*(1), e0115246.

Moore, J. M., Polteau, S., Armstrong, R., Corfu, F., & Tsikos, H. (2012). The age and correlation of the Postmasburg Group, southern Africa: Constraints from detrital zircon grains. *Journal of African Earth Sciences*, *64*, 9-19.

Moore, J. M., Tsikos, H., & Polteau, S. (2001). Deconstructing the Transvaal Supergroup, south Africa: implications for Palaeoproterozoic palaeoclimate models. *Journal of African Earth Sciences*, *33*(3-4), 437-444.

Morgan, J. J. (2005). Kinetics of reaction between O2 and Mn (II) species in aqueous solutions. *Geochimica et Cosmochimica Acta*, *69*(1), 35-48.

Murray, J. W., Dillard, J. G., Giovanoli, R., Moers, H., & Stumm, W. (1985). Oxidation of Mn (II): Initial mineralogy, oxidation state and ageing. *Geochimica et Cosmochimica Acta*, *49*(2), 463-470.

Nägler, T. F., Anbar, A. D., Archer, C., Goldberg, T., Gordon, G. W., Greber, N. D., Siebert, C., Sohrin, Y., & Vance, D. (2014). Proposal for an international molybdenum isotope measurement standard and data representation. *Geostandards and Geoanalytical Research*, *38*(2), 149-151.

Nie, N. X., Dauphas, N., & Greenwood, R. C. (2017). Iron and oxygen isotope fractionation during iron UV photo-oxidation: Implications for early Earth and Mars. *Earth and Planetary Science Letters*, *458*, 179-191.

Olson, S. L., Kump, L. R., & Kasting, J. F. (2013). Quantifying the areal extent and dissolved oxygen concentrations of Archean oxygen oases. *Chemical Geology*, *362*, 35-43.

Ossa Ossa, F., Hofmann, A., Wille, M., Spangenberg, J. E., Bekker, A., Poulton, S. W., Eickmann, B., & Schoenberg, R. (2018). Aerobic iron and manganese cycling in a redox-stratified Mesoarchean epicontinental sea. *Earth and Planetary Science Letters*, *500*, 28-40.

Ostrander, C. M., Nielsen, S. G., Owens, J. D., Kendall, B., Gordon, G. W., Romaniello, S. J., & Anbar, A. D. (2019). Fully oxygenated water columns over continental shelves before the Great Oxidation Event. *Nature Geoscience*, *12*(3), 186.

Paulmier, A., & Ruiz-Pino, D. (2009). Oxygen minimum zones (OMZs) in the modern ocean. *Progress in Oceanography*, *80*(3-4), 113-128.

Polteau, S., Moore, J. M., & Tsikos, H. (2006). The geology and geochemistry of the Palaeoproterozoic Makganyene diamictite. *Precambrian Research*, *148*(3-4), 257-274.

Postma, D. (1985). Concentration of Mn and separation from Fe in sediments—I. Kinetics and stoichiometry of the reaction between birnessite and dissolved Fe (II) at 10 C. *Geochimica et Cosmochimica Acta*, *49*(4), 1023-1033.

Poulton, S. W., Bekker, A., Cumming, V. M., Zerkle, A. L., Canfield, D. E., & Johnston, D. T. (2021). A 200-million-year delay in permanent atmospheric oxygenation. *Nature*, *592*(7853), 232-236. https://doi.org/10.1038/s41586-021-03393-7

Qin, L., & Humayun, M. (2008). The Fe/Mn ratio in MORB and OIB determined by ICP-MS. *Geochimica et Cosmochimica Acta*, *72*(6), 1660-1677.

Riding, R., Fralick, P., & Liang, L. (2014). Identification of an Archean marine oxygen oasis. *Precambrian Research*, *251*, 232-237.

Rogers, A. (1906). Geological survey of parts of Bechuanaland and Griqualand West: Geol. *Comm. CGH, Rept*, *11*, 9-85.

Rouxel, O. J., Bekker, A., & Edwards, K. J. (2005). Iron isotope constraints on the Archean and Paleoproterozoic ocean redox state. *Science*, *307*(5712), 1088-1091.

Schaller, T., & Wehrli, B. (1996). Geochemical-focusing of manganese in lake sediments—an indicator of deep-water oxygen conditions. *Aquatic Geochemistry*, *2*, 359-378.

Schenau, S., Reichart, G.-J., & De Lange, G. (2002). Oxygen minimum zone controlled Mn redistribution in Arabian Sea sediments during the late Quaternary. *Paleoceanography*, *17*(4), 10-11-10-12.

Schier, K., Bau, M., Smith, A. J. B., Beukes, N. J., Coetzee, L. L., & Viehmann, S. (2020). Chemical evolution of seawater in the Transvaal Ocean between 2426 Ma (Ongeluk Large Igneous Province) and 2413 Ma ago (Kalahari Manganese Field). *Gondwana Research*, *88*, 373-388. https://doi.org/10.1016/j.gr.2020.09.001

Schoenberg, R., & von Blanckenburg, F. (2005). An assessment of the accuracy of stable Fe isotope ratio measurements on samples with organic and inorganic matrices by high-resolution multicollector ICP-MS. *International Journal of Mass Spectrometry*, *242*(2-3), 257-272.

Schröder, S., Beukes, N. J., & Armstrong, R. A. (2016). Detrital zircon constraints on the tectonostratigraphy of the Paleoproterozoic Pretoria Group, South Africa. Precambrian Research, 278, 362-393.

Schuth, S., Hurraß, J., Muenker, C., & Mansfeldt, T. (2015). Redox-dependent fractionation of iron isotopes in suspensions of a groundwater-influenced soil. *Chemical Geology*, *392*, 74-86.

Siebert, C., Nägler, T. F., von Blanckenburg, F., & Kramers, J. D. (2003). Molybdenum isotope records as a potential new proxy for paleoceanography. *Earth and Planetary Science Letters*, *211*(1-2), 159-171.

Smith, A. J., Beukes, N. J., & Gutzmer, J. (2013). The composition and depositional environments of Mesoarchean iron formations of the West Rand Group of the Witwatersrand Supergroup, South Africa. *Economic Geology*, *108*(1), 111-134.

Smrzka, D., Zwicker, J., Bach, W., Feng, D., Himmler, T., Chen, D., & Peckmann, J. (2019). The behavior of trace elements in seawater, sedimentary pore water, and their incorporation into carbonate minerals: A review. *Facies*, *65*(4), 41.

Spinks, S. C., Sperling, E. A., Thorne, R. L., LaFountain, F., White, A. J., Armstrong, J., Woltering, M., & Tyler, I. M. (2023). Mesoproterozoic surface oxygenation accompanied major sedimentary manganese deposition at 1.4 and 1.1 Ga. *Geobiology*, *21*(1), 28-43.

Struck, U. (2011). On the use of stable nitrogen isotopes in present and past anoxic environments. In *Anoxia: Evidence for Eukaryote Survival and Paleontological Strategies* (pp. 497-513). Springer.

Sun, W., Kitchaev, D. A., Kramer, D., & Ceder, G. (2019). Non-equilibrium crystallization pathways of manganese oxides in aqueous solution. *Nature communications*, *10*(1), 573.

Taylor, S. R., & McLennan, S. M. (1985). The continental crust: its composition and evolution.

Tchatchueng, R., Ngnotué, T., Njiosseu, E. L. T., Ganno, S., Wabo, H., & Nzenti, J. P. (2021). Contrasting Depositional Environment of Iron Formation at Endengue Area, NW Congo Craton, Southern Cameroon: New Insights from Trace and Rare Earth Elements Geochemistry. *International Journal of Geosciences*, *12*(3), 280-306.

Tebo, B. M., Bargar, J. R., Clement, B. G., Dick, G. J., Murray, K. J., Parker, D., Verity, R., & Webb, S. M. (2004). Biogenic manganese oxides: properties and mechanisms of formation. *Annu. Rev. Earth Planet. Sci.*, *32*, 287-328.

Tsikos, H., Matthews, A., Erel, Y., & Moore, J. M. (2010). Iron isotopes constrain biogeochemical redox cycling of iron and manganese in a Palaeoproterozoic stratified basin. *Earth and Planetary Science Letters*, *298*(1-2), 125-134.

Tsikos, H., Moore, J., & Harris, C. (2001). Geochemistry of the Palaeoproterozoic Mooidraai formation: Fe-rich limestone as end member of iron formation deposition, Kalahari manganese field, Transvaal Supergroup, South Africa. *Journal of African Earth Sciences*, *32*(1), 19-27.

Tsikos, H., & Moore, J. M. (1997). Petrography and geochemistry of the Paleoproterozoic Hotazel Iron-Formation, Kalahari manganese field, South Africa; implications for Precambrian manganese metallogenesis. *Economic Geology*, *92*(1), 87-97.

Villalobos-Orchard, J., Freymuth, H., O'Driscoll, B., Elliott, T., Williams, H., Casalini, M., & Willbold, M. (2020). Molybdenum isotope ratios in Izu arc basalts: the control of subduction zone fluids on compositional variations in arc volcanic systems. *Geochimica et Cosmochimica Acta*, *288*, 68-82.

Wagner, L. J., Kleinhanns, I. C., Weber, N., Babechuk, M. G., Hofmann, A., & Schoenberg, R. (2021). Coupled stable chromium and iron isotopic fractionation tracing magmatic mineral crystallization in Archean komatiite-tholeiite suites. *Chemical Geology*, *576*, 120121.

Wasylenki, L. E., Rolfe, B. A., Weeks, C. L., Spiro, T. G., & Anbar, A. D. (2008). Experimental investigation of the effects of temperature and ionic strength on Mo isotope fractionation during adsorption to manganese oxides. *Geochimica et Cosmochimica Acta*, *72*(24), 5997-6005.

Welch, S., Beard, B., Johnson, C., & Braterman, P. (2003). Kinetic and equilibrium Fe isotope fractionation between aqueous Fe (II) and Fe (III). *Geochimica et Cosmochimica Acta*, *67*(22), 4231-4250.

Weyer, S., & Ionov, D. A. (2007). Partial melting and melt percolation in the mantle: the message from Fe isotopes. *Earth and Planetary Science Letters*, *259*(1-2), 119-133.

Weyer, S., & Schwieters, J. (2003). High precision Fe isotope measurements with high mass resolution MC-ICPMS. *International Journal of Mass Spectrometry*, *226*(3), 355-368.

Willbold, M., Hibbert, K., Lai, Y. J., Freymuth, H., Hin, R. C., Coath, C., Vils, F., & Elliott, T. (2016). High-precision mass-dependent molybdenum isotope variations in magmatic rocks determined by double-spike MC-ICP-MS. *Geostandards and Geoanalytical Research*, *40*(3), 389-403.

Wille, M., Kramers, J. D., Nägler, T. F., Beukes, N., Schröder, S., Meisel, T., Lacassie, J., & Voegelin, A. (2007). Evidence for a gradual rise of oxygen between 2.6 and 2.5 Ga from Mo isotopes and Re-PGE signatures in shales. *Geochimica et Cosmochimica Acta*, *71*(10), 2417-2435.

Wu, W., Swanner, E. D., Kleinhanns, I. C., Schoenberg, R., Pan, Y., & Kappler, A. (2017). Fe isotope fractionation during Fe (II) oxidation by the marine photoferrotroph Rhodovulum iodosum in the presence of Si–Implications for Precambrian iron formation deposition. *Geochimica et Cosmochimica Acta*, *211*, 307-321.

Yin, J., Li, H., & Xiao, K. (2023). Origin of Banded Iron Formations: Links with Paleoclimate, Paleoenvironment, and Major Geological Processes. *Minerals*, *13*(4), 547.

Zhao, P. P., Li, J., Zhang, L., Wang, Z. B., Kong, D. X., Ma, J. L., Wei, G. J., & Xu, J. F. (2016). Molybdenum mass fractions and isotopic compositions of international geological reference materials. *Geostandards and Geoanalytical Research*, *40*(2), 217-226.

Zhu, G., Ma, J., Wei, G., & An, Y. (2020). A novel procedure for separating iron from geological materials for isotopic analysis using MC-ICP-MS. *Journal of Analytical Atomic Spectrometry*, *35*(5), 873-877.

5.10 Supplementary Material

5.10.1 Open System Isotope Fraction of Oxidation-Precipitation Reactions

The primary concept of this model is already employed in studies by Anbar (2004), Beard and Johnson (2004) and Johnson et al. (2004) and is comprehensively summarized in Dauphas and Rouxel (2006). For a detailed review of the model, the reader is referred to the aforementioned studies, while this summary is tailored to outline the parameters specific to this scenario. In the following, all parameters are provided in table 5.S1 rather than in the text for clarity.

The model describes an isotopic evolution curve for an open system without $Fe(II)_{aq}$ replenishment after the starting time t(0). The model presumes $Fe(II)_{aq}$ is oxidized by either free O_2 or iron-oxidizing bacteria to $Fe(III)_{aq}$, which subsequently precipitates out of solution as $Fe(III)_s$.

$$Fe(II)_{aq} \leftrightarrow Fe(III)_{aq} \rightarrow Fe(III)_s \qquad (s1)$$

For the first stage, it is assumed that the dissolved pools of $Fe(II)_{aq}$ and $Fe(III)_{aq}$ maintain equilibrium due to the very fast exchange isotope kinetics between the two phases (Welch et al., 2003). The fractionation factor for the reaction is described in equation s2 and roughly equates to a change of 1.4 ‰ per atomic mass unit (amu).

$$\alpha_{IIaq}^{IIIaq} = \frac{R_{IIIaq}}{R_{IIaq}} \qquad (s2)$$

In the second stage, it is assumed that there is no return of precipitated $Fe(III)_s$ back to the dissolved Fe(III)aq pool. Instead, any precipitated $Fe(III)_s$ is permanently removed from the system. Additionally, by imposing a Rayleigh condition, the fractionation factor can be defined as the ratio of the fluxes of the two isotopes, ^{56}Fe and ^{54}Fe, through the system divided by the initial ratio in the aqueous pool, which approximates a value of -0.5 ‰ per amu.

$$\alpha_{IIaq}^{IIIaq \rightarrow s} = \frac{R_{IIIaq \rightarrow s}}{R_{IIIaq}} \qquad (s3)$$

If the differential equations for a first-order kinetic model provided in Beard and Johnson (2004) and Johnson et al. (2004) are conditioned to 1 (equation s4). The ordinary differential equations (ODEs) can be solved, yielding the solutions provided in equation-set s5, as described in Dauphas and Rouxel (2006).

$$Fe_{aq}^{II} + Fe_{aq}^{III} + Fe_{s}^{II} = Fe_{aq,t(0)}^{II} = 1 \qquad (s4)$$

Ordinary differential equations *Solved ODEs according to eq. s4*

$$\frac{dFe_{aq}^{II}}{dt} = -k_1 Fe_{aq}^{II} \qquad Fe_{aq}^{II} = e^{-k_1 t}$$

$$\frac{dFe_{aq}^{III}}{dt} = k_1 Fe_{aq}^{II} - k_2 Fe_{aq}^{III} \qquad Fe_{aq}^{III} = \frac{k_1}{k_2 - k_1}(e^{-k_1 t} - e^{-k_2 t}) \qquad (s5)$$

$$\frac{dFe_{s}^{III}}{dt} = k_2 Fe_{aq}^{III} \qquad Fe_{s}^{III} = 1 - Fe_{aq}^{II} - Fe_{aq}^{III}$$

The solved ODEs depict the fraction of the different iron species in the system at a given time (t) after t(0), as shown in Figure 5.8B. For the corresponding isotopic ratios, the analytical solution is provided in Dauphas and Rouxel (2006), with a simplified version in δ-notation expressed in equation-set s6, with parameters defined in table 5.S1.

$$\delta_{aq}^{II} = \left(\frac{\Delta_{IIIaq}^{IIIaq\rightarrow s}}{\mu - 1} + \frac{\Delta_{IIaq}^{IIIaq}}{\mu}\right) ln(X) + \left(\Delta_{IIIaq}^{IIIaq\rightarrow s} - \frac{\Delta_{IIaq}^{IIIaq}}{\mu}\right) ln\left(\frac{X - \mu}{1 - \mu}\right)$$

$$\delta_{aq}^{III} = \delta_{aq}^{II} + \Delta_{IIaq}^{IIIaq} \qquad (s6)$$

$$\delta_{s}^{III} = \frac{Fe_{aq}^{II}\delta_{aq}^{II} + Fe_{aq}^{III} + \delta_{aq}^{III}}{Fe_{aq}^{II} + Fe_{aq}^{III} - 1}$$

$$\delta_{aq\rightarrow s}^{III} = \delta_{aq}^{III} + \Delta_{IIIaq}^{IIIaq\rightarrow s}$$

Additionally, the removal rate of Fe/Mn was added onto the modeled iron speciation evolution in Figure 5.8B in a fashion similar to that employed in Tsikos et al. (2010). An initial Fe/Mn reservoir of 70/1 and a constant removal rate of 100/1 between Fe and Mn were assumed. The Fe/Mn evolution line was calculated using equation-set s7 and is independent of the $Fe^{3+}{}_{s}$ speciation line in Figure 5.8b.

$$Mn_{remaining}(t) = 1 - kt$$

$$Fe_{remaining}(t) = Fe_{initial} - Fe_{initial}\frac{t}{250} \qquad (s7)$$

$$k_{Fe/Mn}(t) = \frac{Fe_{remaining(t)}}{Mn_{remaining(t)}}$$

Where t is steps of 1 from 1 to 250 and the rate constant $k = \frac{Fe_{initial} - Fe_{value\ at\ t(2)}}{100}$. By comparing the theoretical Fe/Mn ratio with the corresponding theoretical δ-value of the instantaneous product line at a given time (t) in Figure 5.8A and B against the sample Fe/Mn ratios and δ-values, a cross-validation of the model was achieved. The samples were plotted on the instantaneous product to enhance visual presentation using the 'goal seek' function in Excel.

Table 5.S1. The value for k_1 is adapted from Beard and Johnson (2004) based on initial data from Bullen et al. (2001). The values for k_2,$\Delta\frac{III_{aq}}{II_{aq}}$ and $\Delta\frac{III_{aq\rightarrow s}}{II_{aq}}$ are taken from Dauphas and Rouxel (2006) and represent values plausible for the deposition of Archean BIFs.

Parameter	Description	assigned value
$FeII_{aq}$	Fraction of aqueous ferrous iron	$t_0 = 1$
$FeIII_{aq}$	Fraction of aqueous ferric iron	$t_0 = 0$
$FeIII_s$	Fraction of solid ferric iron	$t_0 = 0$
k_1	Rate constant for oxidation of $FeII_{aq}$	0.0827
k_2	Rate constant for precipitation of $FeIII_{aq}$	$10 \times k_1$
α_{IIaq}^{IIIaq}	Fractionation factor between $FeII_{aq}$ and $FeIII_{aq}$	
$\alpha_{IIIaq}^{IIIaq\rightarrow s}$	Fractionation factor between $FeIII_{aq}$ and $FeIII_s$	
R	Isotopic ratio $\frac{^{56}Fe}{^{54}Fe}$ in a given reservoir	
t	Time	0 to 250 in steps of 1
μ	$\frac{k_2}{k_1}$	x/y
X	$e^{k_1 - k_2 t}$	
$\Delta_{IIaq}^{IIIaq\rightarrow s}$	$\alpha_{IIIaq}^{IIIaq\rightarrow s} - 1 \times 10^3$	$\sim$ 1.4 per amu
Δ_{IIIaq}^{IIIaq}	$\alpha_{IIaq}^{IIIaq} - 1 \times 10^3$	~ -0.5 per amu
δ_{aq}^{II}	Isotopic composition of the $FeII_{aq}$ reservoir (Remaining prod.)	
δ_{aq}^{III}	Isotopic composition of the $FeIII_{aq}$ reservoir (Intermediate prod.)	
δ_s^{III}	Isotopic composition of the $FeIII_s$ reservoir (Accumulated Prod.)	
$\delta_{aq\rightarrow s}^{III}$	Isotopic composition of the instantaneous fraction Fe_s^{III} precipitated (Instantaneous product)	

Chapter 6

Outlook and Perspectives

Upon completing this work, I am both pleased and proud to have kicked the ball a few meters down the lane in our understanding of the Great Oxidation Event. Now, finishing this project has sparked a series of new ideas and research questions, of which I will briefly address some of them in the following chapter.

6.1 The 'Vaalbara Craton' and the Provenance of the Duitschland and Rooihoogte Formations

Chapter 3 of this thesis addresses the idea that the Duitschland and Rooihoogte formations are likely different sedimentary expressions of the same formation deposited at different distances to the paleoshoreline, which is critical knowlegde for our understanding of the GOE. However, another interesting aspect of the Duitschland and Rooihoogte formations is encapsulated in their zircon age distribution patterns and Hf-isotopic compositions. Both formations have a pronounced ~2.4–2.5 Ga zircon age peak (Schröder et al., 2016; Zeh et al., 2020), which coincides with a zircon low in the global geological record (Hawkesworth et al., 2016). However, one prominent rhyolite complex with exactly that age is the 2.45 Ga Woongara Rhyolite in Australia (Barley et al., 1997). Thus, a comparative analysis of Woongara-derived zircons and zircons extracted from the Duitschland and Rooihoogte formations could shed light on the often proposed tectonic connection between Archean and Paleoproterozoic terranes of South Africa and Australia (Beukes & Gutzmer, 2008; Cheney, 1996; de Kock et al., 2009).

6.2 Oxygen Minimum Zones, Nitrogen Isotopes and the Hotazel Formation

In Chapter 5, the *'Bioproductivity hypothesis'* was proposed as a potential depositional mechanism for the Hotazel Formation. This hypothesis is based on the dynamic interplay between the expansion and contraction of oxygen minimum zones (OMZs), which ultimately drive the cyclical precipitation of Fe and Mn layers beneath the OMZ through the process of OMZ-redirection. In low oxygen environments, like oxygen minimum zones, denitrification serves as the main pathway for N-conversion, which at the same time is associated with a

significant negative fractionation of approximately -25 to -35 ‰ (Knoll et al., 2012). That leaves the bioavailable marine nitrate pool comparatively enriched, resulting in positive bulk $\delta^{15}N$ isotopic values in sediments below the OMZs (Struck, 2011). Consequently, measuring nitrogen isotopes could yield valuable information to test the proposed link between oxygen minimum zones and the deposition of the Hotazel Formation. If the hypothesis proves valid, heavier bulk $\delta^{15}N$ values would be expected relative to Neoarchean-Paleoproterozoic seawater.

6.3 The 'Great Titration Event' and Mass-Independent Isotope Fractionation Beyond Sulfur

Currently, it is not known whether the Great Oxidation Event is best categorized as an oscillating transition or a sudden event. In its simplest sense, the Great Oxidation Event can be defined as what I regard as a "Great Titration Event". As the titrant "O_2" is continuously added to the system, the analyte (reducing gases, e.g., CH_4) is continuously oxidized. Once the titrant and analyte have almost reached equilibrium, the first signs of system change are seen at the "Flickering point" (P2; Fig. 6.1A), where the titrant temporarily surpasses the equivalence point before mixing and diffusion reverts the system to its original state, similar to the 'whiffs of oxygen' in the early Earth analogy. Next, once the equivalence point is reached (P3; Fig. 6.1A) — analogous to the disappearance of MIF-S on the early Earth — the titrant surpasses the buffering capacity of the analyte, and O_2 starts to surge (P4; Fig. 6.1A), resulting in an "oxygen overshoot" for the early Earth analogy. I draw this picture because it elegantly illustrates that the normal observations expected during a simple titration are also observable in the sedimentary record from early Earth as the 'Whiffs of oxygen', 'disappearance of MIF-S' and the 'Lomagundi-Jatuli event', although not usually referred to in the context of a titration. The similarities between observations from early Earth and the theoretical framework of a titration curve could indicate that planetary oxygenation occurred rapidly once Earth's buffering capacity was overcome.

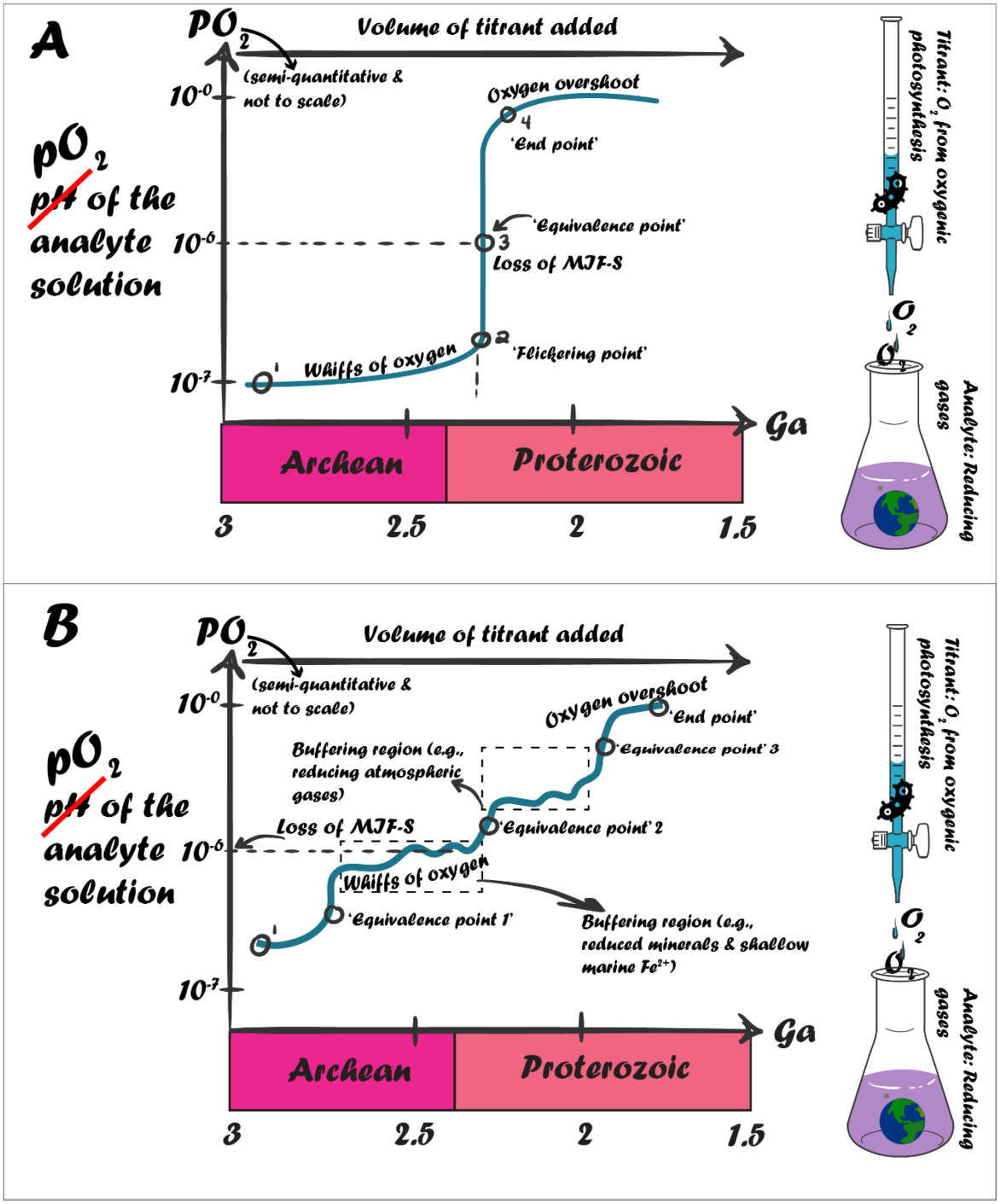

Figure 6.1. **(A):** *The Great Oxidation Event displayed as a conceptual titration curve.* The 'whiffs of oxygen' is the buffering zone occurring before the demise of MIF-S, which is analogized at the 'equivalence point' and followed by an oxygen overshoot effect equated to the Lumagundi-Jatuli Event. **(B)** *The Great Oxidation Event is illustrated as a complex polyprotic titration curve.* This scenario is characterized by multiple buffering zones and equivalence points, reflecting a dynamically changing system of geological sources and sinks of oxygen. The depiction of the basic titration setup (graph, erlenmeyer flask, burette) is adapted from Khan Academy (2008).

However, the above analogy can be critiqued on several grounds. Firstly, the Earth system is not a simple titration system with one titrant and one analyte but rather a multi-buffered complex system with several buffering sinks and variability in the flux rate of both sources and sinks. Therefore, it is also possible, that the Earth's oxygenation will mimic a polyprotic titration with multiple equivalence points and buffering regions (Fig. 6.1B). In this respect, it is essential to consider the different sinks of the early Earth and whether these exhibit an irreversible or reversible behavior. For example, reduced detrital minerals (e.g., pyrite) and, to a certain extent, dissolved iron in the shallow marine realm are two relatively irreversible sinks over short geological times. Thus, once such sinks were overcome by oxygen production from oxygenic phototrophs, it would most probably constitute an inflection point on the 'O_2 titration curve' in Figure 6.1B. In contrast, the oceanic and atmospheric O_2 levels are reversible by, for example, changes in the primary productivity or volcanic outgassing of reduced gases.

To verify which of the two scenarios is correct, it is important to develop more atmospheric redox proxies coupled with atmospheric modeling to refine our understanding of the atmospheric O_2 trajectory during the GOE and other periods. The current geochemical toolbox entails a whole suite of marine redox proxies, improving interpretations of marine redox evolution compared to atmospheric oxygen evolution, which only encompasses a few atmospheric O_2 proxies. Therefore, it is critical to develop more atmospheric redox proxies to investigate whether the GOE is oscillating or sudden in nature, and one possibility in this respect is to investigate mass-independent isotope fractionation in other isotopic systems than sulfur. From a theoretical perspective, the primary mechanism leading to MIF signatures in the atmosphere is UV radiation, and this mechanism is not bound to sulfur isotopes alone (Albarède, 2015; Velivetskaya et al., 2020). Consequently, there is the possibility that other isotope systems may exhibit MIF behavior and also be recorded in the geological record. Any potential candidate to record a MIF signature should be volatile at atmospheric temperatures, must have low bond dissociation energies and thus be susceptible to MIF generation by UV radiation, undertake chemical forms with specific UV radiation wavelength sensitivity, be stable over geological time and record an abundant enough sedimentary MIF signal to be distinguished from any background MDF sources.

There are several isotope systems that fulfill or partially fulfill these requirements, and very importantly, their MIF to MDF switch might occur at slightly different O_3 concentrations compared to MIF-S. Hence, they could track whether the GOE took an oscillating or a sudden

path. If all these MIF signatures disappear at a single point in time, O_2 concentrations likely rapidly surged at the time of MIF-S disappearance. In contrast, if various MIF signals disappear or reappear systematically through the Neoarchean and Paleoprotezoic, the O_2 trajectory probably took an oscillating path.

Atmospheric Se species possess bond dissociation energies that could be broken by UV radiation and are particularly interesting because Se, like S, is part of the chalcogen group on the periodic table of elements. Thus, Se geochemically behaves very similar to sulfur, and it is therefore feasible that Se would act similarly under low ozone conditions (Stüeken et al., 2015; Stüeken, 2017). However, research has shown that despite Se's promising MIF avenue, no MIF-Se signals were found in shales aged 2.1 to 1.8 Ga (Kipp et al., 2020). Based on the logic that the elements requiring the least energy to undergo photodissociation would first lose their MIF signature, a potential explanation could be that Se species in the atmosphere changed from H_2Se to SeO_2 in a pre and post-GOE world. SeO_2 is expected to photodissociate at wavelengths of ~278 nm in contrast to the ~383 nm for H_2Se, as calculated from its bond dissociation energies reported in Luo and Kerr (2012), using equation 1. Since SeO_2 photodissociates at a shorter wavelength than that calculated for H_2Se (~383 nm) but higher than that for SO_2 (~231 nm), it could be beneficial to explore for MIF-Se signatures in shales around 2.4–2.3 Ga, which could yield valuable information for the tempo and mode for the GOE.

$$\lambda = \frac{ch}{B} * 10^9 \quad (1)$$

Where λ is the wavelength required for photodissociation in nm, c is the speed of light in m/s, *h* is the plank's constant in joule-seconds, and B is the bond dissociation energy in joules.

Another element of interest is mercury, which also exhibits low bond dissociation energies, is highly volatile and can undergo several different photochemical reactions, which could lead to MIF-Hg generation (Bergquist & Blum, 2009; Lin & Pehkonen, 1999). In fact, MIF-Hg signals above 6 ‰ have already been experimentally observed (Bergquist & Blum, 2009). In the Archean and Paleoproterozoic geological record, MIF-Hg signals have so far been identified in the ~2.5 Ga upper Naugua Formation in Griqualand West Basin of the Transvaal Supergroup in South Africa (Zerkle et al., 2020). However, such signals were notably absent in the similarly aged (~2.5 Ga) Mount McRae shale Hamersley Group in Australia (Blum & Anbar, 2010). These initial observations of MIF-Hg patterns indicate that MIF-Hg signals may be influenced by local environmental factors (e.g., oxygen oases or depositional effects) or short-lived

oscillations in atmospheric ozone generation. Considering that the Duitschland and Rooihoogte formations record some of the largest and most apparent MIF-S signals in the geological record, these two contemporaneous formations represent a natural place to continue the search for MIF-Hg signals.

Two non-traditional candidates proposed herein that are potentially capable of recording MIF signatures are chlorine and bromine. Atmospheric Cl-species hold bond dissociation energies sensitive to specific UV wavelengths, it is abundant in natural environments, particularly in the ocean and, like sulfur, is found in several chemical forms (Eggenkamp, 2014). Bromine, also being a halogen, behaves geochemically very similar to Cl, thus making Br a viable target for MIF signature investigations. In addition, the relatively low abundance of Br in natural environments enhances the detectability of MIF-Br, as a smaller fraction of the marine Br reservoir would need to undergo MIF conversion to remain distinguishable geochemically. An important aspect to consider if one would hypothetically explore MIF-Cl and MIF-Br signatures is that both systems only possess two stable isotopes. Therefore, their mass-independent fractionation cannot be depicted similarly to S, Se and Hg, which have multiple stable isotopes (e.g. $^{34/32}$S vs $^{33/32}$S). For these elements, a mass-dependent fractionation line could be defined using ratios like $^{81/79}$Br vs $^{37/35}$Cl, in a similar approach to that used for isotope systems with multiple stable isotopes. For the case of Cl and Br, instead of leveraging on the traditional method, one could utilize the strong geochemical similarities between the halogens Cl and Br and assume the same biogeochemical pathways from the atmosphere to sedimentary deposits. Under this assumption, establishing a $^{81/79}$Br vs $^{37/35}$Cl MDF line with an expected slope of ~1 would theoretically be possible. Any deviation from this line could then be interpreted as a MIF signal.

6.4 References

Albarède, F. (2015). Fractionation, Mass Independent and Dependent. *Encyclopedia of Astrobiology*, 1052.

Barley, M., Pickard, A., & Sylvester, P. (1997). Emplacement of a large igneous province as a possible cause of banded iron formation 2.45 billion years ago. *Nature*, *385*(6611), 55-58.

Bergquist, B. A., & Blum, J. D. (2009). The odds and evens of mercury isotopes: applications of mass-dependent and mass-independent isotope fractionation. *Elements*, *5*(6), 353-357.

Beukes, N. J., & Gutzmer, J. (2008). Origin and paleoenvironmental significance of major iron formations at the Archean-Paleoproterozoic boundary.

Blum, J. D., & Anbar, A. D. (2010). Mercury isotopes in the late Archean Mount McRae Shale. Geochimica et Cosmochimica Acta,

Cheney, E. (1996). Sequence stratigraphy and plate tectonic significance of the Transvaal succession of southern Africa and its equivalent in Western Australia. *Precambrian Research*, *79*(1-2), 3-24.

de Kock, M. O., Evans, D. A., & Beukes, N. J. (2009). Validating the existence of Vaalbara in the Neoarchean. *Precambrian Research*, *174*(1-2), 145-154.

Eggenkamp, H. (2014). *The geochemistry of stable chlorine and bromine isotopes*. Springer.

Hawkesworth, C. J., Cawood, P. A., & Dhuime, B. (2016). Tectonics and crustal evolution. *GSA today*.

Khan Academy. (2008). *Acid-base titration curves*. https://www.khanacademy.org/test-prep/mcat/chemical-processes/titrations-and-solubility-equilibria/a/acid-base-titration-curves

Kipp, M. A., Algeo, T. J., Stüeken, E. E., & Buick, R. (2020). Basinal hydrographic and redox controls on selenium enrichment and isotopic composition in Paleozoic black shales. *Geochimica et Cosmochimica Acta*, *287*, 229-250.

Knoll, A. H., Canfield, D. E., & Konhauser, K. O. (2012). *Fundamentals of geobiology*. John Wiley & Sons.

Lin, C.-J., & Pehkonen, S. O. (1999). The chemistry of atmospheric mercury: a review. *Atmospheric environment*, *33*(13), 2067-2079.

Luo, Y.-R., & Kerr, J. A. (2012). Bond dissociation energies. *CRC handbook of chemistry and physics*, *89*, 89.

Schröder, S., Beukes, N. J., & Armstrong, R. A. (2016). Detrital zircon constraints on the tectonostratigraphy of the Paleoproterozoic Pretoria Group, South Africa. *Precambrian Research*, *278*, 362-393.

Struck, U. (2011). On the use of stable nitrogen isotopes in present and past anoxic environments. In *Anoxia: Evidence for Eukaryote Survival and Paleontological Strategies* (pp. 497-513). Springer.

Stüeken, E., Buick, R., Bekker, A., Catling, D., Foriel, J., Guy, B., Kah, L., Machel, H., Montañez, I., & Poulton, S. (2015). The evolution of the global selenium cycle: Secular trends in Se isotopes and abundances. *Geochimica et Cosmochimica Acta*, *162*, 109-125.

Stüeken, E. E. (2017). Selenium isotopes as a biogeochemical proxy in deep time. *Reviews in Mineralogy and Geochemistry*, *82*(1), 657-682.

Velivetskaya, T., Ignatiev, A., & Yakovenko, V. (2020). Mass-independent sulfur isotope fractionation in the photochemical SO 2 processes under the UV radiation of different wave length. *Geochemistry International*, *58*, 1228-1238.

Zeh, A., Wilson, A. H., & Gerdes, A. (2020). Zircon U-Pb-Hf isotope systematics of Transvaal Supergroup – Constraints for the geodynamic evolution of the Kaapvaal Craton and its hinterland between 2.65 and 2.06 Ga. *Precambrian Research*, *345*, doi.org/10.1016/j.precamres.2020.105760. https://doi.org/10.1016/j.precamres.2020.105760

Zerkle, A. L., Yin, R., Chen, C., Li, X., Izon, G. J., & Grasby, S. E. (2020). Anomalous fractionation of mercury isotopes in the Late Archean atmosphere. *Nature communications*, *11*(1), 1709.

Chapter 7

Conclusions

This chapter highlights the core discoveries of the three primary chapters of this thesis (Chapters 3, 4, 5), while the reader is directed to any specific chapters for sub-conclusions.

The Duitschland and Rooihoogte formations represent different sedimentary expressions of the same sedimentary sequence deposited at varying distances to the paleoshoreline. Therefore, the disappearance of MIF-S within these two formations should be interpreted as indicative of a single atmospheric change rather than an oscillating dynamic. This conclusion is reached based on an integrated assessment of sedimentological observations from 11 stratigraphic sections spanning the entire Transvaal Area and extending into the Kanye Basin of Botswana, combined with comprehensive geochemical data from four scientific quality drill cores. The geochemical data (major and trace elements, Sr-Nd isotope compositions, plus zircon ages and patterns) exhibit no discernible difference between the two formations, thus reinforcing the sedimentological observations. Very importantly, neither of the arguments presented excludes a decoupled depositional scenario. However, the integrated and accumulated weight of the entire body of sedimentological and geochemical observations strongly suggests a contemporaneous deposition of the Duitschland and Rooihoogte formations.

During the deposition of the Duitschland and Rooihoogte formations, atmospheric oxygenation is proposed to have driven marine deoxygenation. This conclusion is derived from a basin-wide integration of geochemical redox proxies, including RSTE systematics, total S, total organic carbon, $\delta^{13}C$, $\delta^{34}S$ and $\delta^{98}Mo$ data, which all indicate an environmental change from oxic-suboxic conditions to suboxic-anoxic conditions bracketing the disappearance of MIF-S. The combined trend of increased Fe/Mn ratios, elevated total S and organic C contents coupled with a negative trend in $\delta^{13}C$ and $\delta^{34}S$ and in conjunction with a shift to heavier $\delta^{98}Mo$ values, implies a decline in the marine oxygenation following the disappearance of MIF-S. These observations suggest a causal link between atmospheric oxygenation and declining marine O_2 levels through geobiological feedbacks. It remains to be determined if the observed trends represent a global phenomenon or are constrained to the Transvaal Supergroup.

The genesis of the Hotazel Formation is best explained by the expansion and contraction of oxygen minimum zones driven by fluctuations in primary productivity rates and relative sea level change. This depositional model suggests the existence of fully developed OMZs prior to atmospheric oxygenation and infers that on the 2.5 Ga Neoarchean continental shelves, vertical oxygen gradients similar to those observed in modern environments were, at least locally, operational. This new model is proposed because neither of the commonly proposed scenarios, involving either upwelling or a shallow marine hydrothermal vent system, can effectively explain both sedimentological and geochemical observations. The proposed *Bioproductivity Hypothesis* is grounded in the redox-induced shuttling of iron and manganese through the oxygen minimum zone, facilitated by OMZ-redirection. This mechanism effectively drives δ^{56}Fe values towards progressively lighter values, while trapping isotopically light Mo adsorbed to initially precipitated Mn(hydr)oxides within the OMZ. At the same time, the process of OMZ-redirection accounts for the inverse depositional order of Fe and Mn layers relative to typical redox dynamics.